

New Rare Earth Ion-Doped Hosts for Broadband Fibre Amplifier

By

Shaoxiong Shen

Submitted in accordance with the requirements for the degree of
Doctor of Philosophy

University of Leeds
Department of Materials
November 2000

The candidate confirms that the work submitted is his own and
that appropriate credit has been given where reference has been
made to the work of others

Acknowledgements

The author would like to express his gratitude to Professor Animesh Jha, research supervisor, for his guidance and encouragement throughout this investigation and the preparation of this thesis. Special thanks are also due to Dr Mira Naftaly for her assistance of glass measurement and invaluable discussion during the research and preparation of this thesis.

I sincerely express my thanks to all my colleagues in the Leeds Photonic Materials Research Group for their co-operation; specially I am thankful to Mr Austin Wilson, Mr Mo Javed and Ms Diane Bavister for their help in the preparation of polishing glass and light microscopy. The thesis contains a significant part on Raman spectroscopy, which could not have been realised without the help and guidance given by Prof. Rui Almeida and Dr L Santos at INESC, Lisbon.

Financial support from ORS, Tetley and Lupton scholarship is gratefully acknowledged. I also wish to thank Optiglass company and NORTEL NETWORKS for supporting me in the 4th year of my PhD thesis.

Finally, thanks to my wife, Aijun Wang, who has looked after me and greatly supported me for the last a few years.

Without the assistance of all mentioned above, this work would not have come to fruition.

Abstract

Three kinds of oxide glasses doped with Er^{3+} ions were chosen for investigation. Both the properties of glass and fluorescence from rare earth dopant ions are measured and discussed.

In Er^{3+} ion doped silicate glass, the changes in the structure of glass as a result of fluorine addition are studied by measuring the glass properties: density, molar volume, refractive index, IR and UV edges. The absorption and emission cross-sections of Er^{3+} ion increase with increasing value of F/O ratio as do the full width of half maximum (FWHM) and figure-of-merit (FOM) for gain and bandwidth.

In Er^{3+} ion doped heavy metal germanate glass, the structural units of forming network in germanate glass change with the addition of PbO , Bi_2O_3 , Ga_2O_3 and TeO_2 . The molar volume, glass transition temperature T_g , IR and UV edges have been measured and discussed with the relation of glass structure. More Er^{3+} ion sites result in the increase of absorption and emission cross-sections, emission FWHM and FOM for gain.

In Er^{3+} doped $\text{TeO}_2 - \text{ZnO} - \text{R}_2\text{O}$ ($\text{R}_2\text{O} = \text{Li}_2\text{O}$, Na_2O and K_2O) tellurite glass system, glass properties such as density, molar volume, transition temperature T_g , IR and UV edges are measured and discussed. The glass structure has been characterised using Raman spectra. The role of F^- and Cl^- has also been studied in tellurite glass. Crystallisation kinetics has been analysed in tellurite glass using isothermal and non-isothermal methods. The properties of Er^{3+} absorption and emission have been measured and discussed with the change of glass structure and concentrations. FOM for gain and bandwidth have also been compared and discussed in Er^{3+} doped modifies silicate, HMO germanate, tellurite and ZBLAN fluoride glasses. The tellurite glass fibre has been made and the emission spectra of Er^{3+} ion in fibre have been measured.

Absorption and emission spectra have been studied in Tm^{3+} -doped tellurite glass, it shows to be a highly promising host for a $1.47 \mu\text{m}$ amplifier capable of providing extended short-wavelength gain and a continuous band with the tellurite EDFA. Nd^{3+} -doped tellurite and silicate glasses have also been studied, amplifier operating around $1.34 \mu\text{m}$ is clearly desirable in tellurite glass. A continuous gain band extending from 1310 to 1600 nm may become possible by using Nd^{3+} , Tm^{3+} and Er^{3+} amplifiers.

CONTENTS

Chapter 1 Introduction	1
1.1 Er ³⁺ -doped glass amplifiers at 1.5 μm	1
1.2 Development of broadband amplifiers.....	6
1.3 Rare-earth doped host materials for amplifier.....	7
1.4 Outline of this thesis.....	12
References.....	14
Chapter 2 Literature review	15
2.1 Er ³⁺ -doped silicate glass.....	15
2.2 Er ³⁺ ion sites in silicate glass.....	16
2.3 Er ³⁺ doped germanate glasses.....	19
2.4 Rare earth doped tellurite glasses.....	21
2.5 Objectives of the research.....	25
References.....	26
Chapter 3 Theory of radiative and non-radiative transitions of rare earth ions in glass	31
3.1 Radiative rates.....	31
3.2 Non-radiative transition.....	39
3.2.1 Multiphonon relaxation	39
3.2.2 Energy transfer.....	41
3.3 Pump wavelengths for Er ³⁺ -doped fibre amplifier (EDFA).....	44
References.....	47
Chapter 4 Experimental procedure	48
4.1 Preparation of bulk glass.....	48
4.2 Density measurement.....	49
4.3 Thermal characterisation.....	49
4.4 UV-VIS and FTIR absorption measurement.....	52

4.5 Fluorescence and lifetime.....	53
4.6 Raman spectrum.....	54
Chapter 5 Er³⁺-doped heavy metal oxide germanate glasses.....	57
5.1 Glass compositions.....	57
5.2 Absorption in the UV.....	59
5.3 Absorption in the IR.....	61
5.4 Molar volume and thermal properties of glass.....	63
5.5 Absorption and emission spectra of Er ³⁺ ion doped HMO germanate glasses at 1.5 μm.....	65
5.6 Discussion.....	66
5.7 Conclusions.....	70
References.....	71
Chapter 6 Er³⁺-doped modified silicate glasses.....	72
6.1 Glass composition.....	72
6.2 Molar volume and refractive index in glasses.....	73
6.3 UV edge and IR cut-off.....	75
6.4 Er ³⁺ ion absorption and fluorescence properties at 1.5 μm.....	77
6.5 Discussion.....	80
6.6 Conclusions.....	83
References.....	83
Chapter 7 Physical properties and structure of tellurite glass.....	84
7.1 Density and molar volume of tellurite glass.....	84
7.2 Thermal analysis.....	87
7.2.1 Tellurite glass transition temperature and thermal stability.....	87
7.2.2 Crystallization kinetics of tellurite glasses.....	93
7.2.2.1 Isothermal crystallization.....	93
7.2.2.2 Non-isothermal crystallization.....	99
7.2.2.3 Conclusions of crystallization kinetics.....	100

7.3 Optical properties.....	103
7.3.1 Absorption in the UV.....	103
7.3.2 Absorption in the IR.....	106
7.3.3 The intrinsic loss in tellurite glass.....	106
7.4 Raman spectra of tellurite glass.....	111
7.4.1 Introduction to Raman spectroscopy.....	111
7.4.2 Raman spectrum results in tellurite glasses.....	113
7.4.3 Discussion of Raman spectra	122
7.4.3.1 Intermediate and high frequency range (200-1000 cm^{-1}).....	122
7.4.3.2 Low frequency range ($< 200 \text{ cm}^{-1}$).....	135
7.5 Conclusions.....	138
Reference.....	139
Chapter 8 Properties of Er^{3+} doped tellurite glass.....	141
8.1 Physical properties change with various Er^{3+} concentration.....	141
8.1.1 UV cutoff.....	141
8.1.2 Density and molar volume	141
8.1.3 Glass transition property.....	143
8.1.4 Discussion of the role of Er_2O_3	143
8.2 Er^{3+} absorption spectrum in tellurite glass.....	145
8.2.1 Er^{3+} absorption spectra in $\text{TeO}_2\text{-ZnO-R}_2\text{O}$ ($\text{R}_2\text{O} = \text{Li}_2\text{O}, \text{Na}_2\text{O}$ and K_2O) system glass.....	146
8.2.2 Er^{3+} absorption spectra in tellurite glass modified by heavy metal oxides	151
8.2.3 Er^{3+} absorption spectra in tellurite glass modified by chloride and fluoride.....	152
8.2.4 Er^{3+} absorption spectra in different kinds of glass.....	157
8.3 Er^{3+} fluorescence properties in tellurite glass.....	161
8.3.1 Er^{3+} fluorescence properties in a tellurite glass with.....	161
8.3.1.1 Emission spectra.....	161
8.3.1.2 Oscillator strengths and radiative rate.....	163
8.3.1.3 Er^{3+} concentration quenching and OH^- impurity effect.....	165
8.3.2 Er^{3+} fluorescence properties in tellurite glass with different	

composition and the same Er^{3+} ion concentration.....	171
8.3.2.1 Er^{3+} emission spectra and lifetimes in $\text{TeO}_2\text{-ZnO-R}_2\text{O}$ ($\text{R}_2\text{O} = \text{Li}_2\text{O}, \text{Na}_2\text{O}$ and K_2O) system glass.....	171
8.3.2.2 Er^{3+} emission spectra and lifetimes in tellurite glass modified by heavy metal oxides.....	175
8.3.2.3 Er^{3+} emission spectra and lifetimes in tellurite glass modified by chloride and fluoride.....	177
8.3.2.4 Er^{3+} emission spectra and lifetimes in different kinds of glasses.....	179
8.3.2.5 Emission spectra in Er^{3+} doped tellurite glass fibre.....	181
8.3.3 Discussion.....	183
8.3.3.1 Absorption and emission spectra in Er^{3+} doped glasses.....	183
8.3.3.2 OH^- broadening.....	187
8.3.3.3 Lifetime change in glass.....	188
8.4 Conclusions.....	191
References.....	192

Chapter 9 Tm^{3+} -doped tellurite glass for a broadband

amplifier at 1.46 μm193

9.1 Absorption spectrum of Tm^{3+}	194
9.2 Fluorescent properties of Tm^{3+}	195
9.3 Broadband amplifiers.....	200
9.3.1 Tm^{3+} - Er^{3+} amplifier.....	200
9.3.2 Nd^{3+} - Tm^{3+} - Er^{3+} amplifier.....	201
9.4 Conclusions.....	205
References.....	206

Chapter 10 Recommendations for further work.....208

Appendix.....	209
Publications	209
Patents.....	210

Diagrams

Figure 1.1 A diagram of a conventional optical fibre transmission system with electrically regenerative repeaters.

Figure 1.2 A long distance transmission system with fibre amplifier repeaters.

Figure 1.3 Optical losses of the UV edge, IR edge and the intrinsic scattering losses in vitreous silica, together with the experimental loss curve.

Figure 1.4 Absorption cross section of Er^{3+} in Ed-2 silicate.

Figure 1.5 Energy level and transitions of Er^{3+} in Ed-2 silicate.

Figure 1.6 Some 1.5 μm absorption cross section spectra for different glass types.

Figure 1.7 Some 1.5 μm emission spectra for different glass types.

Figure 3.1 Effect of different terms in Hamilton on energy level positions.

Figure 3.2 Absorption cross-section of Er^{3+} in 80 TeO_2 -10 Na_2O -10 ZnO glass.

Figure 3.3 Three types of energy transfer.

Figure 3.4 The cooperative up-conversion process of Er^{3+} ion.

Figure 3.5 Several gain degradation processes associated with pumping schemes.

Figure 4.1 Principle of DSC

Figure 4.2. Set-up of measuring rare-earth fluorescent properties.

Figure 4.3. Set-up of Raman spectrometer.

Figure 5.1 UV absorption edge in HMO germanate glasses.

Figure 5.2 IR absorption edge in HMO germanate glasses.

Figure 5.3 Molar volume and T_g change with GeO_2 content.

Figure 5.4 Er^{3+} ion absorption cross-section spectra in HMO germanate glasses.

Figure 5.5 Er^{3+} ion absorption cross-section at 1530 nm and the ratio of the shoulder at 1480 nm against peak.

Figure 5.6 Er^{3+} ion emission spectra in HMO germanate glasses.

Figure 5.7 Figure-of-merit for gain and FWHM in HMO germanate glasses.

Figure 6.1 Density and molar volume change with F/O ratio.

Figure 6.2 Refractive index change with F/O ratio.

Figure 6.3 UV absorption edge in modified silicate glasses.

Figure 6.4 IR absorption edge in modified silicate glasses.

Figure 6.5 Absorption and emission cross sections change with F/O ratio.

Figure 6.6 Integrated absorption change with F/O ratio.

Figure 6.7 Normalised emission spectra of Er^{3+} ion in silicate glass with various F/O ratio.

Figure 6.8 FWHM change with F/O ratio.

Figure 6.9 Lifetime change with F/O ratio.

Figure 6.10 Figure-of-merit for gain and bandwidth change with F/O ratio.

Figure 7.1 Densities and molar volumes change with Na_2O concentration.

Figure 7.2 Density change with alkali content in tellurite glass.

Figure 7.3 Molar volume change with alkali content in tellurite glass.

Figure 7.4 Density change with ZnO content in tellurite glass.

Figure 7.5 Molar volume change with ZnO content in tellurite glass.

Figure 7.6 Typical DSC curve in glass.

Figure 7.7 T_g change with alkali content in tellurite glass.

Figure 7.8 $T_x - T_g$ change with alkali content in tellurite glass.

Figure 7.9 T_g change with ZnO concentration in tellurite glass.

Figure 7.10 $T_x - T_g$ change with ZnO concentration in tellurite glass.

Figure 7.10a DTA curve of $80\text{TeO}_2-10\text{Na}_2\text{O}-10\text{ZnO}$ glass.

Figure 7.11 Isothermal DSC traces of TN tellurite glass.

Figure 7.12 Isothermal DSC traces of TNZ tellurite glass.

Figure 7.13 Fraction of crystallised x as a function of time in TN glass.

Figure 7.14 Fraction of crystallised x as a function of time in TNZ glass.

Figure 7.15 JMA equation plots for isothermal crystallisation in TN glass.

Figure 7.16 JMA equation plots for isothermal crystallisation in TNZ glass.

Figure 7.17 $\ln k$ vs $1/T_{\text{iso}}$ for TN glass.

Figure 7.18 $\ln k$ vs $1/T_{\text{iso}}$ for TNZ glass.

Figure 7.19 TTT plots for different values of fraction crystallised x in TN glass.

Figure 7.20 TTT plots for different values of fraction crystallised x in TNZ glass.

Figure 7.21 DTA traces at various heating rates in TN glass.

Figure 7.22 DTA traces at various heating rates in TNZ glass.

Figure 7.23 $\ln T_p^2/\alpha$ vs $1/T_p$ for non-isothermal crystallization of tellurite glasses.

Figure 7.24 Plots of Eq.4.7 at various heating rates in TN glass.

Figure 7.25 Plots of Eq.4.7 at various heating rates in TNZ glass.

Figure 7.26 UV edge absorption in $(90-x) \text{TeO}_2 - x\text{Na}_2\text{O} - 10\text{ZnO}$ ($x = 0, 10, 20$ and 30) glass.

Figure 7.27 UV cut-off change with alkali oxide content in $(90-x) \text{TeO}_2 - x\text{R}_2\text{O} - 10\text{ZnO}$ ($\text{R}_2\text{O} = \text{Li}_2\text{O}, \text{Na}_2\text{O}$ and K_2O , $x = 0, 10, 20$ and 30) glass.

Figure 7.28 UV cut-off change with ZnO content in $(89-x) \text{TeO}_2 - 10\text{Na}_2\text{O} - x\text{ZnO} - 1\text{Er}_2\text{O}_3$ ($x = 4, 9, 14$ and 19) glass.

Figure 7.29 IR edge absorption in $(90-x) \text{TeO}_2 - x\text{Na}_2\text{O} - 10\text{ZnO}$ ($x=0, 10, 20$ and 30) glass.

Figure 7.30 IR cut-off change with alkali oxide content in $(90-x) \text{TeO}_2 - x\text{R}_2\text{O} - 10\text{ZnO}$ ($\text{R}_2\text{O} = \text{Li}_2\text{O}, \text{Na}_2\text{O}$ and K_2O , $x = 0, 10, 20$ and 30) glass.

Figure 7.31 IR cut-off change with ZnO content in $(89-x) \text{TeO}_2 - 10\text{Na}_2\text{O} - x\text{ZnO} - 1\text{Er}_2\text{O}_3$ ($x = 4, 9, 14$ and 19) glass.

Figure 7.32a UV edge fitting of TNZ glass.

Figure 7.32b IR edge fitting of TNZ glass.

Figure 7.32c V-curve of loss in tellurite glass.

Figure 7.33 Raman spectrum of TeO_2 crystal powder.

Figure 7.34 Raman spectra in $10\text{-}200 \text{ cm}^{-1}$ range of $(90-x) \text{TeO}_2 - x\text{Na}_2\text{O} - 10\text{ZnO}$ ($x = 0, 10, 20$ and 30) glass.

Figure 7.35 Raman spectra in $300\text{-}1000 \text{ cm}^{-1}$ range of $(90-x) \text{TeO}_2 - x\text{Na}_2\text{O} - 10\text{ZnO}$ ($x = 0, 10, 20$ and 30) glass.

Figure 7.36 Raman spectra in $10\text{-}200 \text{ cm}^{-1}$ range of $70\text{TeO}_2 - 20\text{X} - 10\text{ZnO}$ ($\text{X} = \text{ZnO}, \text{Li}_2\text{O}, \text{Na}_2\text{O}$ and K_2O) glass.

Figure 7.37 Raman spectra in $300\text{-}1000 \text{ cm}^{-1}$ range of $70\text{TeO}_2 - 20\text{X} - 10\text{ZnO}$ ($\text{X} = \text{ZnO}, \text{Li}_2\text{O}, \text{Na}_2\text{O}$ and K_2O) glass.

Figure 7.38 Raman spectra in $10\text{-}200 \text{ cm}^{-1}$ range of $80\text{TeO}_2 - 10\text{Na}_2\text{O} - 10\text{X}$ ($\text{X} = \text{K}_2\text{O}, \text{BaO}, \text{Ga}_2\text{O}_3, \text{GeO}_2, \text{Nb}_2\text{O}_5$ and WO_5) glass.

Figure 7.39 Raman spectra in $200\text{-}1000 \text{ cm}^{-1}$ range of $80\text{TeO}_2 - 10\text{Na}_2\text{O} - 10\text{X}$ ($\text{X} = \text{K}_2\text{O}, \text{BaO}, \text{Ga}_2\text{O}_3, \text{GeO}_2, \text{Nb}_2\text{O}_5$ and WO_3) glass.

Figure 7.40 Raman spectra in $10\text{-}200 \text{ cm}^{-1}$ range of $80\text{TeO}_2 - 20\text{X}$ ($\text{X} = \text{Na}_2\text{O}, \text{NaCl}$ and NaF) glass.

Figure 7.41 Raman spectra in $200\text{-}1000 \text{ cm}^{-1}$ range of $80\text{TeO}_2 - 20\text{X}$ ($\text{X} = \text{Na}_2\text{O}, \text{NaCl}$ and NaF) glass.

Figure 7.42 Raman spectra in 10-200 cm^{-1} range of $80\text{TeO}_2 - 10\text{Na}_2\text{O} - 10\text{X}$ ($\text{X} = \text{BaO}, \text{BaCl}_2$ and BaF_2) glass.

Figure 7.43 Raman spectra in 200-1000 cm^{-1} range of $80\text{TeO}_2 - 10\text{Na}_2\text{O} - 10\text{X}$ ($\text{X} = \text{BaO}, \text{BaCl}_2$ and BaF_2) glass.

Figure 7.44 Structure units in tellurite glass.

Figure 7.45 Raman intensities of 5 deconvoluted peaks in $(90-x)\text{TeO}_2 - x\text{Na}_2\text{O} - 10\text{ZnO}$ ($x = 0, 10, 20$ and 30) glass.

Figure 7.46 Peak intensity ratio of Raman spectra in $(90-x)\text{TeO}_2 - x\text{Na}_2\text{O} - 10\text{ZnO}$ ($x = 0, 10, 20$ and 30) glass.

Figure 7.47 Raman intensities of 5 deconvoluted peaks in $70\text{TeO}_2 - 20\text{X} - 10\text{ZnO}$ ($\text{X} = \text{ZnO}, \text{Li}_2\text{O}, \text{Na}_2\text{O}$ and K_2O) glass.

Figure 7.48 Peak intensity ratio of Raman spectra in $70\text{TeO}_2 - 20\text{X} - 10\text{ZnO}$ ($\text{X} = \text{ZnO}, \text{Li}_2\text{O}, \text{Na}_2\text{O}$ and K_2O) glass.

Figure 7.49 Schematic representation of $(\text{Te}_3\text{O}_8^{4-})_n$ structural units.

Figure 7.50 Raman intensities of 5 deconvoluted peaks in $80\text{TeO}_2 - 10\text{Na}_2\text{O} - 10\text{X}$ ($\text{X} = \text{K}_2\text{O}, \text{BaO}, \text{Ga}_2\text{O}_3, \text{GeO}_2, \text{Nb}_2\text{O}_5$ and WO_3) glass.

Figure 7.51 Peak intensity ratio of Raman spectra in $80\text{TeO}_2 - 10\text{Na}_2\text{O} - 10\text{X}$ ($\text{X} = \text{K}_2\text{O}, \text{BaO}, \text{Ga}_2\text{O}_3, \text{GeO}_2, \text{Nb}_2\text{O}_5$ and WO_3) glass.

Figure 7.52 Raman intensities of 5 deconvoluted peaks in $80\text{TeO}_2 - 20\text{X}$ ($\text{X} = \text{Na}_2\text{O}, \text{NaCl}$ and NaF) glass.

Figure 7.53 Peak intensity ratio of Raman spectra in $80\text{TeO}_2 - 20\text{X}$ ($\text{X} = \text{Na}_2\text{O}, \text{NaCl}$ and NaF) glass.

Figure 7.54 Raman intensities of 5 deconvoluted peaks in $80\text{TeO}_2 - 10\text{Na}_2\text{O} - 10\text{X}$ ($\text{X} = \text{BaO}, \text{BaCl}_2$ and BaF_2) glass.

Figure 7.55 Peak intensity ratio of Raman spectra in $80\text{TeO}_2 - 10\text{Na}_2\text{O} - 10\text{X}$ ($\text{X} = \text{BaO}, \text{BaCl}_2$ and BaF_2) glass.

Figure 8.1 UV edge absorption in tellurite glass with Er_2O_3 concentration.

Figure 8.2 Density and molar volume change with Er_2O_3 concentration in tellurite glass.

Figure 8.3 T_g, T_x, T_p and $T_x - T_g$ of tellurite glass change with $s \text{Er}_2\text{O}_3$ concentration.

Figure 8.4 Schematic representation of Er^{3+} ions in $\text{TeO}_2\text{-ZnO-Na}_2\text{O}$ glass.

Figure 8.5 Er^{3+} ion absorption spectra in $(90-x)\text{TeO}_2 - x\text{Na}_2\text{O} - 9\text{ZnO} - 1\text{Er}_2\text{O}_3$ ($x = 0, 10, 20$ and 30) glass.

- Figure 8.6 Er^{3+} ion absorption cross-sections change with various Na_2O concentration in tellurite glass.
- Figure 8.7 Er^{3+} ion absorption peak ratio change with various Na_2O concentration in tellurite glass.
- Figure 8.8 Er^{3+} ion absorption cross-sections change with various Li_2O concentration in tellurite glass.
- Figure 8.9 Er^{3+} ion absorption peak ratio change with various Li_2O concentration in tellurite glass.
- Figure 8.10 Er^{3+} ion absorption cross-sections change with various K_2O concentration in tellurite glass.
- Figure 8.11 Er^{3+} ion absorption peak ratio change with various K_2O concentration in tellurite glass.
- Figure 8.12 Er^{3+} ion absorption spectra in $70\text{TeO}_2 - 20\text{R}_2\text{O} - 9\text{ZnO} - 1\text{Er}_2\text{O}_3$ ($\text{R}_2\text{O} = \text{Li}_2\text{O}, \text{Na}_2\text{O}$ and K_2O) glass.
- Figure 8.13 Er^{3+} ion absorption cross-sections in $70\text{TeO}_2 - 20\text{R}_2\text{O} - 9\text{ZnO} - 1\text{Er}_2\text{O}_3$ ($\text{R}_2\text{O} = \text{Li}_2\text{O}, \text{Na}_2\text{O}$ and K_2O) glass.
- Figure 8.14 Er^{3+} ion absorption peak ratio change with different alkali oxides in $70\text{TeO}_2 - 20\text{R}_2\text{O} - 9\text{ZnO} - 1\text{Er}_2\text{O}_3$ ($\text{R}_2\text{O} = \text{Li}_2\text{O}, \text{Na}_2\text{O}$ and K_2O) glass.
- Figure 8.15 Er^{3+} ion absorption cross-sections change with various ZnO concentration in tellurite glass.
- Figure 8.16 Er^{3+} ion absorption peak ratio change with various ZnO concentration in tellurite glass.
- Figure 8.17 Er^{3+} ion absorption spectra in $80.5\text{TeO}_2 - 10\text{Na}_2\text{O} - 9\text{X} - 0.5\text{Er}_2\text{O}_3$ ($\text{X} = \text{BaO}, \text{BaCl}_2$ and BaF_2) glass.
- Figure 8.18 Er^{3+} ion absorption cross-sections change in $80.5\text{TeO}_2 - 10\text{Na}_2\text{O} - 9\text{X} - 0.5\text{Er}_2\text{O}_3$ ($\text{X} = \text{BaO}, \text{BaCl}_2$ and BaF_2) glass.
- Figure 8.19 Er^{3+} ion absorption peak ratio change in $80.5\text{TeO}_2 - 10\text{Na}_2\text{O} - 9\text{X} - 0.5\text{Er}_2\text{O}_3$ ($\text{X} = \text{BaO}, \text{BaCl}_2$ and BaF_2) glass.
- Figure 8.20 Er^{3+} ion absorption spectra in different kind of glasses.
- Figure 8.21 Dipole pattern of Er^{3+} ion.
- Figure 8.22 Er^{3+} ion emission spectra with various Er_2O_3 concentration in $80\text{TeO}_2 - 10\text{Na}_2\text{O} - 10\text{ZnO}$ glass.
- Figure 8.23 Er^{3+} ion absorption and emission cross-sections measured and calculated from McCumber theory in tellurite glass.

Figure 8.24 Er^{3+} ion emission spectra with 3.5 wt% Er_2O_3 in tellurite glass with different pump position.

Figure 8.25 Jud-Ofelt parameters in tellurite glass with various Er_2O_3 concentration.

Figure 8.26 Lifetimes for ${}^4\text{I}_{13/2}$ - ${}^4\text{I}_{15/2}$ transition at 1.5 μm as a function of the Er_2O_3 concentration in tellurite glass.

Figure 8.27 OH^- absorption spectra in tellurite glass melted in different atmosphere.

Figure 8.28 Fluorescence decay of Er^{3+} ion in tellurite glass (N_2) at 1.5 μm .

Figure 8.29 Lifetimes for ${}^4\text{I}_{13/2}$ - ${}^4\text{I}_{15/2}$ transition at 1.5 μm as a function of the OH^- concentration in tellurite glass.

Figure 8.30 Measured total decay rates for ${}^4\text{I}_{13/2}$ - ${}^4\text{I}_{15/2}$ transition at 1.5 μm as a function of the OH^- concentration in tellurite glass.

Figure 8.31 Er^{3+} ion emission spectra with various Na_2O concentration in $(90-x)\text{TeO}_2 - x\text{Na}_2\text{O} - 9\text{ZnO} - 1\text{Er}_2\text{O}_3$ ($x = 5, 10, 15$ and 20) glass.

Figure 8.32 Er^{3+} ion emission spectra with various K_2O concentration in $(90-x)\text{TeO}_2 - x\text{K}_2\text{O} - 9\text{ZnO} - 1\text{Er}_2\text{O}_3$ ($x = 5, 10, 15$ and 20) glass.

Figure 8.33 Er^{3+} ion emission spectra with various Li_2O concentration in $(90-x)\text{TeO}_2 - x\text{Li}_2\text{O} - 9\text{ZnO} - 1\text{Er}_2\text{O}_3$ ($x = 5, 10, 15$ and 20) glass.

Figure 8.34 Er^{3+} ion emission spectra with various ZnO concentration in $(90-x)\text{TeO}_2 - 10\text{Na}_2\text{O} - x\text{ZnO} - 1\text{Er}_2\text{O}_3$ ($x = 4, 9, 15$ and 19) glass.

Figure 8.35 Er^{3+} ion emission spectra with various alkali oxides in $70\text{TeO}_2 - 20\text{R}_2\text{O} - 9\text{ZnO} - 1\text{Er}_2\text{O}_3$ ($\text{R}_2\text{O} = \text{Li}_2\text{O}, \text{Na}_2\text{O}$ and K_2O) glass.

Figure 8.36 Er^{3+} ion emission spectra in different tellurite glass system.

Figure 8.37 Er^{3+} ion emission spectra with various anions in $80.5\text{TeO}_2 - 10\text{Na}_2\text{O} - 9\text{X} - 0.5\text{Er}_2\text{O}_3$ ($\text{X} = \text{BaO}, \text{BaCl}_2$ and BaF_2) glass.

Figure 8.38 Er^{3+} ion emission spectra in different kinds of glasses.

Figure 8.39 Photograph of tellurite glass fibre.

Figure 8.40 Er^{3+} ion emission spectra in tellurite glass fibre.

Figure 8.41 OH^- absorption spectra in modified silicate, HMO germanate and tellurite glasses.

Figure 9.1 Energy diagram of Tm^{3+} ion and amplification in the 1.4 μm region.

Figure 9.2 Tm^{3+} ion absorption cross-sections in tellurite and ZBLAN glasses.

Figure 9.3 Normalised emission spectra of Tm^{3+} ion in tellurite and ZBLAN glasses.

Figure 9.4 Emission cross-section of Tm^{3+} ion in tellurite and ZBLAN glasses.

Figure 9.5 Tm^{3+} ion at 1470 nm fluorescence decay in tellurite glass.

Figure 9.6 Tm^{3+} and Er^{3+} emission spectra in tellurite and ZBLAN glasses.

Figure 9.7 Nd^{3+} , Tm^{3+} and Er^{3+} emission spectra in tellurite glass.

Figure 9.8 Nd^{3+} emission spectra in silicate and tellurite glass.

Tables

- Table 1.1 A comparison of physical properties of glasses for device applications.
- Table 3.1 Parameters describing the nonradiative relaxation of rare earth ions in glass.
- Table 4.1 Preparing process of glasses.
- Table 5.1 Compositions (mol%) of HMO germanate glasses.
- Table 5.2 UV edge cut-off in HMO germanate glasses.
- Table 5.3 IR edge cut-off in HMO germanate glasses.
- Table 5.4 Molar volume and transition temperature in HMO germanate glasses.
- Table 5.5 Lifetime of Er^{3+} ion at ${}^4\text{I}_{13/2}$ level in HMO germanate glasses.
- Table 6.1 Modified silicate glass compositions
- Table 6.2 UV and IR edge cut-off in modified silicate glass.
- Table 6.3 FWHM and lifetime for 4 kinds of glasses.
- Table 7.1 Crystal growth parameters of tellurite glasses obtained by isothermal and non-isothermal methods.
- Table 7.2 Intrinsic loss parameters in $80\text{TeO}_2 - 10\text{Na}_2\text{O} - 10\text{ZnO}$ tellurite glass.
- Table 7.3 peak frequency and depolarisation ratio ρ in $70\text{TeO}_2 - 20\text{X} - 10\text{ZnO}$ ($\text{X} = \text{Li}_2\text{O}, \text{Na}_2\text{O}, \text{K}_2\text{O}$ and ZnO) glass system.
- Table 7.4 Boson peak frequency and depolarisation ratio ρ of ternary $80\text{TeO}_2 - 10\text{Na}_2\text{O} - 10\text{X}$ ($\text{X} = \text{BaO}, \text{BaCl}_2$ and BaF_2) glass system.
- Table 7.5 Field strength of alkali ions and Zn^{2+} .
- Table 7.6 Field strength of different valence ions.
- Table 7.7 Electronegativity and F_a of fluorine, chlorine and oxygen.
- Table 7.8 Values of structural correlation length in ternary $(90-x) \text{TeO}_2 - x\text{Na}_2\text{O} - 10\text{ZnO}$ ($x = 0, 10, 20$ and 30) glass system.
- Table 7.9 Values of structural correlation length in ternary $70\text{TeO}_2 - 20\text{X} - 10\text{ZnO}$ ($\text{X} = \text{Li}_2\text{O}, \text{Na}_2\text{O}, \text{K}_2\text{O}$ and ZnO) glass system.
- Table 7.10 Values of structural correlation length in binary $80\text{TeO}_2 - 20\text{X}$ ($\text{X} = \text{Na}_2\text{O}, \text{NaCl}$ and NaF) glass system
- Table 7.11 Values of structural correlation length in ternary $80\text{TeO}_2 - 10\text{Na}_2\text{O} - 10\text{X}$ ($\text{X} = \text{BaO}, \text{BaCl}_2$ and BaF_2) glass system.
- Table 8.1 Er^{3+} ion absorption cross-sections and peak ratio in tellurite glass modified by HMO.

Table 8.2 Er^{3+} ion absorption cross-sections and peak ratio in tellurite (N2), HMO germanate (GE3), modified silicate (193) and ZBLAN fluoride glasses.

Table 8.3 Bond properties of glass network former in the 4 kinds of glasses.

Table 8.4 Measured and calculated oscillator strengths of Er^{3+} ion and calculated radiative rate ${}^4\text{I}_{13/2} \rightarrow {}^4\text{I}_{15/2}$ in the same host with different concentration..

Table 8.5 Judd-Ofelt parameters, calculated lifetime, measured lifetime and energy transfer rate for ${}^4\text{I}_{13/2} \rightarrow {}^4\text{I}_{15/2}$ level in Er^{3+} ion doped tellurite glass.

Table 8.6 Lifetime of Er^{3+} ion for ${}^4\text{I}_{13/2} \rightarrow {}^4\text{I}_{15/2}$ transition in different tellurite glass systems modified by HMO, Er_2O_3 concentration in all case is 1 mol%.

Table 8.7 Lifetime of Er^{3+} ion for ${}^4\text{I}_{13/2} \rightarrow {}^4\text{I}_{15/2}$ transition in tellurite glass modified by chloride and fluoride

Table 8.8 Er^{3+} lifetime, FWHM, emission cross section of ${}^4\text{I}_{13/2} \rightarrow {}^4\text{I}_{15/2}$ transition and FOM at 1500nm in different kinds of glasses, pump wavelength is 980 nm.

Table 9.1 Spectroscopic parameters of Tm^{3+} -doped tellurite and ZBLAN glasses.

Table 9.2 Emission parameters of Nd^{3+} -doped TZN and silicate glasses.

List of symbols and abbreviations

A = radiative rate (Chapter 3) = absorbance	T = temperature = Transmission of light (Chapter 5)
c = velocity of light in vacuum = molar concentration (Chapter 4)	T_g = Transition temperature
ΔE = energy gap between two J-levels	V_m = Molar volume
f = force constant (Chapter 5) = Oscillator strength (Chapter 3)	ε = Energy (Chapter 3) = molar extinction coefficient (Chapter 4)
g = degeneracy of energy level	α = absorption coefficient
h = Planck constant	λ = Wavelength
$\hbar = h/2\pi$	ν = Frequency
I = Intensity of beam	ω = wavenumber
J = Quantum number of angular momentum	μ = Reduced mass of vibrating ions
k = Boltzmann constant	Ω_t = Judd-Ofelt parameters (t = 2,4,6)
n_d = refractive index	z = ionic charge
σ = Absorption or emission cross-section	IR = Infrared
τ = Lifetime	UV = Ultraviolet
ρ = Density = depolarisation ratio (Chapter 7)	DSC = Differential scanning calorimeter
FOM = Figure-of-Merit	DTA = Differential temperature analysis
ZBLAN = ZrF ₄ -BaF ₂ -AlF ₃ -LaF ₃ -NaF glass	F/O = Fluorine/Oxygen ratio
WDM = Wavelength division multiplexed	HMO = Heavy metal oxide
EDFA = Er ³⁺ doped fibre amplifier	tp = trigonal pyramid
TDFA = Tm ³⁺ doped fibre amplifier	tbp = trigonal bipyramid
NDFA = Nd ³⁺ doped fibre amplifier	NBO = Non-bridging Oxygen
FWHM = Full wavelength at half maximum	NDOS = Non-bridging donated Oxygen site
	LPE = Lone pair electron
	GSA = Ground state absorption
	ASE = Amplified spontaneous emission
	ESA = Excited state absorption

Chapter 1

Introduction

1.1 Er³⁺-doped glass amplifiers at 1.5 μm

Fibre optic communications developed rapidly after the first low-loss fibres were produced in 1970. At that time, the poor amplification characteristics and lack of technical breakthroughs moved research away from active fibres. The basic mechanism of the optical fibre amplifier is very simple: it amplifies an optical signal in a fibre by using stimulated emission of optically excited rare-earth ions in the fibre core. The operating principle of amplifiers is the same of that of lasers, except that amplifiers do not need a cavity whereas lasers need one for oscillation.

With the development of both low-loss, long-length, high-silica fibres and highly reliable semiconductor laser diodes, an extension of the well-established modified chemical vapour deposition (MCVD) method made it possible to fabricate active fibres with excellent transmission characteristics. In addition, the laser technology, which was developed in the period from 1970 to 1985, enabled the efficient pumping of active ions. It can be said that active fibres and fibre amplifiers were reborn in 1985 [1] and in 1987 [2]. Since then, fibre amplifiers, especially erbium-doped fibre amplifiers (EDFAs), have become one of the most exciting new developments in the realm of optical communications, which has revolutionised our ability as human beings to communicate.

Figure 1.1 is a diagram of a conventional optical fibre transmission system with electrically regenerative repeaters. In this system, optical signals, which weaken as they propagate in the fibre, are converted to electrical signals in the repeaters, hence enabling the signals to be totally recovered by electronic circuits with 3R functions such as reshaping, retiming, and regeneration. The optical signal regenerated by this modulating semiconductor laser is then relaunched into the fibre for transmission. In general, these electrically regenerative repeaters require high-speed electronics, which become increasingly complex and problematic in terms of equipment size as the bit rate increases. In addition, since the reliability required for systems consisting a

multichannel repeater is extremely high, this tends to make these repeaters very expensive once they exceed a few gigabits per second

Figure 1.2 shows the transmission system with fibre amplifiers. In this application system, the fibre amplifier repeaters do not require high-speed electronics and so the initial development investment is low, whereas electrically regenerative repeaters require high-speed electronics. This is because the fibre amplifier reshapes the transmission signals completely in the optical domain. This means that the optical gain of fibre amplifiers does not change with bit rate and makes fibre amplifier repeaters compatible with high-speed system. This feature allows system manufacturers to use the same fibre amplifier repeaters for different types of systems with different bit rates with no significant modification to the repeaters themselves.

Nowadays, silica glass optical fibres are the backbone of telecommunication networks. The loss in silica fibre determines the telecommunication transmission windows. Figure 1.3 shows the contribution to optical losses of the ultraviolet edge, the infrared edge and the intrinsic scattering losses in vitreous silica, together with the experimental loss curve [3]. From theoretical and experimental loss curves, silica glass has the lowest transmission loss about 0.2 dB km^{-1} at $1.5 \mu\text{m}$. Therefore, a $1.5 \mu\text{m}$ optical amplifier is essential for the third telecommunication window. Er^{3+} -doped glasses can be used to provide amplification in the $1.5 \mu\text{m}$ band. Figure 1.4 and figure 1.5 illustrate the absorption cross section and energy levels of Er^{3+} in Ed-2 silicate [4]. From the energy level diagram of Er^{3+} , the ${}^4\text{I}_{13/2} \rightarrow {}^4\text{I}_{15/2}$ transition is ideal for making an optical amplifier in the $1.5 \mu\text{m}$ band.

In Er^{3+} -doped glasses, $1.5 \mu\text{m}$ amplifier and laser can be pumped by different sources based on Er^{3+} absorption band in figure 1.4. There are three pump bands (800nm, 980nm and 1480nm) which are able to populate the excited ${}^4\text{I}_{13/2}$ state, Because of the excited state absorption (ESA), the 980 and 1480 nm pump bands are better than 800 nm band for pumping $1.5\mu\text{m}$ devices in oxide glasses. The 800 nm pump needs much higher minimum required pump power than 980 and 1480 nm pump bands.

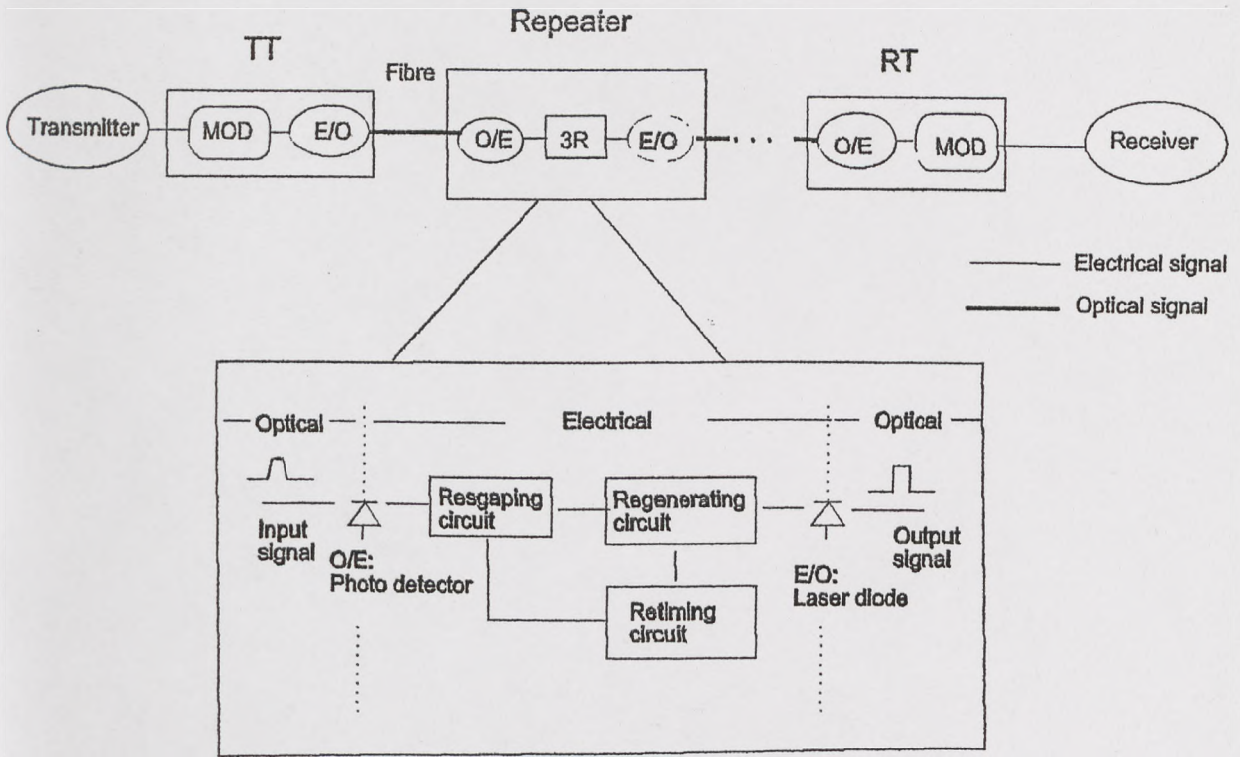


Figure 1.1 An example of conventional optical fibre transmission with electrical repeaters. TT is a transmitter terminal, MOD is an electrical signal modulator, and E/O and O/E are electrical-to-optical and optical-to-electrical signal converters. 3R indicates repetitive signal regeneration, which involves reshaping, retiming, and regeneration and operates in the electrical domain.

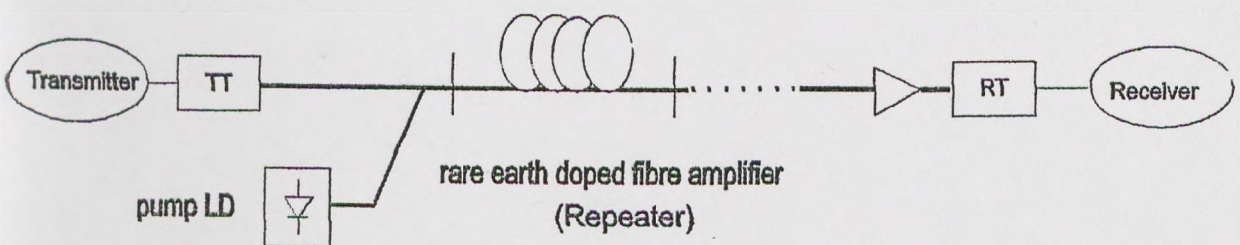


Figure 1.2 A long distance transmission system with fibre amplifier repeaters

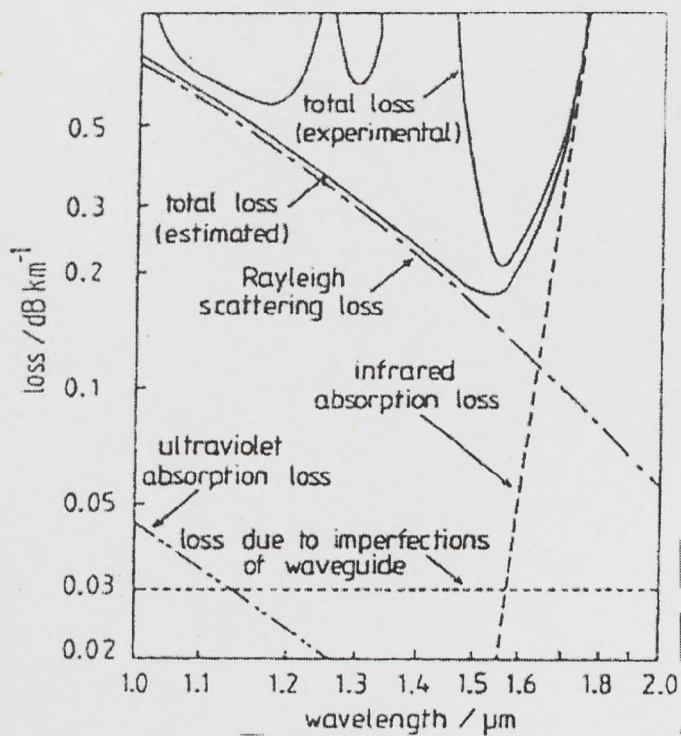


Fig.1.3 Optical losses of the UV edge, IR edge and the intrinsic scattering losses in vitreous silica, together with the experimental loss curve [3].

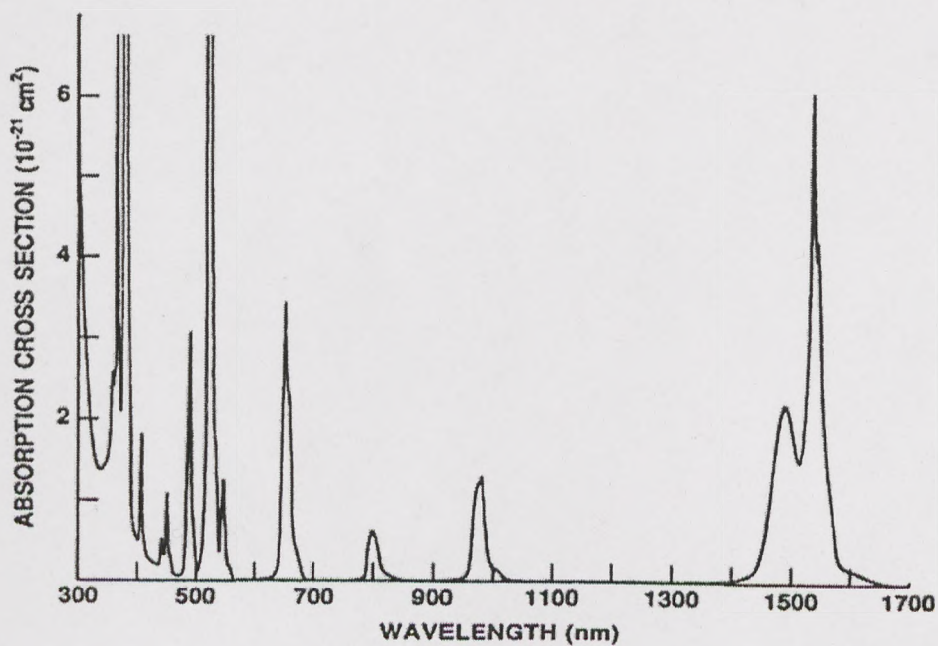


Fig. 1.4 Absorption cross-sections of Er³⁺ in Ed-2 silicate glass [4].

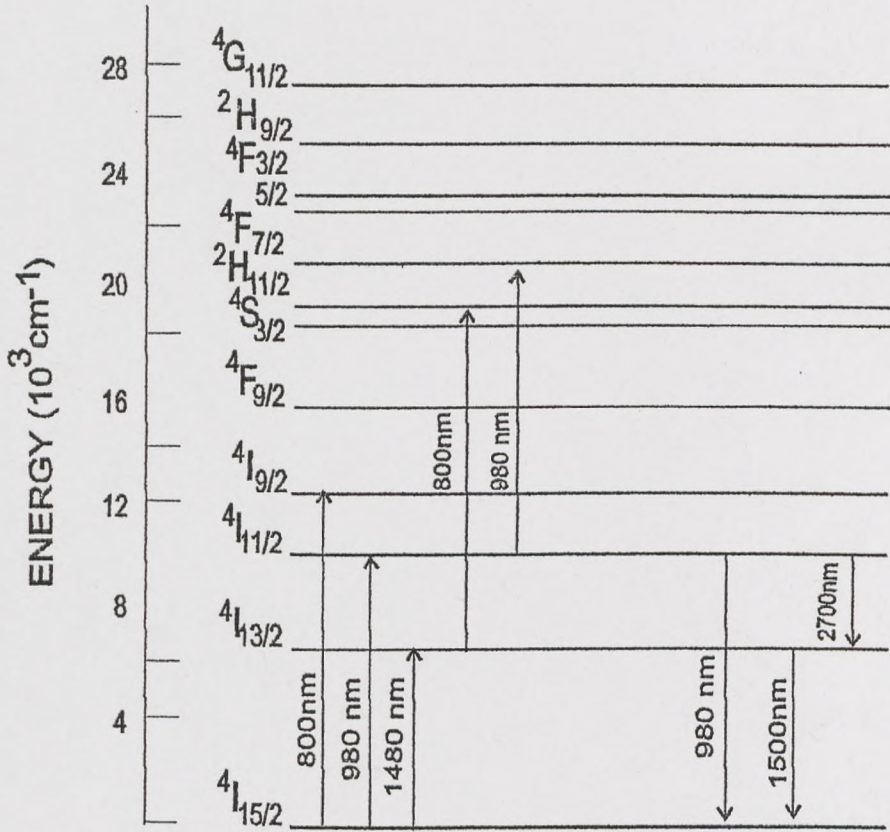


Fig. 1.5 Energy levels and transitions of Er^{3+} in ED-2 silicate

Today, the erbium-doped silica fibre amplifier for 1.5 μm telecommunication window has become a well-established component in telecom systems. The fibre amplifier has been used both in system demonstrations on land and under the sea, and operational systems are commercially available from a number of manufacturers. Their applications for a variety of requirements include high gain, high power, low noise, broadband, and high reliability. In addition, low cost and compactness are required. Unfortunately, however, no one amplifier currently meets all these requirements. Nevertheless, many significant advances have been made very rapidly.

1.2 Development of broadband amplifiers

The main advantage of optical amplifiers in communication systems is that they are useful for amplifying input signals of different bit rates or formats, and they can be used to achieve simultaneous amplification of multiwavelength optical signals over a wide spectral region. These multiwavelength optical signals can carry different signal formats, including digital data, digital video, and analogue video, allowing flexible upgrading in broadband distribution networks by adding extra wavelength division multiplexed (WDM) channels as needed. In WDM system, optical beams with different wavelengths propagate without interfering with one another, so several channels of information (each having a different carrier wavelength) can be transmitted simultaneously over a single fibre. This scheme increases the information carrying capacity of a fibre.

The wavelength region for telecommunications now extends from about 1250 nm to 1650 nm, and silica fibres thus have a large potential for expanding huge bandwidth. The large bandwidth of the optical fibre allows for the use of techniques such as WDM to increase the network capacity. At present, only part of this bandwidth is available for WDM transmissions by the introduction of the EDFA, the maximum unfiltered gain bandwidth of EDFA in silica fibre is about 20 nm [5], as the amplifier gain bandwidth is much smaller than the available wavelength region. Another drawback of the EDFA is that the Er^{3+} gain spectrum is not inherently flat, and spectral gain flattening techniques are necessary to equalise the amplification gain efficiencies for all the WDM signals. Thus, for efficient WDM operation, Er^{3+} -doped amplifiers with broad band and flat gain characteristics are required.

In order to satisfy the rising demand for more WDM channels in telecommunication industry, three main approaches have been adopted to increase the available gain bandwidth of EDFA. One is to expand the amplification band of EDFA by changing the Er^{3+} doped host glass [6,7]. The second approach involves using different band EDFA in a parallel configuration [8]. The third is to complement the EDFA gain with Raman amplifier gain [9]. At ECOC'97 Lucent also reported a cascaded EDFA with Bragg filters, achieving 80 nm bandwidths of gain [10]. Non-silica glass hosts intrinsically capable of broader gain than silica, have also been developed. Fluoride ZBLAN EDFA offers 30 nm of flat gain [6], and is available as a commercial device. Tellurite EDFA capable of 75 nm unfiltered flat gain has been reported by NTT at OFC'97 [7]. From this point, different host glass for EDFA will have significant effect on the gain bandwidth, it is the simplest configuration to achieve broadband EDFA.

1.3 Rare-earth doped host materials for amplifier

The essential amplification properties of active-ion-doped optical fibre depend strongly on the choice of active ions and fibre materials. There are many factors that influence the fabrication and characteristics of practical optical fibres for amplification. The most important of these are as follows:

1. the homogeneous doping of active ions in host materials,
2. the phonon energy properties of materials,
3. the refractive index properties and the controllability of the refractive-index profile in fibres,
4. low intrinsic loss and the potential for extrinsic loss reduction at operating wavelengths,
5. precise control of the shape and size of the cross-section are along the axial direction of fibres, and
6. the high chemical and mechanical durability of materials.

The first five factors strongly affect the amplification characteristics of fibres. The clustering of active ions shortens the lifetime of radiative transitions. The phonon energy of host materials decides the radiative quantum efficiency. The

transmission loss and refractive-index difference between the core and cladding of fibres, which are related to factors 3 and 4, strongly influence the gain coefficient. Factor 6 is necessary for practical fibre fabrication and application. In order to increase the productivity and reliability of fibres and lower the fabrication cost, it is of paramount importance in system design that the fibre material itself has high chemical and mechanical durability.

These materials are classified into three groups: single crystalline, polycrystalline, and glasses. Single crystalline materials have essentially low intrinsic loss because Rayleigh scattering loss due to density fluctuation is very low. The active-ion doping, refractive-index control, and shape control of single crystalline materials are very difficult since doping the host with active ions or refractive index modifiers sometimes prevents single crystal growth and as-grown single crystals have rough specific crystal surface. In addition, because of the low speed of crystal growth, single crystal fibre is difficult to mass produce. By comparison, the speed of fibre fabrication with polycrystalline materials is high and there is little roughness on the surfaces and core/cladding interfaces of fibres. However, polycrystalline materials exhibit a large loss as a result of light scattering at the grain boundary. Glasses are made by cooling certain molten materials in such a manner that they do not crystallise but remain in an amorphous state. Therefore glasses with high thermal stability are easy to make into fibres and the Rayleigh scattering loss in glass is much smaller than the loss caused by grain boundary scattering in polycrystalline materials. Moreover, the refractive indices of these glasses are easily controlled by changing the constituent ratio, which does not severely limit the glass formation conditions.

Low-loss glass materials for fibre amplifiers can be divided into oxide glasses and non-oxide glasses. Oxide glasses can be divided into silica glass, multicomponent silicate glass, and non-silicate glass. Non-silicate glass includes germanate glass and tellurite glass. Silicate glass is the most stable and common glass, but it has some disadvantages in terms of its use as optical fibre for amplification. It is difficult to dope a large concentration of rare earth ions homogeneously. The phonon energy is high compared to other fibre materials. This greatly reduces the radiative quantum efficiency of certain doped ions e.g. Tm^{3+} and Pr^{3+} at 1460 nm and 1300 nm respectively under certain conditions.

Non-oxide glass can be divided into halide glasses and chalcogenide glasses. There are many kinds of halide glass system including fluoride glass, chloride glass and mixed halide glass system. Fluoride glass system are divided into four groups: BeF₂-based glasses, AlF₃-based glasses, ZrF₄ /HfF₄-based glasses, and InF₃ /GaF₃-based glasses. Compared to oxide glass, these halide glasses are thermally not stable. They, in general, are sensitive to environment degradation, particularly in the presence of moisture. Although some fluoride systems can be fully vitrified when they are rapidly cooled from the molten state, they some times crystallize during a reheating process such as fibre drawing. It is very important to select a very stable glass system for fibre fabrication.

Although silica, silicate and fluoride glasses have been widely studied as the host of Er³⁺-doped fiber amplifiers, new glass host materials are being sought to satisfy the need for flattened gain broadband amplifiers. Because host materials have an important influence on the optical characteristic properties of the active ion, such as absorption and emission cross-sections, spectral shapes of the emission and absorption bands, excited state lifetimes, ion-ion interactions, as well as the static and dynamic ion-lattice interactions, these factors will change the Er³⁺ emission spectrum significantly.

Figure 1.6 and figure 1.7 illustrate the absorption cross sections and normalized emission spectra of Er³⁺ for the $^4I_{15/2} \leftrightarrow ^4I_{13/2}$ transition at 1.5 μ m in different glass types [4]. We can see the absorption cross-section and shape are changed in different kinds of host glasses. The emission spectra are becoming broader from silicate ED-2 to fluorohafnate glass.

Tellurite and germanate glasses behave in a different manner compared to silica glass for realizing a broader flat-gain amplifier. Tellurite glass is particularly interesting, scientifically and technologically, on account of its attractive physical properties, some of which include high viscosity at the melting point, high refractive indices and extended mid-IR transmissions, high rare-earth ion solubility and a relatively low phonon energy among oxide glass formers. These properties enable the design of high-quality optical fibres for amplification, switching and laser power transmissions. As we cited above, in 1997, NTT announced a flat-gain Er³⁺-doped

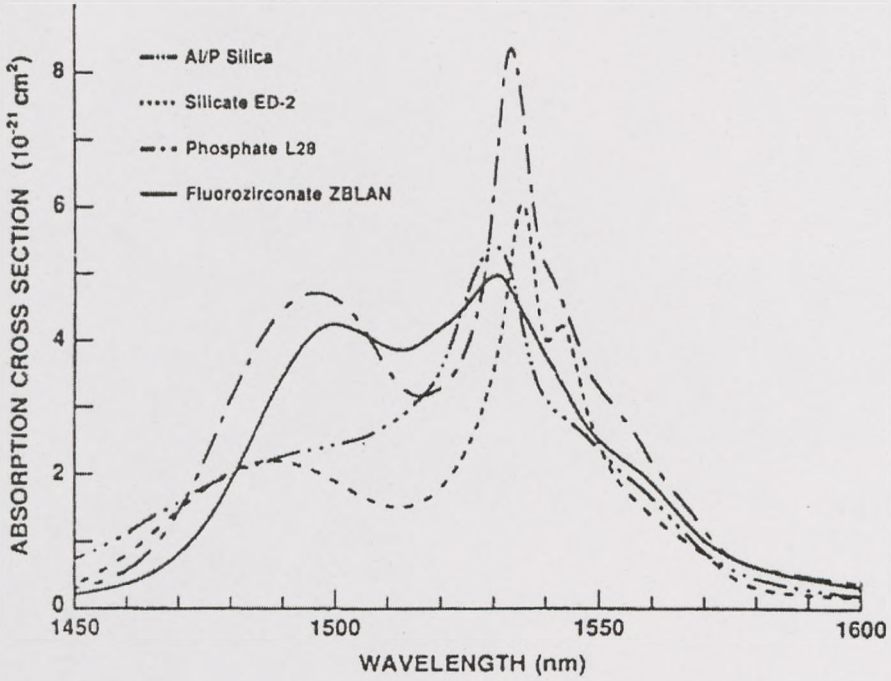


Figure 1.6 Some 1.5 μ m absorption cross-section spectra for different glass types [4].

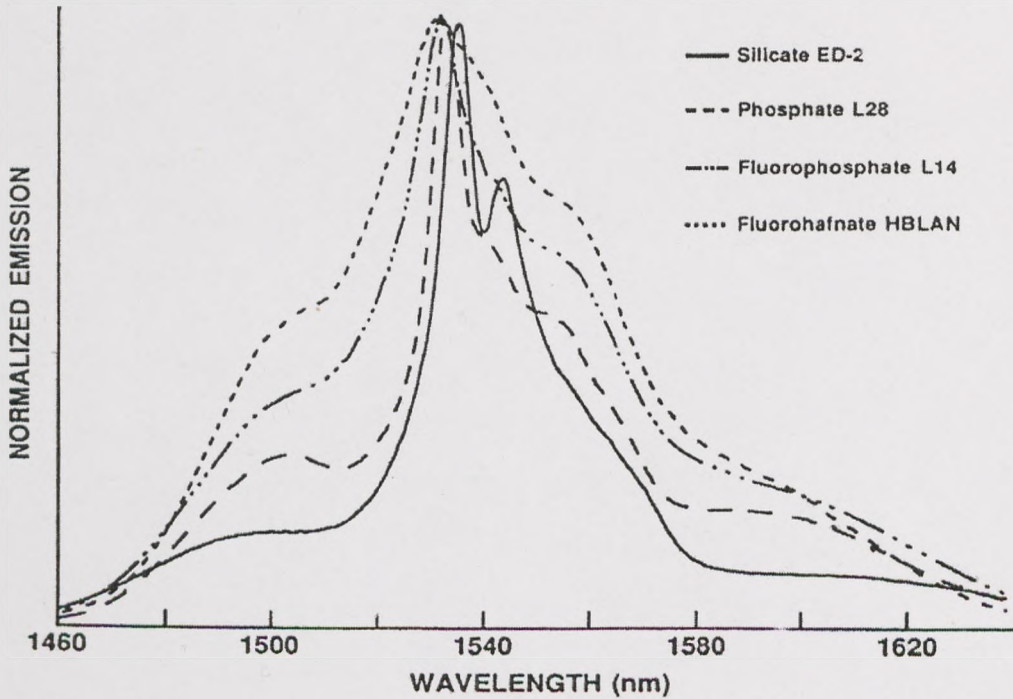


Figure 1.7 Some 1.5 μ m emission spectra normalised to emphasize variations in bandwidth [4].

tellurium oxide glass fibre amplifier [7]. The small-signal gain of more than 20 dB was obtained over a bandwidth as wide as 70 nm from 1530 to 1600 nm.

Tellurite and germanate glasses have the following properties:

1. a reasonably wide transmission region (0.38-5 μ m), compared with only 0.2-3 μ m for silicate glasses;
2. good glass stability and corrosion resistance compared to fluoride glasses which pose major problems;
3. a relatively low phonon energy among oxide glass formers;
4. high linear and nonlinear refractive indices, which are much higher than either fluoride or silicate glasses.

A comparison of the selected optical properties among tellurite, germanate, silica, fluoride and chalcogenide glasses is shown in table 1.1 [11].

Table 1.1 Optical and physical properties of glasses for device applications [11].

Properties	Tellurite	Germanate	Silica	Fluoride	Chalcogenide
<i>Optical properties</i>					
Refractive index (n)	1.9-2.3	1.7-1.8	1.46	1.4-1.6	2-2.83
Abbe number (v)	10-20	25-40	80	60-100	
Nonlinear RI ($n_2, m^2/w$)	2.5×10^{-19}	10^{-19}	10^{-20}	10^{-21}	higher
Transmission range (μ m)	0.4-5	0.38-5	0.2-2.5	0.2-7	0.45-11
Highest phonon energy (cm^{-1})	800	900	1000	500-600	200-300
Bandgap (ev)	3	3.5-4	10	9-11	1-3
<i>Physical properties</i>					
Glass transition ($T_g, ^\circ c$)	300	450	1000	270-300	300-420
Thermal expansion ($10^{-7} ^\circ c^{-1}$)	120-170	100-130	5	150	140
Density (g/cm^3)	5.5	6.4	2.2	5.0	4.5
Dielectric constant	13-35	--	4.0	--	--
Fiber loss (dB/km)	--	--	0.2 (1.5 μ m)	15 (1.5 μ m)	0.4 (6.5 μ m)
Bonding	covalent- ionic	covalent- ionic	covalent- ionic	ionic	covalent
Solubility in water	$<10^{-2}$	$<10^{-2}$	$<10^{-3}$	soluble	$<10^{-4}$

The high nonlinear refractive index and low phonon energy make the tellurite glass particularly suitable for nonlinear and laser application. For example, in a Pr^{3+} -doped tellurite glass, the lower phonon energy results in a lower nonradiative transition rate from the metastable upper level leading to a more efficient device for 1.3 μm amplification than in silica [11].

TeO_2 and GeO_2 -based glasses, having lower phonon energy and high refractive indices, make them suitable candidates for designing high quantum efficiency devices. The low phonon energy as a device property could be useful in realizing important infrared lasers for sensors. It is also believed that tellurite glasses have better glass stability and chemical durability than halide glasses and some low- T_g chalcogenide glasses. Glasses with relatively low refractive indices can be designed for device applications that will have a lower insertion loss than a chalcogenide glass fiber device.

Although tellurites and germanates have been known for some time to form stable glasses, and selected properties of some rare earth ions have been reported [12], their application has not been extended to fibre optics where advantage could be taken of their nonlinear properties and desirable fluorescence properties associated with their low phonon energy spectrum and high refractive index. At this moment, the backbone of the telecom fibre is silica, therefore if Er^{3+} -doped silica glass fibre can be modified to achieve a broadband emission, it will have advantage in connecting the active and passive fibres. In the present research work on rare-earth ion doped glasses for broadband amplifiers, Er^{3+} -doped modified silicate glass, germanate glass and tellurite glass have been made and fluorescence properties of Er^{3+} have been compared. Special attention has been paid to Er^{3+} -doped tellurite glass because of its widest emission spectrum, and it is the most promising glass host for broadband and flat gain amplifiers. Lastly, Tm^{3+} -doped tellurite glass has been studied and the possibility of making Tm^{3+} -doped fibre amplifier (TDFA) at 1.46 μm has been discussed.

1.4 Outline of this thesis

Although the EDFA for the spectral region around 1.5 μm has already been available commercially since 1990, the broadband and flat gain EDFA is necessary

for WDM communication systems. Because the glass host has a large effect on the emission spectrum of Er^{3+} ion, various glasses were studied as host materials for this purpose. These glasses include modified silicate glass, heavy metal oxide germanate glass and tellurite glass. Finally, Nd^{3+} -doped fibre amplifier (NDFA) and TDFA in tellurite glass are discussed and the possibility of covering the whole silica transmission band is also considered by connecting the 2nd and 3rd windows using TDFA.

The thesis is divided into 8 chapters following Introduction:

In chapter 2 “literature review” reviews references related to rare earth doped glass and fibre amplifiers, especially on Er^{3+} doped germanate and tellurite glasses.

In chapter 3 “experimental procedure” describes the techniques used in experiments and measurements.

In chapter 4 “radiative theory of rare earth doped glass” describes the fluorescence theory. With Judd-Ofelt analysis we can determine the emission lifetime and the cross-sections for absorption and stimulated emission. Non-radiative processes include ion-ion transition and multiphonon relaxation.

In chapter 5 “ Er^{3+} -doped modified silicate glass” describes the absorption and emission properties of Er^{3+} ions in modified silicate glass.

In chapter 6 “ Er^{3+} -doped heavy metal oxide germanate glass” describes the absorption and emission properties of Er^{3+} ions in heavy metal oxide germanate glass.

In chapter 7 “physical properties and structure of tellurite glass” describes the physical properties of tellurite glass and the analysis of glass structure change using Raman spectroscopy.

In chapter 8 “ Er^{3+} -doped tellurite glass” studies the absorption and emission properties of Er^{3+} ions in different tellurite glasses and at various Er^{3+} ion concentration.

In chapter 9 “ Tm^{3+} -doped tellurite glass for a broadband amplifier at 1.46 μm ” discusses the TDFA in tellurite glass and possibility of bridging the second and third communication windows.

In chapter 10, further work on the above research areas has been recommended.

References

1. Poole, S. B., D. N. Payne, and M. E. Fermann, *Electron. Lett.* **21**, 737 (1985).
2. Mears, R. J., L. Reekie, I. M. Jauncey, and D. N. Payne, *Tech. Dig. Conf. On Optical Fibre Communication/Int. Conf. Integrated Optics and Optical Fibre Communication (OFC/IOOC'87)*, Reno, Nevada, Feb. 1987, paper W12.
3. Cable, M. and J. M. Parker Eds, 1992 "High-performance glass", Chapter 13, pp260.
4. Miniscalco, W. J., "Optical and Electronic Properties of Rare Earth Ions in Glasses," in *Rare Earth Doped Fiber Lasers and Amplifiers*, M. J. F. Digonnet (Ed.), New York: Marcel Dekker, 1993.
5. Tachibana, M., R. I. Laming, P. R. Morkel, and D. N. Payne, *IEEE Photon. Tech. Lett.*, **3**, 118 (1991).
6. Yamada, M., T.Kanamori, H.Ono, K.Nakagawa, and S.Sudo, *IEEE Photonics Technol. Lett.* **7**, 882 (1996).
7. Mori, A., Y.Ohishi, M.Yamada, H. Ono, Y. Nishida, K. Oikawa, and S. Sudo, *Technical Digest of Optical Fibre Communication Conference*, Washington 1997, Paper PD1.
8. Yamada, M., H. Ono, T. Kanamori, S. Sudo, and Y. Ohishi, *Electron. Lett.* **33**, 710 (1997).
9. Masuda, H., S. Kawai, K. Suzuki, and K. Aida, *ECOC'97*, 1997, pp. 73-76.
10. Wysocki, P. F., J. Judkins, R. Espindola, M. Andrejco, A. Vengsarkar, and K. Walker, *ECOC'97*, Paper PD2.
11. Wang, J. S., E. M. Vogel, and E. Snitzer, *Optical Materials* **3**, 187 (1994).
12. Reisfeld, R., and Y. Eckstein, *J. of Non-Cryst. Solids* **12**, 357 (1973).

Chapter 2

Literature Review

2.1 Er³⁺-doped silicate glass

Since the invention of the laser in 1960 [1], the first laser action in a glass host material was reported by E. Snitzer in 1961 using a potassium barium silicate glass containing 2 wt% neodymium oxide [2]. The first Er³⁺-doped glass laser was demonstrated by Snitzer and Woodcock using the ${}^4I_{13/2} \rightarrow {}^4I_{15/2}$ transition at 1.5 μm in 1965 [3]. The basic ideas that led to the unidirectional travelling-wave optical amplifier were presented in 1962 by J. E. Geusic and H. E. D. Scovil [4]. After that, the first experiments on fibre amplifiers were presented by C. J. Koester and E. Snitzer in 1963 [5] and 1964 [6] in Nd³⁺-doped silicate glass.

The real breakthrough in fibre amplifier technology came in 1987 when a group from Southampton University reported high-gain fibre amplifiers operating in the 1.5 μm wavelength region, which they achieved using Er³⁺-doped silica-based fibres [7]. After that, fibre amplifiers, especially Er³⁺-doped fibre amplifiers (EDFAs), have become one of the most exciting new developments in the realm of optical communications. It is widely recognised that no subject has received more attention than Er³⁺-doped fibre amplifiers.

EDFAs for different application purposes such as broadband [8-10], high gain [11-13], low noise [14, 15], high power [16,17] and reliability [18-20] have been developed.

One of the reasons for the successful and rapid development of EDFAs has been that manufacturing technology could refer to mature silica fibre production methods. Another reason for the success of EDFA was determined by the development of semiconductor lasers which are used to pump amplifiers using the 800, 980, and 1480 nm absorption bands.

Although high silica glasses provide effective host materials for EDFAs, for achieving broadband gain characteristics on WDM systems, alternative glass hosts

may offer improvements in terms of operational gain bandwidths. Except fluoride glasses for broadband amplifier [21, 22], multicomponent silicate glasses, such as aluminosilicate, sodium silicate glass, soda-lime-silicate glasses, have been studied as hosts for EDFA [23, 24]. The absorption and emission spectra of Er^{3+} ions have been studied in these glasses. Broadening occurred with the incorporation of either i) other high field strength ion oxides such as ZrO_2 and HfO_2 , or ii) glass forming intermediates such as Al_2O_3 , Ga_2O_3 and In_2O_3 . There is no significant change observed in the absorption or emission spectra for the glass containing glass former GeO_2 [25]. The observed broadening may be due to distortions of the network which affects the local coordination symmetry of the Er^{3+} ions. For Er^{3+} -doped silicate glass, the magnitude of the Stark split is slightly different in each ion because of the site-to-site difference in the crystal field surrounding the rare-earth ions. Next part is going to review Er^{3+} different sites in silicate glass.

2.2 Er^{3+} ion sites in silicate glass

Structurally, silicate glass is a continuous random network lacking of both symmetry and periodicity. The basic structural units which make up the network, SiO_4 tetrahedra, have a definite geometry but connected at corners to form a random three-dimensional network [26]. Network modifier cations, such as alkali, alkaline earth, and higher valence state ions, are accommodated randomly in the network in close proximity to non-bridging anions. On a macroscopic scale, glass is homogeneous, on a microscopic, it epitomises an inhomogeneous system. Being a disordered medium, the environment of each ion in a glass is not identical as in a crystal. In addition, due to differences in the bonding to nearest neighbour ions in multicomponent glass, the local fields at individual ion sites vary. This results in site-to-site differences in the energy levels and the radiative and nonradiative transition probabilities of paramagnetic ions in glasses.

Because the Stark splitting is caused by the crystal field and local coordination, the magnitude of the Stark split ranges from 200 to 400 cm^{-1} for Er^{3+} -doped fluoride, fluorophosphate, and silicate glasses [27-30]. Due to the site-to-site difference in the crystal field surrounding the rare-earth ions, the Stark level has an apparent broadening originating from this difference in the Stark levels of individual ions. This broadening is commonly called the inhomogeneous broadening and originates

from the local differences in the material structure [31]. In addition, the individual Stark levels fluctuate and broaden as a result of the fluctuation of the crystal fields caused by thermal atomic motions. This broadening due to thermal fluctuation is commonly called the homogeneous broadening [32]. The magnitudes of inhomogeneous and homogeneous broadening are about 27 to 60 cm^{-1} [33-36] and 8 to 49 cm^{-1} [33, 34, 36-38], respectively. The energy spacing ΔE between adjacent Stark sub-levels range from 20 to 80 cm^{-1} and its average value is 50 cm^{-1} .

The luminescence detection of transitions between individual Stark levels is obscured by the broadening (both homogeneous and inhomogeneous) present in the emission spectrum of rare earth ions in glasses. The homogeneous broadening of individual Stark levels can be made negligible by cooling the samples to cryogenic temperature [39]. In order to reduce the effect of inhomogeneous broadening, the technique of fluorescence line narrowing (FLN) was employed to detect the different sites.

When a narrow band source is used for excitation, only those ions resonant with the excitation quanta to within the homogeneous linewidth are excited. This site-selective excitation effectively reduces the inhomogeneous broadening and a line-narrowed fluorescence spectrum is obtained. Pioneering investigation on glass structure using FLN was carried out by Denisov and Kizel in 1967 [40]. With the advent of laser-excited FLN, we have a unique microscopic probe of the environment at an impurity site with which to test any proposed structure model. Equipped with FLN measurements of site-to-site variations in energy levels and transition probabilities, one can also invert this information to create a geometric model of glass structure. It is very useful tool to detect micro-structure of glass. This was attempted firstly by Brecher and Riseberg using FLN data of Eu^{3+} first in a silicate glass [41] and later in a fluoroberyllate glass [42].

In order to simplify the interpretation, it is important to perform the experiments at temperatures low enough to ensure that only the lowest energy Stark level of a given J-manifold is thermally excited. Thus, the Stark split of a given J-manifold was deduced and shown to be on the order the site-to-site variations. Zemon et al [27, 37] first studied Er^{3+} -doped fluoride, fluorophosphate, and silicate

bulk glasses from FLN measurement at 4.2K. The Stark levels of the $^4I_{15/2}$ ground state manifold for these glasses have been determined. Splits between adjacent Stark levels were observed to be 20-80 cm^{-1} . The total energy spread of the manifold ranged from 335 to 400 cm^{-1} . The Stark energies varied from 0 to 60 cm^{-1} for the range of Er^{3+} sites. The site-to-site variations are of the same order of magnitude as the Stark splits.

In alkali silicate binary glass doped with Er_2O_3 , C. C. Robinson [43, 44] provided evidence for the existence of different Er^{3+} sites using low temperature spectra and pointed out that there are four distinguishable sites for Er^{3+} ion which are assigned as A, B, C and D. The A site is the most common and appears in all glasses regardless of the alkali size. The Er^{3+} is sixfold coordinated in a site which approaches octahedral. The B site occurs only in Li^+ and Na^+ binary silicate glasses. This site may also be sixfold coordinated, with the rare-earth ion appearing at more than one edge of the silica tetrahedra. The presence of this site is sensitive to alkali size, and it does not appear for the larger alkali ions. The C site is present only in the K^+ , Rb^+ , and Cs^+ silicate glasses. This site may be similar to the Er^{3+} C_2 site in Er_2O_3 crystal structure. The D site, which observed in the K^+ and Cs^+ glasses, may be a variation of the B site in which not as many rare-earth ions appear at the edges of the SiO_4 tetrahedra, thus producing a spectrum more similar to that of the site A.

In Er^{3+} -doped silica fibre amplifier, E. Desurvire et al [33, 34, 38, 45] were the first to measure the homogeneous and inhomogeneous broadening. When the fibre core is alumino-silicate, the spectral gain hole-burning at $\lambda_0 = 1.53 \mu\text{m}$ was observed at temperature 4.2 and 77 K, the room-temperature homogeneous linewidth for this transition is determined to be $\Delta\lambda_h = 11.5 \text{ nm}$ [38]. In this glass amplifier, it has large (26 nm) homogeneous gain bandwidth with comparatively small (11.5 nm) inhomogeneous component [38]. A theoretical model is presented to model both homogeneous and inhomogeneous gain saturation in EDFA [45]. The strong spectral dependence of gain saturation is described very well by the homogeneous model. The in homogeneous model is seen to provide a more detailed description on the change in the amplified spontaneous emission (ASE) spectrum. In EDFA with $\text{GeO}_2:\text{SiO}_2$ core, J. L. Zyskind has measured the homogeneous linewidth by spectral gain hole-burning [33]. At room temperature, the extrapolated homogeneous linewidth is 4 nm

and the inhomogeneous linewidth is 8 nm. It shows that for fibres the homogeneous linewidth is less than the inhomogeneous linewidth and considerably smaller than for Al₂O₃-doped silica fibres. This smaller homogeneous linewidth explains the fact that inhomogeneous gain saturation is observed to be more important in germano-silicate EDFA than in aluminosilicate EDFA.

With the success of the Er³⁺-doped fibre amplifiers, Er³⁺ doped fluoride glass has been studied [21, 46]. In fluoride glasses rare earth ions are believed to substitute only for network former, resulting in less inhomogeneous broadening as well as a more symmetric and lower crystal field strength than for oxide glasses [47]. This is consistent with the observed Stark splitting [48], and on the basis alone narrower emission bands would be expected. The large measured bandwidths lead one to the conclusion that the distribution of strengths among the Stark transitions determines the spectral shape rather than the Stark splits. From this dense and packed spectrum in the 1.5 μm region, the fluoride based EDFA has a wider and flatter gain spectrum than silica-based EDFA. Thus, the fluoride environment is better than the oxide one. The solubility of the rare earth is also better in the fluoride medium than in the oxide one. Oxyfluoride silicate glass doped with rare earth ions has also been studied for photonic applications such as amplifiers at 1.31, 1.46, 1.55 μm, for up-conversion lasers and three dimensional displays [49]. This kind of glass can benefit from the low phonon energy of a fluoride and the durability and mechanical properties of silicate glass.

2.3 Er³⁺ doped germanate glasses

Germanium oxide (GeO₂) has long been recognised as a good glass former. GeO₂ based glasses exhibit better infrared transmission than SiO₂-based glasses due to the larger size and the heavier mass of germanium compared to that of silicon. Ternary glass-forming systems with all kinds of oxides such as R₂O, RO, R₂O₃, RO₂, R₂O₅ and RO₃ based on GeO₂ were studied [50]. The research data showed the glass-forming regions in the GeO₂ liquid with the addition of above oxides and some physical and chemical properties of these glasses are also reported.

The structure of binary alkali germanate glasses was studied using laser Raman spectroscopy, and FTIR techniques were used to study the structure of these glasses

[51,52]. When small amounts of alkali oxide are added to GeO_2 , the glass creates 6- and 5- coordinated Ge atoms without forming non-bridging oxygens (NBOs). The network has corner-shared $[\text{GeO}_4]$ tetrahedra connected in a random structure. The refractive index and dispersion in $\text{Na}_2\text{O-GeO}_2$ glasses were also studied [53]. The refractive index of GeO_2 glasses containing 5-30 mol% Na_2O were measured in the wavelength range of 0.334 μm to 1.71 μm using the minimum deviation method. With the addition of Na_2O , the refractive index n_d increased at $5 < \text{Na}_2\text{O} < 15$ mol%. The refractive index showed a maximum around 15 mol% Na_2O and decreased with further addition. The Abbe number V_d decreased monotonically. The variation of n_d and V_d with Na_2O content was related to the oxygen coordination number of Ge ions.

Since the invention of glass lasers, rare earth ion doped germanate glasses have been widely studied. Optical spectra of Er^{3+} in $\text{K}_2\text{O-BaO-GeO}_2$ germanate glass have been reported by Reisfeld [54, 55]. Oscillator strengths, emission spectra and excitation decay lifetimes of Er^{3+} and Tm^{3+} were measured. The spontaneous transition probabilities of the $^4\text{S}_{3/2}$ and $^4\text{F}_{9/2}$ to all terminal levels of Er^{3+} were calculated using the Judd-Ofelt theory. Quantum efficiencies of the $^4\text{S}_{3/2}$ and $^4\text{F}_{9/2}$ fluorescence were also measured in germanate glass.

For most of the researches on the Er^{3+} doped germanate glasses, the interest is focused on the upconversion. In $\text{Na}_2\text{O-GeO}_2$ sodium germanate glass, upconversion fluorescences of the green $^4\text{S}_{3/2} \rightarrow ^4\text{I}_{15/2}$ and red $^4\text{F}_{9/2} \rightarrow ^4\text{I}_{15/2}$ transitions of the Er^{3+} ions were studied by Murata using Yb^{3+} and Er^{3+} codopants [56]. The phonon energy of the glass network is discussed in terms of glass structure. With the lower phonon energy of glass, the Er^{3+} ions have higher upconversion fluorescence efficiency.

Er^{3+} doped PbO-GeO_2 and $\text{PbO-TeO}_2\text{-GeO}_2$ glasses have been studied by Pan [57-59]. The research concentrated on the infrared-visible upconversion. It has also been found that the $^4\text{S}_{3/2} \rightarrow ^4\text{I}_{15/2}$ radiative transition rate of Er^{3+} in the $\text{PbO-TeO}_2\text{-GeO}_2$ glass is about twice as large as observed in PbO-GeO_2 glass and the upconversion efficiency in the $\text{PbO-TeO}_2\text{-GeO}_2$ glass is about four times larger than that in the PbO-GeO_2 glass. These host-dependent properties are mainly attributed to the

enhanced local oscillator fields and the reduced multiphonon rates in lead-tellurium-germanate glass compared to lead-germanate glass.

In PbO-GeO₂ germanate glass, optical properties of rare earth ions (Pr, Nd, Sm, Eu, Dy, Ho, Er, and Tm) have also been studied by Wachtler et al [60]. As the amount of lead increases, the covalency of the rare earth ion and oxygen bond changes, this affects the symmetry of the rare earth site and the dopant site distribution, the peak of stimulated emission cross-section rank among the highest found for oxide glasses. Therefore, it is worthwhile to study the fluorescence properties in Er³⁺-doped heavy metal oxide germanate glass.

2.4 Rare earth doped tellurite glasses

Tellurium oxide (TeO₂) does not form glass by itself, but it forms glasses with modifying oxides [64]. TeO₂ based glasses also exhibit better infrared transmission than SiO₂ based glasses due to the larger size and the heavier mass of tellurium when compared to that of silicon. Tellurium oxide with R₂O, RO, R₂O₃, RO₂, R₂O₅ and RO₃, glass forming- systems were studied [50]. These research data showed the glass formation regions of TeO₂ with all kinds of oxides and some physical and chemical properties of these glasses.

The structure of binary TeO₂-Na₂O glass was studied by using the magic angle spinning NMR experiment [62]. The sodium coordination change was found to vary from about six at low modifier concentration to about five at high concentration. Mixed alkali effect was also investigated in tellurite glass system 30[(1-x)Li₂O·xNa₂O]: 70TeO₂ [63]. Electrical conductivity and glass transition temperature were measured. σ and T_g all showed non-linear behaviour upon substitution of one alkali ion by another. The minima in σ and T_g at Na/(Na+Li) = 0.6 were observed.

The structure of binary R₂O-TeO₂ (R = Li, Na, K) glass, binary MO-TeO₂ (M = Mg, Sr, Ba and Zn) glass and binary tellurite glasses containing tri- or tetra-valent cations was studied by Raman spectroscopy [64-67]. The structure change has been also measured from room temperature to high temperature [68]. The glasses have a continuous network based on TeO₄ trigonal bipyramids and TeO₃₊₁ polyhedra having one non-bridging oxygen (NBO) atom per unit structure. In these glasses, TeO₃

trigonal pyramids with NBO are also formed in the continuous network. The glass formation, thermal properties and structure of ZnO-TeO₂ and PbO-GeO₂-TeO₂ glass system were also studied by using DSC, X-ray diffraction and Raman spectroscopy [69, 70].

Rare-earth doped tellurite glasses have been studied widely because of their lowest phonon energy in oxide glasses.

In Pr³⁺-doped tellurite glass, radiative and non-radiative transition probabilities of the luminescent levels ³P₁, ¹D₂ and ¹G₄ were measured [71]. Their lifetimes and the concentration dependence of the cross-relaxation rates were also measured. Upconversion fluorescence of Pr³⁺ in tellurite glass was observed at 487nm (³P₀-³H₄), following excitation with 593 nm tuned to the ¹D₂ level [72]. In Pr³⁺-doped Na₂O-ZnO-TeO₂ glass [73], ¹G₄→³H₅ fluorescence spectrum of Pr³⁺ was measured which was pumped at 1.02 μm. The peak fluorescence appears at 1.33 μm and the bandwidth is around 90 nm, the measured lifetime is 22 μs. The lifetime is shorter than in fluoride glasses because of the higher phonon energy of TeO₂-based glass and the peak of emission shifts to longer wavelengths as a result of the nephelauxleutic effect. Pr³⁺-doped tellurite glass for 1.3 μm optical amplifiers have been reported [74]. The emission from ¹G₄→³H₅ transition has a spectral bandwidth of 100 nm. The lifetime of the ¹G₄ level is 24 μs, and the quantum efficiency is about 2.6%, which is comparable to that in fluorozirconate glasses.

With regarded to Nd³⁺-doped tellurite glasses, in ⁴F_{3/2}→⁴I_{11/2} transition, bulk glass laser operating at 1.06 μm was described [75]. Single mode tellurite glass fibre laser at 1.06 μm was also developed in this transition [76]. In order to optimise the 1.3 μm amplification, Nd³⁺-doped Na₂O-ZnO-TeO₂ glass was studied [73]. Comparisons of spectroscopic and laser properties of the ⁴F_{3/2}→⁴I_{13/2} transition among various glasses were given. Nd³⁺-doped tellurite glass appears to be a less promising material for the 1.3 μm window telecommunication application because the emission spectrum red-shifts outside the 1.3 μm window.

Er³⁺-doped glasses were first investigated for eye safe range finders, the great interest of Er³⁺ dope glasses is the fibre amplifiers for the 1.55 μm

telecommunication window [77, 78]. As the development of EDFA, it is important to flatten the gain spectrum and broaden the amplification bandwidth of EDFA in order to increase the transmission capacity of wavelength-division-multiplex (WDM) transmission networks. As we introduced in chapter 1, there are three approaches to achieve broad amplification bandwidth. Of these approaches changing the host is the simplest configuration. As tellurite glass has high refractive index n , relatively low phonon energy, high rare earth solubility and good glass stability [73], the stimulated emission cross section σ_e is related to the refractive index (n) of host glasses, expressed by: $\sigma_e \propto (n^2+2)^2/9n$, thus tellurite glasses are capable of providing a large stimulated emission cross section over a broad bandwidth. The Er^{3+} -doped tellurite fibre amplifier has the potential for greatly broadening the flat amplification bandwidth.

In Er^{3+} -doped $\text{TeO}_2\text{-R}_2\text{O}$ glass (where $\text{R}_2\text{O} = \text{Li}_2\text{O}, \text{Na}_2\text{O}, \text{K}_2\text{O}, \text{Rb}_2\text{O}, \text{Cs}_2\text{O}$), with about 1wt% Er_2O_3 , the Judd-Ofelt parameters and radiative lifetimes for the transitions ${}^4\text{I}_{13/2} \rightarrow {}^4\text{I}_{15/2}$ and ${}^4\text{I}_{11/2} \rightarrow {}^4\text{I}_{15/2}$ have been reported [79]. The spontaneous transition probabilities of the ${}^4\text{S}_{3/2}$ and ${}^4\text{F}_{9/2}$ to all terminal levels of Er^{3+} were calculated using the Judd-Ofelt theory [80]. The absorption and emission cross sections, fluorescence spectra of the ${}^4\text{I}_{13/2} \rightarrow {}^4\text{I}_{15/2}$ transition at 1.54 μm with different concentrations of Er^{3+} were measured in $\text{TeO}_2\text{-R}_2\text{O-ZnO}$ glass [73]. The lifetimes of the ${}^4\text{I}_{13/2} \rightarrow {}^4\text{I}_{15/2}$ transition were 2 ~ 4 ms when doped Er^{3+} concentration in this glass was varied from 0.05 to 2.55 mol%.

Er^{3+} -doped tellurite single mode fibre was fabricated and signal amplification and laser oscillation were demonstrated for the first time by Mori et al in 1996 [81]. A small signal gain of 16 dB at 1.56 μm was obtained with a pump power of 130 mW at 978 nm. After that, tellurite-based Er^{3+} -doped fibre amplifier (EDFA) was demonstrated by a research group in NTT Opto-Electronics Laboratories for flattened gain amplifier application [82]. Small signal gains exceeding 20 dB were obtained over a bandwidth as wide as 80 nm from 1530 to 1610 nm. Low-noise and gain-flattened tellurite-based EDFA has been developed by employing a hybrid configuration in which tellurite EDFA joined to a 0.98 μm pumped silica EDFA. The gain flatness was improved by employing a Mach-Zehnder type gain equalizer [83-85]. They also demonstrated a parallel-type amplifier with a flat amplification

bandwidth 113 nm [86], it is composed of a tellurite based EDFA and a 1.45 μm band gain flattened Tm-doped fluoride fibre amplifier, the flat and wide gain spectrum of these amplifiers will allow us to greatly increase the capacity of WDM networks. In tellurite based EDFA, signal gain and noise figure were compared as pump at 980 and 1480 nm [87]. A small signal gain of 34 dB was obtained at 1533 nm for a pump power of 150 mW + 50 mW at 980 nm. The higher gain was obtained with less pump power at 1480 nm. Regarding noise figure characteristics, 980 nm pumping shows a lower noise figure than 1480 nm pumping.

In addition to Pr^{3+} , Nd^{3+} and Er^{3+} , Tm^{3+} has been intensively studied for use in optical amplifiers [88,89]. Eigen states and radiative transition probabilities for Tm^{3+} in tellurite glass have been calculated [90]. Both 2.3 μm (${}^3\text{H}_4 \rightarrow {}^3\text{H}_5$) and 1.88 μm (${}^3\text{F}_4 \rightarrow {}^3\text{H}_6$) emission in Tm^{3+} are attractive for chemical sensing, medical and atmosphere transmission application, and the 1.47 μm (${}^3\text{H}_4 \rightarrow {}^3\text{F}_4$) emission is near the third telecommunication window of silica fiber. TDFA (Tm^{3+} doped fibre amplifier) is potential to expand the 1.5 μm transmission window and then increases the WDM channels. Although Tm^{3+} doped silica fibre laser [90] and fluorozirconate fibre laser [89] have been reported, the former suffer from high phonon energy (1100 cm^{-1}) and the later from the poor glass stability, the low phonon energy tellurite glass (650 cm^{-1}) will provide much higher quantum efficiencies than silica glass at 1.47 μm and 1.88 μm .

For 1.47 μm lasing action to occur, it is necessary to quench the relatively long-lived lower laser level to eliminate the self-terminating behaviour of thulium. Codoping with terbium [91] and holmium [92] for thulium in the fluoride glasses has been demonstrated. The results indicated that holmium co-doping decreased the lifetime of lower lasing level by nearly two orders of magnitude with much less effect on the upper lasing level. Therefore, Ho^{3+} was selected for quenching the lower lasing level of Tm^{3+} emitting at 1.47 μm . Tm^{3+} - Ho^{3+} co-doped TeO_2 - BaO glasses have been reported by J. S. Wang et al [93, 94]. Emission from 1.47, 1.88 and 2.3 μm has been measured and the effect of Ho^{3+} concentration on the fluorescence strength of these transitions has been discussed. At the Tm_2O_3 concentration of 0.2 wt%, the lifetimes of ${}^3\text{H}_4$ and ${}^3\text{F}_4$ levels are 290 and 1879 μs , respectively. From the

emission spectrum of ${}^3\text{H}_4$, it extends over 1.5 μm region, it is very possible to make amplifier to compensate C-band of EDFA at short wavelength and then increase the communication wavelength band, providing more choice for broadband optical fibre amplifier.

2.5 Objectives of the research

The objectives of this thesis are to search a glass host for broadband and flat gain EDFA, therefore different kinds of glasses include modified silicate glass, heavy metal oxide germanate glass and tellurite glass doped with Er^{3+} ion are studied. Tellurite glass fibre will be drawn and fluorescence property of Er^{3+} ion in fibre will be measured. Another way to increase the communication bandwidths is to connect the 2nd and 3rd windows using TDFA. Therefore, Nd^{3+} and Tm^{3+} -doped tellurite glass are studied and NDFA and TDFA in tellurite glass are discussed.

References

1. Maiman, T. H., *Phys. Rev. Lett.* **4**, 564 (1960).
2. Snitzer, E., *Phys. Rev. Lett.* **7**, 444 (1961).
3. Snitzer, E., and R. Woodcock, *Appl. Phys. Lett.* **6**, 45 (1965).
4. Geusic, J. E., and H. E. D. Scovil, *Bell System Tech. J.* **41**, 1371 (1962).
5. Koester, C. J., and E. Snitzer, *J. Opt. Soc. Amer.* **53**, 515 (1963).
6. Koester, C. J., and E. Snitzer, *Appl. Optics* **3**, 1182 (1964).
7. Mears, R. J., L. Reekie, I. M. Jauncey, and D. N. Payne, *Tech. Dig. Conf. On Optical Fibre Communication/Int. Conf. Integrated Optics and Optical Fibre Communication (OFC/IOOC'87)*, Reno, Nevada, Feb. 1987, paper W12.
8. Ainslie, B. J., S. P. Craig, S. T. Davey, and B. Wakefield, *Mat. Lett.* **6**, 139 (1988).
9. Tachibana, M., R. I. Laming, P. R. Morkel, and D. N. Payne, *IEEE Photon. Tech. Lett.* **3**, 118 (1991).
10. Georges, E. S., *Tech. Digest of OAA '95*, 1995, Paper TH5-1.
11. Shimizu, M., M. Yamada, M. Horiguchi, T. Takeshita, and M. Okayasu, *Electron. Lett.* **26**, 1641 (1990).
12. Laming, R. I., L. Reekie, D. N. Payne, P. L. Scrivener, F. Fontana, and A. Righetti, *Tech. Digest of ECOC '88, Part 2*, 1988, pp.25-28.
13. Shimizu, M., M. Yamada, M. Horiguchi, and E. Sugita, *IEEE Photon. Tech. Lett.* **2**, 43 (1990).
14. Laming, R. I., P. R. Morkel, D. N. Payne, and L. Reekie, *Tech. Digest of ECOC '88, Part 1*, 1988, pp. 54-57.
15. Yamada, M., M. Shimizu, M. Okayasu, T. Takeshita, M. Horiguchi, Y. Tachikawa, and E. Sugita, *IEEE Photon. Tech. Lett.* **2**, 205 (1990).
16. Townsend, J. E., W. L. Barnes, K. P. Jedrzejewski, and S. G. Grubb, *Electron. Lett.* **27**, 1958 (1991).
17. Grubb, S. G., *Tech. Digest of OFC '95*, Feb 1995, Paper Tuj1.
18. Kagi, N., A. Oyobe, and K. Nakamura, *IEEE J. Lightwave Tech.* **9**, 261 (1991).
19. Marcerou, J. F., H. Fevrier, P. M. Gabla, and J. Auge, *Tech. Digest of OFC '94*, Vol. 4, Feb. 1994, pp. 302-304.
20. Arai, S., A. Oyobe, A. Umeda, and K. Kokura, *Tech. Digest of OEC '94*, July 1994, pp. 42-43.

21. Yamada, M., T. Kanamori, Y. Terunuma, K. Oikawa, M. Shimizu, and S. Sudo, *IEEE Photon. Tech. Lett.* **8**, 882 (1996).
22. Bayart, D., B. Clesca, L. Hamon, and J. L. Beylat, *IEEE Photon. Tech. Lett.* **6**, 613 (1994).
23. Yamada, M., M. Shimizu, Y. Ohishi, M. Horiguchi, S. Sudo and A. Shimizu, *Electron. Lett.* **30**, 1762 (1994).
24. Kashiwada, T., M. Shigematsu, M. Kakui, M. Onishi, and M. Nishimura, *Tech. Digest of OFC'95*, Feb. 1995, pp.77-78.
25. Neeves, A. E., A. J. Bruce, W.A. Reed, E. M. Rabinovich, W. H. Grodkiewicz, N. A. Kopylov, A. Lidgard, and D. G. Digiovanni, *Solid-State Optical Materials* **10**, 353 (1993).
26. Zachariasen, W. H., *J. Am. Chem. Soc.* **54**, 3841 (1932).
27. Zemaon, S., G. Lambert, W. J. Miniscalco, and L. J. Andrew, *Fibre Laser Sources and Amplifiers*, Vol. 1171: SPIE, 1989, PP.219-236.
28. Gruber, J. B., J. R. Henderson, M. Muramoto, K. Rajnak, and J. G. Conway, *J. Chem. Phys.* **45**, 477 (1966).
29. Gruber, J. B., W. F. Krupke, and J. M. Poinserter, *J. Chem. Phys.* **41**, 3363 (1964).
30. Desurvire, E. and J. R. Simpson, *Optics Lett.* **15**, 547 (1990).
31. McCumber, D. E., and M. D. Sturge, *J. Appl. Phys.* **34**, 1682 (1963).
32. Selzer, P. M., D. L. Huber, D. S. Hamilton, W. M. Yen, and M. J. Weber, *Phys. Rev. Lett.* **36**, 813(1976).
33. Zyskind, J. L., E. Desurvire, J. W. Sulhoff, and D. J. DiGiovanni, *IEEE Photon. Tech. Lett.* **2**, 869 (1990).
34. Zyskind, J. L., E. Desurvire, J. W. Sulhoff, and D. J. DiGiovanni, *Tech. Digest of OAA'90*, MD4, 1990, pp.507-509.
35. Laming, R. I., L. Reekie, P. R. Morkel, and D. N. Payne, *Electron. Lett.* **30**, 455 (1989).
36. Miniscalco, W. J., "Optical and Electronic Properties of Rare Earth Ions in Glasses," in *Rare Earth Doped Fiber Lasers and Amplifiers*, M. J. F. Digonnet (Ed.), New York: Marcel Dekker, 1993.
37. Zemaon, S., G. Lambert, W. J. Miniscalco, and B. A. Thompson, *Fibre Laser Sources and Amplifiers III*, Vol. 1581: SPIE, 1991, pp. 91-100.

38. Desurvire, E., J. L. Zyskind, and J. R. Simpson, *IEEE Photon. Tech. Lett.*, Vol. 2, Apr. 1990, pp. 246-248.
39. Macfarlane, R. M., and R. M. Shelby, *J. Lumin.* 36, 179 (1987).
40. Denisov, Y. V., and V. A. Kizel, *Opt. Spectrosc.* 23, 251 (1967).
41. Brecher, C. and L. A. Riseberg, *Phys. Rev. B* **13**, 81 (1976).
42. Brecher, C. and L. A. Riseberg, *Phys. Rev. B* **21**, 2607 (1980).
43. Robinson, C. C., *J. of Non-Cryst. Solids* **10**, 1 (1974).
44. Robinson, C. C., *J. of Non-Cryst. Solids* **10**, 11 (1974).
45. Desurvire, E., J. W. Sulhoff, J. L. Zyskind, and J. R. Simpson, *IEEE Photon. Tech. Lett.* **2**, 653 (1990).
46. Millar, C. A., M. C. Brierley, and P. W. France, *Tech. Digest of EOCO'88, 1988*, pp.66-69.
47. Lucas, J., *J. Less-Common Metals* **112**, 27 (1985).
48. Zemaon, S., G. Lambert, L. J. Andrew, W. J. Miniscalco, B. T. Hall, and, R. C. Folweiler, *J. Appl. Phys.* **69**, 6799 (1991).
49. Dejneka, M. J., *MRS Bulletin*, Nov 1998, pp57.
50. Mazurin, O.V., M. V. Streltsina, and T. P. Shvaiko-shvaikovskaya, *Physical Sciences Data 15 "handbook of glass data" Part D ternary non-silicate glasses.*
51. Mochida, N., K. Sakai, and K. Kikuchi, *J. of the Ceram. Soc. of Jap* **92**, 164 (1984).
52. Wang, J. S., and M. H. Hon, *Ceramics International* **21**, 113 (1995).
53. Mito, T., H. Takebe, and K. Morinaga, *J. of the Ceram. Soc. of Jap* **103**, 886 (1995).
54. Reisfeld, R., and Y. Eckstein, *J. Non-Cryst. Solids* **15**, 125 (1974).
55. Reisfeld, R., and Y. Eckstein, *J. Non-Cryst. Solids* **12**, 357 (1973).
56. Murata, T., H. Takebe, and K. Morinaga, *J of Amer. Ceram. Soc.* **81**, 249 (1998).
57. Pan, Z., S.H. Morgan, A. Loper, V. King, B. H. Long, and W. E. Collings, *J. of Appl. Phys.* **77**, 4688 (1995).
58. Pan, Z., S. H. Morgan, K. Dyer, A. Ueda, and H. M. Liu, *J. of Appl. Phys.* **79**, 8909 (1996).
59. Pan, Z., and S. H. Morgan, *J. of Luminescence* **75**, 301 (1997).
60. Wachtler, M., A. Speghini, K. Gatterer, H. P. Fritzer, D. Ajo, and M. Bettinelli, *J of Amer. Ceram. Soc.* **81**, 2045 (1998).
61. Werner Vogel, 2nd Edition 1992, "Glass Chemistry"

62. Tagg, S. L., R. E. Youngman, and J. W. Zwanziger, *J. of Phys. Chem.* **99**, 5111 (1995).
63. Balaya, P., and C. S. Sunandana, *J. Non-Crystal. Solids* **175**, 51 (1994).
64. Himei, Y., A. Osaka, T. Nanba, and Y. Miura, *J. Non-Crystal. Solids.* **177**, 164 (1994).
65. Sekiya, T., N. Mochida, A. Ohtsuka, and M. Tonokawa, *J. Non-Crystal. Solids.* **144**, 128 (1992).
66. Sekiya, T., N. Mochida, and A. Ohtsuka, *J. Non-Crystal. Solids* **168**, 106 (1994).
67. Sekiya, T., N. Mochida, and A. Soejima, *J. Non-Crystal. Solids* **191**, 115 (1995).
68. Tatsumisago, M., S. K. Lee, T. Minami, and Y. Kowada, *J. Non-Crystal. Solids* **177**, 154 (1994).
69. Burger, H., K. Kneipp, H. Hobert, and W. Vogel, *J. Non-Crystal. Solids* **151**, 134 (1992).
70. Pan, Z., and S. H. Morgan, *J. Non-Crystal. Solids* **210**, 130 (1997).
71. Eyal, M., and R. Reisfeld, *J. of Less-Common Metals* **148**, 223 (1989).
72. Ilkim, S., and S. I. Yun, *J. of Luminescence* **60 & 61**, 233(1994).
73. Wang, J. S., E. M. Vogel, and E. Snitzer, *Optical Materials* **3**, 187 (1994).
74. Man, S. Q., E. Y. B. Pun, and P. S. Chung, *Optics Communications* **168**, 369 (1999).
75. Lei, N., B. Xu, and Z. Jiang, *Optics Communications* **127**, 263 (1996).
76. Wang, J. S., D. P. Machewirth, F. Wu, E. Snitzer, and E. M. Vogel, *Optics Letters* **19**, 1448 (1994).
77. Miniscalco, W. J., "Erbium Doped Glasses for Fiber Amplifiers at 1500 nm," *IEEE J. Lightwave Technol.* **9**, 234 (1991).
78. Atkins, C. G., *Electron Letters* **25**, 910 (1989).
79. Wang, J. S., E. Snitzer and G. H. J. Sigel, *MRS Symp. Proc.*, Boston, MA (1991).
80. Reisfeld, R., and Y. Eckstein, *Solid State Communications* **13**, 741 (1974).
81. Mori, A., Y. Ohishi, and S. Sudo, *Electronics Letters* **33**, 863 (1997).
82. Mori, A., Y. Ohishi, M. Yamada, H. Ono, Y. Nishida, K. Oikawa, and S. Sudo, *OFC'97*, Washington, 1997, PD1.
83. Mori, A., K. Kobayashi, M. Yamada, T. Kanamori, K. Oikawa, Y. Nishida, and Y. Ohishi, *Electronics Letters* **34**, 887 (1998).
84. Yamada, M., A. Mori, H. Ono, K. Kobayashi, T. Kanamori, and Y. Ohishi, *Electronics Letters* **34**, 370 (1998).

85. Yamada, M., A. Mori, K. Kobayashi, H. Ono, T. Kanamori, K. Oikawa, Y. Nishida, and Y. Ohishi, *OAA'1998*, pp. 86-89
86. Yamada, M., A. Mori, K. Kobayashi, H. Ono, T. Kanamori, K. Oikawa, Y. Nishida, and Y. Ohishi, *IEEE Photon. Tech. Lett.* **10**, 1244 (1998).
87. Nakai, T., Y. Noda, T. Tani, Y. Mimura, T. Sudo, and S. Ohno, *OAA'1998*, pp. 82-85
88. Neeves, A. E., A. J. Bruce, W. A. Reed, E. M. Rabinovich, W. H. Grodkiewicz, N. A. Kopylov, A. Lidgard, and D. J. DiDiovanni, *Proceeding of the Symposium on Solid-State Optical Materials*, Cincinnati, OH, 1991.
89. Carter, J. N., R. G. Smart, A. C. Tropper, and D. C. Hanna, *7th International Symposium on Halide Glasses*, Lorne, Victoria, Australia, 1991.
90. Hanna, D. C., R. M. Percival, R. G. Smart, and A. C. Tropper, *Optics Comm.* **75**, 283 (1990).
91. Rosenblatt, G. H., R. Finther, J. R. C. Stone, and L. Esterowitz, *OSA Proc. Tunable Solid State Laser Conference*, Cape Cod, Mass. 1989, pp373.
92. Pafchek, R., J. Aniano, E. Snitzer, and J. G. H. Sigel, *MRS*, 1989.
93. Wang, J. S., E. Snitzer, E. M. Vogel and J. G. H. Sigel, *ICL '93*, Connecticut, 1993
94. Wang, J. S., E. Snitzer, E. M. Vogel and J. G. H. Sigel, *J. of Luminescence* **60&61**, 145 (1994).

Chapter 3

Theory of radiative and non-radiative transitions of rare earth ions in glass

Rare earth ions have a long history of applications in optical and magnetic devices. Among these, luminescent devices using single crystals, powders and glasses have been particularly important. For rare-earth doped glasses, such as glass fibre lasers and amplifiers, the radiative and non-radiative energy transitions of rare earth ions are critical to the properties of application. They decide the absorption and emission spectra lineshape, the lifetime of excited energy level and quantum efficiency of rare-earth ions in glass. Thus the performance of glass laser and fibre amplifier is greatly affected by the radiative and non-radiative properties.

In this chapter we will describe the radiative transition rates, transition intensity, and Judd-Ofelt theory. We will also describe the nonradiative processes, including the multiphonon relaxation process and ion-ion interactions, which influence the quantum efficiency of rare earth doped devices, especially radiative and nonradiative properties of Er^{3+} -doped glasses. Finally, the pump wavelengths for Er^{3+} -doped fibre amplifier will be discussed.

3.1 Radiative Rates

The rare earth series in the periodic table consist of 14 elements from Ce (atomic number Z of 56) to Lu ($Z = 71$). In condensed matter, the trivalent ($3+$) state is the most stable for rare earth ions, and most optical devices use the properties of the trivalent state. The electronic configuration of trivalent rare earth elements is given by

$$1s^2 2s^2 2p^6 3s^2 3p^6 3d^{10} 4s^2 4p^6 4d^{10} 4f^N 5s^2 5p^6 \quad (N = 1, \dots, 14)$$

The radiative relaxation rate between electronic energy levels of rare-earth ions in a solid depends on the nature of the electronic wave function. These wave functions are determined by the Hamiltonian, which can be written as:

$$H = H_0 + H_{\text{coul}} + H_{\text{so}} + H_{\text{cf}} \quad 3.1$$

where H_0 represents the interaction of electrons with the nucleus in a free ion, H_{coul} represents the Coulomb interaction of the electrons, H_{so} is the spin-orbit interaction, H_{cf} is the interaction of the electrons with the crystal field from the surrounding ions in the solid. The relative strengths of the different terms in Equation 3.1 are different for rare-earth ions, so each must be treated separately.

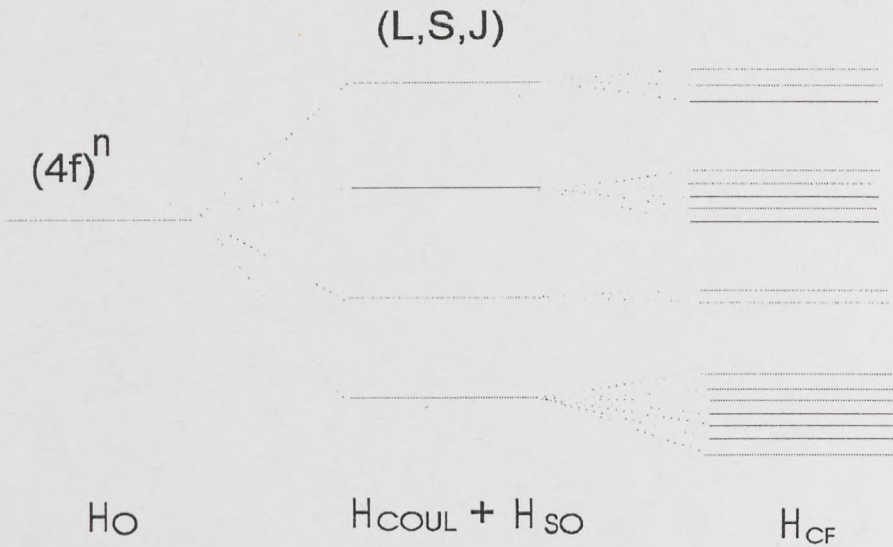


Fig 3.1 Effect of different terms in the Hamiltonian on energy level positions

For rare-earth doped materials, the observed infrared and visible optical spectra are a consequence of transitions between 4f states. Since the outer 5s and 5p electrons shield the 4f electrons from the effects of the environment, the effect of crystal field on the optical transitions involved in the 4f electrons is the smallest in Eq.3.1. It can be treated as a perturbation. The other three terms give rise to a set of states labelled by total spin S , total orbital angular momentum L , and total angular momentum J . J is the total of L and S which are vectorially added to form. Each one is $(2J+1)$ -fold degenerate. The multiplets are usually identified by using Russell-Saunders coupling which are labelled $^{2S+1}L_J$.

The crystal field interaction H_{cf} breaks the spherical symmetry of the Hamiltonian, and removes the $(2J+1)$ degeneracy of the levels. This so-called Stark splitting is generally a few hundred cm^{-1} in magnitude, compared with a few thousand cm^{-1} for the splitting between $\{L, S, J\}$ levels. Radiative transitions can occur from any Stark

component of one $\{L, S, J\}$ multiplet to any Stark component of another $\{L, S, J\}$ multiplet as shown in figure 3.1.

For Er^{3+} -doped tellurite glass, figure 3.2 shows the absorption cross-section spectrum and figure 1.5 illustrates the corresponding energy level diagram. The eight lasing transitions reported for crystalline hosts [1] are also indicated in figure 1.5. Because of the application Er^{3+} doped fibre amplifier (EDFA) in optical communication, most of the following discussion on the fluorescence properties pertains to the ${}^4I_{13/2} \rightarrow {}^4I_{15/2}$ transition at 1500 nm, since this is the most important and most extensively studied one.

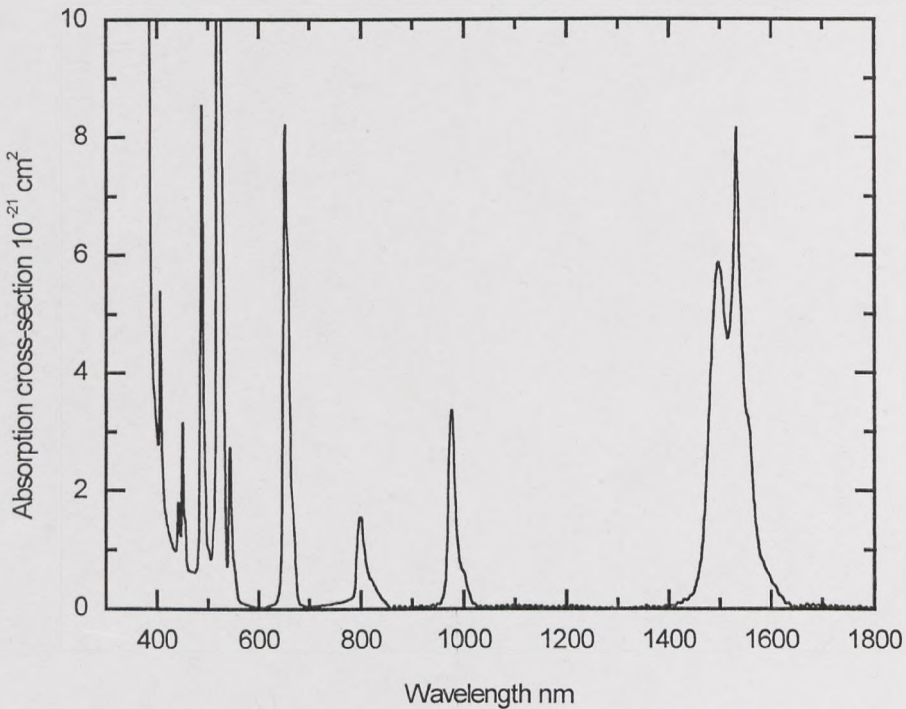


Fig. 3.2 Absorption cross-section of Er^{3+} in $80\text{TeO}_2\text{-}10\text{Na}_2\text{O-}10\text{ZnO}$ glass

The usual definition for oscillator strength is in terms of the integrated absorption cross-sections from the ground $\{L, S, J\}$ multiplet to some higher multiplet.

$$f_{abs} = \left[4\pi \epsilon_0 \right] \frac{mc}{\pi e^2} \int \sigma_{abs}(\nu) d\nu \quad 3.2$$

where m and e are the mass and charge of the electron, c is the speed of light, and ν is the frequency. The integral is over the entire absorption lineshape (i.e., all Stark components are included), and the optional prefactor in square brackets is for SI units. One can similarly define an oscillator strength for emission as follows:

$$f_{emit} = [4\pi \epsilon_0] \frac{mc}{\pi e^2} \int \sigma_{SE}(\nu) d\nu \quad 3.3$$

where σ_{SE} is the stimulated emission cross-section. For a given pair of levels 1 and 2, the absorption and emission oscillator strengths are related by

$$f_{emit} = \frac{g_1}{g_2} f_{abs} \quad 3.4$$

where g_1 is the degeneracy of the lower level, and g_2 that of upper level. Eq. 3.4 is an exact result only if the upper and lower levels of interest are truly degenerate. The radiative rate from level 2 (upper level) to level 1 (lower level) is related to the integrated emission cross-section by

$$A = \frac{8\pi \nu^2 n^2}{c^2} \int \sigma_{SE}(\nu) d\nu \quad 3.5$$

or to the emission oscillator strength by

$$A = \frac{8\pi^2 \nu^2 e^2 n^2}{[4\pi \epsilon_0] mc^3} f_{emit} \quad 3.6$$

where A is the probability per unit time for a radiative transition, and n is the index of refraction of the medium.

If a is an excited state that decays only by the emission of photons, its observed relaxation rate is the sum of the probabilities for transitions to all possible final states, f , the total rate is the reciprocal of the excited state lifetime τ_a :

$$\frac{1}{\tau_a} = \sum_f A_{a,f} \quad 3.7$$

ΣA_a is the sum of all transition from excited level a. The branching ratio $\beta_{a,b}$, for the transition $a \rightarrow b$ is the fraction of all spontaneous decay processes that occur through that channel and defined as follows:

$$\beta_{a,b} = \frac{A_{a,b}}{\sum_f A_{a,f}} = A_{a,b} \tau_a \quad 3.8$$

The branching ratio, which has an important influence on the performance of a device based on particular transition, appears often in the discussion of specific ions. It has a significant impact on the threshold of a laser and the efficiency of an amplifier. For the ${}^4I_{13/2} \rightarrow {}^4I_{15/2}$ transition of Er^{3+} in tellurite glass, the branching ratio β is 1, because there is only one decay channel.

The oscillator strength f_{abs} for each transition can be calculated from Eq.3.2. In general, the measured oscillator strength has contributions from both electric dipole f_{ed} and magnetic dipole f_{md} transitions:

$$f_{abs} = f_{ed} + f_{md} \quad 3.9$$

The magnetic dipole contribution can be found directly by calculating the matrix elements of the angular momentum operators:

$$f_{md} = \frac{h\nu \chi_{md}}{6(2J+1)n^2 m c^2} \left| \langle a \| L + 2S \| b \rangle \right|^2 \quad 3.10$$

where $\chi_{md} = n^3$ is the local field correction for magnetic dipole transitions.

Oscillator strengths are approximately one for fully allowed electron-dipole transitions and are roughly seven orders of magnitude weaker for magnetic dipole transitions. Most of the time, magnetic dipole transitions can be neglected. But for the

${}^4I_{13/2} \rightarrow {}^4I_{15/2}$ transition of Er^{3+} ion, the magnetic dipole transition contributes significantly to the oscillator strength, it is about 20 ~ 30 % of the total strength.

A useful semi-empirical technique for calculating the strength of rare earth transitions was developed independently by Judd [2] and Ofelt [3]. The Judd-Ofelt theory is a powerful tool to characterise the electric dipole 4f transitions in rare earth – doped glasses. The calculation of 4f transition probabilities is made tractable by assuming that all the states of the perturbing opposite parity configurations have a single average energy and by introducing a small number of phenomenological intensity parameters which contain the strength of the electric field. The spectrally integrated, electric-dipole strength of the transition from level a and b then reduced to a simple expression involving three empirical parameters (Ω_2 , Ω_4 and Ω_6) and the appropriate reduced matrix elements in Eq 3.11:

$$f_{ed} = \frac{8\pi^2 m \nu \chi_{ed}}{3h(2J+1)n^2} \sum_{t=2,4,6} \Omega_t \left| \langle a || U^{(t)} || b \rangle \right|^2 \quad 3.11$$

where $\chi_{ed} = n(n^2+2)^2/9$ is a local field correction factor for electric dipole radiation, J is the angular momentum quantum number of the initial level in the transition, and the $|\langle a || U^{(t)} || b \rangle|^2$ are doubly reduced matrix elements of the tensor operator $U(t)$. They are almost independent of material and have been tabulated by Carnall (1977) [4]. The host dependence is contained in three intensity parameters Ω_t , which are empirically determined for a given combination of dopant and host. The Judd-Ofelt parameters Ω_2 , Ω_4 and Ω_6 are determined by first measuring the integrated absorption cross-section for a number of transitions from the ground $\{L,S,J\}$ state multiplet to higher $\{L,S,J\}$ multiplets. There is no clear physical meaning to the intensity parameters other than that Ω_2 is correlated with the degree of covalence: ionic materials like fluorides have very small values of Ω_2 , while covalent materials like silicates have large values. It will be seen that this gives rise to a significant composition dependence for some important transitions. The Judd-Ofelt analysis is accurate to about 10-15% and is particularly valuable for obtaining strengths of transitions for which direct measurements are difficult or impossible. It is possible to calculate all

the oscillator strengths and rates of absorption and emission transitions in the 4f configuration on the basis of the absorption spectrum and can subsequently be used to determine important radiative lifetimes, cross sections for stimulated emission and ESA (excited state absorption) transitions.

For Er³⁺ doped tellurite glass, by connecting Eq.3.2 and Eq.3.11, Eq.3.12 can be obtained and can be used to calculate the Judd-Ofelt parameters Ω_2 , Ω_4 and Ω_6 by performing a least-squares fit of this equation.

$$\frac{27hc \epsilon_0 (2j+1)n}{2\pi^2 e^2 (n^2+2)^2} \cdot \frac{\int \sigma_{(v)} dv}{\nu} = \sum_{t=2,4,6} \Omega_t \left| \langle a \| U^{(t)} \| b \rangle \right|^2 \quad 3.12$$

In a two-level system, the stimulated emission cross-section for a rare-earth ion transition can be calculated from the absorption cross-section [5]. If the lower state (level 1) and the upper state (level 2) are split into multiple components, the relationship becomes:

$$g_1 \int \nu^2 \sigma_a(\nu) d\nu = g_2 \int \nu^2 \sigma_e(\nu) d\nu \quad 3.13$$

where g_1 is the degeneracy of the lower level 1, and g_2 is that of upper level 2, ν is the photon frequency, σ_a and σ_e are the absorption and stimulated emission cross-sections. Equation 3.13 is valid for rare-earth ions only if one of the two following conditions is met: (1) all components of the two levels must be equally populated, and (2) all the transitions must have the same strength regardless of the components involved. This method is very convenient. However, the relationship does not always provide accurate emission cross-sections of rare earths because the manifold width of the 4f state often exceeds 300 cm⁻¹, and the first condition is not satisfied at room temperature (kT ~200 cm⁻¹). Furthermore, the transition strength is sensitive to the Stark levels [6].

The McCumber theory provides another method of transformation between the absorption and emission cross-sections. The only assumption needed by this theory is that the time required to establish thermal distribution within each manifold be short

compared with the lifetime of the manifold. The absorption and emission cross-sections are then related by [7]

$$\sigma_e(\nu) = \sigma_a(\nu) \exp[(\varepsilon - h\nu) / \kappa T] \quad 3.14$$

where ε is the temperature-dependent excitation energy. The physical interpretation of ε is as the net free energy required to excite electrons from the ground state to an excited state at temperature T . At frequency ν higher than ν_c ($\nu_c = \varepsilon/h$), the emission cross section is smaller than the absorption cross section and vice versa for $\nu < \nu_c$.

In rare-earth ion doped glass, the crystal field interaction is responsible for the observed shape of the emission and the absorption. Considering a transition between two J multiplets, the interaction determines the positions of the Stark components for each multiplet and therefore the wavelengths at which emission or absorption occurs. It also determines the intensity of the process for each pair of components involved. The crystal field terms vary from material to material, and this is the most important factor affecting the host dependence of spectra. The optical transitions can be broadened by three distinct processes. First, the degeneracy of a level can be split (the Stark splitting), resulting in a manifold of levels wider than the original level. Each of the resulting individual levels can then be widened by either homogeneous or inhomogeneous broadening. Homogeneous broadening refers to the width of each individual ion's transition, whereas inhomogeneous broadening refers to the ensemble width that results from the variation of the ion's optical properties from site to site.

Transition rates, emission cross-section and the emission oscillator strength of Er^{3+} ion in tellurite glass can be calculated from Eq.3.6, Eq.3.5 and Eq.3.11 respectively. From Eq.3.6, when the refractive index of glass is higher, the radiative transition rate is higher, the excited state lifetime will be lower. From Eq.3.10 and 3.11, the magnetic dipole and electric dipole oscillator strength is higher when the glass has a higher refractive index. We can compare these properties in different glass compositions and try to analyse the relation between fluorescence properties of Er^{3+} in different glass host. From the McCumber theory, we also can calculate the emission cross section and spectrum from the absorption spectrum, and compare these results with the Judd-Ofelt calculation and the measurement.

3.2. Non-radiative Transition

If the radiative relaxation were the only process depopulating an excited state, the measured fluorescence lifetime of that level would be given by $1/\tau = A$. However it is sometime found to be too long to account for the measured value of τ . This can be due to a non-radiative relaxation process, in which the energy of an excited state is dissipated via phonon vibration. For rare-earth ions in glasses there exist two types of non-radiative transition processes: one is the interaction of rare-earth ions, energy transfer, the other is that between the rare earth ions and the glass hosts, non-radiative relaxation process.

The total decay rate of an excited state can then be written

$$\frac{1}{\tau} = A + W_{nr} + W_x \quad 3.15$$

where W_{nr} is the single ion nonradiative rate due to the multiphonon energy relaxation, and W_x is the effective nonradiative rate due to energy transfer.

3.2.1 Multiphonon relaxation

Multiphonon relaxation between various 4f states occurs as a result of the simultaneous emission of several phonons that conserve the energy of the transitions. These multiphonon processes arise from the interaction of the electronic levels of the rare-earth ions with the vibration of the host lattice. The lattice vibrations are quantized as phonons having excited energies determined by the masses of the constituent ions and the bond energies between the ions.

The theory of multiphonon relaxation of rare earth ions was first formulated for crystals by Kiel [8] and extended by Risberg and Moos [9]. Layne and coworkers extended it to glass hosts [10]. The large variation in vibration spectra among materials makes the nonradiative relaxation rate extremely host dependent. For energy gaps much larger than the energy of the phonons involved, the nonradiative decay rate W_{nr} is inversely proportional to the exponential of energy gap separating the two levels [10,11]

$$W_{nr} = C [n(T) + 1]^p e^{(-\alpha \Delta E)} \quad 3.16$$

In this expression C and α are host dependent parameters, ΔE is the energy gap, p is the number of phonons required to bridge the gap, $n(T)$ is the Bose-Einstein occupation number for the effective phonon mode,

$$n(T) = \frac{1}{\exp(\hbar\omega / kT) - 1} \quad 3.17$$

where $\hbar\omega$ is the phonon energy. The parameter α is related to the coupling constant for the interaction γ , by $\alpha = -\ln(\gamma)/\hbar\omega$. From Eq.3.16 and 3.17, the nonradiative rate decreases with decreasing temperature. In practice, C, α , and p (or $\hbar\omega$) are regarded as empirical parameters that are host dependent but insensitive to the rare earth ion and energy levels involved. They are obtained by fitting Eq.3.16 to the non-radiative rates observed for as many energy gap as possible using different levels and ions in the same host. Reisfeld and Jorgenson have assembled these parameters from measurements by a large number of authors [11] and the values are listed in table 3.1.

Table 3.1 Parameters describing the nonradiative relaxation of rare earth ions in glass

Host	C (s ⁻¹)	α (10 ⁻³ cm)	$\hbar\omega$ (cm ⁻¹)
Borate	2.9×10^{12}	3.8	1400
Phosphate	5.4×10^{12}	4.7	1200
Silicate	1.4×10^{12}	4.7	1100
Germanate	3.4×10^{12}	4.9	900
Tellurite	6.3×10^{12}	4.7	700
Fluorozirconate	1.59×10^{12}	5.2	500
Sulfide	10^6	2.9	350
LaF3 (Crystal)	6.6×10^8	5.6	350

For different hosts, the oxide glasses have larger non-radiative rates because their strong covalent bonds result in higher phonon frequencies. The weaker ionic bonds of halide and sulphide glasses lead to a much lower W_{nr} as well as higher transparency at mid-infrared wavelengths. In general, glasses have much larger non-radiative rates

than the crystals of similar composition because of the larger effective phonon frequencies (larger C) and stronger electron-phonon coupling (small α). For glasses the vibrations causing nonradiative relaxation are the high energy, relatively localised, stretching modes of polyhedra forming the network.

For Er^{3+} doped tellurite glass, the transition ${}^4I_{13/2} \rightarrow {}^4I_{15/2}$ has an energy gap 6500 cm^{-1} which is responsible for the 1500 nm emission. From Eq.3.16, 3.17 and table 3.1, the multiphonon relaxation rate W_{nr} is $4.3 \times 10^{-3} \text{ s}^{-1}$, and is very small compared with the radiative rate A which is about $200 \sim 400 \text{ s}^{-1}$. The nonradiative relaxation is significant at room temperature only for borates [12]. In phosphate glass, there have been reports of slightly reduced quantum efficiencies for this level [13].

3.2.2 Energy transfer

There are three basic types of energy transfer illustrated in figure 3.3. In process 1, referred to as energy migration, the donor in an excited state transfers all of its excitation energy to a similar acceptor ion that is initially in the ground state. This leaves the donor in the ground state and the acceptor in the excited state. This process can be repeated many times, resulting in the migration of the excitation energy through the material. The energy migration will continue until some other mechanism depletes the excited state. The excitation energy may be transferred to a trap site, at which a defect or an ion in a perturbed environment dissipates the energy nonradiatively. Luminescence is quenched by transfer to trap sites, but not by the energy migration process itself.

The second energy transfer process shown in figure 3.3 is referred to as cross relaxation. If an ion excited to the metastable c level interacts with a nearby ion in the ground state, the first ion transfers part of its energy to the second. Both ions occupy the intermediate b states. When the energy gaps to the lower lying states are small, both ions decay nonradiatively to the ground state from the intermediate state. As a result, part of the excitation energy is converted into heat. Since the population of upper level is decreased every time such a cross relaxation occurs, it is much more effective than energy migration in quenching the luminescence from the upper level.

The third energy transfer process is co-operative up-conversion shown in figure 3.3 and is the inverse of cross relaxation. When two ions are in an excited state **b**, one transfers its energy to the other, leaving itself in the ground state **a** and the other in a higher excited state **c**.

Concentration quenching is a phenomenon of the quantum efficiency reduction of an emission transition of an ion with increasing concentration of that ion due to the ion-ion interactions. It can occur as a result of the energy transfer processes of cross-relaxation and co-operative up-conversion and have important implications for the performance of fibre amplifiers because it leads to a reduction in pump efficiency. It usually manifests itself as a shortening of the excited state lifetime.

For Er^{3+} doped devices, co-operative up-conversion and impurity quenching are believed to be the major cause of inefficiency at 1500 nm.

For Er^{3+} -doped tellurite glass, concentration quenching is mainly due to up-conversion process, the process is shown in figure 3.4. In A, both interacting ions are excited to the metastable ${}^4\text{I}_{13/2}$ level. In B, the donor ion transfers all its energy to the acceptor, leaving itself in the ground state ${}^4\text{I}_{15/2}$ and the acceptor in the ${}^4\text{I}_{9/2}$ state. For tellurite glass, the acceptor ion quickly decays nonradiatively back to the ${}^4\text{I}_{13/2}$ level.

Another deleterious process for the metastable ${}^4\text{I}_{13/2}$ level involves energy transfer to the OH^- complex, which serves as a trap and is extremely effective in quenching excited rare earth ions. At high OH^- concentration, this can occur through direct transfer from an excited ion. At low OH^- concentration, there is fast energy transfer between interacting donor ions until the excitation reaches one near an OH^- impurity [12], this behaves like the energy transfer process 1 in figure 3.3. This process depends on Er^{3+} concentration, it will control the quenching rate.

From Eq.3.15, at very low concentration of rare earth ion, the energy transfer rate is very small, W_x becomes negligible. The nonradiative rate can be determined from measured fluorescence lifetime and the calculated radiative rate:

$$W_{nr} = \frac{1}{\tau_{\text{exp}}} - A_{\text{calc}} \quad 3.18$$

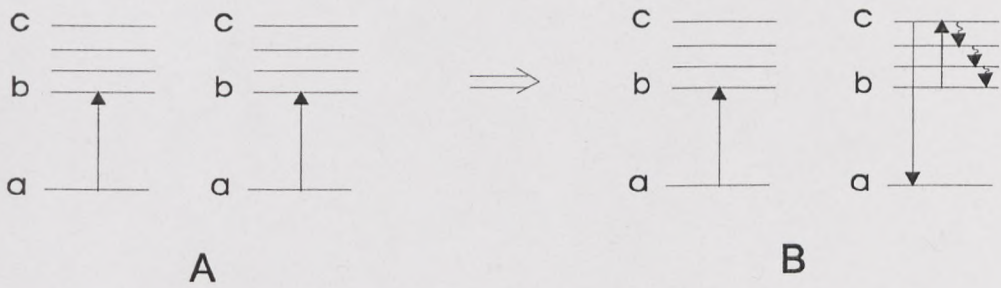
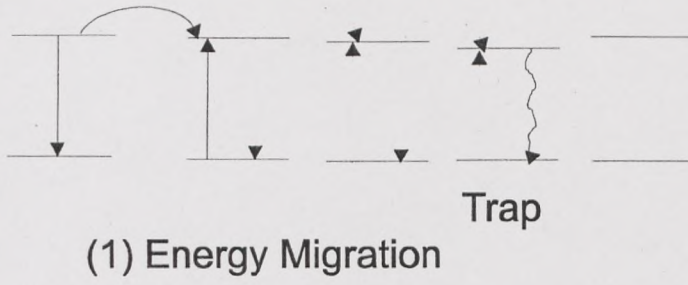


Figure 3.3 Three types of energy transfer

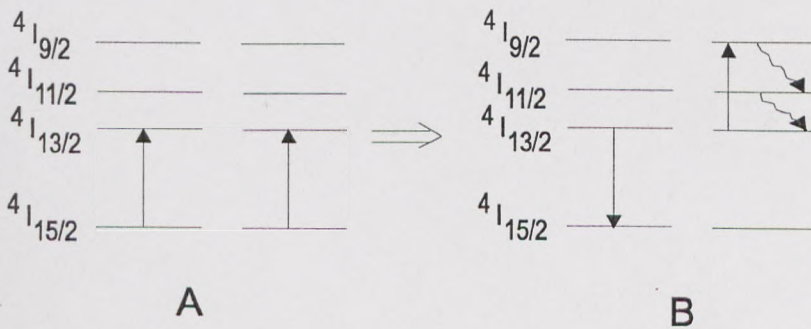


Figure 3.4 The cooperative up-conversion process for Er^{3+}

In Er^{3+} -doped tellurite glass, the nonradiative rate for ${}^4\text{I}_{13/2} \rightarrow {}^4\text{I}_{15/2}$ transition at room temperature, W_{nr} , is also negligibly small. At a certain Er^{3+} concentration, the energy transfer rate W_x or concentration quenching rate can be calculated from the measured lifetime and calculated radiative rate by the following Eq.3.19.

$$W_x = \frac{1}{\tau_{\text{exp}}} - A_{\text{calc}} \quad 3.19$$

3.3 Pump wavelengths for Er^{3+} -doped fibre amplifier (EDFA)

For Er^{3+} doped fibre amplifier, pump wavelength can be selected from every Er^{3+} absorption band in Figure 3.2 which lies at wavelengths greater than 450 nm. The first consideration in the choice of pump wavelength is the gain transition desired, followed by efficiency and the availability of pump sources. In EDFA at 1.5 μm , three wavelengths 800 nm, 980 nm and 1480 nm are used to create the excited ${}^4\text{I}_{13/2}$ state. Figure 3.5 shows several well-known gain degradation processes associated with pumping schemes in EDFAs [14~17].

- 800 nm pump band

The ${}^4\text{I}_{15/2} \rightarrow {}^4\text{I}_{9/2}$ transition gives rise to an absorption band peaking near 800 nm. The ${}^4\text{I}_{9/2}$ state is short-lived, decaying to metastable ${}^4\text{I}_{13/2}$ by multiphonon emission. An ion in this metastable state can then be promoted to the ${}^2\text{H}_{11/2}$ level through the absorption of a second 800 nm phonon. This is called pump excited state absorption (ESA). In high phonon energy oxide glasses, the ${}^2\text{H}_{11/2}$ terminal state for this 800 nm ESA process quickly decays through the intervening levels back to the ${}^4\text{I}_{13/2}$ state through multiphonon emission, the net result being the conversion of the second pump phonon into heat. In low phonon energy oxide glass like tellurite, 800 nm pump ESA can have 550 nm emission from ${}^4\text{S}_{3/2}$ state. As a result, pumping at 800 nm is inefficient. It needs much higher pump power to achieve a specified signal output power, pump ESA is a serious dissipative process for these materials and avoiding it is a primary concern in optimising device performance. In most instances, the performance of 1500 nm amplifiers pumped in this band has been rather poor because the ground state absorption (GSA) is weak and overlaps a much stronger ${}^4\text{I}_{13/2}$ ESA.

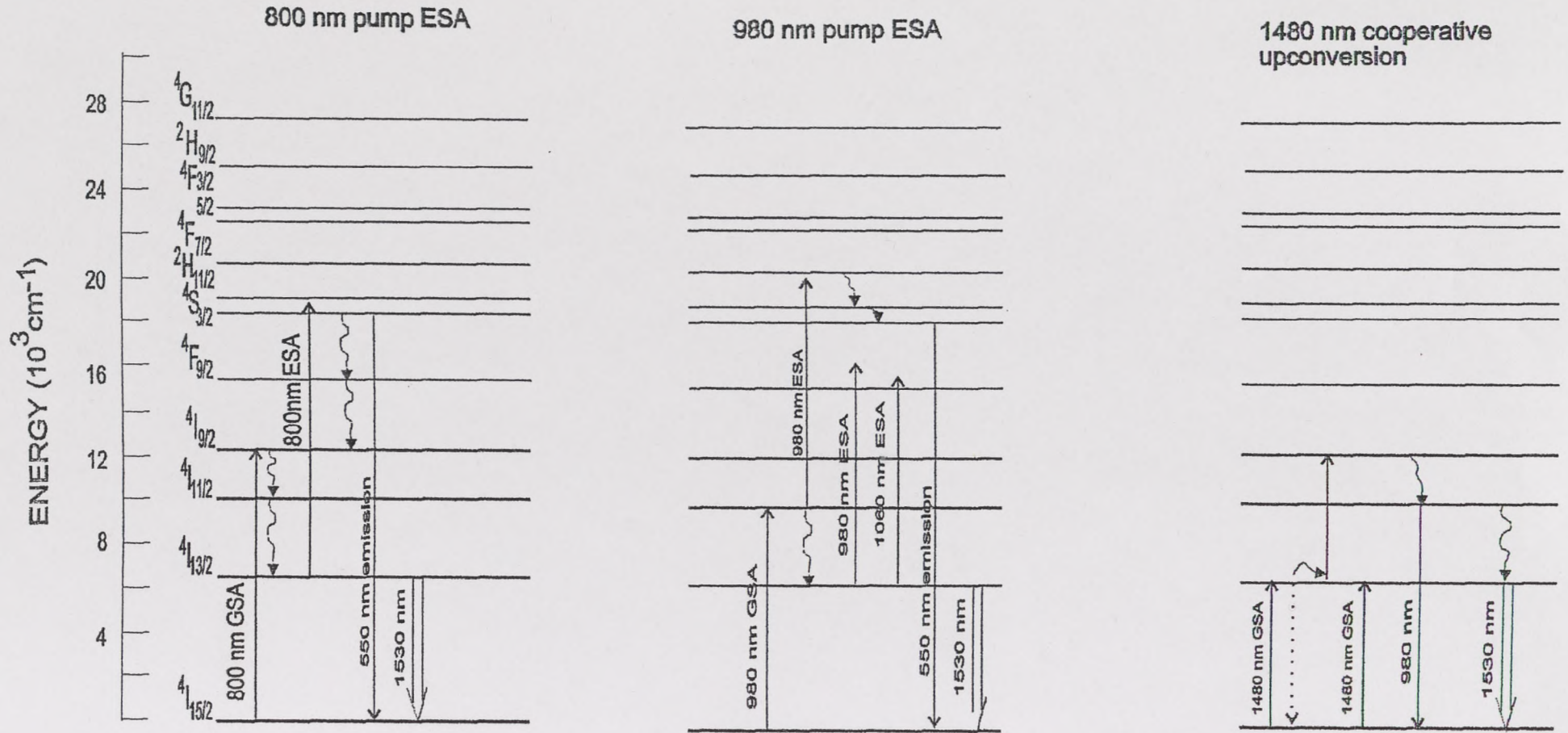


Figure 3.5 Several gain degradation processes associated with pumping schemes

- 980 nm pump band

The ${}^4I_{15/2} \rightarrow {}^4I_{11/2}$ transition of Er^{3+} corresponds to an absorption band peaking near 980 nm, which has proved to be very valuable for exciting fibre devices at 1.5 μm . This success is due to the large absorption cross section for this band. Pumping the 980 nm band, the excited state ${}^4I_{11/2}$ can have radiative 2700 nm emission or non-radiative relaxation to ${}^4I_{13/2}$ level depending on the host glass. At pump level ${}^4I_{11/2}$, there is 980 nm pump ESA (${}^4I_{11/2} \rightarrow {}^4F_{7/2}$), it results in strong 550 nm emission from ${}^4S_{3/2}$ state. The advantage of 980 nm pump band is that it overcomes the ${}^4I_{13/2}$ level ESA which is a serious problem for 800 nm band. It needs small pump power that it is within the reach of semiconductor pump diodes. Therefore, the pumping at 980 nm band has shown to be both practical and very attractive. It produces small signal noise and high gain efficient at 1.5 μm EDFA.

- 1480 nm pump band

From figure 3.2, there is a strong absorption peak near 1480 nm due to the ${}^4I_{15/2} \rightarrow {}^4I_{13/2}$ transition. Snitzer et al. first demonstrated that 1500 nm Er^{3+} amplifiers and lasers can be excited directly into the ${}^4I_{13/2}$ metastable state by pumping near 1480 nm [18]. ESA is not a problem for this band because ${}^4I_{13/2} \rightarrow {}^4I_{9/2}$ transition lies near 1670 nm, too long a wavelength to effectively pump the level. But there is co-operative up-conversion from the excited ${}^4I_{13/2}$ level which will decrease the quantum efficiency. It can also create 980 nm emission from ${}^4I_{11/2}$ state. Excellent results have been obtained by pumping silica and fluorozirconate 1500 nm lasers and amplifiers in the 1470-1490 nm range. This procedure, combined with the commercial availability of high power diode lasers for this band, has led to extensive use of resonantly pumped amplifiers in systems demonstrations and field trials optical communication applications. The disadvantage of this pump is that there is no gain below 1530 nm.

In general, the available evidence indicates that the 980 and 1480 nm pump bands are the best for pumping 1.5 μm devices in oxide glasses, with the 800 nm band a distant third. Because of its inefficiency, the 800 nm pump needs much higher minimum required pump power than 980 and 1480 nm pump bands. It is commonly recognised that a 1480- nm pumping scheme is more suitable for high-power

operation and 980-nm pumping scheme is more suitable for low noise operation. At the same time, the reliability and availability have to be taken into account.

References:

1. Kaminskii, A. A., *Laser Crystals*, Vol.14 in Springer Series in Optical Sciences (D. L. MacAdam ed), Springer-Verlag, Berlin, 1990.
2. Judd, B. R., *Phys. Rev.* **127**, 750 (1962).
3. Ofelt, G. S., *J. Chem. Phys.* **37**, 511 (1962).
4. Carnall, W. T., G. Crosswhite, and H. M. Crosswhite, *Energy Level Structure and Transition Probabilities of the Trivalent Lanthanides in LaF₃*, Argonne, IL: Argonne National Laboratory.
5. D'Arturo, B., *Optical Interactions in Solids*, New York, Wiley, 1968.
6. Zemon, S. G., G. Lambert, W. J. Miniscalco, L. J. Andrews, and B. T. Hall, *Proc. SPIE*. Vol 1171, 219-236 (1989).
7. McCumber, D. E. *Phys. Rev.* **134**, 299 (1964).
8. Kiel, A., *Third International Conference on Quantum Electronics*, Vol 1, Columbia University Press, New York, 765-772 (1963).
9. Riseberg, L. A., and H. W. Moos, *Phys. Rev.* **174**, 429 (1968).
10. Layne, V. B., W. H. Lowdermilk, and M. J. Weber, *Phys. Rev. B* **16**, 10 (1977).
11. Reisfeld, R., and C. K. Jorgensen, *Excited State Phenomena in Vitreous Materials*, Elsevier, Amsterdam, pp 1-90, 1987.
12. Gapontsev, V. P., S. M. Matisin, A. A. Isineev, and V. B. Kravchenko, *Opt. Laser Technol.* **14**, 189 (1982).
13. Alekseev, N. E., V. P. Gapontsev, M. E. Zhabotinskii, V. B. Kravchenko, and Y. P. Rudnitskii, *Laser Phosphate Glasses*, Nauka Publishing House, Moscow, 1983.
14. Pedersen, B., S. Zemon, and W. J. Miniscalco, *Electron Lett.* **27**, 1295 (1991).
15. Quimby, R. S., W. J. Miniscalco, and B. Thompson, *Fibre Laser Sources and Amplifiers*, vol 1581, SPIE 1991, pp72-79.
16. Quimby, R. S., *Appl. Opt.* **30**, 2546 (1991).
17. Masud, H., and A. Takada, *Electron. Lett.* **26**, 661 (1990).
18. Snitzer, E., H. Po, F. Hakimi, R. Tumminelli, and B. C. McCollum, *Proc. OFC/OFS'88*, PP2, New Orleans, Optical Society of American.

Chapter 4

Experimental Procedure

4.1 Preparation of bulk glass

Three kinds of glass were prepared. For making heavy metal oxide (HMO) germanate glass, high-purity commercial oxides and carbonates such as GeO_2 , PbO , Bi_2O_3 , Ga_2O_3 , TeO_2 , Na_2CO_3 respectively, and rare-earth oxide Er_2O_3 as a dopant were used. For making oxyfluoride silicate glass, commercial chemicals SiO_2 , GeO_2 , NaPO_3 , B_2O_3 , Al_2O_3 , Na_2CO_3 , NaF , AlF_3 , LaF_3 , PbF_2 and ErF_3 were used. For making tellurium oxide glasses, oxides (TeO_2 , ZnO , Ga_2O_3 , GeO_2 , Nb_2O_5 , WO_3), carbonates (Na_2CO_3 , K_2CO_3 , Li_2CO_3 , BaCO_3), fluorides (NaF , BaF_2), and Chlorides (NaCl , BaCl_2) were used. Rare earth oxides (Er_2O_3 , Tm_2O_3 and Nd_2O_3) were added as dopants. All of these chemicals were supplied by Aldrich. The purity of each chemical was 99.99% or above. These chemicals were stored in a sealed glove box under dry nitrogen. Powders of these materials, weighed to conform to the molar percentages as indicated in the text, were mixed homogeneously and then transferred to a melting crucible. The melting process of these three kinds of glasses is shown in table 4.1. Melts were cast into preheated brass moulds and put into an annealing furnace to cool to room temperature naturally. Samples were cut from these glasses, and the surfaces were polished to a 0.3~1 μm finish for different optical and spectroscopic characterization

Table 4.1 Preparing process of glasses

Glass	Melting T (°C)	Melting time (hr)	Annealing T (°C)	Crucible
HMO germanate glass	1100 ~1200	1 ~ 2	380 ~ 400	Platinum
Oxyfluoride glass	1350~ 1500	1 ~ 2	460 ~ 500	Platinum
Tellurite glass	750 ~900	1 ~ 2	240 ~ 280	Gold

4.2 Density measurement

The density is defined as the ratio of mass of the material to its volume. The bulk glass density was measured using a Doultton Densometer. This method is based on the Archimede's principle. When an object is immersed in a fluid, the buoyancy is equal to the weight of fluid displaced by the object. In this measurement, mercury is used as the buoyant fluid. The bulk glass sample density (ρ_g) can be calculated from the following equation:

$$\rho_g = (W_1/W_2) \times \rho_{Hg} \quad 4.1$$

where W_1 is the weight of the sample, W_2 is the buoyancy, ρ_{Hg} is the density of mercury. The accuracy of weighing is 0.01g. For different room temperature, an appropriate value of density ρ_{Hg} can be selected from a table of mercury density as a function of temperature.

4.3 Thermal characterisation

Thermal analysis was employed to determine the effect of glass composition on glass stability. Differential scanning calorimetry (DSC) is a very effective tool for glass thermal property study. Figure 4.1 shows the principle of DSC. Sample and reference are put into different holders with separated heater and thermocouple. The sample is kept at the same temperature with the reference by controlling the heat flow. At a constant power supply, the variation of input current is proportional to the input power. Therefore, if sample has energy absorbed or radiated at some temperature, the energy can be compensated by adding or subtracting an equivalent amount of electrical energy to a heater located in the sample holder to sustain the same temperature between the sample and reference. At a certain heating rate, the heat flow can be plotted against time or temperature. Platinum resistance heaters and thermometer are used in the DSC7 to accomplish the temperature and energy measurements in this design.

In a Perkin-Elmer DSC7, samples weighing 10-20 mg were sealed in aluminium pans and usually heated at a rate of 10 °C/min in the range of 200-550°C. The data

and graph were recorded by computer. Glass transition temperature T_g and crystallisation temperature T_x can be calculated from the recorded data, as can be seen in subsequent chapter. Using isothermal and non-isothermal methods, crystallisation kinetics of tellurite glasses was studied.

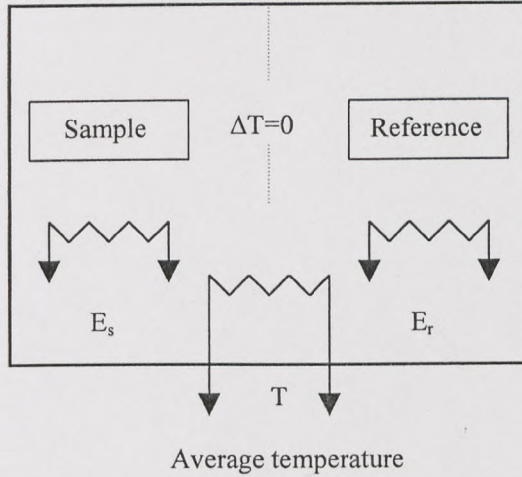


Figure 4.1 Principle of DSC

Analysis of crystallization kinetics of telluride glasses is based on the Johnson-Mehl-Avrami theory which describes the growth of crystals in a glass at a constant temperature:

$$-\ln(1-x) = (kt)^n \quad 4.2$$

where x is the volume fraction of crystals after time t , k is the rate constant, and n is a dimensionless exponent related to the morphology of crystal growth. Taking the logarithm of Equation 4.2 produces a linear relationship:

$$\ln[-\ln(1-x)] = n \ln k + n \ln t \quad 4.3$$

Using Equation 4.3, the constants n and k can be determined from an isothermal DSC scan by a linear fit. The rate constant k is temperature dependent, as described by the Arrhenius equation:

$$k = \nu \exp(-E/RT) \quad 4.4$$

$$\text{or } \ln k = \ln \nu - E/RT$$

where ν is a frequency constant, E is the activation energy for crystallization, R is the gas constant, and T is the absolute temperature. By performing isothermal scans at different temperatures, the activation energy E and the constant ν can be determined from a linear fit to Equation 4.4. Alternatively, it may be assumed that at the exotherm maximum t_m the volume fraction crystallized x_m is independent of the temperature, and that $x_m = 0.5$. Then, from Equations 4.3 and 4.4:

$$\ln t_m = -0.367/n - \ln \nu + E/RT \quad 4.5$$

which also yields E and ν through a linear fit. Once ν , E and n are known, time-temperature-transformation (TTT) curves can be calculated from Equations 4.2 and 4.3 for different values of x , and are usually plotted as T versus $\ln(t)$.

In non-isothermal DTA scans the temperature, and therefore k , changes continuously at a constant rate. As a consequence, Equations 4.4 can no longer be solved analytically, and approximate solutions are used to obtain parameters. The peak of crystallization exotherm T_p shifts to higher temperatures with increased scan rate α in accordance with the relation:

$$\ln(T_p^2/\alpha) = \ln(E/R) - \ln \nu + (E/RT_p) \quad 4.6$$

By scanning at different rates, E and ν can be determined from Equation 4.6. The exponent n is then approximated by the slope of the relationship valid for $x < 0.2$:

$$\ln(Y) = -(nE/R)(1/T) + C \quad 4.7$$

where Y is the height of the exotherm and C is a constant

Although parameters obtained from isothermal data are more accurate than from non-isothermal scans, the two methods should yield similar parameter values. However, in some glasses, the kinetics of crystal growth may be affected by

continuously increasing temperature, causing non-isothermal results to differ significantly from isothermal ones.

4.4 UV-VIS and FTIR absorption measurement

When the light waves propagate in a dielectric medium, the photon energy is absorbed both intrinsic and extrinsic. The intrinsic absorption is caused by UV absorption, IR absorption and Rayleigh scattering. The UV absorption takes place at short wavelengths and is due to the electronic band gap of the materials. The IR absorption is due to the lattice vibration of ions. Rayleigh scattering is caused by inhomogeneity of materials such as the density and compositional fluctuations. Extrinsic absorption is due to impurities present in the medium such as transition metal ions, rare earth ions and OH^- , SO_4^{2-} , NO_3^- , CO_3^{2-} etc. The photon energy in an isotropic medium can also be dissipated due to the presence of extrinsic scattering centres e.g. crystals, inclusions and gas bubbles. In designing glasses, the extrinsic absorption and scattering can be minimised, and in some cases eliminated to reach the theoretical limit. This is clearly demonstrated by the example of the development of ultralow loss silica fibre for telecommunication network.

If I_0 is the intensity of a parallel beam of radiation incident normally on a glass, and I is the intensity of the transmitted beam, the absorption (α) follows Lambert-Beer law,

$$I = I_0 \exp(-\epsilon ct) \quad 4.8$$

where ϵ is called the molar extinction coefficient given in terms of molar concentration unit, c is the concentration of absorbing ions and t is the thickness. $\alpha = (\epsilon c)$ is the absorption coefficient.

The transmission T is defined as:

$$T = 100I/I_0 \quad 4.9$$

The absorbance A is defined as:

$$A = \log_{10}(I_0/I)$$

4.10

Perkin-Elmer FT-IR Spectrometer 1725x was used to measure the IR absorption spectra of glass. The scanned range was from 4000 to 400 cm^{-1} .

Perkin-Elmer UV/VIS/NIR Lambda-19 was used to measure the absorption spectra from UV range to near IR range (300 ~ 3200 nm). The scan speed was 30 ~ 120 nm/min.

For all absorption measurement, air as a reference medium must be run as a background. The ambient temperature is room temperature.

4.5 Fluorescence and lifetime

Fluorescence is light emission due to electronic transitions. When an incident photon interacts with material, it can be completely absorbed and the molecule concerned is thereby raised to excited electronic level. The electrons or molecules dwell in the excited state before being de-excited. After a certain lifetime in this upper state, the molecule undergoes a downward transition and thereby radiates light of a frequency lower than the excitation wavelength. Fluorescence spectroscopy is a powerful tool for investigating the glass local structure, the spectroscopic properties of ions in glass, ion site-to-site variation, electron-phonon coupling, ion-ion interactions and the effects of these interactions on energy levels and relaxation processes.

The main excitation source used for fluorescence and lifetime measurements was a Schwarz Electro-optic Ti-sapphire CWBB laser pumped by two Coherent 200-5w argon ion lasers. The equipment setup is shown in figure 4.2. The pump laser wavelength is 980 nm for the measurement of the fluorescence spectra and lifetimes of the $^4I_{13/2} \rightarrow ^4I_{15/2}$ transition at 1500 nm in Er^{3+} doped glasses and 800 nm for the fluorescence properties of Tm^{3+} and Nd^{3+} doped glasses. For fluorescence spectrum measurement, the sample was positioned in the pump beam to obtain a long path length. An InGaAs detector collected fluorescence signals through a scanning spectrometer designed by Macam Photometrics, the computer read and recorded the signal at each wavelength. The fluorescence spectra were obtained by plotting

wavelengths and intensities. The lifetime measurements were made with a chopper between the pump light and the sample. The fluorescence signals were detected by fast response InGaAs detector. The signal decay curve can be checked by an oscilloscope and handled by a digital storage adapter. After that, the intensity decay was recorded by a computer. The lifetime of the metastable level can be determined by fitting the exponential function to the measured fluorescence intensity decay data.

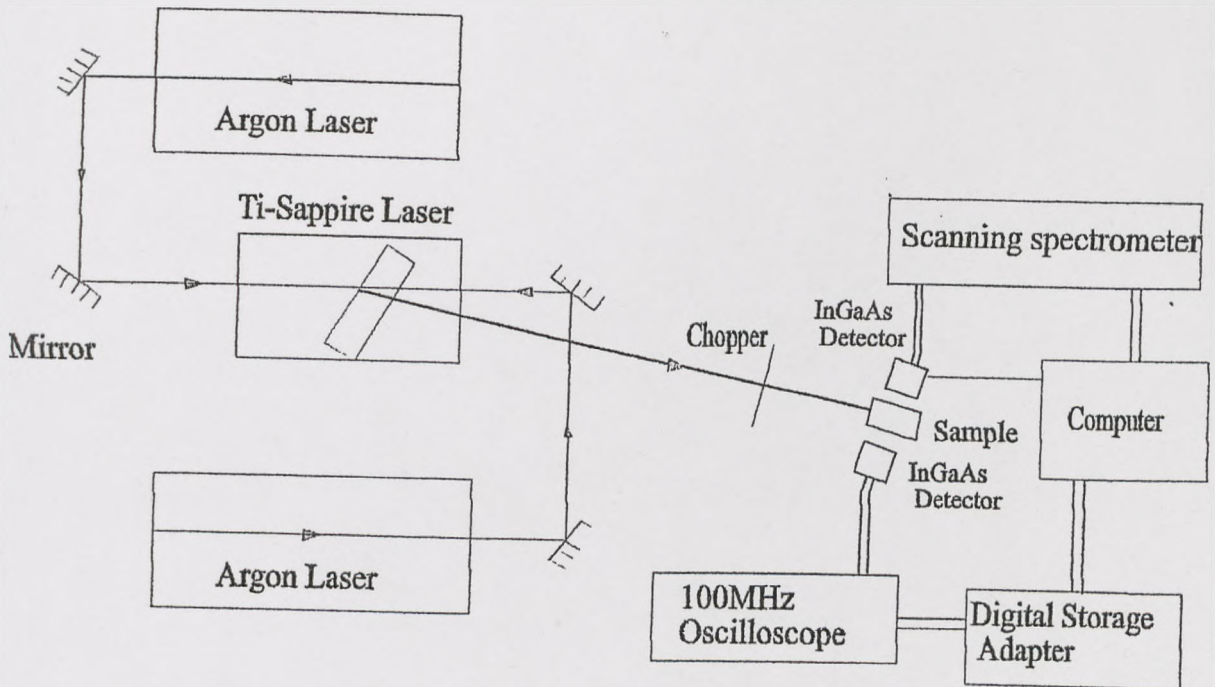


Figure 4.2 Set-up of measuring Rare-earth fluorescent properties

4.6 Raman spectrum

Consider a clear substance (solid, liquid, or gas) irradiated by monochromatic light ν_0 (usually in visible region) whose frequency is chosen so that it does not correspond to any absorption line/band in the sample. Almost all of the light energy will pass through the sample unaffected, but a very small part of it will be scattered by molecules in directions different from that of the incident beam. When the scattered light is analysed spectroscopically, it is found that a high proportion of the

scattered energy has the same frequency ν_0 as the primary light. This is called Rayleigh scattering, it was first discovered by Rayleigh in 1871. Rayleigh scattering can be explained as the elastic collision of light with molecules. The scattering intensity is proportional to the fourth power of ν_0 . A very small part of the scattered light also has a proportion of energy which is at a different frequency to the primary light ν_0 . This effect was observed experimentally by Raman in 1928. The spectrum of the scattered light, which shows a pattern of lines of shifted frequency, is called the Raman spectrum. The shifts (Raman frequencies) are independent of the exciting frequency ν_0 and characteristic of the species giving rise to the scattering.

Raman effect can simply be understood by inelastic collision of phonon with molecule in sample. The energy transfer between phonon and molecule results in the frequency change of incident light. If the frequency of incident light is ν_0 , the energy of phonon is $h\nu_0$. After the collision, if it is inelastic, there may have two situations. The first is when molecule is in the low energy level, it may cause the molecule to undergo a quantum transition to a higher energy level, it absorb energy $h\nu_1$ with the result that the photon loses energy and is scattered with lower frequency ($\nu_0 - \nu_1$). The other situation is if the molecule is already in an energy level above its lowest energy level, an encounter with the phonon may cause it to undergo a transition to a lower energy, in which case the photon will gain energy $h\nu_1$ and it is scattered with increased frequency ($\nu_0 + \nu_1$). No matter which kind of situation, the frequency of scattered photon has been changed. It increases or decreases by ν_1 . ν_1 is called the Raman shift. Raman shift lines with negative ($\nu_0 - \nu_1$) are called "Stokes lines", lines with positive ($\nu_0 + \nu_1$) are called "anti-Stokes lines". The probability of the positive and negative shifts are the same, but the population of a higher level is less than that of a lower level, we can understand why the intensity of Stokes lines are stronger than anti-Stokes lines. Therefore, Stokes lines are the main lines measured in Raman spectrum application.

Inelastically scattered photons are produced by the interaction of the electromagnetic field of the incident photons with the electronic polarisability. As a function of frequency shift, the Raman spectrum displays peaks due to discrete vibrational modes, or features due to continuous modes, depending on selection rules

and coupling strengths for Raman processes in particular geometry. The set of Raman frequencies of the scattering species constitutes its Raman spectrum. Study of glass structure using Raman scattering spectrum began in the 1950s. Since its development in 1960s, laser Raman spectroscopy has been used as a major tool for studying glass structure.

For analysing the vibrational structure of tellurite glass, Raman spectrometer was used. The principle set-up for Laser Raman spectrometer is shown in figure 4.3. The Raman spectra were measured at room temperature with a SPEX 1403 model double monochromator at 2 cm^{-1} resolution, using an argon-ion laser (Spectra-Physics 2016) for excitation, at 488.0 nm or 514.5 nm, with a power of 100-500 mW at the source, and a photomultiplier detector (Hamamatsu) with photon-counting electronics. The scanned range is $10 \sim 1000\text{ cm}^{-1}$. Polarized Raman scattering measurements were performed in the 90° scattering geometry from a large face of the samples in the polarized (HH) and depolarized (HV) configurations. The monochromator was scanned at 1 cm^{-1} increments, with a counting period of 5 s. The error in frequency values is estimated at $\pm 1\text{ cm}^{-1}$, from repeated scans.

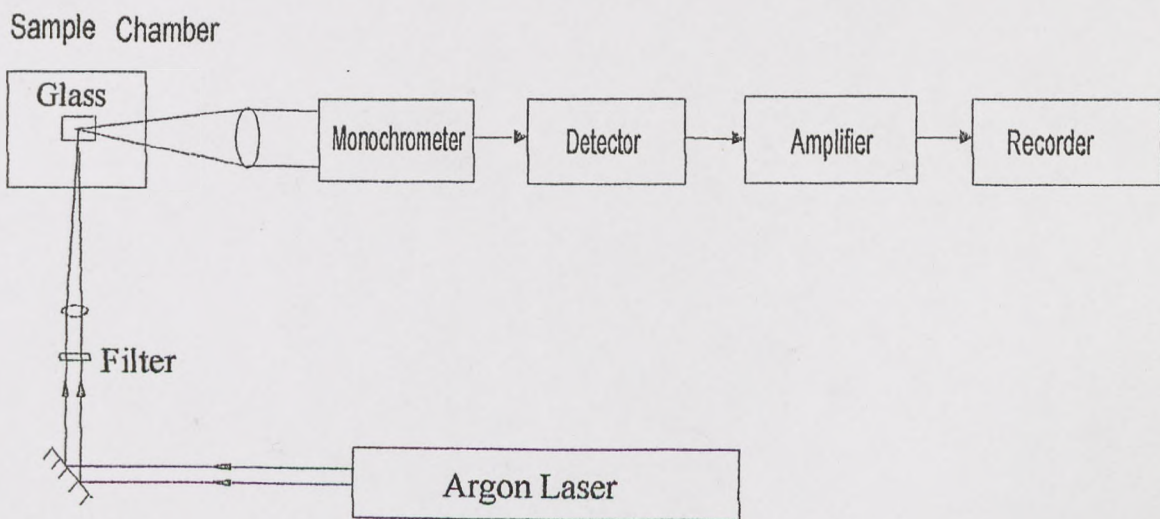


Figure 4.3 Setup of Raman spectrometer

Chapter 5

Er³⁺-doped heavy metal oxide germanate glasses

In order to obtain broadband and flat gain Er³⁺ doped amplifier, host glass is the critical factor. In oxide glass host, heavy metal germanate, modified silicate and tellurite glasses were selected. In the following chapters we compare the properties of the glass and rare-earth dopant ions. In this chapter, the optical and thermal properties of heavy metal oxide (HMO) germanate glass were measured, and the emission and absorption spectra of Er³⁺ dopant were measured. The potential for using germanate glasses as Er³⁺-doped fibre amplifier is also discussed.

5.1 Glass compositions

GeO₂ has a similar glass-forming properties as SiO₂. In the silica glass structure, distorted SiO₄ tetrahedra join each other at corners. GeO₂ glass has a tetrahedral quartzlike structure. As the Ge/O radius ratio is 0.414, it is on the border between tetrahedral and octahedral structures. Neutron diffraction studies show that the primary Ge-O bond is 1.73 Å, it is about 8% larger than the Si-O bond, the average Ge-O-Ge bond angle is 133° (compared to about 144° for the Si-O-Si bond angle in silica glass). With the addition of modifier alkali, the coordination number of Ge changes from 4 to 6. The conversion continues to occur up to 35% [GeO₆] at around 30% added alkali [1].

The main reason for selecting GeO₂ glasses was to achieve a larger emission cross-section and broadband emission bandwidths. The large emission cross-section is achievable because of the higher refractive index compared to silica. With increasing refractive index the emission and absorption cross-sections also increase. Another important reason for investigating heavy-metal oxide (HMO) glasses is to extend the absorption edge of oxide glasses as far as possible into the infrared to expand the IR communication range. The principle of forming glass with infrared transmission at longer wavelengths is based on the use of compounds whose cation-oxygen bonds are relatively weak, giving low fundamental vibration frequencies. The influence of a given cation-oxygen bond on the absorption edge can be estimated from equation 5.1.

$$\omega = \frac{1}{2\pi} \sqrt{f / \mu} \quad 5.1$$

where ω is the vibrational frequency, f is a force constant for the elastic restoring force, and μ is the reduced mass of the vibrating ions, $(m_c+m_o)/m_c m_o$. Since a table of force constants for cation-oxygen bonds is not readily available, field strength has been used as an indication of relative magnitude of the force of attraction. Field strength is the charge on the cation divided by the square of the interionic distance. Bismuth and lead oxides with their low field strengths and large masses should produce glasses with the longest infrared cut-off. Ga_2O_3 can impart resistance to devitrification in PbO - and Bi_2O_3 -based glass system [2]. Therefore, GE1 is the typical GeO_2 - Na_2O binary glass. GE2 and GE3 were designed as lead germanate and heavy metal germanate glass. Based on HMO germanate glass, tellurite was added to this glass in order to study the effect of the mixture GeO_2 and TeO_2 on the structure of glass and on the spectroscopy of Er^{3+} . In GE4 and GE5 glasses, between 10 and 20 mol% of GeO_2 and Ga_2O_3 were replaced by TeO_2 , respectively. Table 5.1 shows the compositions of germanate glasses. The preparation processes of these glasses have been explained in chapter 4. The glasses were melted in platinum crucible at 1100 ~ 1200 °C for 2 hours, melts were cast into preheated brass moulds and put into an annealing furnace at 380 ~ 400 °C to cool to room temperature naturally. Samples were cut from these glasses, and the surfaces were polished to a 0.3 ~ 1 μm finish for different optical and spectroscopic characterization. There was no evidence for crystallization in these glasses.

Table 5.1 Compositions (mol%) of HMO germanate glasses

Sample	GeO_2	Na_2O	Ga_2O_3	PbO	Bi_2O_3	TeO_2	Er_2O_3
GE1	80	19	--	--	--	--	1
GE2	59	--	--	35	5	--	1
GE3	50	--	14	20	15	--	1
GE4	42	--	12	20	15	10	1
GE5	34	--	10	20	15	20	1

5.2 Absorption in the UV

The UV edge absorption, which limits transparency at shorter wavelengths, is caused by transitions between the electronic states of the glass. This absorption is a function of the energy gap of the materials and the incident photon energy. As the frequency of the incident photons is increased, the fraction absorbed will also increase. The short wavelength cut-off is known as the Urbach tail. The absorption coefficient α_{uv} at the tail can be expressed as:

$$\alpha_{uv} = \alpha_0 \exp(-A(E_g - E) / kT) \quad 5.2$$

where A and α_0 are material dependent parameters, E_g is the photon energy corresponding to the ultraviolet absorption edge, i.e. the optical bandgap, E is the energy of incident photons, k is the Boltzman constant and T is the absolute temperature. Temperature of glass will affect the UV edge absorption. At a constant temperature, Eq.5.2 can be simplified as following Eq.5.3:

$$\alpha_{uv} = \alpha_0 \exp(A/\lambda) \quad 5.3$$

where A and α_0 are also material dependent parameters, and λ is the photon wavelength. This equation can be used to fit the measured absorption spectrum to calculate A and α_0 parameters.

Absorption spectra of germanate glass samples were obtained using a Perkin-Elmer UV/VIS/NIR Lambda 19. These spectra are shown in figure 5.1. The data were further processed using the SIGMA PLOT software, and the derivative of absorption against wavelength $dA/d\lambda$ was calculated. The maximum point of the derivative curve in the UV edge range is designated as the UV edge cut-off wavelength of the glass. As these samples were doped with Er^{3+} , the Er^{3+} absorption peak at 407 nm can be observed in all the samples, while peaks at 365 and 378 nm can only be seen in GE1 because the UV cut-off wavelength was shifted to much lower range.

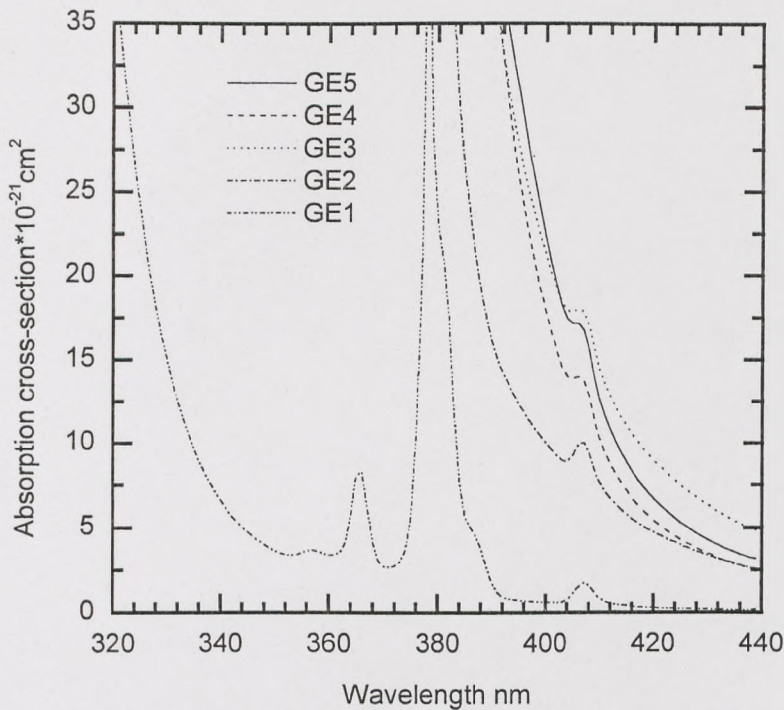


Fig. 5.1 UV absorption edge in HMO germanate glasses

Table 5.2 UV edge cut-off in germanate glass

	GE1	GE2	GE3	GE4	GE5
UV edge ± 2 nm	324	385	395	396	398

In these germanate glasses, with the decrease of GeO_2 content in the glass, the UV cut-off wavelength increases, the edge shifts to longer wavelength. From Eq.5.2, if the energy gap E_g of glass is higher, α_{uv} will be smaller, it means E (incident photon energy) must be higher to increase α_{uv} , therefore, the glass can transmit shorter wavelength, the UV edge will shift to shorter wavelength. Thus, in these germanate glasses with the decrease of GeO_2 content and increase of heavy metal oxides, the UV cut-off wavelength increases, the energy band gap of this glass decreases.

The ultraviolet cut-off wavelength of inorganic glasses mainly depends on the atomic number of anions and cations. The main influence on the UV absorption wavelength is of non-bridging oxygen ions. The electronic shell of oxygen ions is affected by the polarizing action of modifying ions, which decreases with increasing ionic radius, thus resulting in progressive loosening of the electronic shell of non-bridging oxygen and consequently leads to increased absorption wavelength. For cations like Pb^{2+} and Bi^{3+} , which have loose electronic structure with $6s^2$ electrons in

the outer shell, will lower the energy gap in glass between conduction and valence band. Glasses containing these cations have longer cut-off wavelength value. With the decrease of GeO_2 content and the increase of heavy metal oxide, the non-bridging oxygen in HMO germanate glass increases and the field strength (Z/a^2) decreases, the energy gap drops, therefore, the UV cut-off wavelength shifts to longer wavelength.

5.3 Absorption in the IR

In glass IR absorption is due to lattice vibrations. It is a dominant factor in determining the intrinsic minimum losses. In general, the IR spectrum can be divided into the fundamental and multiphonon regions. The fundamental resonances provide intense absorption and can be used to understand the glass structure. The frequency of the fundamental has been determined empirically to obey the Szigeti equation which is shown in Eq.5.1. From this equation, we can conclude that heavier ions and weaker bonding are preferable for extended IR transmission.

The position of the multiphonon edge is related to the fundamental absorption. At shorter wavelengths the multiphonon edge tails back into the visible region and determines the minimum losses. The absorption coefficient of the tail, α_{IR} , follows the expression

$$\alpha_{\text{IR}} = A \exp(-\gamma\omega/\omega_0) \quad 5.3$$

where A and γ are constants characteristic of the materials and ω_0 is the fundamental optical phonon frequency, the vibrational frequency ω_0 is expressed in Eq.5.1, and ω is the frequency of the incident photon.

Each material has a number of characteristic lattice vibration frequencies, related to particular structural units. Depending upon the vibrational mode i.e. stretching or bending, the frequency will be different. The IR absorption or the multiphonon edge is the sum of all the frequencies, i.e. fundamental vibration, 1st and other smaller harmonics.

For most oxide glasses the multiphonon edge (IR cut-off) lies in the range of 2200-1500 cm^{-1} (4500-6500 nm). Clearly the edge will be determined by the glass

composition. To increase the IR cut-off (longer wavelength), heavier ions and weaker bonds are required.

The IR absorption spectra of these HMO germanate glasses were obtained using a Perkin-Elmer FTIR Spectrophotometer 1725x. Figure 5.2 shows the edge absorption spectra. The data were further processed using the SIGMA PLOT software, and the derivative of absorption against frequency $dA/d\nu$ is calculated. The maximum point at this curve is designated as the IR cut-off wavenumber of the glass. The multiphonon cut-off edges are shown in table 5.3.

Table 5.3 IR edge cut-off in germanate glass

	GE1	GE2	GE3	GE4	GE5
IR edge $\pm 10\text{cm}^{-1}$	1740	1685	1650	1595	1585

From figure 5.2, it shows the IR cut-off shifts to lower frequency as GeO_2 was replaced by heavy metal oxides such as PbO , Bi_2O_3 and TeO_2 . In Ge1 glasses, the IR edge is at 1740 cm^{-1} , when heavy metals were incorporated in germanate glass in place of GeO_2 and Na_2O , the IR edge shifted to 1740 to $1685\text{-}1650\text{ cm}^{-1}$. When the GeO_2 was replaced by a weaker bond oxide TeO_2 , the IR edge shifted further to lower frequency $1595\text{-}1580\text{ cm}^{-1}$.

In binary lead germanate glass system [3], PbO can be up to 57 mol% to form glass. There is an equilibrium between $\text{Pb}^{2+} \leftrightarrow \text{Pb}^{4+}$ to form $[\text{PbO}_2]$ and $[\text{PbO}_4]$ respectively. $[\text{PbO}_4]$ tetrahedron is a pure network while $[\text{PbO}_2]$ exists as a dispersed molecule in glass. Pure Bi_2O_3 glass cannot be obtained, in line with the low field strength of Bi^{3+} . However, very small additions (e.g. 1% SiO_2 or B_2O_3 , but also of some CdO , BaO , ZnO , PbO) promote reasonably good glass formation [3]. In $\text{Bi}_2\text{O}_3\text{-CdO-GeO}_2$ glass system, Rao et al. [4] deduced that Bi^{3+} ions form clusters consisting of BiO_6 group, acting as a network former. From the IR spectra of $\text{Bi}_2\text{O}_3\text{-B}_2\text{O}_3$ glasses, BiO_3 trigonal pyramids are also structural units [5-8]. Bi^{3+} ions act as a network modifier at low Bi_2O_3 content and network former at high Bi_2O_3 content in $\text{Bi}_2\text{O}_3\text{-B}_2\text{O}_3$ glasses. From X-ray radial distribution analysis, IR and Raman spectroscopy indicated Ga^{3+} ions are tetrahedrally coordinated in binary alkali and alkaline earth gallate glasses [9, 10]. In $\text{PbO-Bi}_2\text{O}_3\text{-Ga}_2\text{O}_3$ glass system, the fraction

of non-bridging oxygen in GaO_4 tetrahedra decreases with increasing PbO and Bi_2O_3 contents [11]. Most of Pb^{2+} and Bi^{3+} ions act as a network-former, and Pb^{2+} and Bi^{3+} ions may be present as PbO_4 square pyramids and distorted BiO_6 octahedra, respectively.

In these HMO germanate glass, the oxides which become a part of the network forming unit in the structure, shift the multiphonon edge to longer wavelengths than those which simply modify the structure. PbO , Bi_2O_3 and Ga_2O_3 all form glass with GeO_2 and therefore may contribute to the IR edge shift. Heavy metal oxides in germanate glass increase the IR transmission range and decrease the multiphonon energy.

5.4 Molar volume and thermal properties of glass

In order to study the effect of the modifying oxide additions on the basic glass structure, density ρ and molar volume V_m were measured. These two properties are governed both by the atomic mass of the components and by the structure of glass network. The molar volume was calculated using the following equation:

$$V_m = \frac{1}{\rho} \sum_i x_i M_i \quad 5.4$$

where x_i is the molar fraction of component i , M_i is its molar mass, ρ is the density.

To investigate the glass stability, differential scanning calorimetry (DSC) was adopted. The glass transition temperature (T_g) is important information in the thermal analysis. In the transformation range, it corresponds to a viscosity of $10^{12} \sim 10^{13}$ Pa·s and is defined as the temperature region in which the behaviour of the material changes from solid-like to liquid-like.

Molar volume and T_g of all the samples are shown in table 5.4. Figure 5.3 illustrates how these properties change with GeO_2 concentration. From this figure, we can see that the molar volume increases sharply and then decreases gently with decreasing GeO_2 content. As we explained above, PbO , Bi_2O_3 , and Ga_2O_3 are intermediates in glass. With these heavy metal oxides (HMO) in place of GeO_2 , a part of HMO behaviour as network modifiers, the other part of them behaviour as a

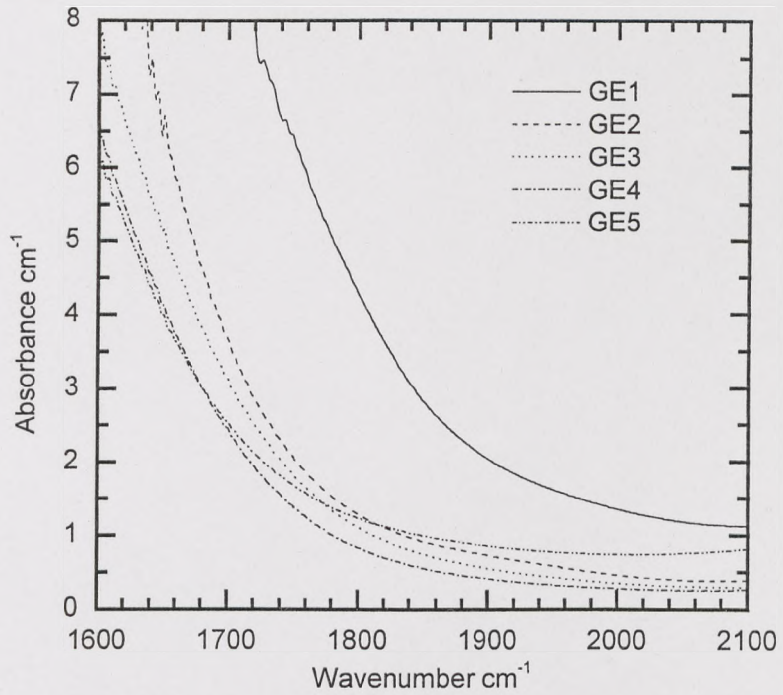


Fig. 5.2 IR absorption edge in HMO germanate glasses

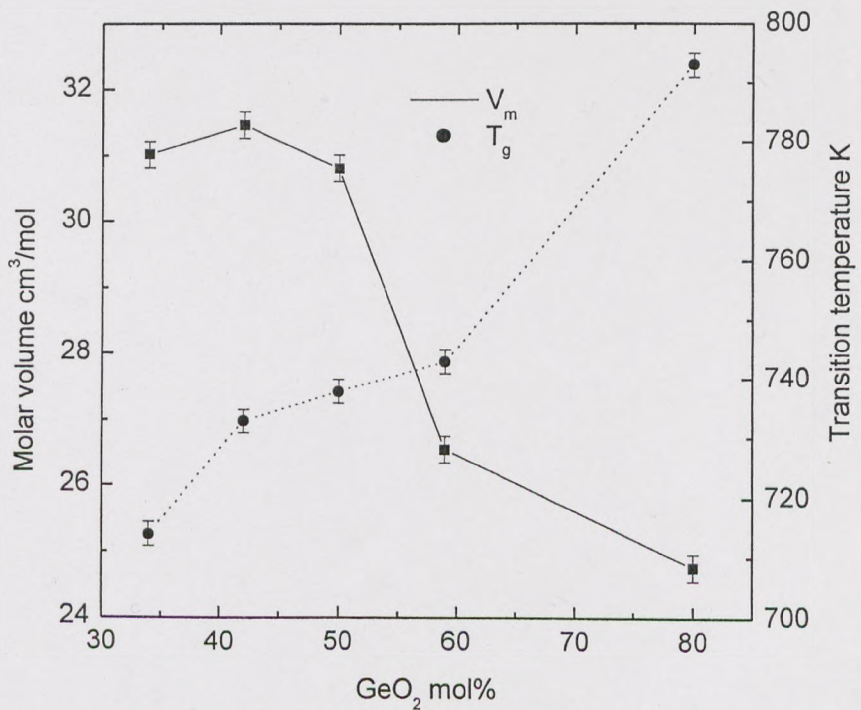


Fig. 5.3 Molar volume and T_g change with GeO_2 content

network former. They increase the non-bridging oxygen in the glass, thus the $[\text{GeO}_4]$ tetrahedral continuous network is broken. It results in the glass structure becoming looser.

Table 5.4 Molar volume and transition temperature in germanate glass

	GE1	GE2	GE3	GE4	GE5
$V_m \pm 0.2 \text{ cm}^3$	24.8	26.5	30.8	31.5	31.1
$T_g \pm 2 \text{ K}$	793	743	738	733	714

Normally, in $\text{Na}_2\text{O}-\text{GeO}_2$ binary system, when the modifier ions exceed 30 mol%, $[\text{GeO}_4]$ begins to form $[\text{GeO}_6]$, the network is broken more severely [1]. In HMO germanate glass, the ability of HMO is less than Na^+ ion because of the larger ion size, the small field strength (Z/a^2) comparing with Na^+ ion, the molar volume increases sharply when the modifier ions exceed 40 mol%. With TeO_2 in place of GeO_2 , the molar volume changes very little, because TeO_2 can exist as network former $[\text{TeO}_4]$ to connect the structure, it should decrease the V_m of the glass; on the other hand, the structure unit of $[\text{TeO}_4]$ is larger than $[\text{GeO}_4]$ because the distance of Te-O-Te is longer than Ge-O-Ge. Furthermore, TeO_2 can also exist as $[\text{TeO}_3]$ trigonal pyramid in the gap of network to enlarge the molar volume. By balancing these factors, the V_m changes slightly with 20 mol% TeO_2 in place of GeO_2 .

The variation of T_g in HMO germanate glass also reflects the glass structure change. The same reason results in the changing trend of T_g with the V_m . Higher T_g shows higher strength of glass. Because the bond strength of Te-O is lower than that of Ge-O, the T_g of glass decreases with TeO_2 in stead of GeO_2 even though the V_m decreases.

5.5 Absorption and emission spectra Er^{3+} ion doped HMO germanate glasses at 1.5 μm

For Er^{3+} doped glasses, the ${}^4\text{I}_{13/2} \rightarrow {}^4\text{I}_{15/2}$ transition is the most important because it can provide high gain and low noise at the important optical communications wavelength of 1.5 μm . For this 3-level gain system, not only the stimulated emission, but also the absorption cross-section play important roles in determining the performance of a device. In HMO germanate glass, the absorption cross-section,

emission spectra and lifetimes have been measured and discussed together with the figures of merit for gain.

Figure 5.4 shows the absorption cross-sections of Er^{3+} at the ${}^4\text{I}_{15/2} \rightarrow {}^4\text{I}_{13/2}$ transition in HMO germanate glasses. From figure 5.4, the absorption cross-section and the shoulder at $1.49 \mu\text{m}$ are changing remarkably. The absorption cross-section at $1.53 \mu\text{m}$ and the ratio of shoulder cross-section at $1.49 \mu\text{m}$ against the peak at $1.53 \mu\text{m}$ are shown in figure 5.5. The ratio reflects the absorption bandwidth. From figure 5.5, It illustrates the absorption cross-section and the ratio increase as the content of GeO_2 decreases when HMO are added into these glasses. Er^{3+} ion has significantly higher absorption cross-section and peak ratio in HMO germanate glass than in $\text{Na}_2\text{O-GeO}_2$ binary glass. Among HMO germanate glasses, these properties change very gently.

Figure 5.6 shows the normalised emission spectra of Er^{3+} ion at the ${}^4\text{I}_{13/2} \rightarrow {}^4\text{I}_{15/2}$ transition in HMO germanate glasses. From the normalised emission spectra, the spectrum shape has changed and peak wavelength also shifts to shorter wavelength when the content of GeO_2 decreases and HMO are added into these glasses. From some point, the emission spectra also become broader. The shoulder of emission spectrum also increases. The lifetime of this transition ${}^4\text{I}_{13/2} \rightarrow {}^4\text{I}_{15/2}$ in these glasses is shown in table 5.5. It increases as the content of GeO_2 decreases and HMO increase. When TeO_2 replaces GeO_2 , the lifetime starts to decrease.

Table 5.5 Lifetime of Er^{3+} ion at ${}^4\text{I}_{13/2}$ level in germanate glass

	GE1	GE2	GE3	GE4	GE5
$\tau \pm 0.2 \text{ ms}$	3.0	3.8	4.5	4.3	3.2

5.6 Discussion

In order to compare the difference of the shape of the emission spectrum in different hosts, FWHM (full-width at half maximum) is used as the indication of bandwidth. From the normalised emission spectra, the FWHM of these glasses have been calculated. The figure-of-merit (FOM) for gain is defined as the product of

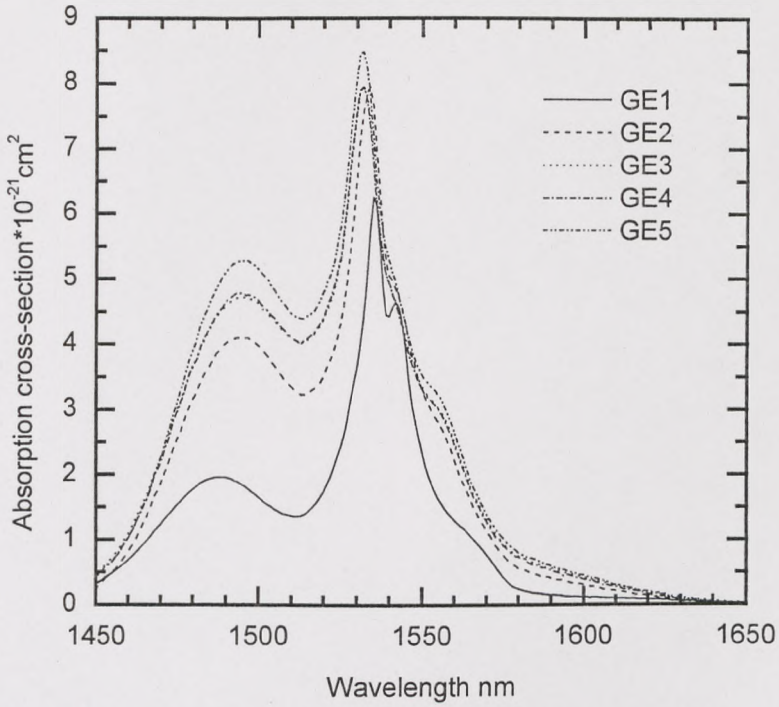


Fig. 5.4 Er^{3+} ion absorption cross-section spectra in HMO germanate glasses

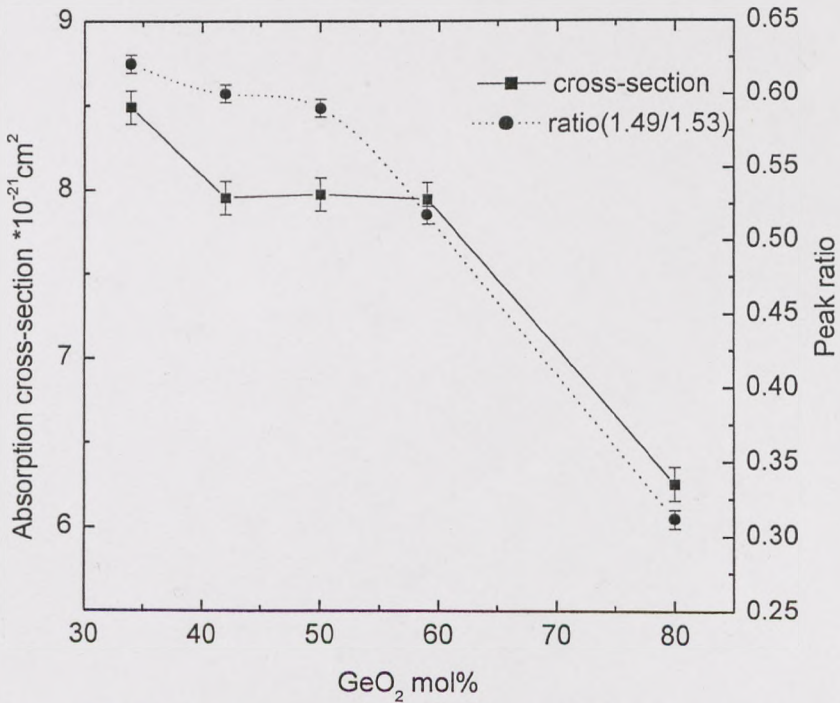


Fig. 5.5 Er^{3+} absorption cross-section at 1530 nm and the ratio of the shoulder at 1480 nm against peak

lifetime τ and emission cross-section σ_e . The emission cross-section σ_e can be calculated from the McCumber equation which was shown in chapter 3.

The calculated results of FWHM and FOM with various GeO_2 content are shown in figure 5.7. With the addition of HMO in germanate glass, FWHM increases from 28 nm to 51 nm. It reflects the emission spectra broadening. The FOM of gain has a peak around 40~50 mol% GeO_2 . When PbO and Bi_2O_3 replace GeO_2 in the glass structure, the lifetime τ and emission cross-section σ_e increase. However, when TeO_2 substitutes for GeO_2 , the values of σ_e increases and the lifetime τ decreases, thereby lowering the FOM.

From the results of V_m , T_g , UV and IR cut-off in HMO germanate glass, they show the glasses have lower T_g , higher V_m , longer IR cut-off wavelength and lower energy bandgap with the addition of HMO in germanate glass. These are caused by the structural changes in glass. The substitution of HMO in the GeO_2 glass network increases the non-bridging oxygen sites and the glass network comprises of different units e.g. $[\text{TeO}_4]$, $[\text{PbO}_4]$, $[\text{BiO}_6]$, and $[\text{GaO}_4]$. The bond strength of these structural units is weaker than $[\text{GeO}_4]$, which is apparent from the phonon energy values $h\omega$ (TeO_4) = 750 cm^{-1} , $h\omega$ (GaO_4) = 570 cm^{-1} , $h\omega$ (PbO_4 and BiO_6) = $400\sim 550 \text{ cm}^{-1}$ [11]. The energy bandgap decreases and multiphonon edge shifts to longer wavelength, which strongly suggests that the glass has weaker field strength of cations.

The ligand fields of cations, such as $[\text{TeO}_4]$, $[\text{PbO}_4]$, $[\text{BiO}_6]$, and $[\text{GaO}_4]$ etc, also affect the absorption and emission cross-sections of Er^{3+} ion. Normally, when glasses are formed with small amounts of Er^{3+} ions, these ions enter the glass structure mainly as network modifier ions. A glass has a large number of sites to accommodate ions, and these sites differ from each other in the arrangement of the neighbouring ions. Consequently, the energy levels of the Er^{3+} ions in these sites are not identical. Under broadband optical pumping, whereby Er^{3+} ions in all different sites are excited, the luminescence is inhomogeneously broadened, due to the convolution of all of emissions from the ions in the different sites. The variation in cationic field strength thus represents the site-to-site variation.

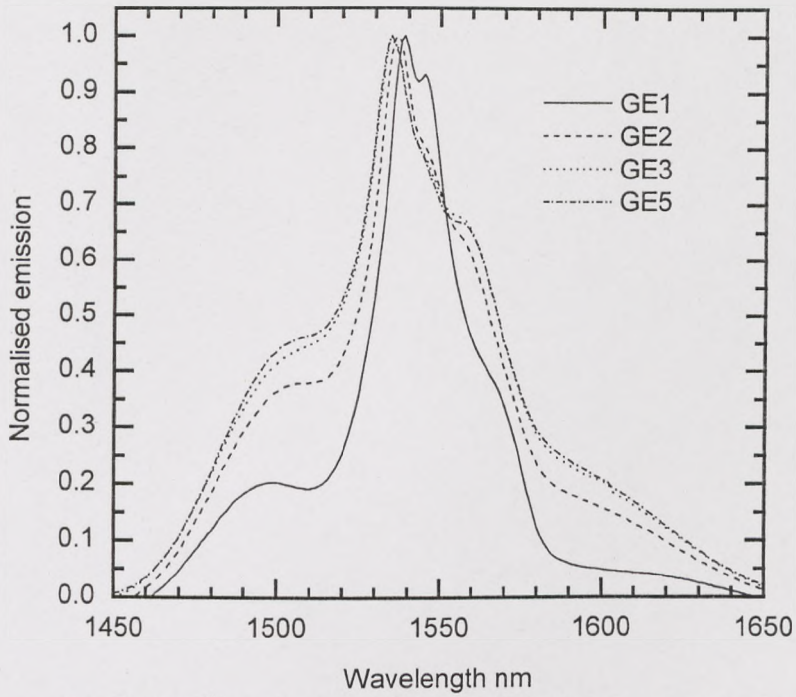


Fig. 5.6 Er^{3+} emission spectra in HMO germanate glasses

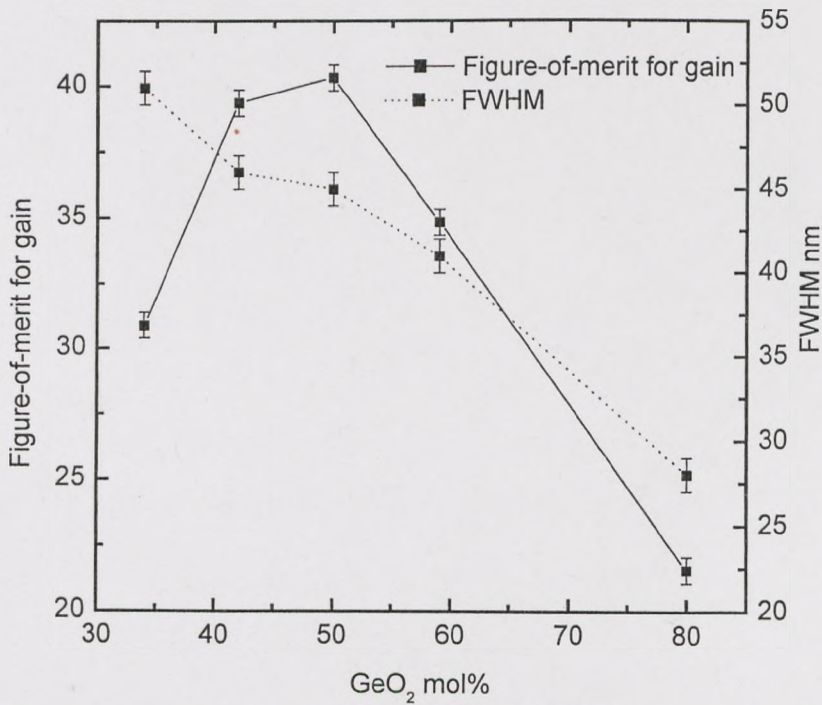


Fig. 5.7 Figure-of-merit for gain and FWHM in germanate glasses

In HMO germanate glasses, Er^{3+} ions exist as $[\text{ErO}_6]$. When HMO and TeO_2 replace GeO_2 , there are more different sites such as $[\text{GeO}_4]$, $[\text{GeO}_6]$, $[\text{TeO}_4]$, $[\text{TeO}_3]$, $[\text{PbO}_2]$, $[\text{PbO}_4]$, $[\text{BiO}_3]$, $[\text{BiO}_6]$, and $[\text{GaO}_4]$ around Er^{3+} ion. As the bond strength of these structural units is weaker than $[\text{GeO}_4]$, the field strength around $[\text{ErO}_6]$ thus becomes weaker with more HMO in place of GeO_2 , the strength of Er-O bond becomes relatively stronger, this increases the interaction of Er^{3+} ions with the glass host. Therefore, the Stark split of Er^{3+} ion energy levels shifts to a wider range, it causes higher and wider absorption and broader emission range. More sites and stronger crystal field strength are the reasons that the absorption and emission spectra become broader with the addition of HMO and TeO_2 .

5.7 Conclusions

1. With the increase of heavy metal oxides in germanate glass, the molar volume V_m increases, T_g decreases, the IR edge and UV edge shift to longer wavelengths.
2. In Er^{3+} doped HMO germanate glass, the absorption and emission cross-sections, FWHM and FOM for gain increase with HMO in place of GeO_2 .
3. In Er^{3+} doped HMO germanate glass, with TeO_2 in place of GeO_2 , the emission spectrum of Er^{3+} ion becomes broader, the lifetime becomes shorter, and FOM for gain decreases.

References

1. Scholze, H., *Glass: nature, structure and properties*, translated by M. J. Lakin, New York, London: Springer, 1991.
2. Dumbaugh, W., and J. C. Lapp, *J. Am. Ceram. Soc.* **75**, 2315 (1992).
3. Vogel, W., *Chemistry of Glass*, translated by N. Kreidl, the American Ceramic Society, 1985.
4. Rao, B. V. J., *J. Am. Ceram. Soc.* **45**, 555 (1962).
5. Bishay, A., and C. Maghrabi, *Phys. Chem. Glasses* **10**, 1 (1969).
6. Mochida, N., and K. Takahashi, *Yogyo-Kyokai-Shi* **84**, 415 (1976).
7. Wong, J., and C. Angell, *Glass Structure by Spectroscopy*, Marcel, Dekker, New York, 1976.
8. Miyaji, F., T. Yoko and S. Sakka, *J. Non-Cryst. Solids* **126**, 173 (1990).
9. Fukumi, K., and S. Sakka, *J. Non-Cryst. Solids* **95&96**, 193 (1987).
10. Fukumi, K., and S. Sakka, *Phys. Chem. Glasses* **29**, 1 (1988).
11. Fukumi, K., and S. Sakka, *J. Non-Cryst. Solids* **134**, 77 (1991).

Chapter 6

Er³⁺-doped modified silicate glasses

Virtually all present-day optical communications make use of fibres in which the core and cladding glasses are composed of vitreous silica (SiO₂), often doped with small amounts of germanium (GeO₂), boron (B₂O₃), alumina (Al₂O₃) or phosphorus (P₂O₅) compounds to produce the appropriate refractive index difference. Fused silica is a highly durable and refractory glass. Silica based EDFA is a very important device for optical communications. In order to increase the capacity of communications, broadband and flat gain EDFA is required for WDM system. Non-silica glass hosts intrinsically capable of broader gain than silica, have also been developed [1-3]. However, non-silica devices pose problems in terms of compatibility with standard silica fibre, and none have been widely adopted by the industry. Therefore, modified silicate glass would combine the advantages of broadband gain and compatibility with silica fibres. In this chapter, we present a range of silicate glass hosts which are modified by fluorides, oxide modifiers and oxide formers and compare the fluorescence properties of Er³⁺ ion in these glasses.

6.1 Glass composition

This investigation has been carried out to improve the spectral characteristic of Er³⁺ doped modified silicate glasses and try to achieve a broader and flatter emission spectrum. Based on the SiO₂-Na₂O binary glass system, some oxides, fluorides, phosphate, germanate and borate were incorporated to modify the optical properties of the glass and Er³⁺ fluorescence. Table 6.1 shows the compositions of these glasses. F/O ratio is defined as the molar fraction of fluorine divided by that of oxygen in glass. The preparation processes of these glasses have been explained in chapter 4. There was no evidence for crystallisation in these glasses.

Samples from MS162 to MS193 contain one glass former (SiO₂), oxide modifiers and fluorides. In these glasses the molar volume, refractive index, optical absorption and emission properties of Er³⁺ were measured or calculated. While samples from MS179 to MS189 contain another glass former such as GeO₂, P₂O₅ and B₂O₃ and less

fluorides, only fluorescent properties of Er^{3+} were measured and discussed in the following parts.

Table 6.1 Modified silicate glass compositions

Number	Glass compositions	F/O ratio
MS162	$70\text{SiO}_2-15\text{Na}_2\text{O}-14\text{NaF}-1\text{ErF}_3$	0.110
MS163	$65\text{SiO}_2-15\text{Na}_2\text{O}-15\text{NaF}-4\text{PbF}_2-1\text{ErF}_3$	0.179
MS164	$65\text{SiO}_2-15\text{Na}_2\text{O}-10\text{NaF}-4\text{PbF}_2-5\text{AlF}_3-1\text{ErF}_3$	0.248
MS168	$65\text{SiO}_2-15\text{Na}_2\text{O}-10\text{NaF}-4\text{PbF}_2-5\text{GaF}_3-1\text{ErF}_3$	0.248
MS176	$65\text{SiO}_2-9\text{Na}_2\text{O}-3\text{Al}_2\text{O}_3-10\text{LaF}_3-10\text{PbF}_2-2\text{NaPO}_3-1\text{ErF}_3$	0.344
MS192	$65\text{SiO}_2-11\text{Na}_2\text{O}-3\text{Al}_2\text{O}_3-10\text{LaF}_3-10\text{PbF}_2-1\text{ErF}_3$	0.353
MS193	$61\text{SiO}_2-11\text{Na}_2\text{O}-3\text{Al}_2\text{O}_3-12\text{LaF}_3-12\text{PbF}_2-1\text{ErF}_3$	0.444
MS179	$60\text{SiO}_2-10\text{Na}_2\text{O}-5\text{Al}_2\text{O}_3-10\text{NaF}-4\text{PbF}_2-10\text{GeO}_2-1\text{ErF}_3$	0.120
MS181	$65\text{SiO}_2-15\text{Na}_2\text{O}-5\text{Al}_2\text{O}_3-9\text{NaF}-5\text{NaPO}_3-1\text{ErF}_3$	0.069
MS189	$66\text{SiO}_2-11\text{Na}_2\text{O}-2\text{Al}_2\text{O}_3-10\text{PbF}_2-10\text{B}_2\text{O}_3-1\text{ErF}_3$	0.128

6.2 Molar volume and refractive index in glasses

In oxyfluoride silicate glass, the fluorine/oxygen (F/O) ratio is the most important parameter determining the glass structure and properties. Figure 6.1 shows the density and molar volume (V_m) change with different F/O ratio and figure 6.2 shows the refractive index (n_d) in these glasses, there is a decrease of n_d when F/O is 0.248, it does not mean special. With increasing F/O ratio, there is increasing non-bridging oxygen in the glass. Therefore, the volume of V_m increases and the glass structure becomes more open, at the same time, small cation ions fill in the gaps in the network, so that the density of the glass increases, and therefore the refractive index n_d increases as well.

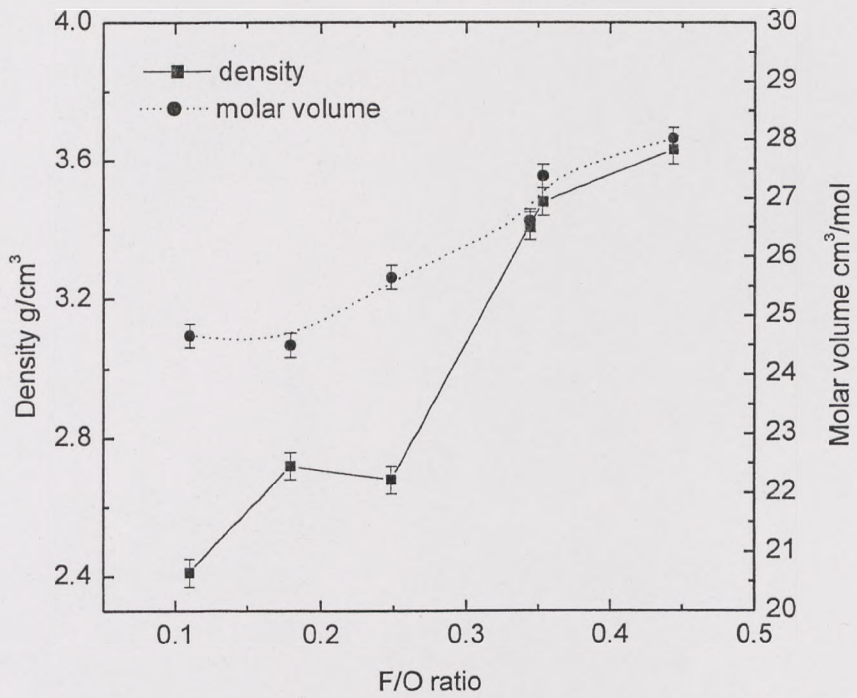


Fig. 6.1 Density and molar volume change with F/O ratio

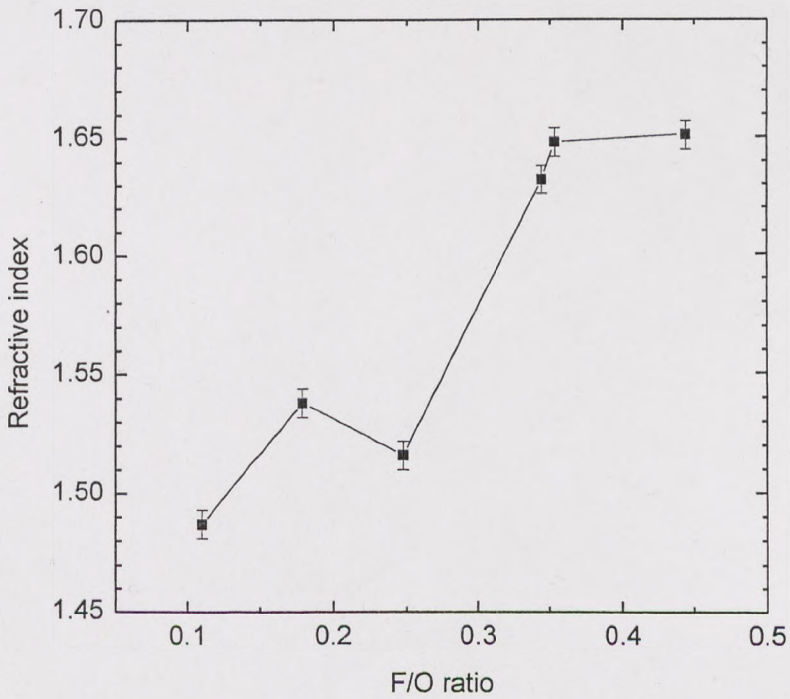


Fig. 6.2 Refractive index change with F/O ratio

6.3 UV edge and IR cut-off

Figure 6.3 and 6.4 show respectively the UV edge and IR cut-off spectra of these oxyfluoride silicate glasses. Table 6.2 lists the calculated results of UV edge and IR cut-off. These results were calculated in the same way that was explained in chapter 5.

Table 6.2 UV and IR cut-off in modified silicate glasses

Glass composition	MS162	MS164	MS168	MS176	MS192
UV cut-off ± 2 nm	268	288	291	304	308
IR cut-off ± 10 cm^{-1}	2290	2250	2200	2155	2110

It is evident from figure 6.3 for oxyfluoride silicate glasses that as the F/O ratio increases, the UV edge cut-off shifts to longer wavelength indicating that the electronic bandgap of the glasses reduces. A similar trend is observed when heavy metal oxides are added. The electronic bandgap in silica glass is 11.7 eV, it is due to electron transition between bonding and anti-bonding levels of Si-O chemical bond with bridging oxygen [4]. If non-bridging oxygen exists, the energy gap drops down to 10.5 eV. In $\text{Na}_2\text{O} \cdot 2\text{SiO}_2$ glass additional transition appears in energy gap at 8.5 eV, which is caused by electronic transition of Na-O chemical bond with non-bridging oxygen [4]. With more modified oxides, the energy gap drops more. In these fluorine modified silicate glasses, they are between 6.5 to 8.0 eV, lower than in $\text{Na}_2\text{O} \cdot 2\text{SiO}_2$ glass. This is due to the Na-O non-bridging oxygen and metal fluorine bond M-F forming additional transitions. By comparing modified silicate with HMO germanate glass, in which the UV edge cut-off is between 324 nm to 398 nm, the UV edge is shifted to much shorter wavelengths, which points out that the bonding electrons experience a much stronger cationic field than observed in HMO germanate glasses.

From figure 6.4, IR cut off has a red shift from 2290 cm^{-1} ($4.37 \mu\text{m}$) to 2110 cm^{-1} ($4.74 \mu\text{m}$) with increasing F/O ratio. Comparing with HMO germanate glass, in which the IR cut-off is between 1740 cm^{-1} ($5.75 \mu\text{m}$) to 1585 cm^{-1} ($6.31 \mu\text{m}$), the IR transparent range is much shorter in silicate glasses. The reason is that the strength of the inter-molecular bonds in silicate is much stronger than in HMO germanate, consequently, the IR edges in modified silicate have a short wavelength cut-off.

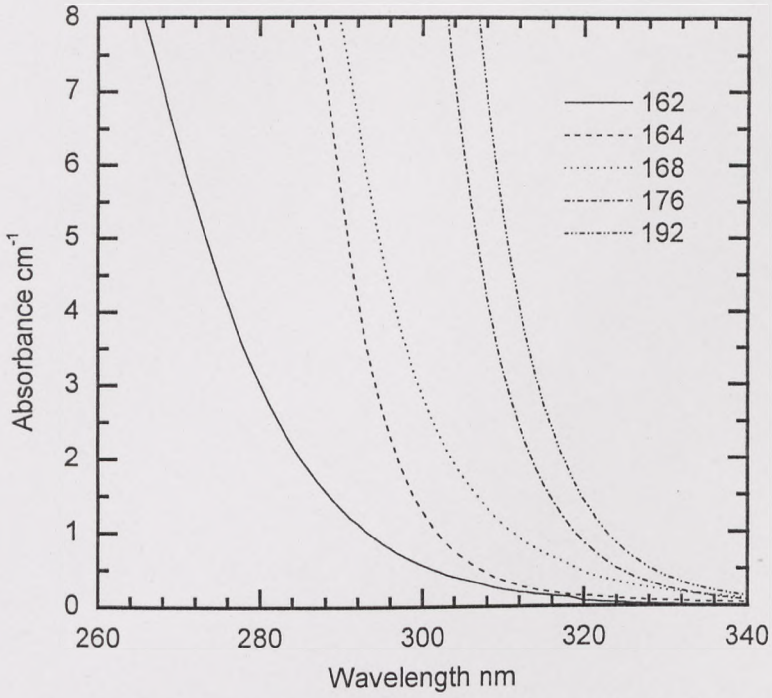


Fig. 6.3 UV absorption edge in modified silicate glasses

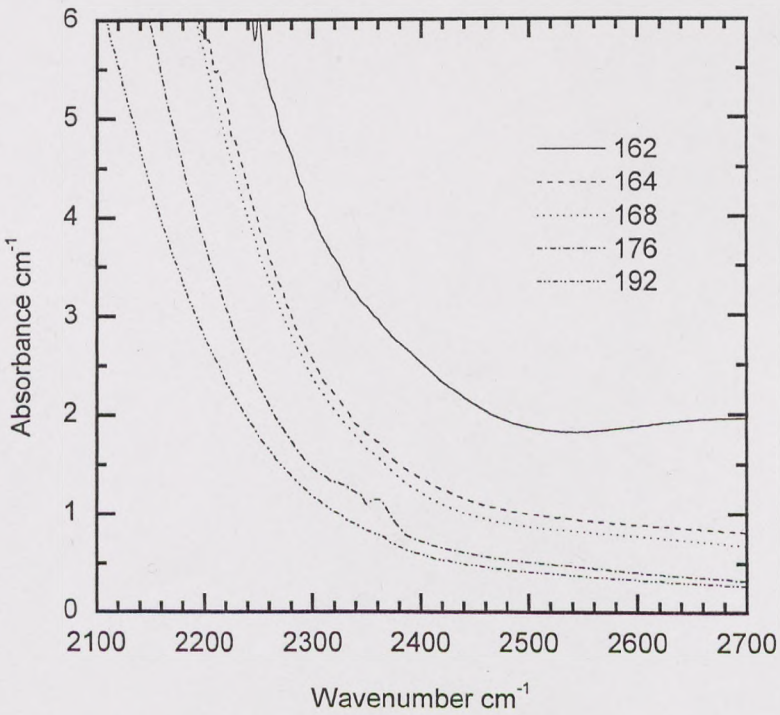


Fig. 6.4 IR absorption edge in modified silicate glasses

6.4 Er³⁺ ion absorption and fluorescence properties at 1.5 μm

For Er³⁺ doped oxyfluoride silicate glass, the research was only concentrated on the ⁴I_{13/2} → ⁴I_{15/2} transition. The absorption cross-section, emission spectra and lifetime have been measured and discussed together with the figure of merit for gain. For amplifier, figure-of-merit (FOM) for gain is defined as the product of lifetime and emission cross-section $\tau \times \sigma_{\text{emiss}}$. The gain bandwidth of an amplifier is determined largely by the width of the emission spectrum and the stimulated emission cross-section. We may therefore define a figure-of-merit (FOM) for bandwidth as the product $\sigma_{\text{emiss}} \times \text{FWHM}$. This character will be able to respond to the gain bandwidth broadness.

Figure 6.5 shows the changes in the absorption and emission cross-sections of the 1.53 μm with different F/O ratio. The emission cross-section is calculated by McCumber theory, it is slightly higher than the absorption cross-section. With increasing the F/O ratio, the cross-sections of Er³⁺ ion increase. The integrated absorption K_a is calculated from equation 6.1. It reflects the transition intensity at 1.53 μm. Figure 6.6 shows the change of K_a with F/O ratio. With increasing F/O ratio, the integrated absorption cross-section K_a also increases. The transition intensity becomes stronger.

$$K_a = \int \sigma_{\text{abs}}(\nu) d\nu \quad 6.1$$

Figure 6.7 compares normalised emission spectra for 3 samples with various F/O ratio. Figure 6.8 illustrates the emission spectrum change in the full width at half maximum (FWHM) with the F/O ratio. With increasing F/O ratio, the FWHM increases from 19 to 36 nm and the emission spectra become broader. For pure silica, Ge/P silica and Al/P silica fibres, the FWHM respectively are 7.9 nm, 24.7 nm and 43.3 nm [5]. In these oxyfluoride silicate glasses, the widest is 36 nm and the emission shape changes smoothly. These mixed anion glasses result in inhomogeneous broadening. Although it is narrower than Al/P silica fibre, it is wider than most of silica fibres and easy to fabricate.

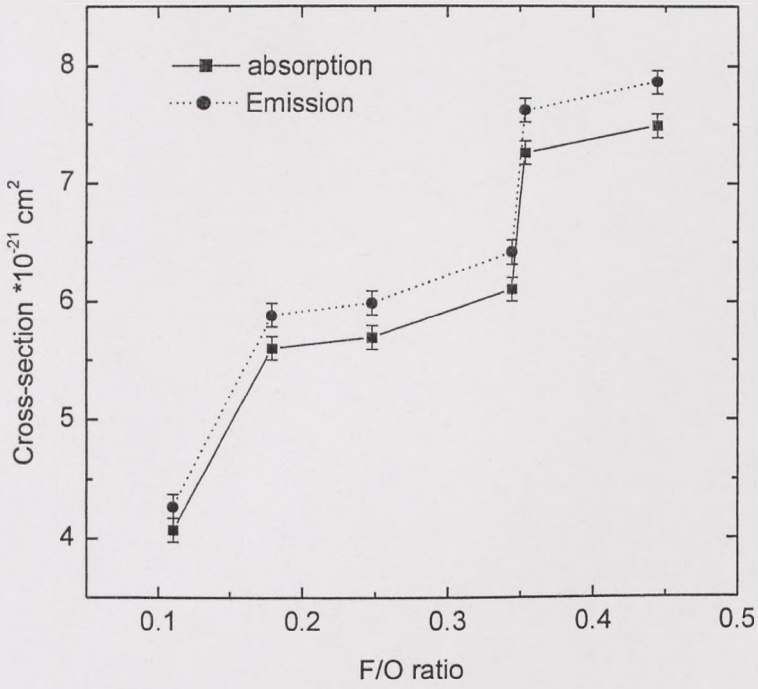


Fig. 6.5 Absorption and emission cross-section change with F/O ratio

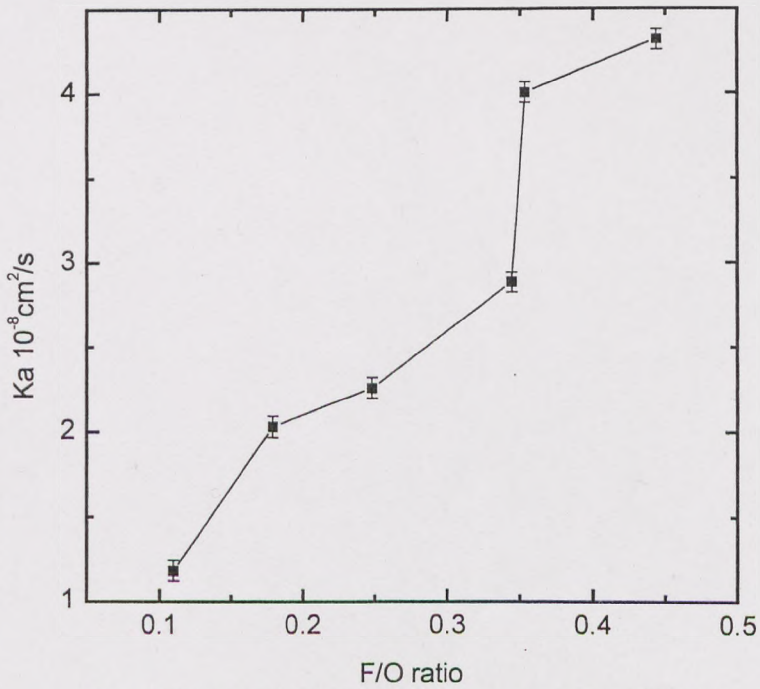


Fig. 6.6 Integrated absorption change with F/O ratio

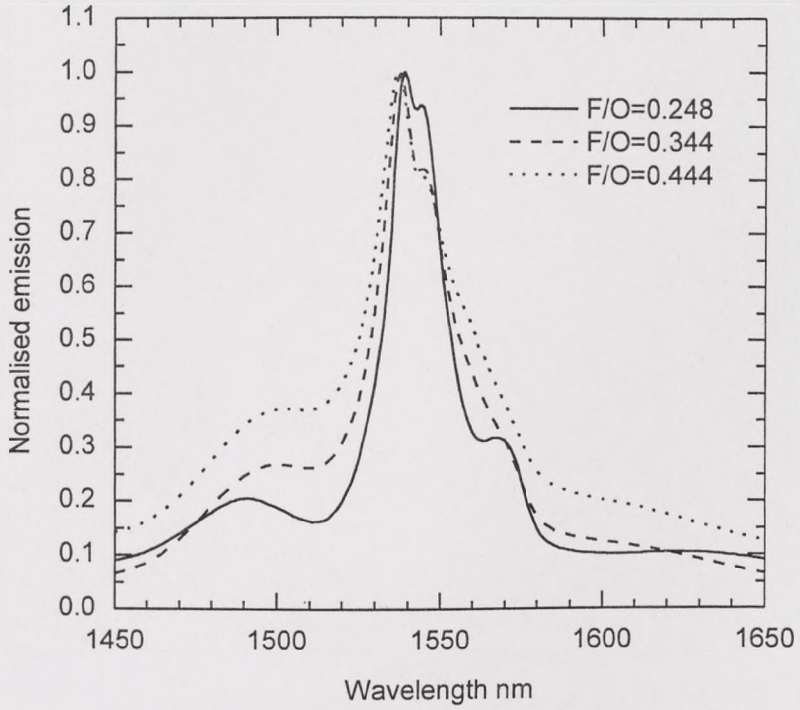


Fig. 6.7 Normalised emission spectra of Er^{3+} ions in silicate glass with various F/O ratio

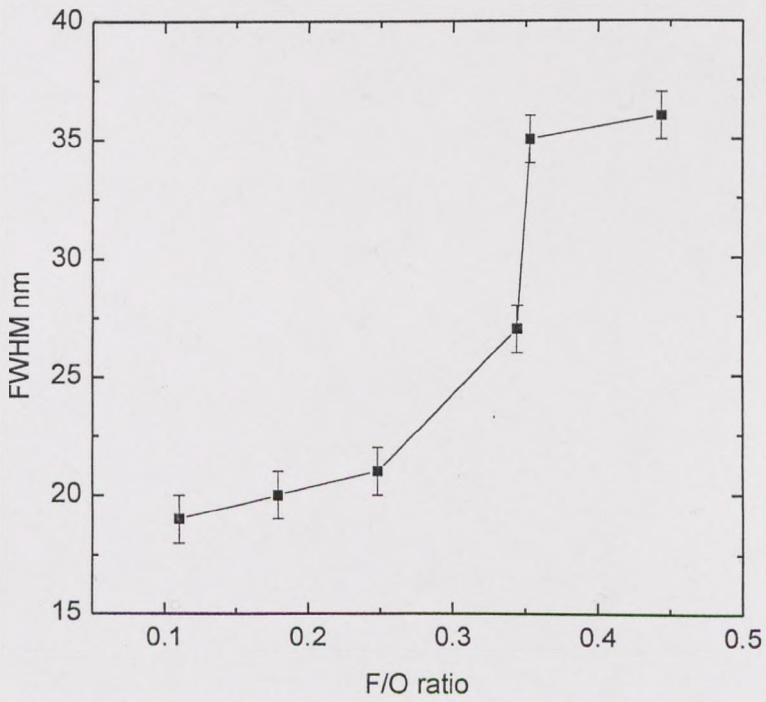


Fig. 6.8 FWHM change with F/O ratio

Figure 6.9 illustrates the changes in the lifetime with the F/O ratio. With the increasing F/O ratio, lifetime increases, but its behaviour is not as sensitive as other properties to high F/O ratio. When F/O is higher than 0.15, the lifetimes are very close to each other. As it is mainly decided by the radiative rate. This rate is dependent on the crystal field strength around the doped Er^{3+} ion.

In the Er^{3+} doped oxyfluoride silicate glasses, we also measured the emission spectrum and lifetime when fluorides were replaced by another glass former. The values of FWHM and the measured lifetimes are shown in table 6.2. From this table, the Er^{3+} emission spectrum in silicate glass becomes wider with the addition of GeO_2 , NaPO_3 and B_2O_3 . Among these three different glass formers, phosphate has the strongest effect, borate is the second and germanate has the least effect. Because phosphorous is 5+ valence cation, the $[\text{PO}_4]$ unit has P=O double bond, borate is 3+ valence cation, it can form $[\text{BO}_4]$ and $[\text{BO}_3]$, germanate structure unit $[\text{GeO}_4]$ is very similar to silicate. Therefore, $[\text{PO}_4]$ and $[\text{BO}_4]$ can cause much more inhomogeneous broadening than $[\text{GeO}_4]$. From the comparison of lifetime results, the samples MS179 and MS181 are very close to MS163. With the addition of B_2O_3 , the lifetime decreases fast. Because B_2O_3 has the highest phonon energy (1400 cm^{-1}) in oxides, it increases the non-radiative rate of Er^{3+} ion in ${}^4\text{I}_{13/2} \rightarrow {}^4\text{I}_{15/2}$ transition, this results in the decrease of lifetime.

Table 6.2 FWHM and lifetime for 4 kinds of glasses

Sample	MS163	MS179 (10% GeO_2)	MS181 (5% NaPO_3)	MS189 (10% B_2O_3)
FWHM ± 1 nm	21	22	33	28
Lifetime ± 0.2 ms	11.0	10.5	11.8	3.8

6.5 Discussion

All the above results show a similar trend with the change in the F/O ratio. As the F/O ratio increases in oxyfluoride silicate glass, it results in more non-bridging oxygen, the glass has a open network structure, which is evident from the increase of molar volume of glass. The glass density is increasing due to the presence of heavier

cations. The red shift in the UV and multiphonon edges strongly points out that glass has a decreasing field strength with the increase of F/O ratio. This weakening field strength in the glass network will result in the stronger field strength between Er^{3+} and non-bridging oxygen, which is responsible for increasing the interaction between rare earth ions and oxygen and fluorine sites. This effect will increase Stark split of Er^{3+} energy levels, it causes broader absorption and emission spectra and increases the absorption and emission cross-sections. On the other hand, with increasing F/O ratio, a part of Er^{3+} ions will connect with F^- to form $[\text{ErF}_6]$, the interaction between Er-F is stronger than Er-O, this is another cause of broadening of the emission spectrum. Furthermore, a more open structure signals additional dopant sites with varying site configuration. Multiple dopant sites are also responsible for broader, absorption and emission spectra. All these effects increase the inhomogeneous broadening.

The figure-of-merit (FOM) for gain is a product of the emission cross-section and the measured lifetime $\sigma_e^* \tau$, whereas the FOM for bandwidth is defined by the product of σ_e times $\Delta\lambda$ (FWHM). These two FOMs are compared in figure 6.10. With the increasing F/O ratio, both for amplifier gain ($\sigma_e^* \tau$) and bandwidth ($\sigma_e^* \text{FWHM}$) increase. In Al silica, Ge/Al silica and Al/P silica fibres, $\sigma_e^* \tau$ respectively are 57.1, 59.4 and 59.2 ($10^{-21} \text{ cm}^2 \cdot \text{ms}$). By comparison in oxyfluoride silicate glass, the maximum $\sigma_e^* \tau$ is about 95 ($10^{-21} \text{ cm}^2 \cdot \text{ms}$), which is much higher than those for standard silica fibres. The investigated oxyfluoride silicate glasses are therefore more promising hosts for EDFA with extended flat gain than the state-of-art silica fibres.

For the addition of different glass former, borate reduces the lifetime of Er^{3+} , it has the lowest quantum efficiency because of its highest phonon energy which results in the highest non-radiative rate. The addition of phosphates appears on the other hand to favour broadening of emission band together with a modest increase in the lifetime. The broadening emission is due to the structural unit $[\text{PO}_4]$ which has a double bond. It is more effective than $[\text{BO}_4]$ and $[\text{GeO}_4]$ on the change of emission spectrum of Er^{3+} ion. The change in the glass structure however cannot be assumed to be continuous due to the immiscibility between the phosphates and silicates, which also limits the improvement in Er^{3+} ion spectrum. Germanate has very little effect on the emission spectrum and lifetime of Er^{3+} in oxyfluoride silicate glass, it is a kind of component which is suitable for modifying the refractive index of these glasses.

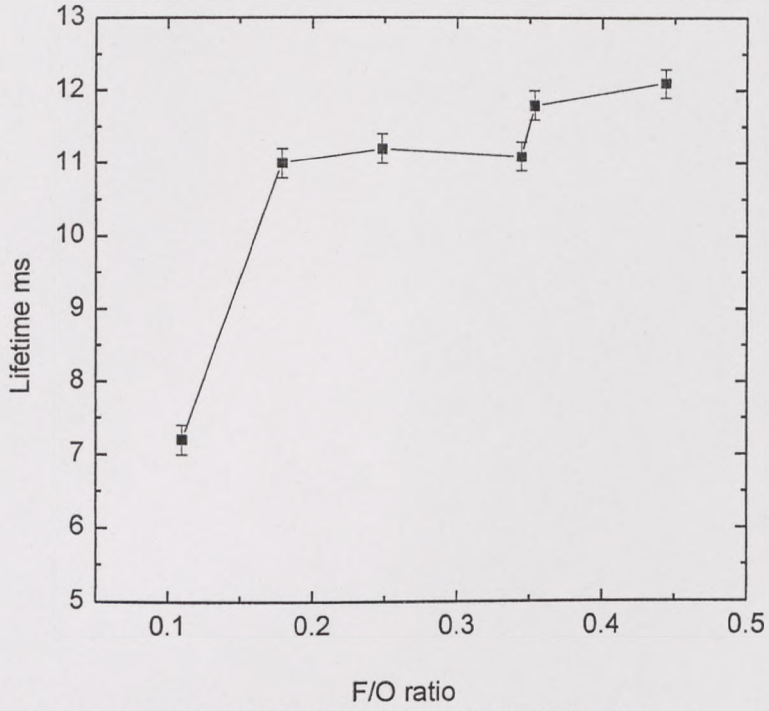


Fig. 6.9 Lifetimes change with F/O ratio

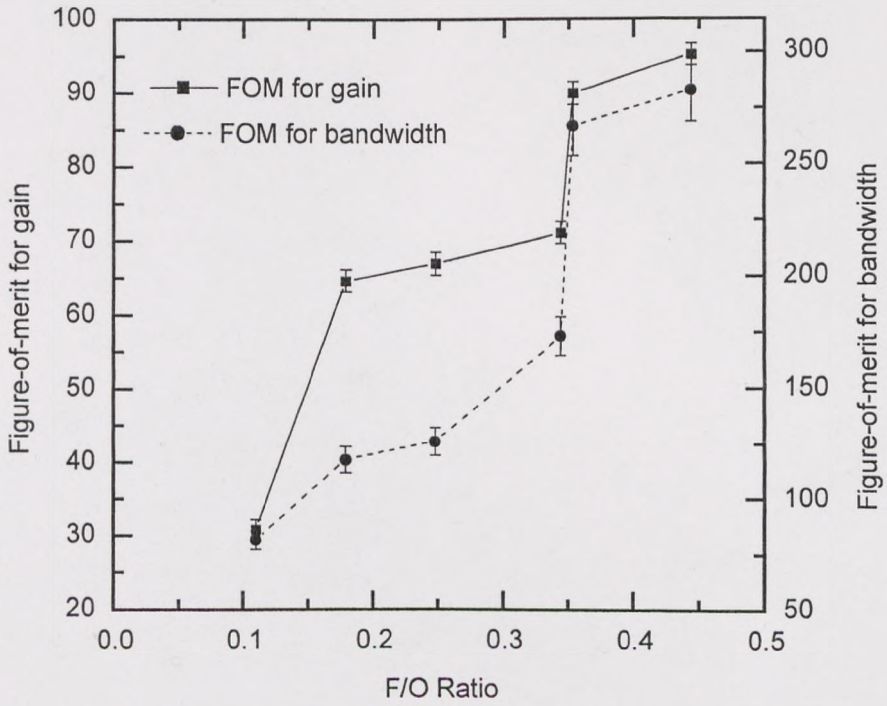


Fig. 6.10 Figure-of-merit for gain and bandwidth change with F/O ratio

6.6 Conclusions

1. With the increase of F/O ratio, the modified silicate glass has increasing molar volume and refractive index. The change in the F/O ratio also shifts the IR edge and UV edge to longer wavelength.
2. In Er^{3+} doped modified silicate glasses, the absorption and emission cross-sections, emission FWHM and FOM for gain and bandwidth increase with the increase of F/O ratio.
3. The Er^{3+} doped modified silicate glasses having another oxide glass former, P_2O_5 has the strongest effect in contributing to the spectral broadening of Er^{3+} ion than either B_2O_3 or GeO_2 . The addition of B_2O_3 in the modified silicate glass quenches the lifetime of $^4\text{I}_{13/2}$ level by promoting the non-radiative rate, which was not observed in the case of addition P_2O_5 or GeO_2 , as they have much smaller phonon energies.

References

1. Sun, Y., J. V. V. Sulhoff, A. K. Srivastava, and C. Wolf, *IOOC-ECOC'97*, Vol 5, Ch23, No448.
2. Yamada, M., T.Kanamori, H.Ono, K.Nakagawa, and S.Sudo etal, *IEEE Photonics Technol. Lett.* **7**, 882 (1996).
3. Mori, A., K Kobayashi, H Oho, T Oikawa, Y Nishida, and Y Ohishi, *IEEE Photon Tech Lett.* **8**, 882 (1996).
4. Gan Fuxi, "*Optical and Spectroscopic Properties of Glass*", Chapter 3 "*Eigen Absorption in Glass*", Springer-Verlag Berlin Heidelberg New York, 1991.
5. J F Dignonnet Ed. "*Rare earth doped fiber lasers and amplifiers*", chapter 2 "*optical and electronic properties of rare earth ions in glasses*", Marcell Dekker, 1993.

Chapter 7

Physical properties and structure of tellurite glass

The main advantages of tellurite family of glasses, as described in Chapter 1, are worth considering for designing optical devices. In this chapter, some physical properties of tellurite glass such as density, molar volume, thermal stability and optical properties were measured. The glass structure was analysed using the Raman spectroscopy technique. The relationships between the composition and the glass structure are also discussed.

7.1 Density and molar volume of tellurite glass

The density ρ is defined as the mass per unit volume. From the density of a glass, the volume of 1 mole of this glass can easily be determined with $V = M/\rho$, M is the molar weight of the glass.

For a binary $(100-x)\text{TeO}_2 - x\text{Na}_2\text{O}$ tellurite glass composition studies, the densities and molar volumes are shown in figure 7.1. As Na_2O concentration increases, the

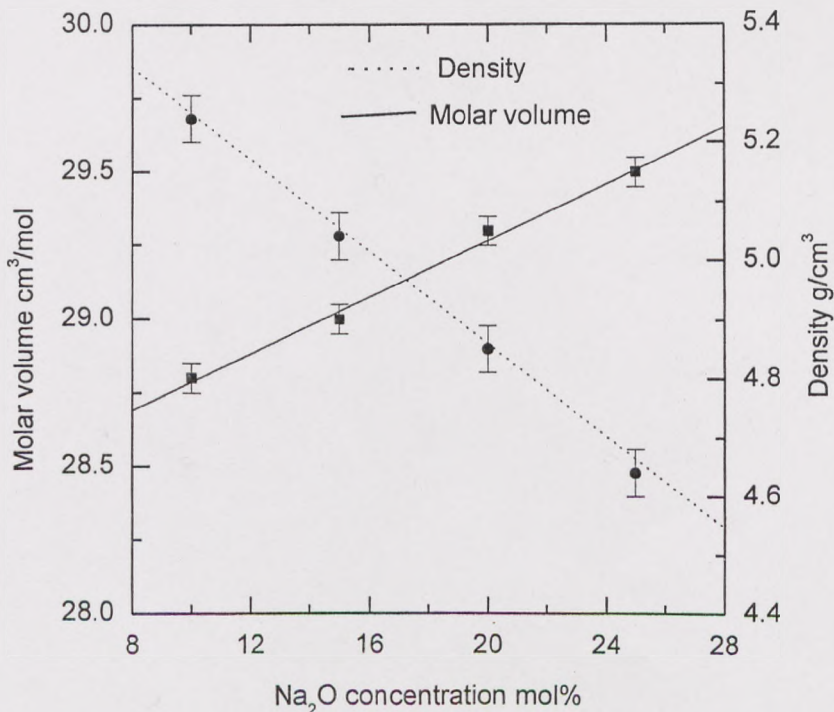


Fig. 7.1 Density and molar volume change with Na_2O concentration

density of glass decreases, the molar volumes increase. The densities and molar volumes in the system $\text{TeO}_2\text{-Na}_2\text{O}$ depend linearly on the molar concentration of components, and the linear relation is also shown in figure 7.1. The relation between the molar volume, V_m , of binary glass has been described by Yakkind [1]. From our measurement, the relation between V_m and Na_2O content is: $V_m = 4.85 m_{\text{Na}_2\text{O}} + 28.31$.

Tellurite glasses have a continuous network structure based on the sharing of TeO_4 corners of trigonal bipyramids and TeO_{3+1} polyhedra having one non-bridging oxygen (NBO) atom [2]. With the increase of network modifier, TeO_4 trigonal bipyramids can be transferred to TeO_3 trigonal pyramids which have NBO atoms. It results in a less closely packed glass structure. Therefore, the V_m of glasses increased and density decreased with the addition of Na_2O .

In ternary $(90-x) \text{TeO}_2 - x\text{R}_2\text{O} - 10\text{ZnO}$ ($\text{R}_2\text{O} = \text{Li}_2\text{O}, \text{Na}_2\text{O}$ and K_2O) glass system, figure 7.2 and 7.3 show respectively the densities and molar volumes change with alkali content. The density always decreases linearly with the increasing alkali content. At the same content with different alkali ions, the densities change following this sequence $\text{Li}_2\text{O} > \text{Na}_2\text{O} > \text{K}_2\text{O}$. For molar volume in figure 7.3, it is more complex with increasing alkali content. The V_m of glasses decreases linearly with increasing Li_2O , it increases linearly with increasing K_2O . With increasing Na_2O , V_m changes marginally, it also decreases slightly in linear relation. For the same content of alkali ions, V_m is the largest and density is the smallest in glass containing K_2O , V_m is the smallest and density is the largest when R_2O is Li_2O . For tellurite glass containing Na_2O , falls in between tellurite compositions containing Li_2O and K_2O . The reason of these variations is that the ion radius of alkali and bond length of cation-oxygen. The ion radius is 0.74, 1.02, 1.38 Å for Li^+ , Na^+ , and K^+ . The distance between cation-oxygen is respectively 2.10, 2.30 and 2.76 Å for Li-O, Na-O and K-O [3]. It is obvious that K^+ ion has the largest radius and K-O has the longest bond distance. When alkali ions are incorporated in the tellurite glass structure, the glass network is broken, and consequently the molar volume of glass V_m should increase. However the alkali ions exhibit an additional effect, some of these ions not only find room in the empty space of the network, but more over produce a contraction of the network. Such a structural contraction leads to a decrease in the glass molar volume. Li^+ ion contributes the largest contraction of the network because it has the strongest field

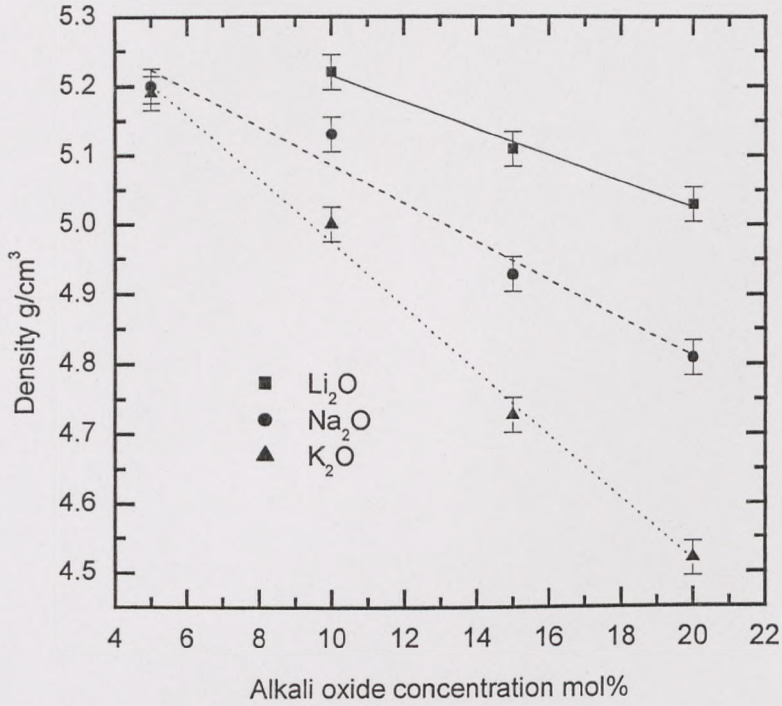


Fig. 7.2 Density change with alkali content in tellurite glass

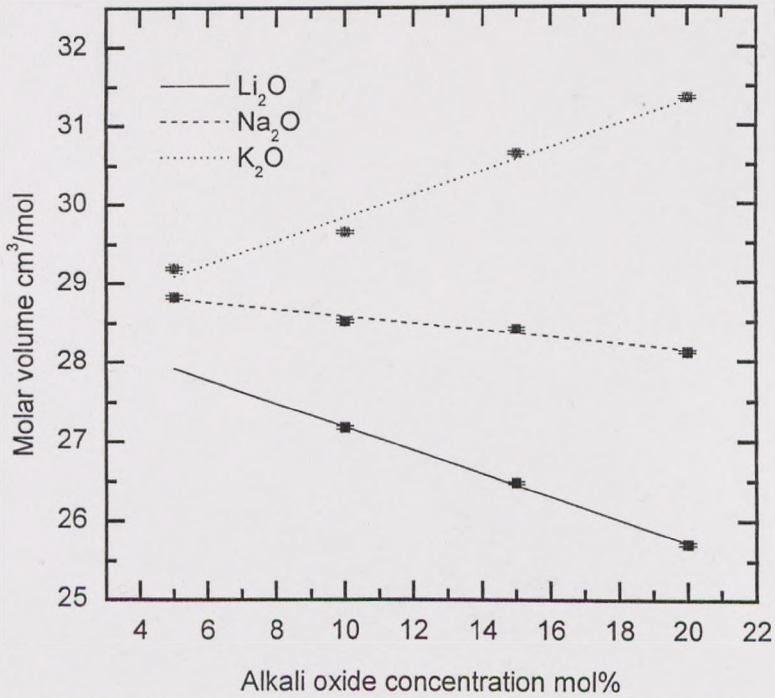


Fig. 7.3 Molar volume change with alkali content in tellurite glass

strength and is the smallest among the alkali ions. The interplay of the bond length and the cationic radius therefore contribute to the structural changes manifested by the molar volume and densities of alkali-containing glasses.

For the ternary $(90-x) \text{TeO}_2 - x \text{ZnO} - 10 \text{R}_2\text{O}$ ($\text{R}_2\text{O} = \text{Na}_2\text{O}$ and K_2O) glass system, the figures 7.4 and 7.5 show respectively the densities and molar volumes change with ZnO concentration. With the increase of ZnO, the densities and molar volumes decreased linearly. ZnO is a network intermediary, it can connect the broken network. The ionic radius of Zn^{2+} is 0.75 Å. For 4-fold coordinated Zn, the O-Zn distance is 2.03 Å; for a 6 coordinated Zn, the bond length is 2.15 Å. The O-Te distance varies between 1.88 and 2.12 Å for 4 coordination, $[\text{ZnO}_4]$ and $[\text{TeO}_4]$ are nearly the same size. Because there is 10 mol% Na_2O in glass, ZnO acts as a network former or stabiliser. This results in the decrease of molar volume. As the unit $[\text{TeO}_4]$ is much heavier than $[\text{ZnO}_4]$, the density of glass will decrease when ZnO replaces TeO_2 . These two figures also show that for the same ZnO containing glasses, the addition of Na_2O results in a higher density and lower molar volume than when Na_2O is replaced by K_2O . These results are consistent with the data compared in figures 7.2 and 7.3.

7.2 Thermal analysis

7.2.1 Tellurite glass transition temperature and thermal stability

To investigate the glass stability, differential scanning calorimetry (DSC) was employed to measure the glass transition temperature (T_g) and crystallisation onset temperature (T_x). These two characteristic temperatures are very important for glass thermal analysis. The glass transition temperature (T_g), which corresponds to a viscosity of $10^{12} \sim 10^{13}$ Pa, was defined as the temperature region in which the behaviour of the material changes from solid-like to liquid-like. The crystallisation temperature indicates the range in which the glass viscosity is sufficiently low to permit rapid crystal growth. It can be defined as the extrapolated onset of the first crystallisation exotherm. The quantity of $T_x - T_g$ has been frequently used as a rough measure of glass stability. To achieve a large working range during operations such as preform preparation and fibre drawing, it is desirable to have $(T_x - T_g)$ as large as

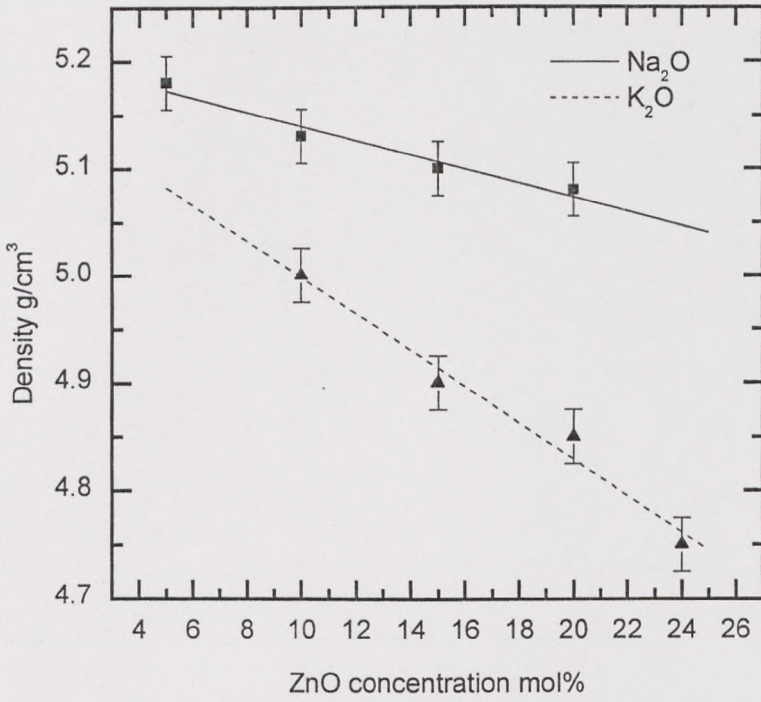


Fig. 7.4 Density change with ZnO content in tellurite glass

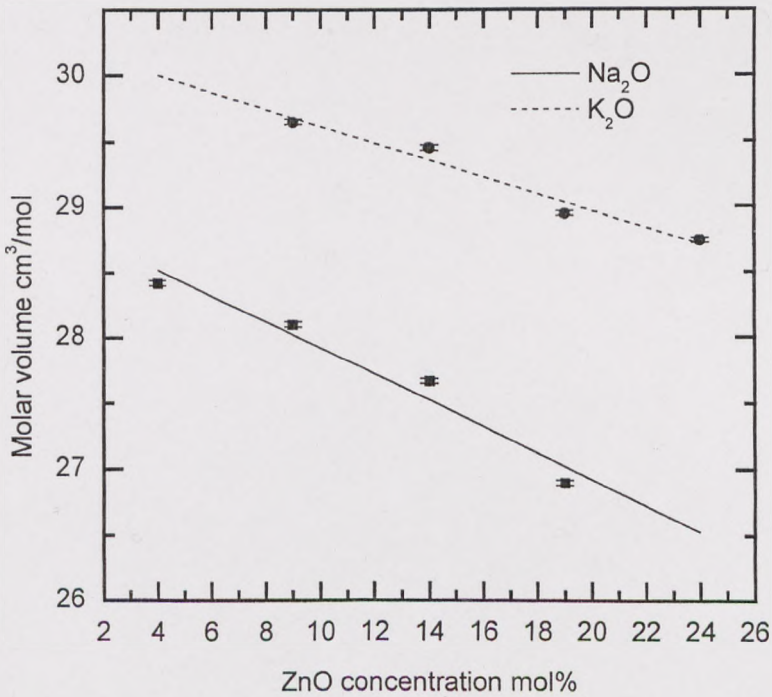


Fig. 7.5 Molar volume change with ZnO concentration in tellurite glass

possible. A typical DSC curve for this measurement is illustrated in figure 7.6. T_p is the peak crystallisation temperature.

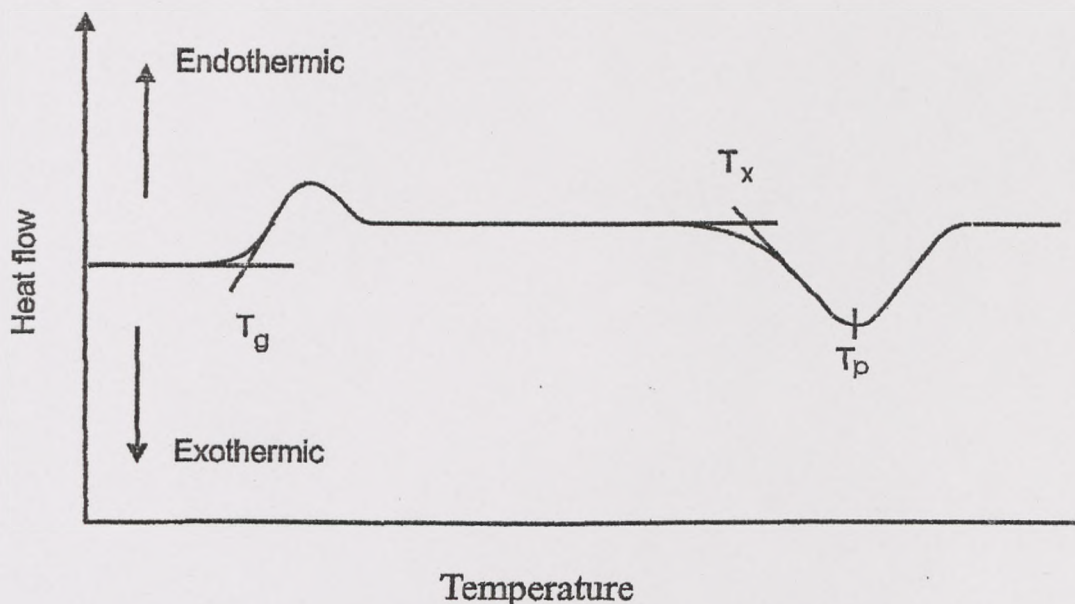


Fig. 7.6 Typical DSC curve in glass

For the ternary $\text{TeO}_2 - \text{R}_2\text{O} - \text{ZnO}$ ($\text{R}_2\text{O} = \text{Li}_2\text{O}, \text{Na}_2\text{O}$ and K_2O) glass system, the density and molar volume have already been discussed above. Using DSC, we can verify the thermal stability of these glasses and the following figures show the relation between the glass compositions and thermal stability.

In ternary $(90-x) \text{TeO}_2 - x\text{R}_2\text{O} - 10\text{ZnO}$ ($\text{R}_2\text{O} = \text{Li}_2\text{O}, \text{Na}_2\text{O}$ and K_2O) glass system, figure 7-7 and 7-8 show the transition temperature T_g and $(T_x - T_g)$ change with alkali content, respectively. With the increase of R_2O , the transition temperatures of these glasses decrease. The trend is the same for $\text{Li}_2\text{O}, \text{Na}_2\text{O}$ and K_2O . For an identical concentration of R_2O , the T_g of glasses containing Li_2O have slightly higher values than those for Na_2O . On the other hand, K_2O has much more effect on the glass transition temperature. At low R_2O content, which is less than 10 mol%, glass containing K_2O has the highest T_g , at whereas the high R_2O (more than 15 mol%), it has the lowest T_g . The reason for this result is from molar volume change in figure 7.3 which shows that only K_2O increases the molar volume of glass. The molar volume of glass increases with the addition of K_2O , decreases with the addition of Li_2O , marginally decreases when Na_2O replaces Li_2O , and K_2O has much more effect on the

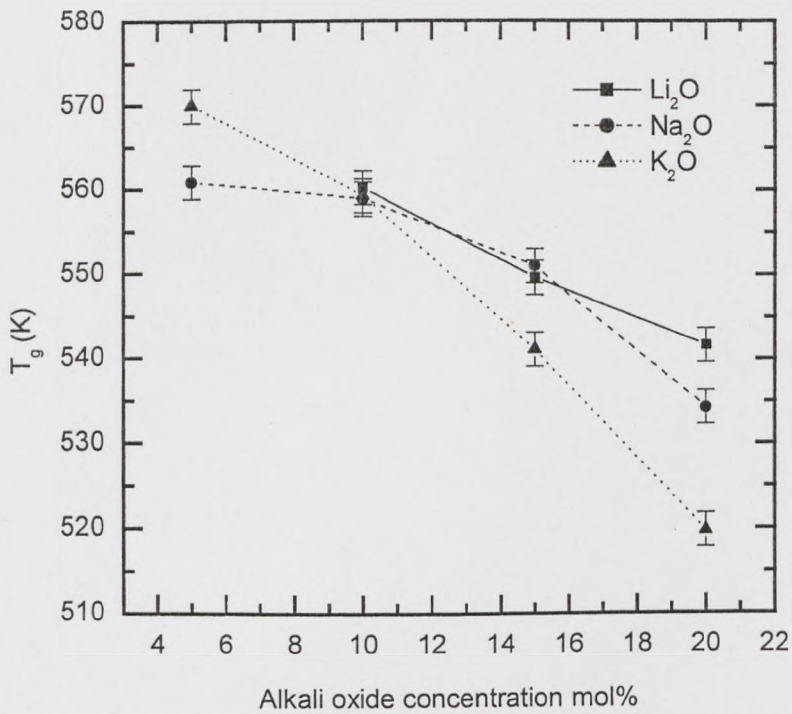


Fig. 7.7 T_g change with alkali oxide content in tellurite glass

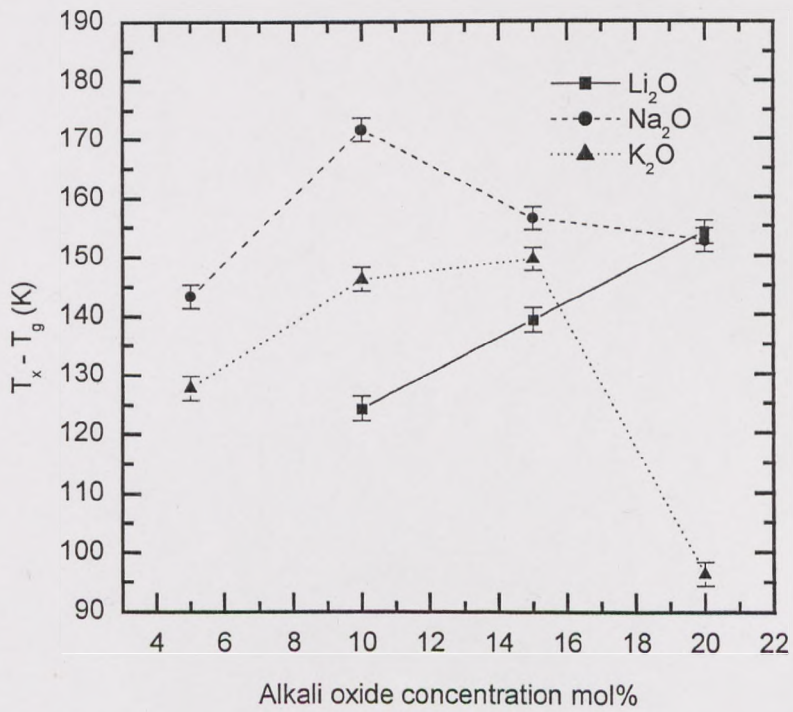


Fig. 7.8 $T_x - T_g$ change with alkali oxide content in tellurite glass

glass structure change. Thus, in the same range of alkali oxide content, the T_g of glass changes more when glass contains K_2O .

It is apparent from figure 7.8 that at 16 mol% R_2O , glass containing Na_2O has the highest thermal stability. K_2O containing glasses are comparatively less stable, and the compositions with Li_2O are relatively the least stable. At around 10-15 mol% Na_2O or K_2O , the glass has the best thermal stability. As Li_2O has the shortest bond distance and smallest ionic radius of alkali among all the alkali metals, the glass structure will be most likely more closed packed than with either Na^+ or K^+ ion. This is clearly manifested by the compositional dependence of molar volumes and densities for Li_2O glasses. In figure 7.8, the $T_x - T_g$ for Li_2O glass increases from 10 to 20 mol%, the trend for Li_2O therefore differs from Na_2O and K_2O .

In the $(90-x) TeO_2 - 10R_2O - xZnO$ ($R_2O = Na_2O$ and K_2O) ternary system, when alkali concentration was fixed at 10 mol%, the ZnO content was varied from 4 to 19 mol%, the relationships between T_g , the thermal stability $T_x - T_g$ and ZnO are shown in figures 7.9 and 7.10 respectively. With increasing ZnO content, T_g of glass increases slightly from 558K to 563K. The modest rise in T_g due to the presence of ZnO is in contrast with the effect R_2O of on T_g . This is because ZnO and R_2O are two different types of oxides which participates in glass formation. R_2O oxides are typical network modifiers which break the glass network by forming non-bridging oxygen sites, ZnO is a network intermediate which can form $[ZnO_4]$ to connect the broken network. It is the network contribution effect of ZnO which help in increasing the transition temperature T_g and thermal stability.

The effect of R_2O , e.g. Na_2O and K_2O on thermal stability of ZnO containing glasses are compared in figure 7.10 which is consistent with the data presented in figure 7.8. In the ternary compositions, when the ZnO content is 15 mol%, the effect of R_2O on glass stability is more remarkable when Na_2O as an additive is compared with K_2O .

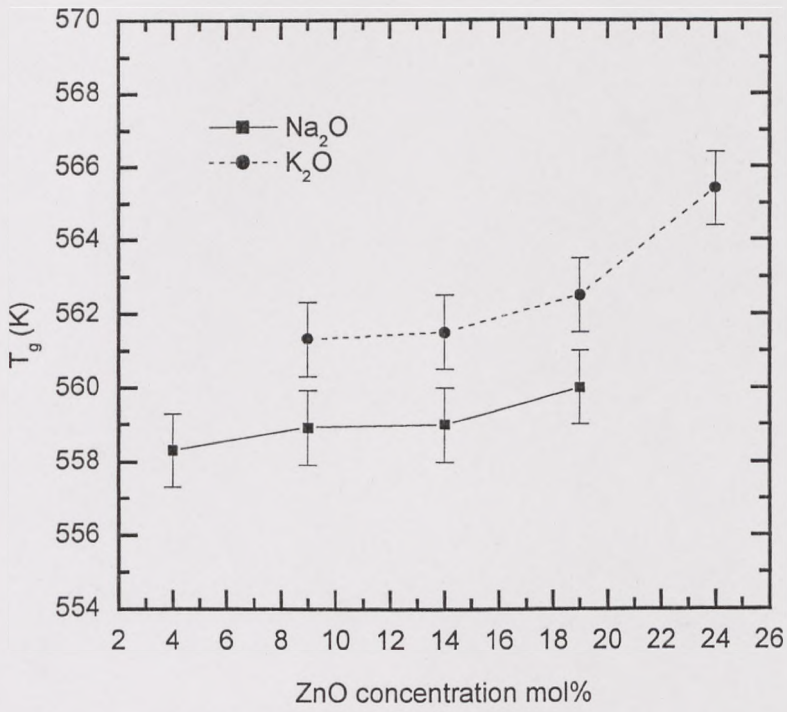


Fig. 7.9 T_g change with ZnO concentration in tellurite glass

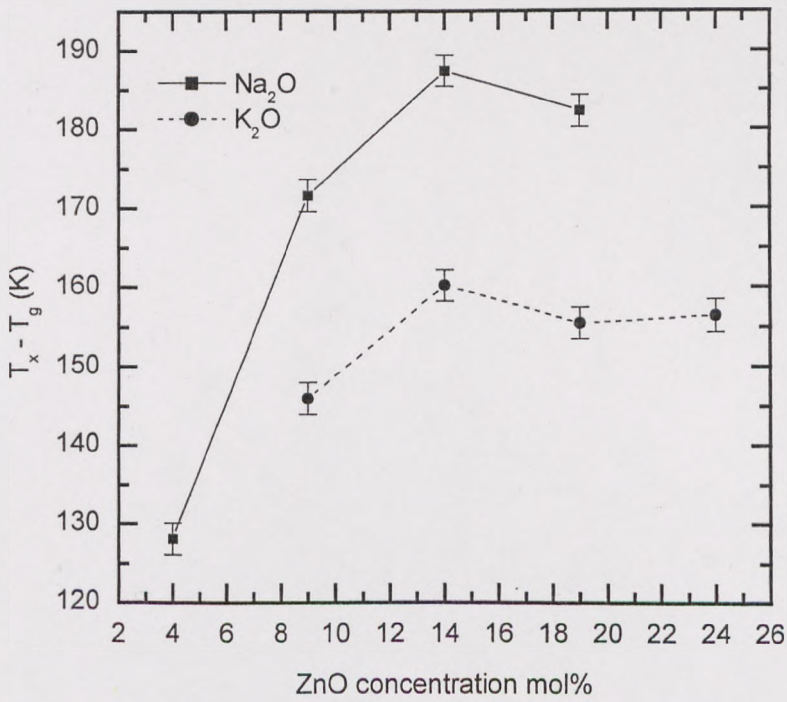


Fig. 7.10 $T_x - T_g$ change with ZnO concentration in tellurite glass

7.2.2 Crystallization kinetics of tellurite glasses

In order to study the crystallization kinetics in tellurite glasses, isothermal and non-isothermal crystallization methods were used. As crystallisation peak cannot be observed in some very stable tellurite glasses, the DTA curve in one example (80TeO₂:10Na₂O:10ZnO) of tellurite glasses is shown in figure 7.10a, therefore two tellurite glass compositions in which there is a crystallisation peak were investigated: a binary glass 85TeO₂:15Na₂O (TN), and a ternary glass 85TeO₂:5Na₂O:10ZnO (TNZ).

7.2.2.1 Isothermal crystallisation

Crystallisation isotherms for the two glasses were recorded by the DSC at various temperatures T_{iso} between 673 K and 723 K; typical curves for each glass are shown in Figures 7.11 and 7.12. Figures 7.13 and 7.14 plot the volume fraction of glass crystallized at time t , $x(t)$, calculated as the normalized integral of the crystallization exotherm. The linear Johnson-Mehl-Avrami equation (Equation 4.3) is plotted for different temperatures in Figures 7.15 and 7.16. It is seen that all the plots are approximately linear, confirming that the crystallization process is well described by Equation 4.3. The values of n and k for each glass have been determined from linear fits to the plots in figures 7.15 and 7.16. In both glasses the slopes, and therefore the exponents n , remain approximately constant at different temperatures, indicating that the morphology of crystal growth remains unchanged. The activation energy E and the constant ν were determined for both glasses using Equations 4.4 and 4.5, as shown respectively in figures 7.17 ($\ln k$ vs $10^3/T_{\text{iso}}$) and 7.18 ($\ln t_m$ vs $10^3/T$). The data in both figures show good agreement with linear behaviour. The results of the two measurements, summarised in table 7.1, agree within experimental error.

The averaged values of n , ν and E (listed in table 7.1) were used to calculate the time-temperature-transformation (TTT) curves for the two glasses, shown in figures 7.19 and 7.20. TTT curves demonstrate clearly that the binary glass TN is more resistant to devitrification than the ternary glass TNZ. The replacement of 10 mol% of Na₂O by ZnO network modifier therefore decreases glass stability.

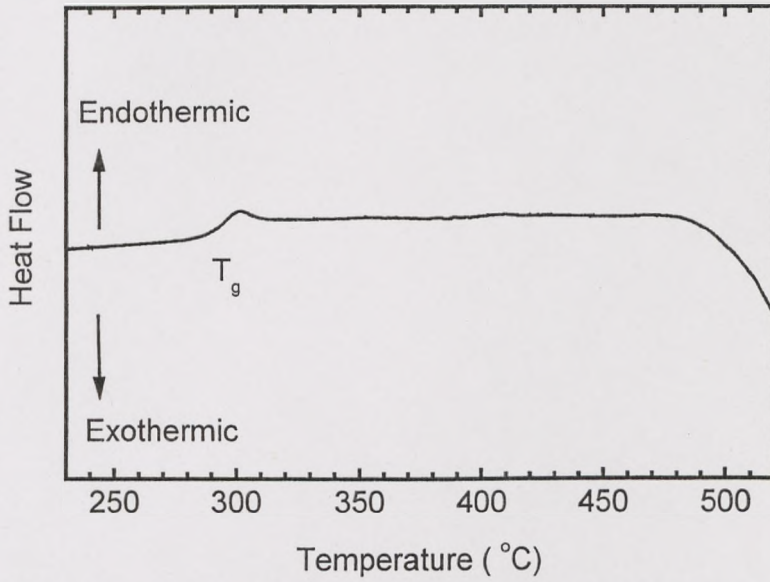


Fig.7.10a DTA curve of 80TeO₂-10ZnO-10Na₂O glass

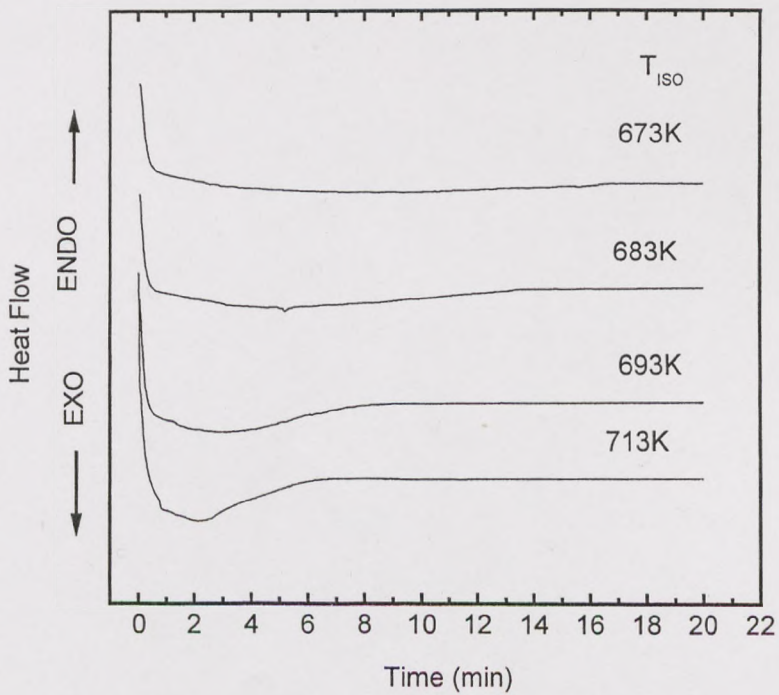


Fig 7.11 Isothermal DSC traces of TN glass

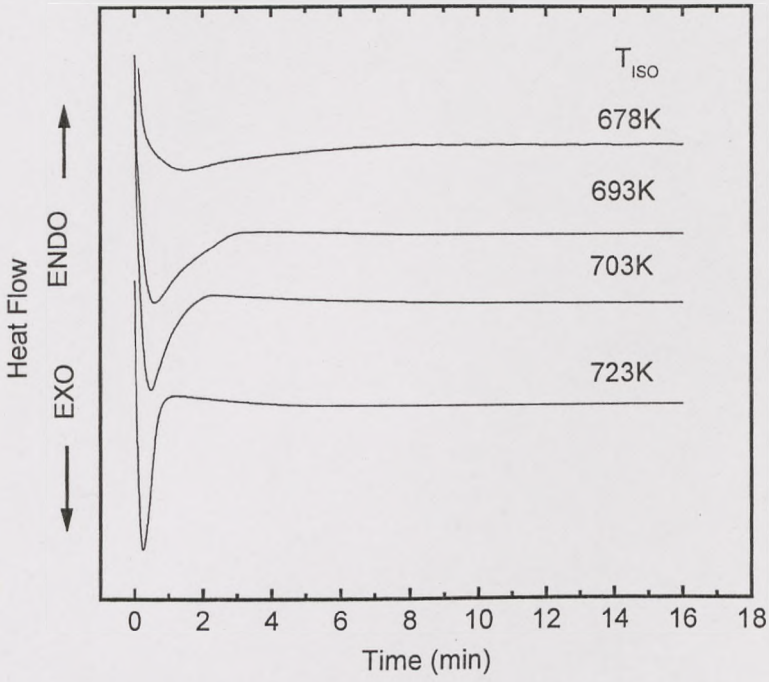


Fig. 7.12 Isothermal DSC traces of TNZ glass

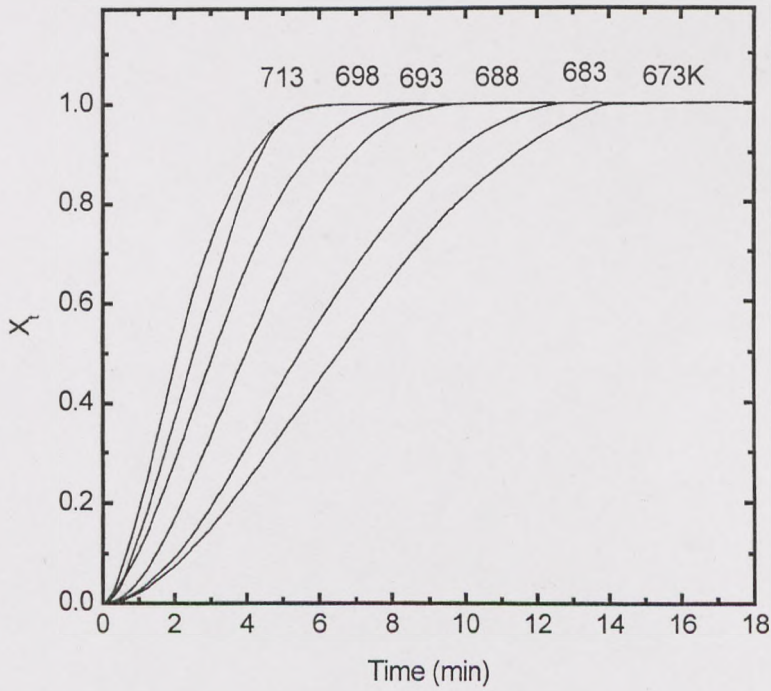


Fig. 7.13 Fraction crystallised x as a function of time in TN Glass

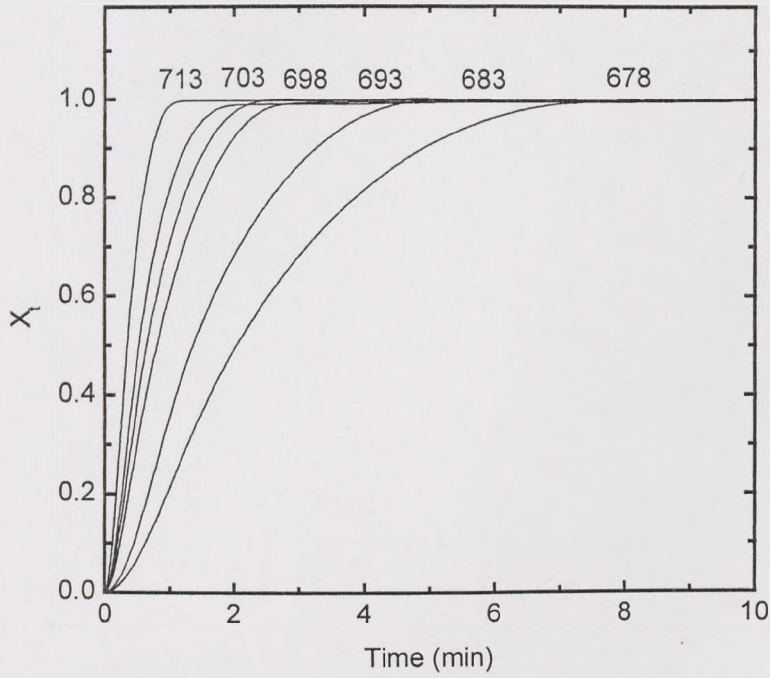


Fig. 7.14 Fraction crystallised x as a function of time in TNZ glass

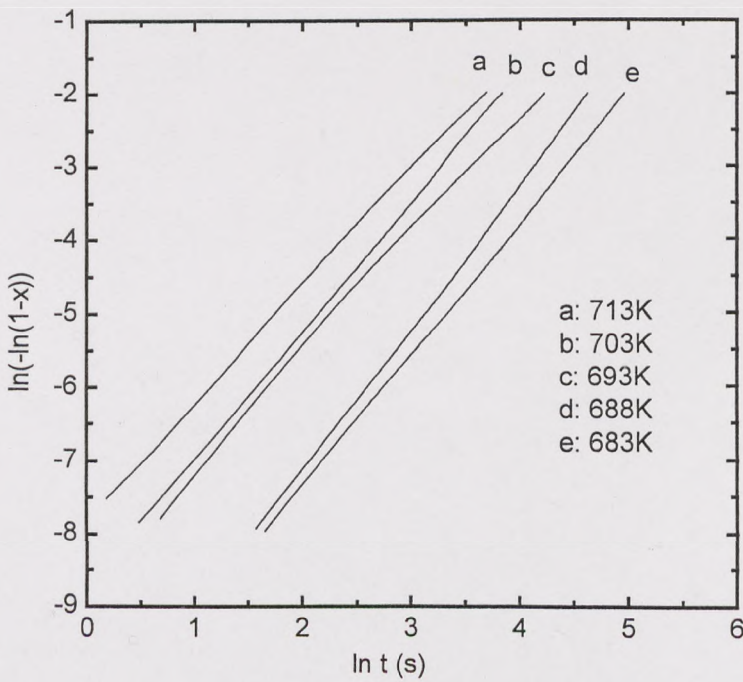


Fig. 7.15 JMA equation plots for isothermal crystallisation in TN glass

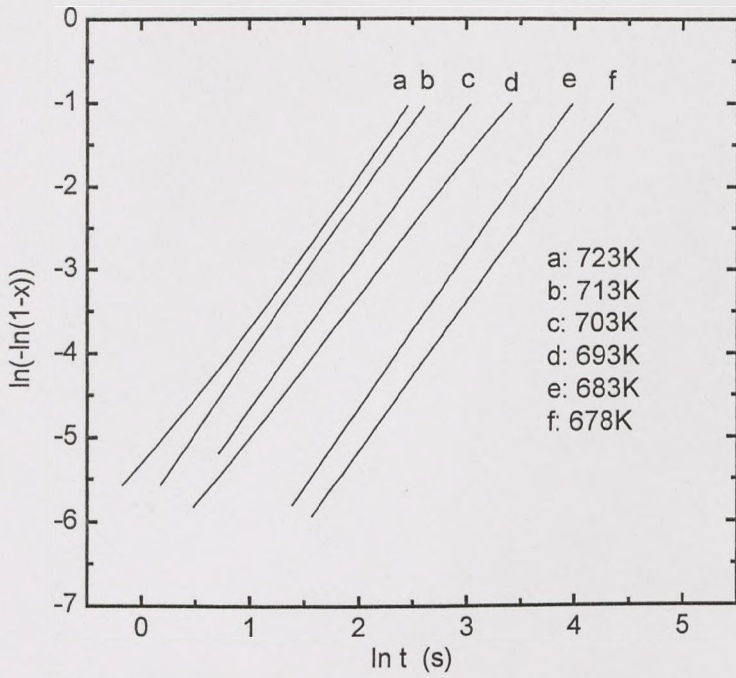


Fig. 7.16 JMA equation plots for isothermal crystallisation in TNZ glass

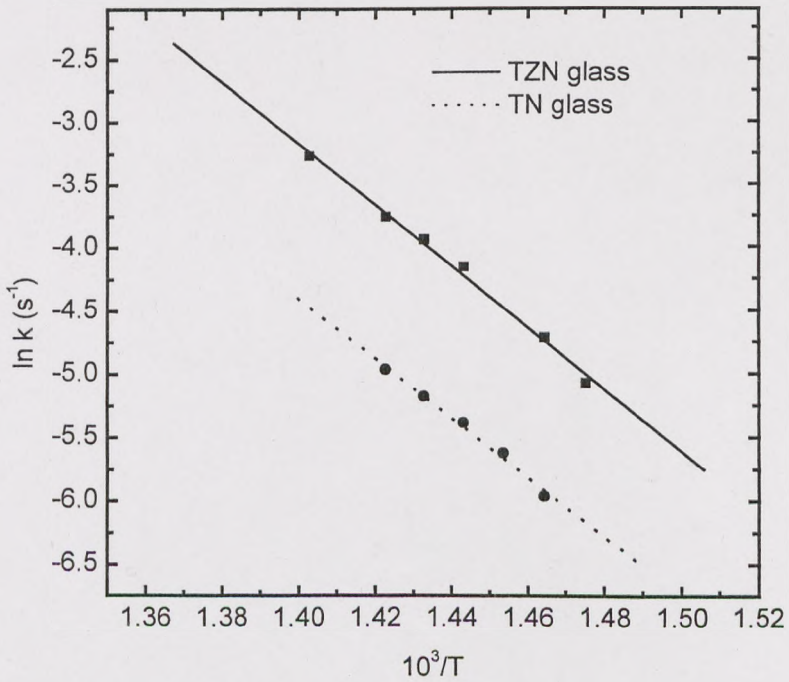


Fig. 7.17 $\ln k$ vs $1/T_{iso}$ for TN and TNZ glasses

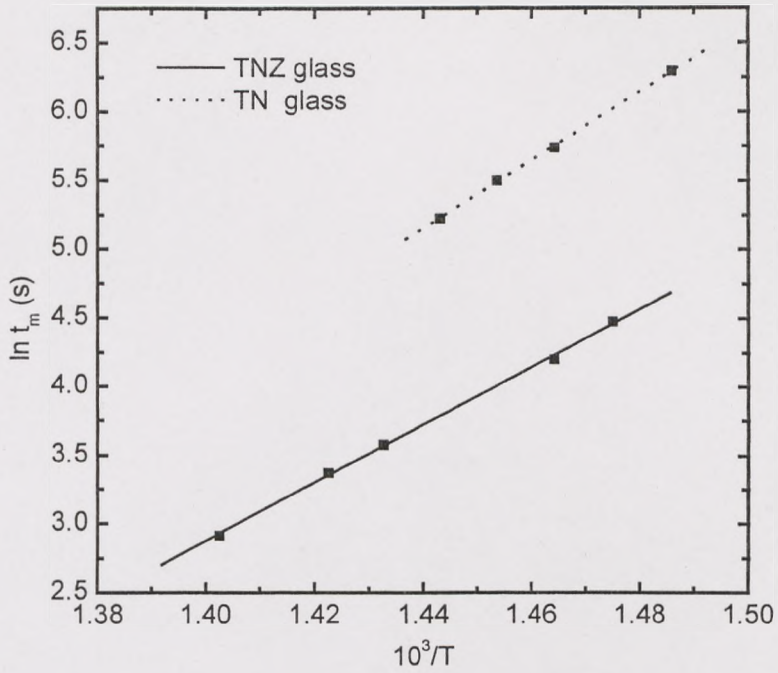


Fig. 7.18 $\ln t_m$ vs $1/T_{iso}$ for TN and TNZ glasses

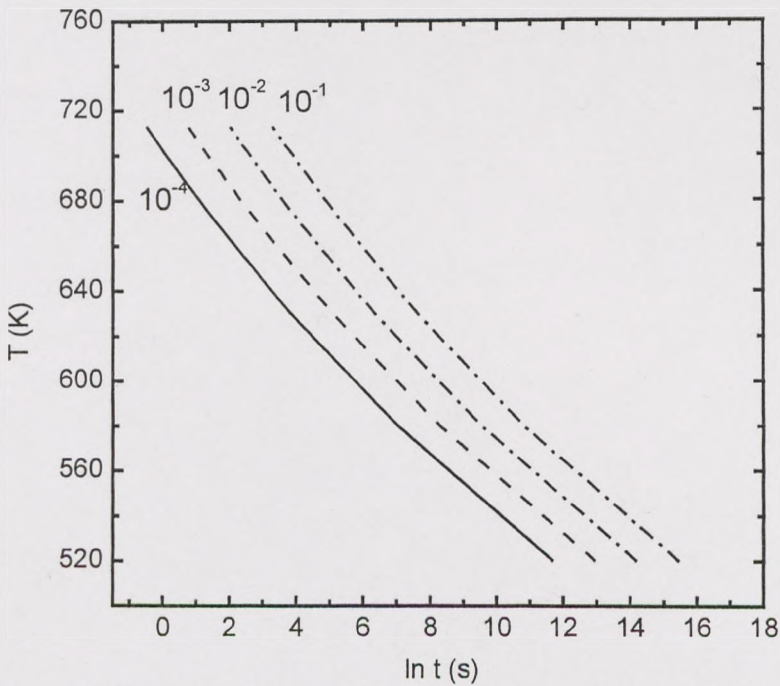


Fig. 7.19 TTT plots for different values of fraction crystallised x for TN glass

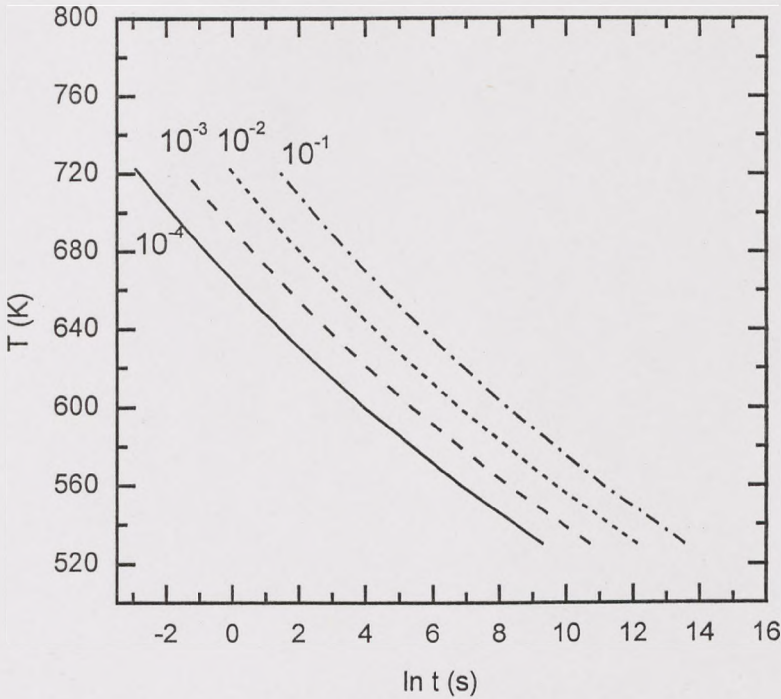


Fig. 7.20 TTT plots for different values of fraction crystallised x for TNZ glass

7.2.2.2 Non-isothermal crystallization

Non-isothermal crystallization exotherms for the two glasses were recorded by the DTA at various scanning rates; typical curves for each glass are shown in figures 7.21 and 7.22. In figure 7.23 the relationship between the peak temperature T_p and the scanning rate α is plotted (see equation 4.6) in order to calculate the activation energy E and the constant ν . The data for both glasses show good agreement with linear behaviour. The calculated activation energy is reported in table 7.1, and is similar to that obtained from isothermal data. However, the constant ν differs strongly from that observed in isothermal experiments, indicating that it is influenced by the thermal history and/or the measurement method.

In figures 7.24 and 7.25, equation 4.7 is plotted for different scanning rates in order to determine the exponent n . It is seen that the slopes of the data sets vary with the scanning rate, possibly due to differences in crystal formation. Moreover, the

average value of n , listed in table 7.1, is significantly different from that obtained in isothermal experiments, also implying that crystal growth morphology may be affected by temperature scanning.

Table 7.1. Crystal growth parameters (average values) of tellurite glasses obtained by isothermal and non-isothermal methods.

	Isothermal method					Non-isothermal method		
	n ± 0.02	Equation 4.4		Equation 4.5		n ± 0.05	$\ln(\nu)$ s^{-1} ± 4	E kJ/mol ± 5
		\ln s^{-1} ± 2	(ν) kJ/mol ± 4	$\ln(\nu)$ s^{-1} ± 2	E kJ/mol ± 4			
TN	1.84	28	194	28	188	2.59	50	208
TNZ	1.65	31	183	26	175	3.45	50	195

7.2.2.3 Conclusions of crystallisation kinetics

From the analysis of crystallization kinetics in two tellurite glasses using isothermal and non-isothermal measurement methods, the devitrification process in both glasses was seen to conform to the JMA theory of crystal growth. TTT curves were calculated and compared in a binary and a ternary tellurite glasses, and it was shown that the binary glass has better stability than the ternary glass.

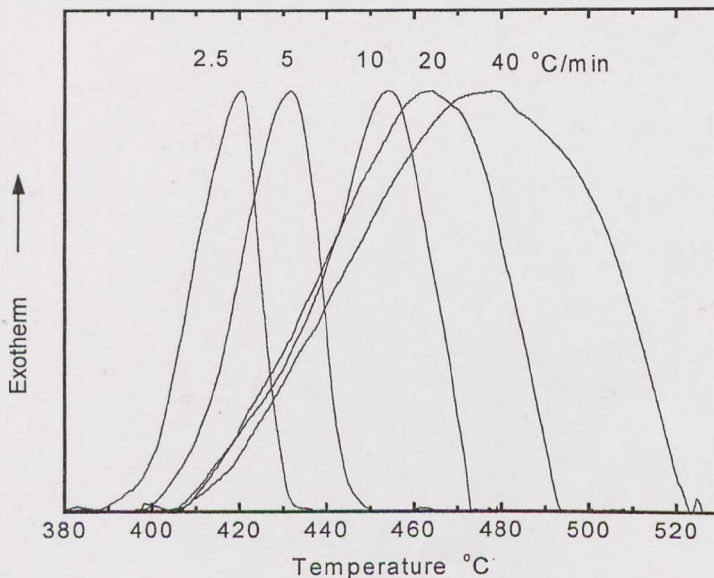


Fig. 7.21 DTA traces at various heating rates in TN glass

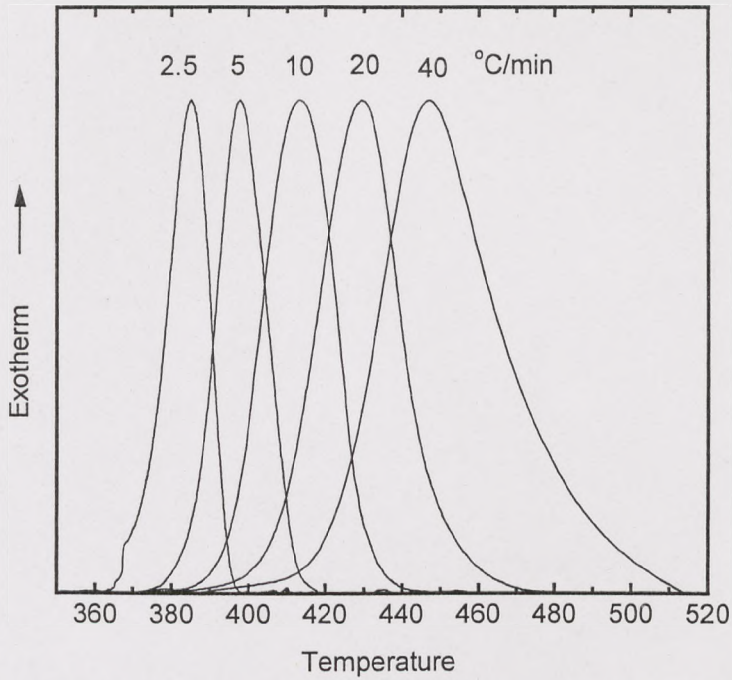


Fig. 7.22 DTA traces at various heating rates in TNZ glass

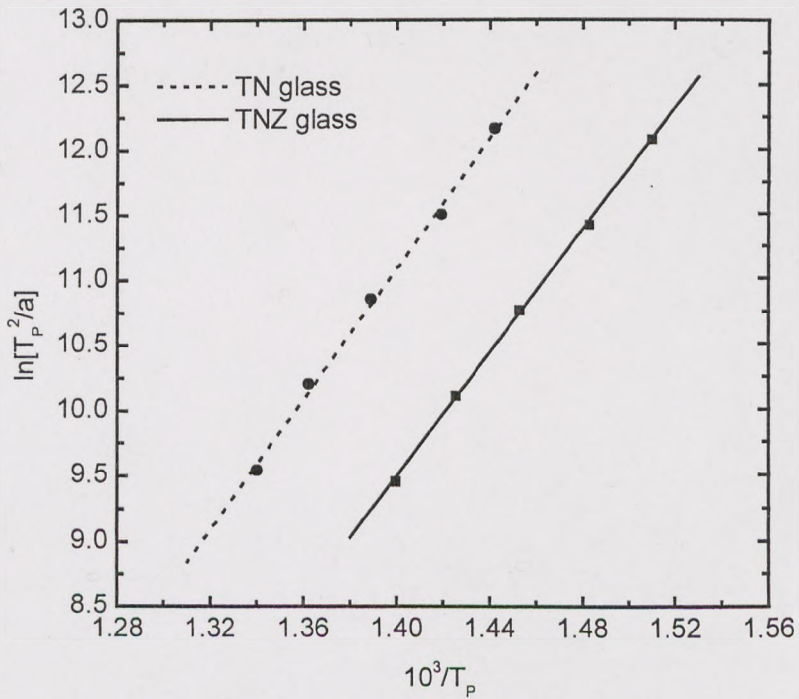


Fig. 7.23 $\ln T_p^2/a$ vs $1/T_p$ for non-isothermal crystallisation of tellurite glasses

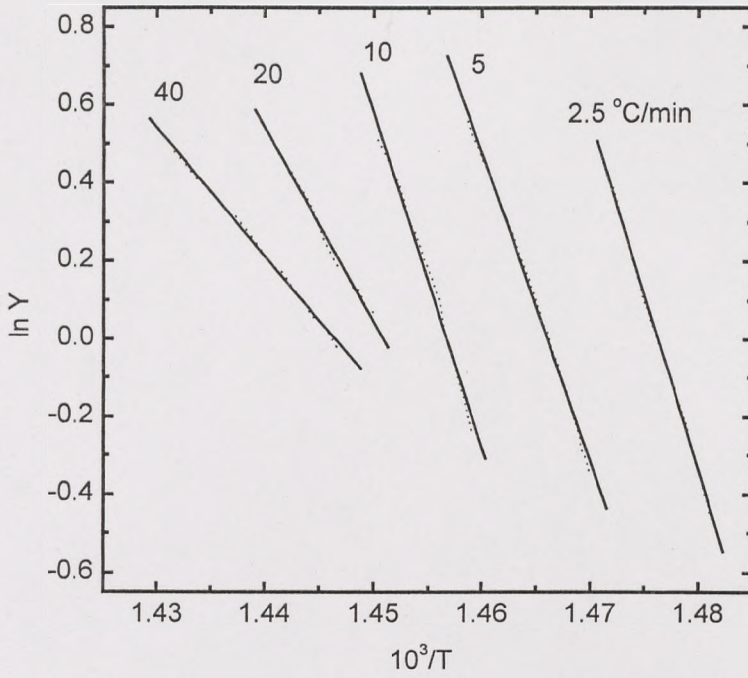


Fig. 7.24 Plots of Eq.4.7 at various heating rates in TN glass

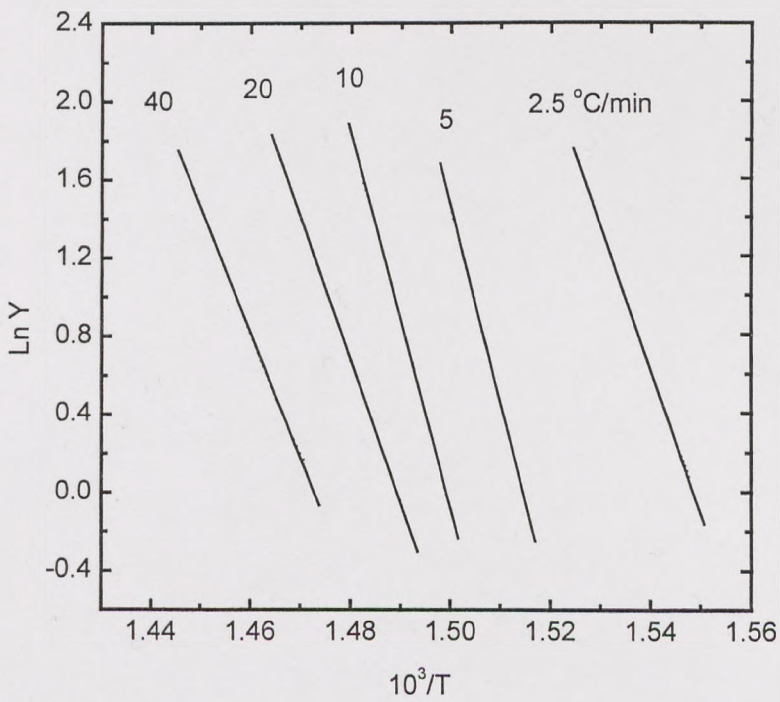


Fig. 7.25 Plots of Eq.4.7 at various heating rates in TNZ glass

7.3 Optical properties

In this part, we continue to study the ternary $\text{TeO}_2 - \text{R}_2\text{O} - \text{ZnO}$ ($\text{R}_2\text{O} = \text{Li}_2\text{O}, \text{Na}_2\text{O}$ and K_2O) glass system. For glass, the intrinsic loss as a function of wavelength λ is given by the following equation:

$$\alpha_t = A_0 \exp(A_1/\lambda) + B_0 (1/\lambda^4) + C_0 \exp(-C_1/\lambda) \quad 7.1$$

where A_0, A_1, B_0, C_0 and C_1 are material constants. The first and third terms describe the losses due to ultraviolet absorption from the electronic band edge and infrared edge losses arising from multiphonon absorption respectively. The second term indicates the loss due to light scattering from microscopic density and composition fluctuations in the material, which is called Rayleigh scattering. These effects decrease rapidly with increasing wavelength. The UV and IR absorption spectra of these ternary tellurite glasses were obtained using Perkin-Elmer UV/VIS/NIR Lambda 19 and FTIR Spectrophotometer 1725x, respectively.

7.3.1 Absorption in the UV

As described in chapter 5, the UV edge absorption, which limits transparency at shorter wavelengths, is caused by transitions between the electronic states. This absorption is a function of the energy band gap of the materials and the incident photon energy which was shown in the equation 5.2. Figure 7.26 shows the UV edge absorption spectra of $(90-x)\text{TeO}_2 - x\text{Na}_2\text{O} - 10\text{ZnO}$ ($x = 0, 10, 20, 30$) glass. These absorption spectra can be fitted reasonably well by Equation 5.3. From this figure, the UV cut-off shifts to the shorter wavelength with the increase of Na_2O ($x = 0 \rightarrow x = 30$) in this glass.

For the ternary $(90-x)\text{TeO}_2 - x\text{R}_2\text{O} - 10\text{ZnO}$ ($\text{R}_2\text{O} = \text{Li}_2\text{O}, \text{Na}_2\text{O}$ and K_2O) and $(90-x)\text{TeO}_2 - 10\text{Na}_2\text{O} - x\text{ZnO}$ glass systems, the UV cut off wavelengths were calculated in the same way which was explained in chapter 5. Figures 7.27 and 7.28 illustrate these results when the concentrations of R_2O and ZnO change. From these two figures, the UV cut-off wavelength of these glasses decreases as the concentration of alkali oxides and ZnO increases. The trend of shifting to the shorter wavelength

after the addition of R_2O and ZnO is due to the presence of lone pair electron (LPE) in tellurite glass structure. As the LPE sites in the structure are shared by Li^+ , Na^+ , K^+ and Zn^{2+} , the conductivity of the glass decreases, the electronic edge then shift to shorter wavelengths. For the $R_2O = Li_2O$, Na_2O and K_2O , the UV cut-off edge is the shortest value for Li_2O , and K_2O has the longest edge, the edge for containing Na_2O glasses fall in between Li_2O and K_2O . The reason is that the Li^+ ion has the strongest field strength and the smallest size among alkali ions. Glass containing Li_2O is the least ionic, it results in the largest band gap in tellurite glass so that it shifts the UV cut-off to the lowest wavelength.

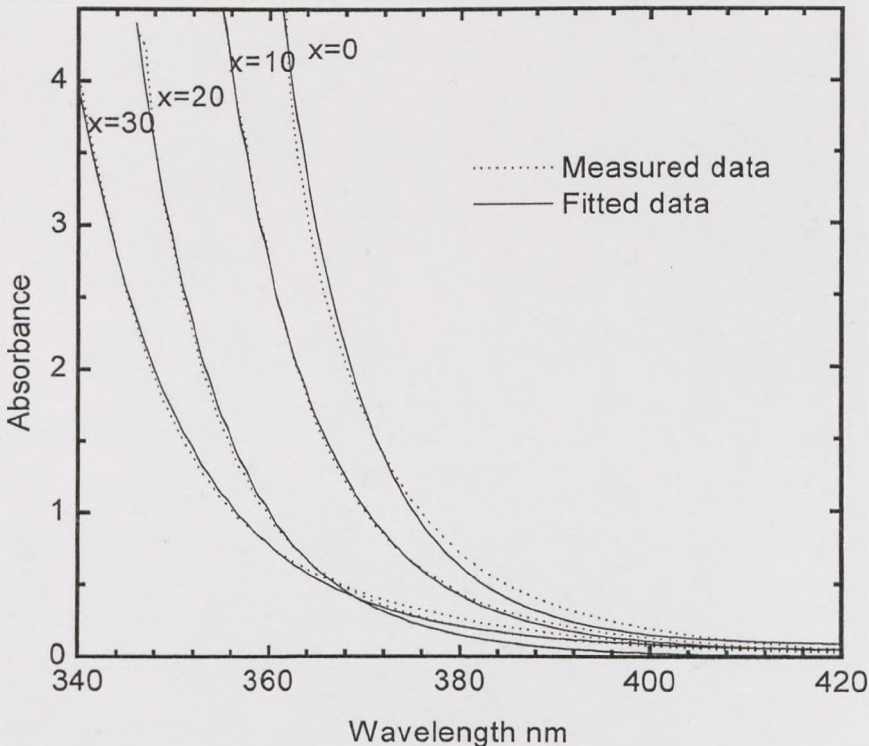


Fig. 7.26 UV edge absorption in $(90-x)TeO-10ZnO-xNaO$ ($x=0, 10, 20$ and 30) tellurite glass

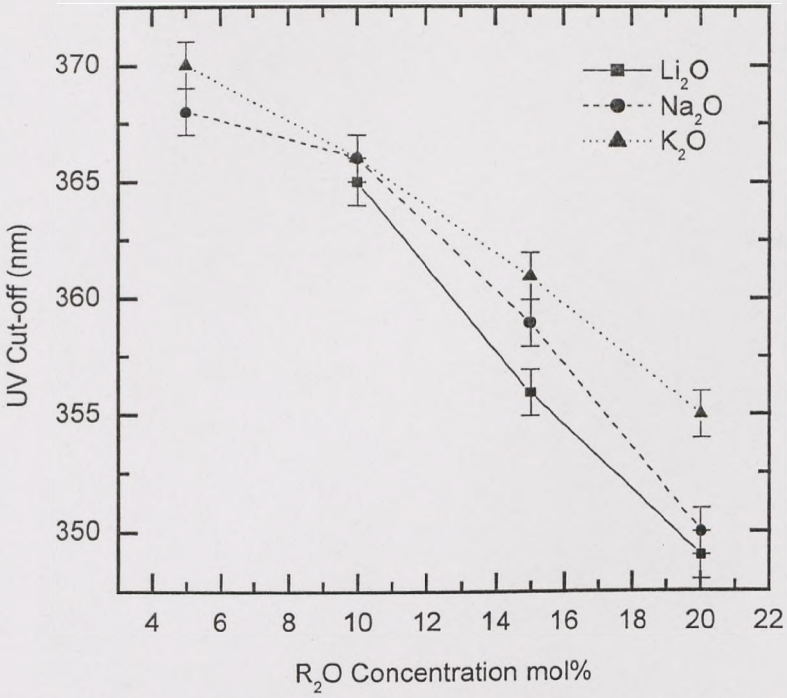


Fig. 7.27 UV cut-off change with alkali oxide in $(90-x)\text{TeO}-10\text{ZnO}-x\text{R}_2\text{O}$ ($\text{R}_2\text{O} = \text{Li}_2\text{O}, \text{Na}_2\text{O}, \text{and } \text{K}_2\text{O}, x = 0, 10, 20 \text{ and } 30$) glass

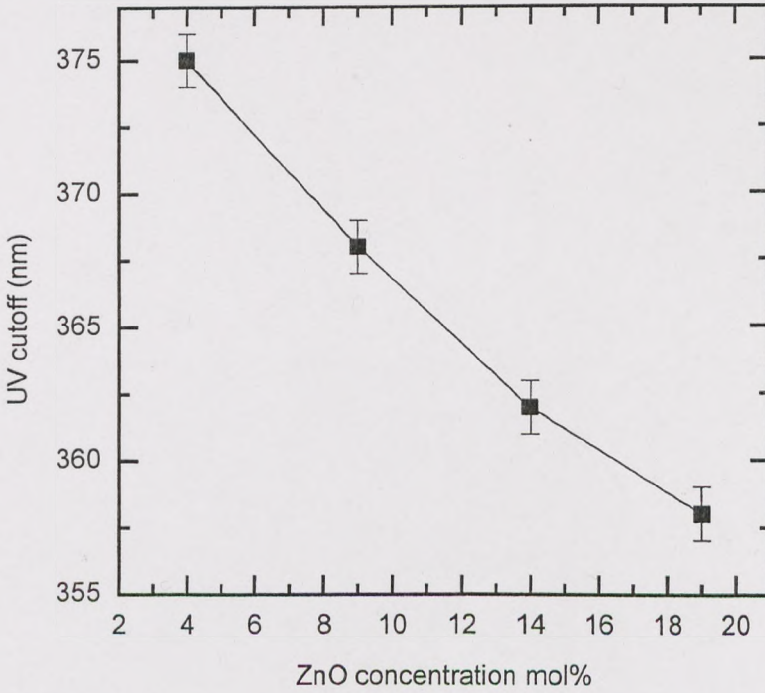


Fig. 7.28 UV cut-off change with ZnO in $(89-x)\text{TeO}-x\text{ZnO}-10\text{Na}_2\text{O}-1\text{Er}_2\text{O}_3$ ($x = 4, 9, 14, \text{ and } 19$) glass

7.3.2 Absorption in the IR

As described in chapter 5, the position of the multiphonon edge is related to the fundamental absorption. Each material has a number of characteristic lattice vibration frequencies, related to particular structural units. For most oxide glasses the multiphonon edge (IR cut-off) lies in the range of $2200\text{-}1500\text{ cm}^{-1}$ ($4500\text{ - }6500\text{ nm}$). Clearly the edge will be determined by the glass composition. To increase the IR cut-off (longer wavelength), heavier ions and weaker bond are required, because they lower the lattice vibration frequencies. In this section, IR edge cut-off wavelength is also calculated in the same way which was explained in chapter 5.

Figure 7.29 shows the IR edge absorption spectra of $(90-x)\text{TeO}_2 - x\text{Na}_2\text{O} - 10\text{ZnO}$ ($x = 0, 10, 20, 30$) glass. As x increases, the IR edges shift to higher wavenumber or shorter wavelength, this is because the light metal oxide Na_2O replaced the heavy metal oxide TeO_2 .

For the ternary $(90-x)\text{TeO}_2 - x\text{R}_2\text{O} - 10\text{ZnO}$ ($\text{R}_2\text{O} = \text{Li}_2\text{O}, \text{Na}_2\text{O}$ and K_2O) and $(90-x)\text{TeO}_2 - 10\text{Na}_2\text{O} - x\text{ZnO}$ glass systems, Figures 7.30 and 7.31 illustrate the IR cut off wavenumber shift when the concentrations of R_2O and ZnO change respectively. With the increase of R_2O and ZnO , the IR cut-off wavenumber increases, it means the IR cut-off wavelength becomes shorter. The reason is the same as given above.

For the $\text{R}_2\text{O} = \text{Li}_2\text{O}, \text{Na}_2\text{O}$ and K_2O , the IR cut-off edge is the largest value in wavenumber for Li_2O , and K_2O has the smallest value, the edge for containing Na_2O glasses fall in between Li_2O and K_2O . The reason is that Li^+ is the smallest ion and Li-O bond is the strongest among Li^+, Na^+ and K^+ , thus, these result in higher IR cut-off frequency or shorter wavelength from Equation 5.1.

7.3.3 The intrinsic loss in tellurite glass

Losses in tellurite glass fibres were estimated by fitting the loss equation to the visible and infrared absorption spectra measured in bulk glass. The V-curve of intrinsic loss in glass (α) is generated by adding the contributions of ultraviolet and infrared absorption and Rayleigh scattering from Equation 7.1. Figure 7.32a shows

the measured ultraviolet absorption edge together with a fit to α_{UV} . It is seen that the fit is very good. Figure 7.32b similarly plots the infrared absorption edge, the fit is fair over a narrower range than in Figure 7.32a. Figure 7.32c shows the complete V-curve of intrinsic absorption, calculated from the fitting parameters obtained from figure 7.32a and 32b. The Rayleigh scattering coefficient R was taken from Wang et al [4], since a similar glass composition was investigated by those authors. The loss parameters are listed in table 7.2. It is seen that the UV absorption coefficient and wavelength are somewhat different from those quoted by Wang et al [4] for a somewhat different glass composition. It has been observed that in tellurite glasses the UV absorption edge is strongly dependent on the glass composition in the previous part, which may be responsible for this discrepancy. Nevertheless, the minimum loss value and wavelength are only slightly affected by the difference in UV absorption. The projected minimum loss is 5×10^{-3} dB/km at $2.83 \mu\text{m}$. In the context of the Er^{3+} -doped amplifier, losses at $1.5 \mu\text{m}$ (signal) and $0.98 \mu\text{m}$ (pump) are respectively 0.06 dB/km and 0.4 dB/km.

Table 7.2 Intrinsic loss parameters in $80\text{TeO}_2 - 10\text{Na}_2\text{O} - 10\text{ZnO}$ tellurite glass

Parameter	
Ultraviolet absorption	$A_0 = (3.0 \pm 0.2) \times 10^{-10}$ dB/km; $A_1 = 13.0 \pm 0.3 \mu\text{m}$
Raleigh Scattering	$B_0 = 0.29$ dB/km [4]
Infrared absorption	$C_0 = (2.3 \pm 0.2) \times 10^{15}$ dB/km; $C_1 = 122 \pm 4 \mu\text{m}$
Minimum loss	$(5.0 \pm 0.2) \times 10^{-3}$ dB/km
Minimum loss wavelength	$2.8 \pm 0.1 \mu\text{m}$
Loss at $1.5 \mu\text{m}$	~ 0.06 dB/km
Loss at $0.8 \mu\text{m}$	~ 0.4 dB/km

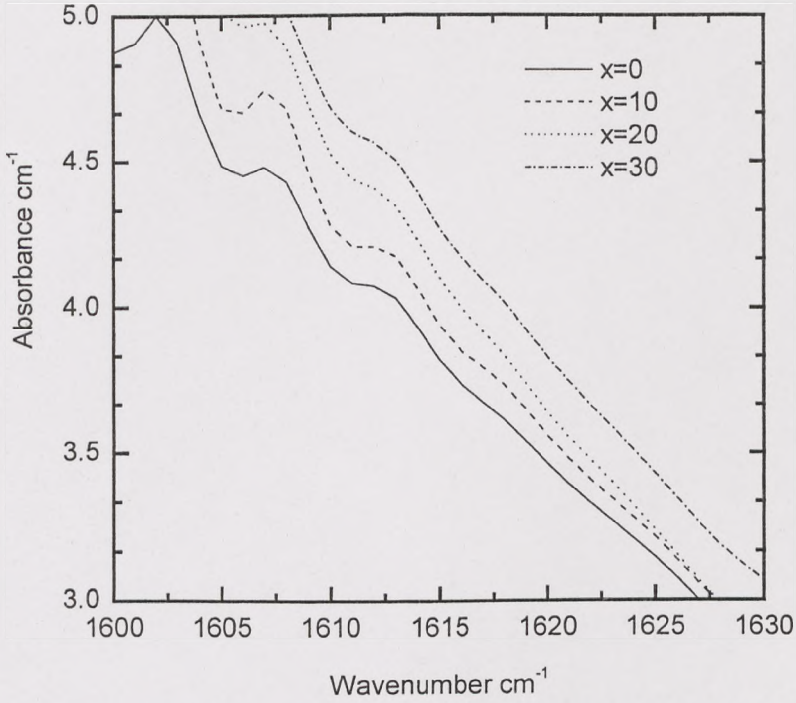


Fig. 7-29 IR edge absorption in $(90-x)\text{TeO}-10\text{ZnO}-x\text{Na}_2\text{O}$ ($x=0, 10, 20$ and 30) tellurite glass

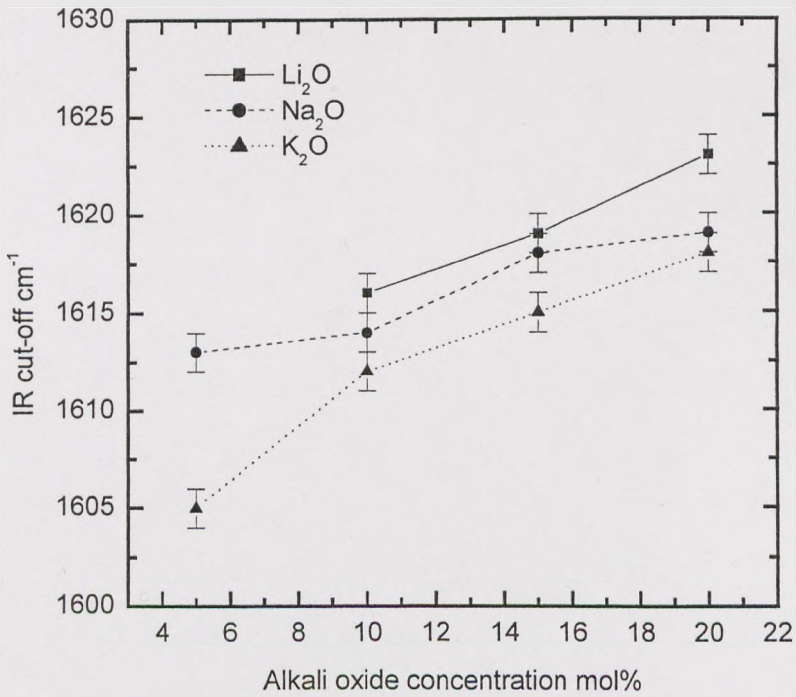


Fig. 7.30 IR cut-off change with alkali oxide in $(90-x)\text{TeO}-10\text{ZnO}-x\text{R}_2\text{O}$ ($\text{R}_2\text{O} = \text{Li}_2\text{O}, \text{Na}_2\text{O},$ and $\text{K}_2\text{O}, x = 0, 10, 20$ and 30) glass in tellurite glass

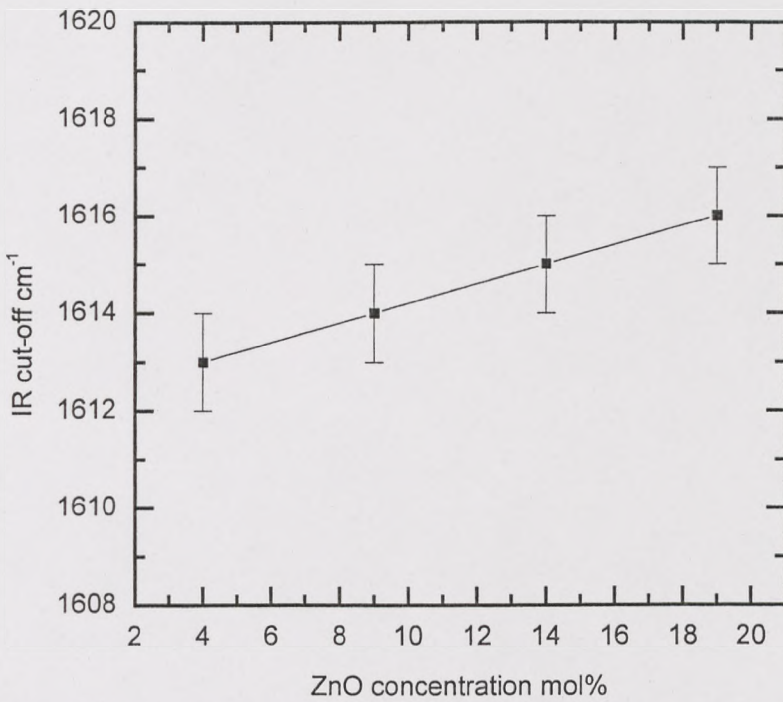


Fig. 7.31 IR cut-off change with ZnO content in $(89-x)\text{TeO}-x\text{ZnO}-10\text{Na}_2\text{O}-\text{E}_2\text{rO}_3$ ($x = 4, 9, 14$ and 19) tellurite glass

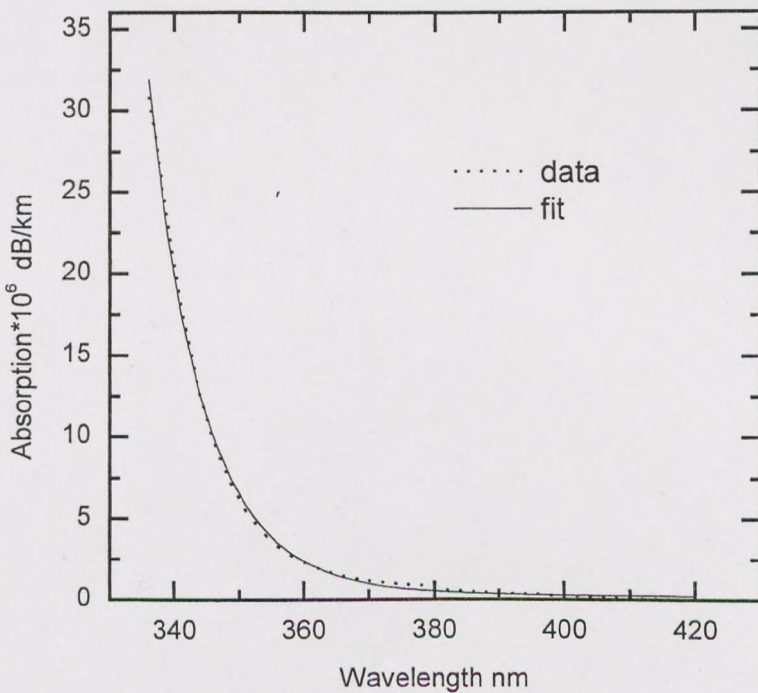


Fig. 7.32a UV edge fitting in TNZ glass

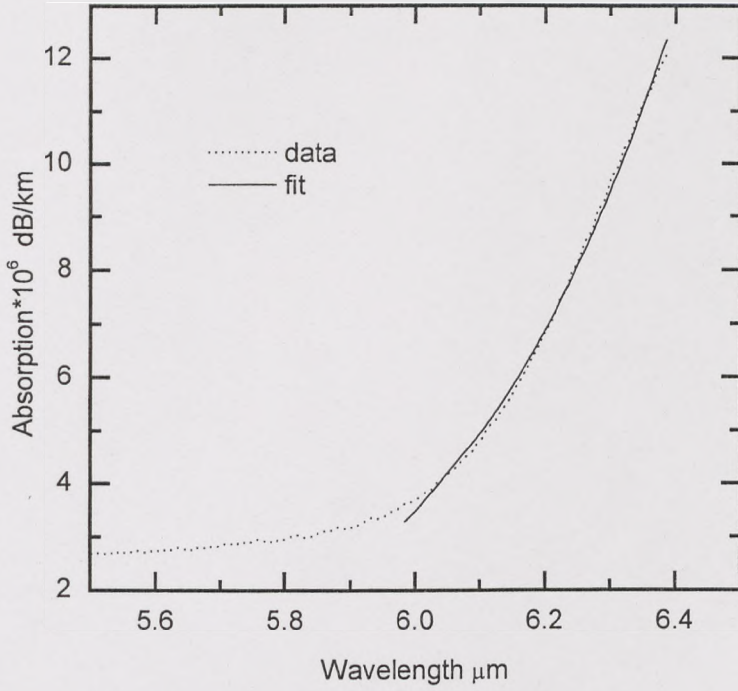


Fig. 7.32b IR edge fitting of TNZ glass

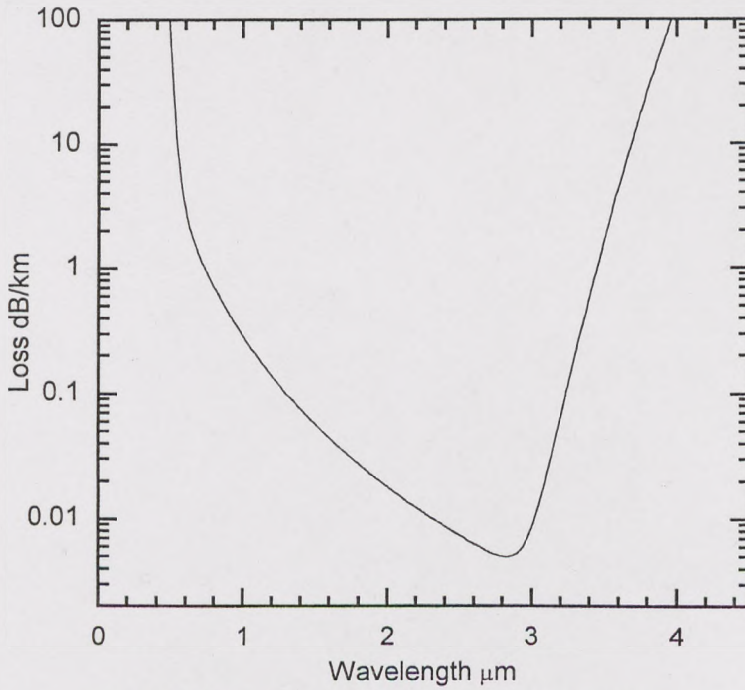


Fig 7.32c V-curve of loss in tellurite glass

7.4 Raman spectra of tellurite glass

7.4.1 Introduction to Raman spectroscopy

As pointed out in chapter 4, Raman spectroscopy uses photons to probe vibrational modes of matter. The excitation of vibrational modes is manifested by a frequency-shifted spectrum of scattered light from the material. The spectral characteristics depend on the types (symmetry) of vibrations and their coupling coefficients with the electromagnetic wave. It is sensitive to local structure, and is therefore especially useful for detecting, identifying, monitoring and analysing spatial variations as well as temporal changes in chemical composition and structure in glass. Glass spectra are best understood in the context of vibrational properties of molecules, crystals and disordered solids.

Since a crystal is composed of a very large number of atoms, it could, in principle, possess a continuum of vibrational modes of variable frequencies and wavelengths. However, because the atoms are arranged in a perfectly periodic array, only wavelengths corresponding to motions within individual cells of crystal are allowed. Actually, the vibrational spectrum consists of several types of modes, $3N-3$ to be exact, where N is the number of atoms in a unit cell. Each mode spans a range of frequencies as a function of continuous wavenumber \mathbf{k} .

Since the wavenumber of light is very small, light only couples directly to optical phonons near $\mathbf{k} = 0$. This restriction is sometimes expressed as conservation of energy and momentum between photons and phonons. In the crystalline case, the vibrational frequencies span a continuum of values; however, since light only couples to optical modes near $\mathbf{k} = 0$, the spectrum consists of discrete lines. That is the reason that the Raman spectral lines are sharp in crystals.

Glass has a short-range order and an absence of a long-range order. The difference between glass and crystalline materials essentially lies in the fact that periodicity cannot be used to simplify the dynamics. For a “totally” disordered amorphous material, the species of atoms in the material and their locations are totally uncorrelated. Such a material would possess a continuum of vibrations, corresponding to the virtually unlimited number of arrangements of its atoms, moreover, since the

atoms are randomly arranged, there are no universal selection rules governing the coupling the light to materials. The Raman spectrum becomes continuous and proportional to the density of modes at each frequency for this hypothetical solid.

In reality, amorphous materials like glass are not “totally” disordered, but possess some form of short-range order. They often display a mix of properties, some representative of short-range order, e.g., isolated structural units or molecules in molecular crystals, and others of long-range order, similar to crystalline materials. Therefore, vibrational properties in glass are often attributable, at least in part, to the existence of individual, localised structural units, containing varying numbers, types and arrangements of atoms. Within the units, structural parameters such as bond lengths and strengths may vary randomly, although the average macroscopic properties are fixed. Therefore, the Raman spectra do not simply mimic the vibrational density of states as they would in a perfectly disordered system, rather, the spectrum will be dominated by features associated with each type of unit in the material. The statistically distributed structural parameters, plus the interactions between units, cause broadening of the symmetry-allowed spectral lines, and introduce additional spectral features due to previously “forbidden” vibrations. Thus the spectrum will consist of distinct spectral features characteristic of the individual units.

A related interaction of the spectral characteristics of glass considers how crystalline spectra change as the structure derives from the ideal crystal. In this picture, the vibrational modes are very nearly those of the crystal; the main difference in glass is the breakdown in the \mathbf{k} -selection rules, which allows photons to couple with vibrations other than $\mathbf{k} = 0$, i.e. The resulting spectrum is therefore a continuum rather than narrow line. Thus the Raman spectral lines in glass are much broader than those in crystals. However, the actual shape of the spectrum is determined by the coupling strength as a function of \mathbf{k} , which depends on the details of the structural disorder and therefore cannot be predicted in general. Therefore, the structural disorder in glass results in the multiplicity of vibrational modes and the broadening of the spectrum.

7.4.2 Raman spectrum results in tellurite glasses.

For Raman spectrum measurements, the glass samples were not doped with rare earth ions. Because in rare earth ion doped samples, the luminescence is so strong that it obscures the Raman signals.

Figure 7.33 shows the Raman spectrum of a pure TeO_2 powder sample, from which it is clear that the spectrum consists of sharp peaks due to the crystalline phase. There is one strong peak at 645 cm^{-1} , a medium strong peak at 392 cm^{-1} and four weak peaks at 338 , 589 , 718 and 765 cm^{-1} .

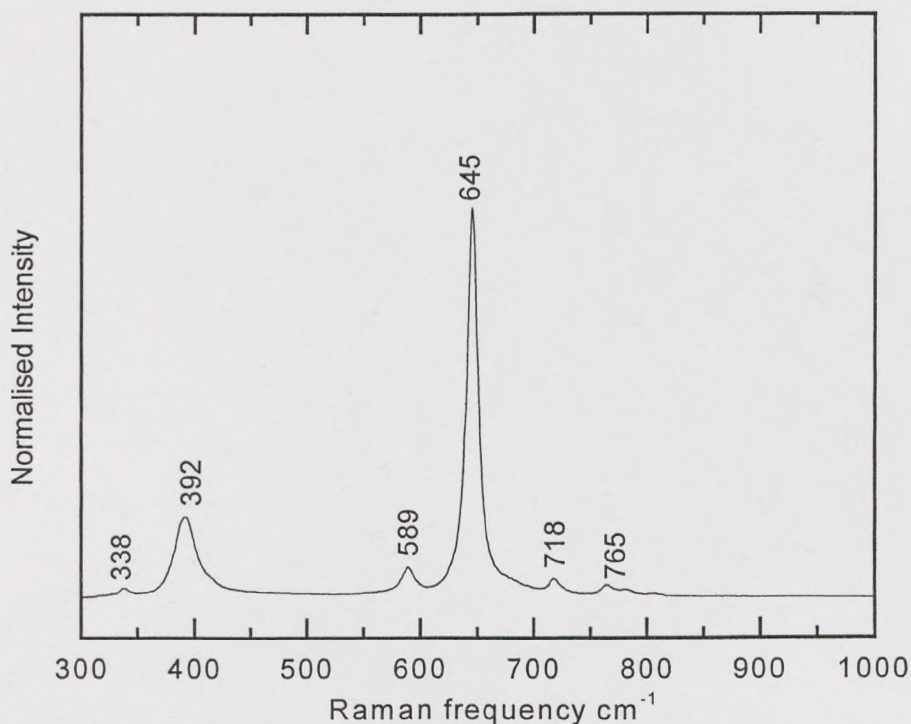


Fig. 7.33 Raman spectrum of TeO_2 crystal powder

For tellurite glass structure study, firstly, we measure the effect of concentration variation of glass former TeO_2 . In ternary $(90-x) \text{TeO}_2 - x\text{Na}_2\text{O} - 10\text{ZnO}$ ($x = 0, 10, 20$ and 30) glass system, Figure 7.34 and 7.35 show the Raman spectra from $10 - 200 \text{ cm}^{-1}$ and $300-1000 \text{ cm}^{-1}$ respectively. In figure 7.34, the peak around 40 cm^{-1} is called “Boson peak”. It is assigned to the low-frequency broad band in the Raman spectrum, this will be discussed later. With the increase of Na_2O and decrease of TeO_2 , the peak slightly shifts to a higher frequency from 38 to 42 cm^{-1} . The peak shape is very similar, a shoulder however appears around 90 cm^{-1} with the increasing percentage of Na_2O content. In figure 7.35, the intensities of peaks change with the variation of Na_2O . With the increase of Na_2O and decrease of TeO_2 , the intensities of peaks around 450 cm^{-1} and 660 cm^{-1} decrease, around 780 cm^{-1} increase.

Secondly, we determined the structural changes of TeO_2 glass with different oxide modifiers.

In ternary $70\text{TeO}_2-20\text{X}-10\text{ZnO}$ ($\text{X} = \text{ZnO}, \text{Li}_2\text{O}, \text{Na}_2\text{O}$ and K_2O) glass system, the effect of different alkali ions on the zinc tellurite glass structure has been determined. Figure 7.36 and 7.37 show the Raman polarised (HH and HV) spectra from $10 - 200 \text{ cm}^{-1}$ and $200-1000 \text{ cm}^{-1}$ respectively. Here HH means that the incident and scattered electric vectors are parallel, while HV indicates that they are perpendicular.

The depolarisation ratio is defined as $\rho = I_{\text{HV}}/I_{\text{HH}}$, where I_{HV} and I_{HH} are the intensities of the scattered radiation at ω from HV and HH spectra. The depolarisation ratio ρ is related to the symmetry of the vibrations. In figure 7.36 and 7.37, we can see there is a slight shift of the Boson peak and other main peaks even though the Raman spectra are very similar when glass contains Li_2O or $\text{Na}_2\text{O}, \text{K}_2\text{O}$. ρ is also changing. Table 7.3 shows the Boson peak frequency and depolarisation ratio ρ at three different optical phonon frequencies. The depolarisation ratio ρ in glass when x is ZnO is the highest for all the peaks, ρ is higher in Na_2O than that in Li_2O and K_2O . Another trend is that the ρ decreases as the frequency increases. The lower Raman frequency shift is, the higher is the depolarisation ratio in the glass.

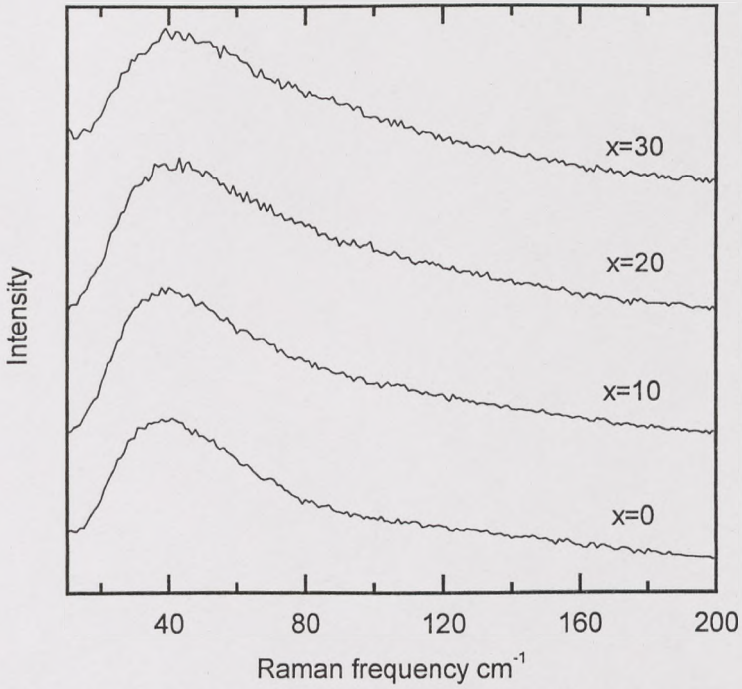


Fig. 7.34 Raman spectra in $10 - 200 \text{ cm}^{-1}$ range of $(90-x)\text{TeO}_2-x\text{Na}_2\text{O}-10\text{ZnO}$ ($x=0, 10, 20$ and 30) glass

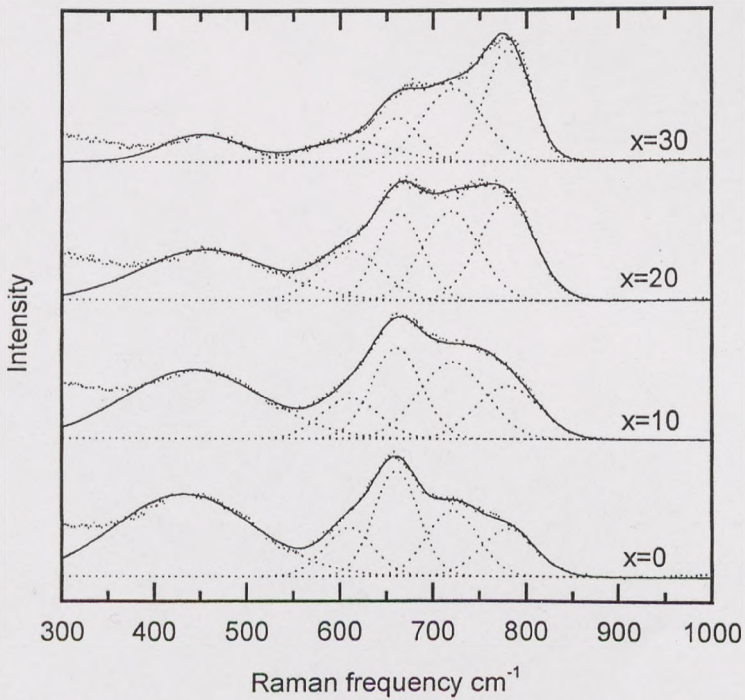


Fig. 7.35 Raman spectra in $300 - 1000 \text{ cm}^{-1}$ range of $(90-x)\text{TeO}_2-x\text{Na}_2\text{O}-10\text{ZnO}$ ($x=0, 10, 20$ and 30) glass

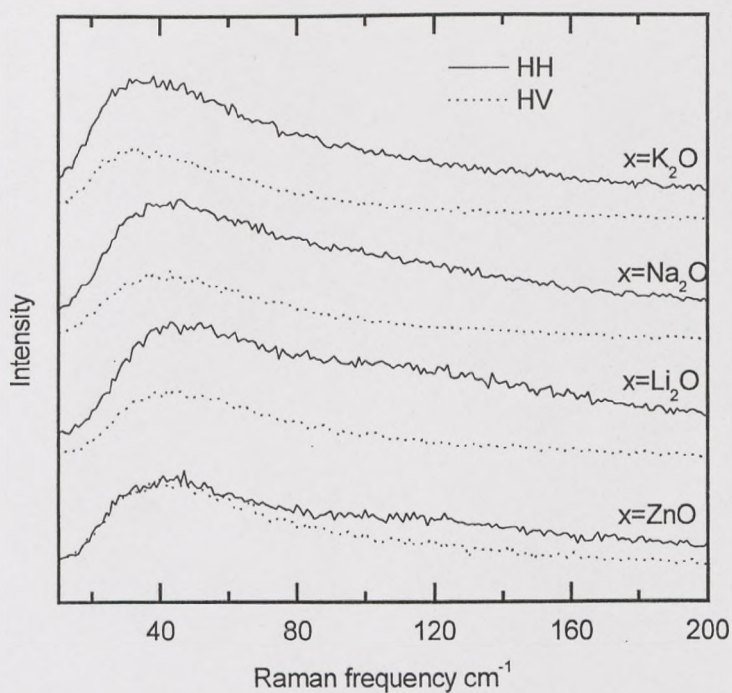


Fig. 7.36 Raman spectra in 10 - 200 cm^{-1} range of 70TeO_2 - 20X - 10ZnO ($\text{X}=\text{ZnO}$, Li_2O , Na_2O and K_2O) glass

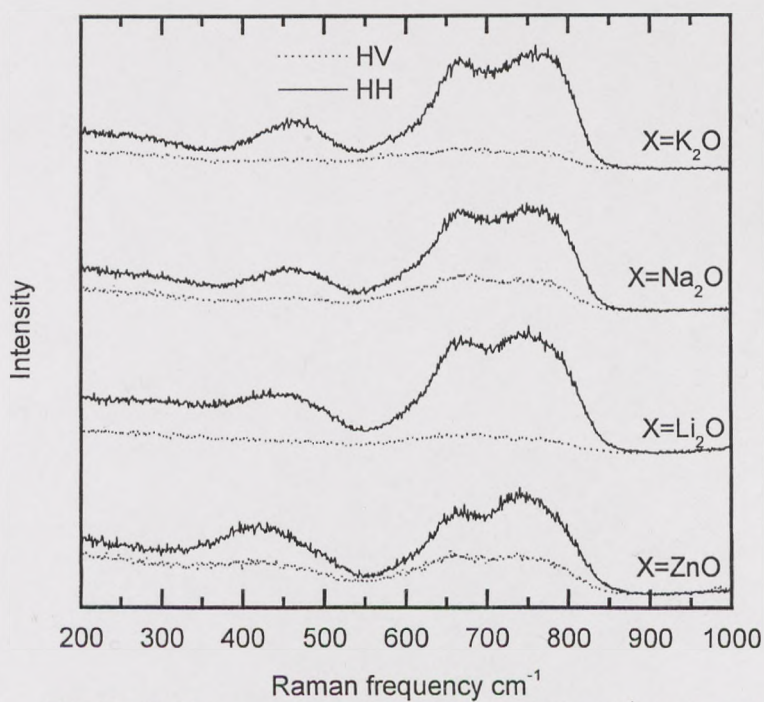


Fig. 7.37 Raman spectra in 200 - 1000 cm^{-1} range of 70TeO_2 - 20X - 10ZnO ($\text{X}=\text{ZnO}$, Li_2O , Na_2O and K_2O) glass

Table 7.3 peak frequency and depolarisation ratio ρ in 70TeO₂-20X-10ZnO (X = Li₂O, Na₂O, K₂O and ZnO) glass system

	ZnO	Li ₂ O	Na ₂ O	K ₂ O
Boson peak $\omega \pm 1 \text{ cm}^{-1}$	48	44	40	35
$\rho \pm 0.02$ at Boson peak	0.82	0.56	0.54	0.54
$\rho \pm 0.02$ at 455 cm^{-1}	0.48	0.23	0.37	0.26
$\rho \pm 0.02$ at 660 cm^{-1}	0.43	0.16	0.34	0.19
$\rho \pm 0.02$ at 780 cm^{-1}	0.35	0.11	0.28	0.15

For different cations with different valence, they behave as glass modifier, intermediater, and glass former in tellurite glass. In order to check the effect of different bond valences on the tellurite glass structure, Raman spectra of 80TeO₂-10Na₂O-10X (X = K₂O, BaO, Ga₂O₃, GeO₂, Nb₂O₅ and WO₃) glass were measured and shown in figure 7.38 and 7.39 for 10 – 200 cm^{-1} and 200-1000 cm^{-1} respectively. The cations varied from monovalent K⁺ to hexavalent W⁶⁺. From figure 7.38, the Boson peak shifts slightly around 40 cm^{-1} , the shape is very similar to each other. From figure 7.39, Raman spectra in middle and high frequency are different because different valence cations have different roles in the tellurite glass formation. K₂O and BaO are typical glass modifier. Ga₂O₃ is a glass network contributor, GeO₂ is a glass former, and Nb₂O₅ and WO₃ can also be glass former and network contributor respectively. The first four spectra are very similar, the difference is the shoulder around 760 cm^{-1} decreases. When the modifier oxides are Nb₂O₅ and WO₃, there is an extra peak between 850 to 950 cm^{-1} and another peak around 350 cm^{-1} for WO₃.

The third part of the present investigation on glass structure and its dependence on the composition is to check the effect of halides on tellurite glass. Binary and ternary tellurite glasses were melted and measured. For binary 80TeO₂-20X (X = Na₂O, NaCl and NaF) glass system, Raman spectra are shown in Figure 7.40 and 7.41 for 10 – 200 cm^{-1} and 200-1000 cm^{-1} region, respectively. In figure 7.40, there is a little shift around the Boson peak. When X is Na₂O, the peak is at 36 cm^{-1} , it is 38 cm^{-1} for NaCl and 40 cm^{-1} for NaF. In figure 7.41, Raman spectra between 550 cm^{-1} and 850 cm^{-1} are same for NaCl and NaF, but the sample of high frequency peak for Na₂O containing glass changes significantly at higher frequencies.

For ternary $80\text{TeO}_2\text{-}10\text{Na}_2\text{O-}10\text{X}$ ($\text{X} = \text{BaO}$, BaCl_2 and BaF_2) glass system, polarised Raman spectra are shown in Figure 7.42 and 7.43 for $10 - 200 \text{ cm}^{-1}$ and $200\text{-}1000 \text{ cm}^{-1}$ region, respectively. In figure 7.42, we can see the Boson peak shifts to slightly higher frequency following BaO , BaCl_2 and BaF_2 sequence and ρ is different. In figure 7.43, we also find the Raman spectra are nearly the same for BaCl_2 and BaF_2 containing TeO_2 glasses. When X is BaO , the high frequency peaks above 660 cm^{-1} have much higher intensities than when BaCl_2 and BaF_2 are incorporated in the glass. Table 7.4 shows the Boson peak frequency and depolarisation ratio ρ at the four main peaks.

From the table 7.4, the depolarisation ratio is much higher when TeO_2 glass contains BaF_2 . At the main peaks around 660 and 780 cm^{-1} , the depolarisation ratio ρ is $0.15 \sim 0.16$ when glasses contain BaO and BaCl_2 comparing with ρ is 0.38 for BaF_2 containing glass. At the Boson peak, BaF_2 containing glass ρ ($= 0.78$) is also much higher than BaO and BaCl_2 containing glasses (ρ is $0.45\sim 0.49$). The depolarisation ratio at Boson peak is much higher than at the main peaks around 660 and 780 cm^{-1} . It is also found that the ρ decreases as the frequency increases in all these Raman spectra.

Table 7.4 Boson peak frequency and depolarisation ratio ρ of ternary $80\text{TeO}_2\text{-}10\text{Na}_2\text{O-}10\text{X}$ ($\text{X} = \text{BaO}$, BaCl_2 and BaF_2) glass system

	BaO	BaCl ₂	BaF ₂
Boson peak $\omega \pm 1 \text{ cm}^{-1}$	38	42	44
$\rho \pm 0.02$ at Boson peak	0.45	0.49	0.78
$\rho \pm 0.02$ at 455 cm^{-1}	0.28	0.34	0.55
$\rho \pm 0.02$ at 660 cm^{-1}	0.16	0.15	0.38
$\rho \pm 0.02$ at 780 cm^{-1}	0.16	0.15	0.38

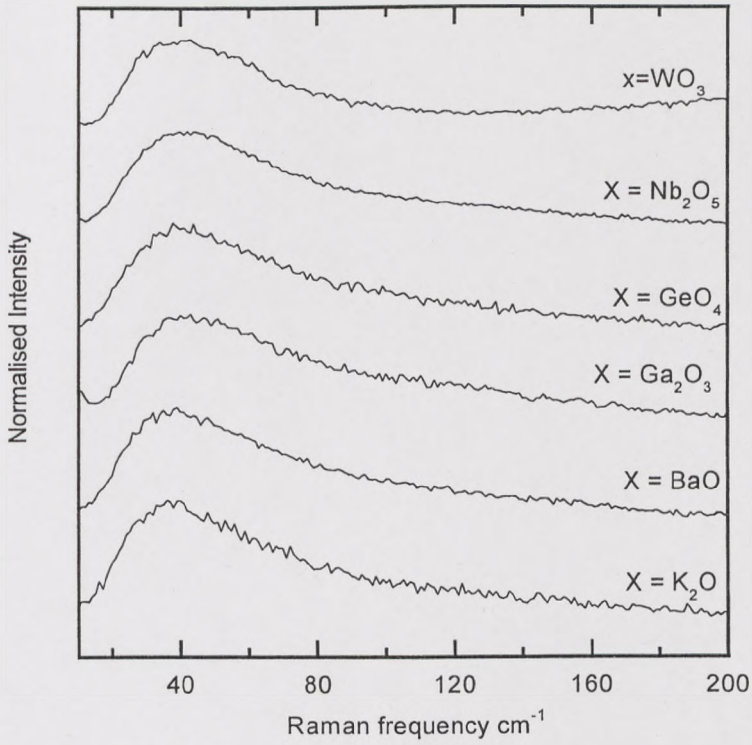


Fig. 7.38 Raman spectra in 10 - 200 cm⁻¹ range of 80TeO₂-10Na₂O -10X (X = K₂O, BaO, Ga₂O₃, GeO₂, Nb₂O₅ and WO₃) glass

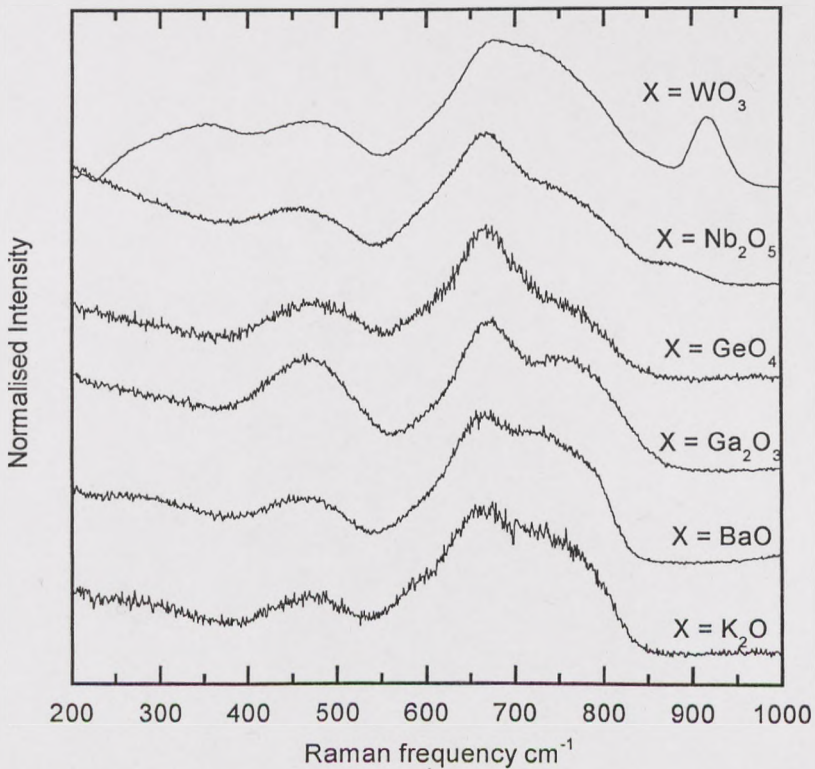


Fig. 7.39 Raman spectra in 200 - 1000 cm⁻¹ range of 80TeO₂ -10Na₂O-10X (X = K₂O, BaO, Ga₂O₃, GeO₂, Nb₂O₅ and WO₃) glass

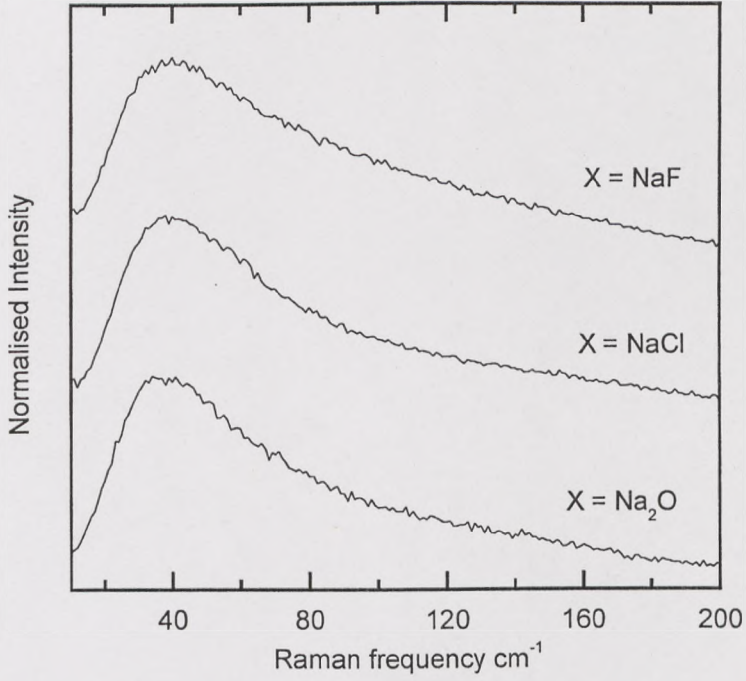


Fig. 7.40 Raman spectra in 10 - 200 cm⁻¹ range of 80TeO₂-20X (X = Na₂O, NaCl and NaF) glass

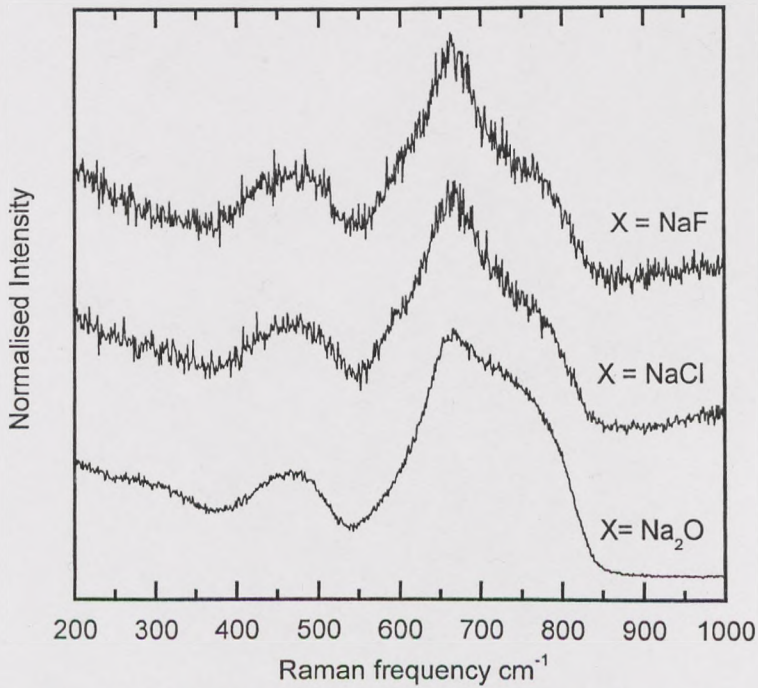


Fig. 7.41 Raman spectra in 200 - 1000 cm⁻¹ range of 80TeO₂-20X (X = Na₂O, NaCl and NaF) glass

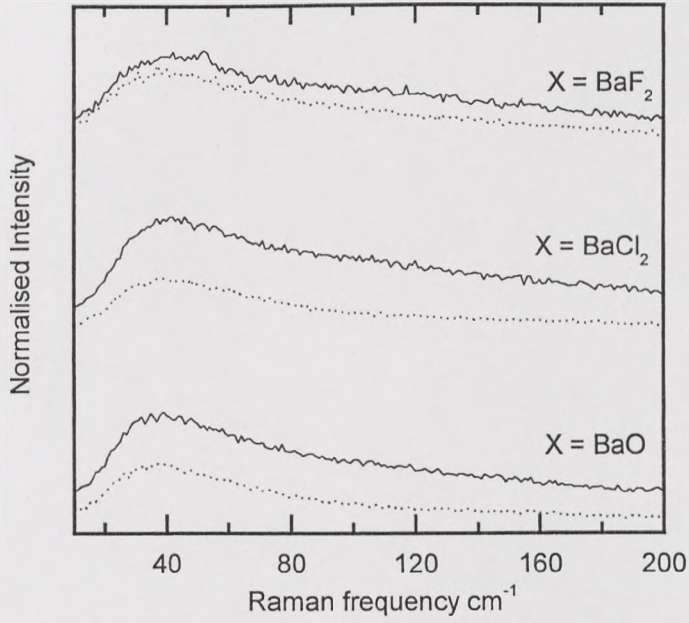


Fig.7.42 Raman spectra in 10 - 200 cm⁻¹ range of 80TeO₂-10Na₂O-10X (X = BaO, BaCl₂ and BaF₂) glass

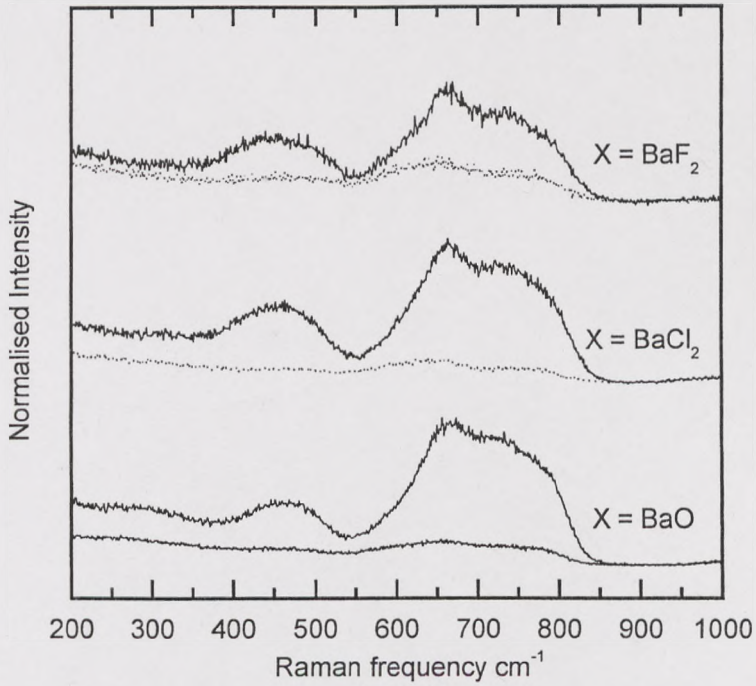


Fig. 7.43 Raman spectra in 200 - 1000 cm⁻¹ range of 80TeO₂-10Na₂O-10X (X = BaO, BaCl₂ and BaF₂) glass

7.4.3 Discussion of Raman Spectra

In Raman spectrum of glass, low frequency ($<300\text{ cm}^{-1}$) scattering is attributed to the collective modes of local structures and heavy metal vibrational modes [5, 6]. Raman scattering in the intermediate region ($300\text{-}580\text{ cm}^{-1}$) has generally been attributed to the deformation vibrational modes of glass network structure with bridged oxygen [7-10]. In the frequency region ($>600\text{ cm}^{-1}$) it has generally been attributed to the stretching vibrational modes of glass network former [7-10]. These spectra in tellurite glass can be divided into two regions. The first range is low frequency from $10\text{-}200\text{ cm}^{-1}$ in which there is a peak around 40 cm^{-1} regarded as the Boson peak. The second range is from $200\text{-}1000\text{ cm}^{-1}$ in which peaks reflect the glass structure units and vibrational modes.

7.4.3.1 Intermediate and high frequency range ($200\text{-}1000\text{ cm}^{-1}$)

The structure of TeO_2 may be described in terms of a three-dimensional network built up from TeO_4 units, each oxygen atom being shared by two units, and bonded in the equatorial position to one tellurium atom in the axial position to another. The basic unit TeO_4 of the structure is built up from four oxygen atoms coordinated to one tellurite atom to form a trigonal bipyramid (tbp) with one of the equatorial positions unoccupied. Because Te has 6 electrons in the outer shell, there is a lone-pair electron (LPE) occupying the equatorial position. In this structure unit, there are 4 bridging oxygens (BO). Because an LPE is equivalent to an oxide (O^{2-}) ion, the site for an oxide ion and an LPE could therefore interchange mutually, it actually affects the 4 Te-O bonds. Along the equatorial triangle plane of tbps, the perihelion Te-O bonds are shorter in length (0.185 nm) than that of aphelion Te-O bonds (the length is 0.195 nm), the axial Te-O bond lengths are the largest and vary between 0.205 and 0.215 nm [11, 12].

Another structure unit in tellurite glass is TeO_3 . It forms a trigonal pyramid (tp). In this structure unit, there are two bridging oxygens and one non-bridging oxygen (NBO) which is a double bond $\text{Te}=\text{O}$. These two structure units are shown in figure 7.44.

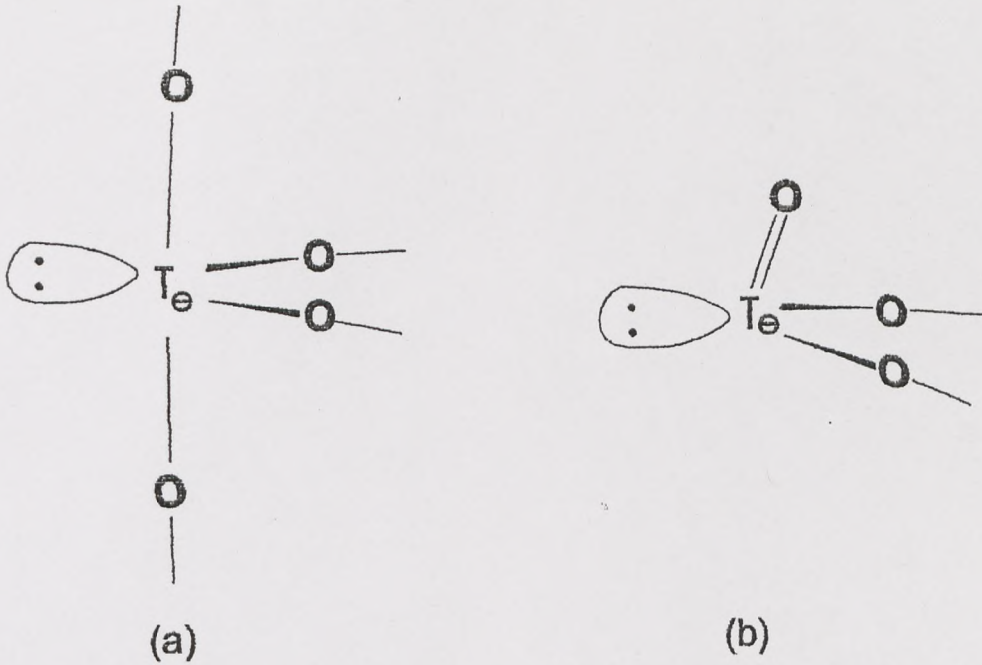


Fig. 7.44 Structure units in tellurite glass
 (a) TeO₄ trigonal bipyramid (tbp)
 (b) TeO₃ trigonal pyramid (tp)

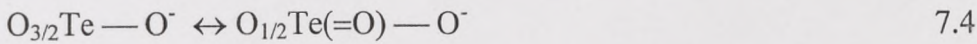
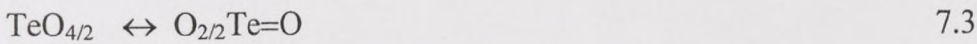
From Raman spectrum of pure TeO₂ crystal powder, figure 7.33, all these peaks correspond to the vibrations of structure unit TeO₄ tbp in crystal. Based on the normal vibrational analysis of TeO₂ crystal, peaks at 765, 718, 645, 589 and 392 cm⁻¹ are assigned to ν_{s2} TeO₄ (and ν_{s2+as} TeO₄), ν_{s1+as} TeO₄, ν_{s1} TeO₄, ν_{as} TeO₄ and δ_{s1} TeO₄ (and δ_{s2} TeO₄), respectively, and that the former four and the other are assigned to ν_{as} Te-eqO_{ax}-Te and ν_s Te-eqO_{ax}-Te, respectively [13]. It was indicated that, in TeO₂ crystal, most of tellurium atoms form TeO₄ tbp's, which are connected at vertices by forming Te-eqO_{ax}-Te linkages [13].

The Raman spectrum of glassy TeO₂ have been reported by Sekiya et al [11] and Pine and Dresselhus [14]. Three sharp peaks at 395, 592 and 649 cm⁻¹ are also observed and assigned the vibrations of TeO₄ trigonal bipyramid and movements of bridging oxygen atoms in Te-eqO_{ax}-Te linkages. Comparing with crystal TeO₂, Raman frequencies in glassy state shift to higher frequencies.

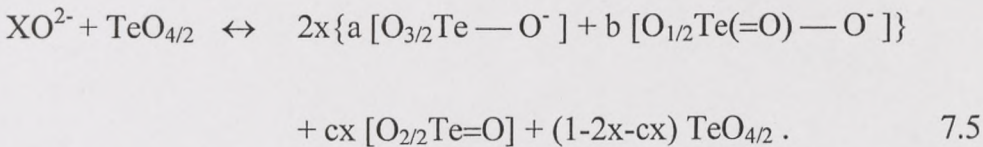
When a network modifying oxide is incorporated into the TeO_2 to form glass, there are two types of structural changes based on non-bridging oxygen model. The first model is similar to that for silicate glass as shown in equation 7.2:



The second model is more complex, it considers the structure units transfer between tbp and tp . They are expressed in equation 7.3 and 7.4, it shows that the transition produces one more non-bridge oxygen between $[\text{TeO}_4]$ and $[\text{TeO}_3]$.



Based on these units change, when a network modifying oxide is incorporated into the TeO_2 to form glass, the vitrification reaction in model 2 can be represented as equation 7.5. Here a , b and c are parameter less than unity and $a + b = 1$.



From Himei's study [15], structure change of tellurite glass is more likely in model 2 when network modifying oxide is incorporated into the TeO_2 glass structure. It produces $[\text{TeO}_4]^-$, $[\text{TeO}_3]^-$ and $[\text{TeO}_3]$. This means there are many different structure units in tellurite glass. In these structure units, $\text{Te}=\text{O}$ and $\text{Te}-\text{O}^-$ are assigned as non-bridging in glass.

In order to analyse their shape change, the Raman spectra were deconvoluted into Gaussian functions in the wavenumber range from 350 to 1000 cm^{-1} on the basis of the method proposed by Mysen et al [16]. Figure 7.35 also indicates the result of peak deconvoluted of the spectra of all these samples. Based on the Raman spectrum of pure TeO_2 , all the spectra in these ternary glasses were deconvoluted in the same way into five peaks about 455, 610, 660, 720 and 780 cm^{-1} [15]. These peaks are named A, B, C, D and E, respectively. The peak A observed at about 450 cm^{-1} is assigned to symmetric stretching (and bending) vibrations of $\text{Te}-\text{e}_q\text{O}_{ax}-\text{Te}$ linkages which are

formed by sharing vertices of TeO_4 tbp, $\text{TeO}_{3+\delta}$ polyhedra and TeO_3 tp. Peak B observed at about 610 cm^{-1} is assigned to a vibration of the continuous network composed of TeO_4 tbp. Peak C observed around about 660 cm^{-1} is assigned to antisymmetric vibrations of $\text{Te}_{\text{IV-eq}}\text{O}_{\text{ax}}\text{-Te}_{\text{IV}}$, $\text{Te}_{\text{IV-eq}}\text{O -Te}_{\text{III}}$, $\text{Te}_{\text{IV-O-Te}_{\text{III}+\delta}}$, $\text{Te}_{\text{III}+\delta}\text{-O-Te}_{\text{III}+\delta}$ and $\text{Te}_{\text{III}+\delta}\text{-O-Te}_{\text{III}}$ linkages. These linkages are characterized by the connection of a long and a short Te-O bonds. It is the main peak related with TeO_4 tbp. Peak D observed at about 720 cm^{-1} is assigned to the stretching vibration between tellurium and non-bridging oxygen (NBO) atoms. The NBO atom is formed in $\text{TeO}_{3+\delta}$ polyhedra or TeO_3 tp and interacts weakly with adjacent tellurium atoms, where the symbol, NBO, represents the oxygen atoms forming Te=O and Te-O^- , and their resonating bonds. Peak E observed at about 780 cm^{-1} is assigned as a vibration of the continuous network composed of TeO_4 tbp and a Te-O^- stretching vibration of $\text{TeO}_{3+\delta}$ polyhedra or TeO_3 tp. The two peaks D and E are related to TeO_3 tp.

The intensity ratios of the Raman peaks $I(720)/I(660)$ ($I_{\text{D}}/I_{\text{C}}$) and $I(780)/I(660)$ ($I_{\text{E}}/I_{\text{C}}$) may represent the ratio of the fractions of TeO_3 tp and TeO_4 tbp: $\text{TeO}_3/\text{TeO}_4$.

From Raman spectra in figure 7.35 for ternary $(90-x)\text{ TeO}_2 - x\text{ Na}_2\text{O} - 10\text{ ZnO}$ ($x = 0, 10, 20$ and 30) glass system, the intensities of deconvoluted 5 peaks and intensity ratios of peaks at 720 and 780 against 660 cm^{-1} are shown in figure 7.45 and 7.46, respectively. Normally tellurite glass is a continuous network structure composed of TeO_4 tbp's, TeO_{3+1} polyhedra and TeO_3 tp's sharing vertices. As x increases, the increase of Na_2O and decrease of TeO_2 , intensity of peak A, B and C decrease, these indicate a decrease of Te-O-Te linkages. Intensities at peak D and E increase, the ratios of $I_{\text{D}}/I_{\text{C}}$ and $I_{\text{E}}/I_{\text{C}}$ increases, these indicate an increase of TeO_3 tp units and NBO sites. Cleavage of Te-O-Te linkages and formation NBO sites result in the conversion of TeO_4 tbp's to $\text{TeO}_{3+\delta}$ polyhedra and TeO_3 tp having NBO sites. Another change is at peak A. Not only the intensity decreases, the frequency also shifts to higher position. Because peak A is assigned to symmetric stretching (and bending) vibrations of Te-O-Te linkages which are formed by sharing vertices of TeO_4 tbp, $\text{TeO}_{3+\delta}$ polyhedra and TeO_3 tp, this shift indicates the connectivity of structure unit becomes less integral. This also proves the conversion of TeO_4 tbp's to $\text{TeO}_{3+\delta}$ polyhedra and TeO_3 tp. This process follows the reaction in equation 7.5.

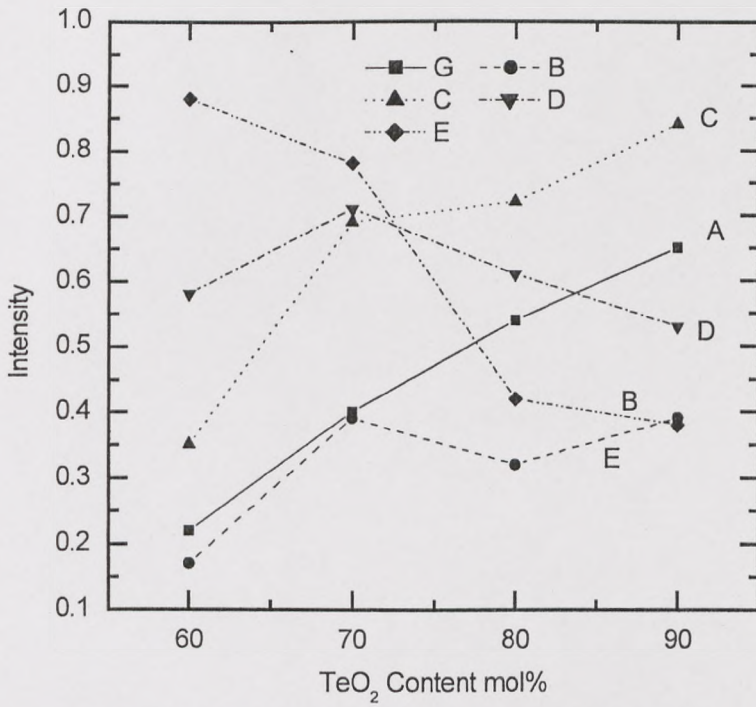


Fig. 7.45 Intensities of 5 deconvoluted peaks in (90-x)TeO₂-xNa₂O-10ZnO (x=0, 10, 20 and 30) glass

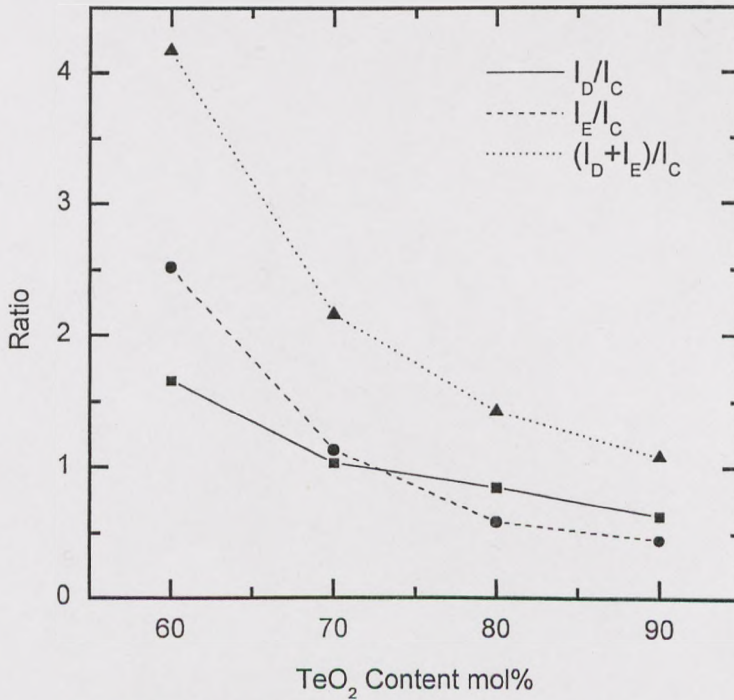


Fig. 7.46 Intensities of 5 deconvoluted peaks in (90-x)TeO₂-xNa₂O-10ZnO (x=0, 10, 20 and 30) glass

Field strength $F (=Z_c/a^2)$ is introduced to represent the interacting forces between cation and anion in oxide glass. Z_c is the valence of cation, $a = r_c + r_a$, r_c and r_a are the radii of cation and anion. The cation with a less field strength must be satisfied with a higher coordination number, in this case, compound formation and crystallisation are favoured. Therefore field strength of different oxide modifiers will result in the change of the Raman intensity and peak intensity ratio.

With different alkali ions in ternary $70\text{TeO}_2 - 20\text{X} - 10\text{ZnO}$ ($\text{X} = \text{Li}_2\text{O}, \text{Na}_2\text{O}, \text{K}_2\text{O}$ and ZnO) glass system, the intensities of deconvoluted 5 peaks and intensity ratios of peaks at 720 and 780 cm^{-1} against 660 cm^{-1} versus the field strength of modifying ions are shown in figure 7.47 and 7.48, respectively. Table 7.5 shows the field strength of alkali ions and Zn^{2+} in tellurite glass.

Table 7.5 field strength of alkali ions and Zn^{2+}

	K_2O	Na_2O	Li_2O	ZnO
Field strength Z_c/a^2	0.13	0.19	0.23	0.46

When X is ZnO , it becomes $70\text{TeO}_2 - 30\text{ZnO}$ binary glass system, the intensity ratio of I_D/I_C and I_E/I_C is slightly higher than that when X is alkali ions, peak A has much higher intensity and lower frequency, these mean that the structure not only produces more TeO_3 tp, but also increases the connectivity of network because it produces much less non-bridging oxygen ion than alkali ions. This glass structure has been studied by Sekiya et al. [11]. With increasing ZnO , the glass structure becomes increasingly $\text{Zn}_2\text{Te}_3\text{O}_8$ -like ($60\text{TeO}_2 - 40\text{ZnO}$) and consists of a $^1_\infty[\text{Te}_3\text{O}_8]$ chain like structure with $\text{TeO}_{3+\delta}$ and TeO_4 groups. Figure 7.49 shows this structure connection. Every 3 Te atoms have 2 bridging oxygen ions. As ZnO decreases and TeO_2 increases, the glass may have more bridging oxygen ions and the structure can be modified to three dimensions.

The higher depolarisation ratio of all the peaks suggests that the structure is more asymmetric. It means ZnO goes into the network as $[\text{ZnO}_4]$ to increase the asymmetry of tellurite glass. It also can stay in the gap of network as $[\text{ZnO}_6]$. Especially for peak A, intensity in depolarisation spectra is very low, because this peak reflects the symmetry stretching vibration mode of Te-O-Te . Because ZnO is intermediate oxide,

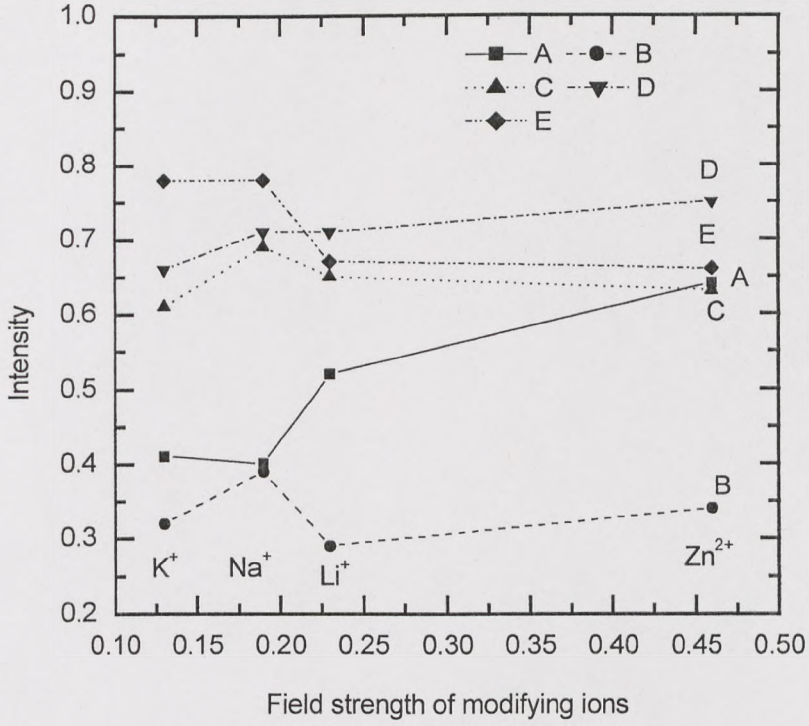


Fig. 7.47 Intensities of 5 deconvoluted peaks in 70TeO₂-20X-10ZnO (x=k₂O, Na₂O, Li₂O and ZnO) glass

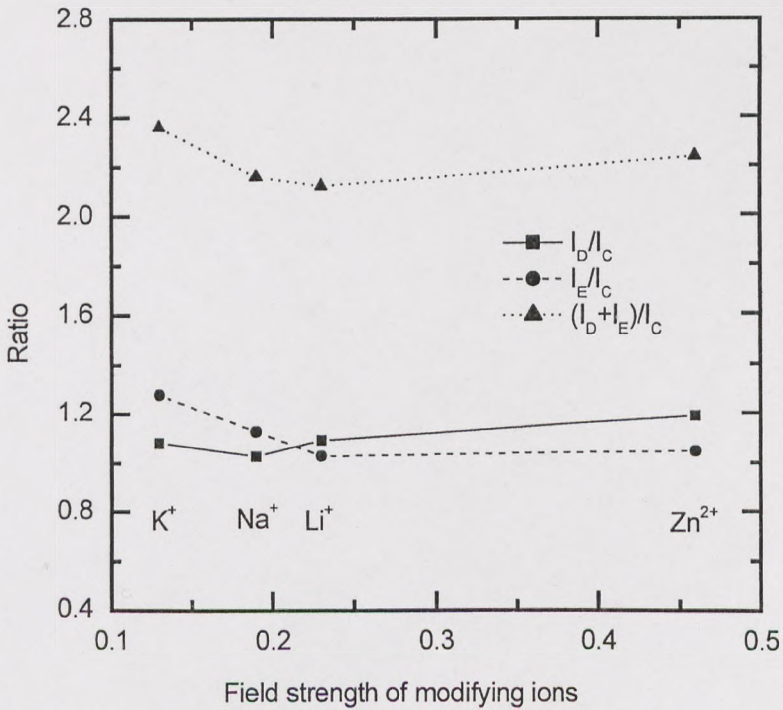


Fig. 7.48 Peak intensity ratio in 70TeO₂-20X-10ZnO (X = K₂O, Na₂O, Li₂O and ZnO) glass

it can link up with the broken TeO_3 - TeO_4 chain network and also break the network to produce non-bridging oxygen.

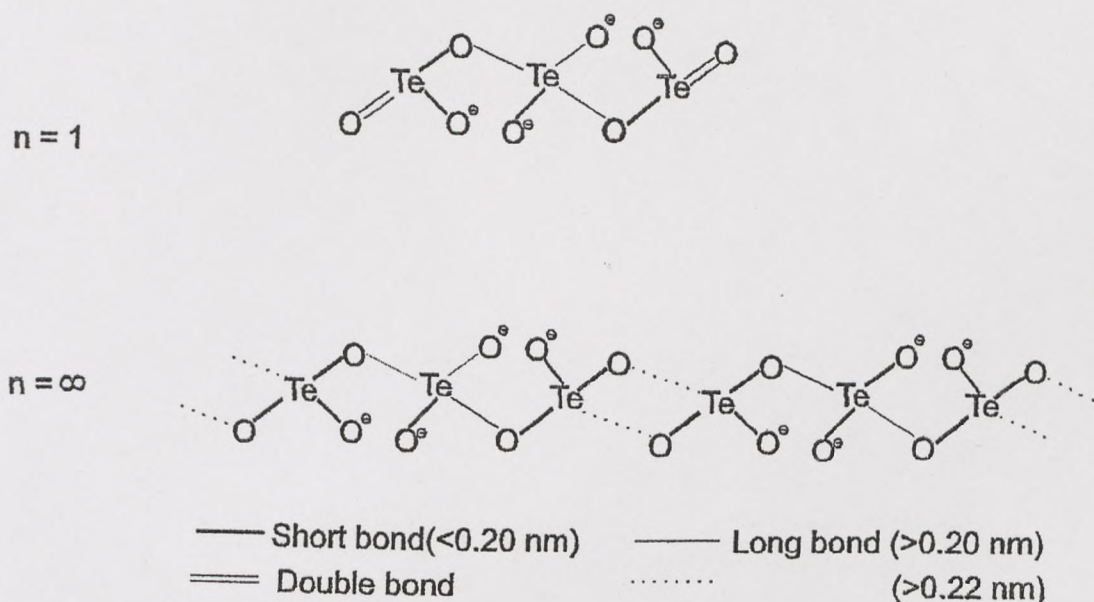


Fig. 7.49 Schematic representation of $(\text{Te}_3\text{O}_8^{4-})_n$ structural units, $\text{Te}_3\text{O}_8^{4-}$ ion ($n=1$) and $(\text{Te}_3\text{O}_8^{4-})_{\infty}$ chain ($n=\infty$).

The role of K_2O , Na_2O and Li_2O is very similar in tellurite glass. Peak A slightly shifts to lower frequency, intensities of peak A and ratio of $\text{TeO}_3/\text{TeO}_4$ slightly decrease by following the K_2O , Na_2O and Li_2O sequence. It means that the glass structure was distorted more when containing K_2O than Li_2O , and the connectivity of structure is slightly increased by following the K_2O , Na_2O and Li_2O sequence because of the increasing field strength of alkali ion in glass.

For different kinds of cation with increasing bond valence, Raman spectra of 80TeO_2 - $10\text{Na}_2\text{O}$ - 10X ($\text{X} = \text{K}_2\text{O}$, BaO , Ga_2O_3 , GeO_2 , Nb_2O_5 and WO_3) glass were shown in figure 7-39, the intensities of deconvoluted 5 peaks and intensity ratios versus the field strength of modifying ions are shown in figure 7.50 and 7.51,

respectively. The field strength of modifying ions is shown in table 7.6. As the valence of ion increases, the field strength increases.

Table 7.6 Field strength of different valence ions

	K ₂ O	BaO	Ga ₂ O ₃	GeO ₂	Nb ₂ O ₅	WO ₃
Field strength Z_c/a^2	0.13	0.26	0.74	1.06	1.20	1.53

The intensity at peak C is strongest when the modifier oxide is GeO₂. Because it is a typical glass former, it exists as [GeO₄] in glass to connect the network, it mainly increases the intensity of peak C. When the modifier oxide is Ga₂O₃, the intensity at peak A is strongest, because it is a typical glass intermediate, it can also connect the network as [GaO₄] form. K₂O and BaO are typical glass modifier, the intensities at peak D and E are higher than that in other oxide modifiers. They have the same role which has been discussed before. When the modifying oxide is Nb₂O₅, there is an extra peak around 880 cm⁻¹, it is caused by octahedron [NbO₆] [17]. When the glass modified by WO₃, there are two extra peaks around 350 and 920 cm⁻¹, they are supposed to be caused by [WO₄] tetrahedron structural units [17]. Peak around 450 cm⁻¹ shifts to a further lower frequency because of the strong gathering role of high valence for the broken network.

From the intensity ratio, I_D/I_C and I_E/I_C decrease with increasing valence, it arrives at the lowest point when modified oxide is GeO₂, then, it increases again when the modifying oxides are Nb₂O₅ and WO₃. This clearly demonstrates that monovalent alkali oxide can produce the most TeO₃ units among these various valences. Glass former oxide produces the least TeO₃ units. Tri-, penta- and hexa- valence oxides have the role between network modifier and network former.

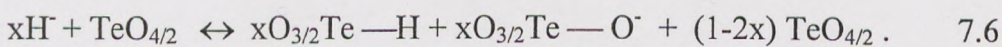
Above we discussed the glass modifiers are oxides. For the same cation with different anions, the effect on the glass structure has also been measured. Fluorine, chlorine and oxygen are compared. For anions, the electronegativity (X_i), which is respond to the bond ionic character, is important to the glass forming bond structure. If we define the ability of anion (F_a) to break glass network as the ability of element gets one electron, electronegativity divided by negative charge could represent F_a . Table 7.7 shows the electronegativity and F_a of fluorine, chlorine and oxygen.

Table 7-7 Electronegativity and F_a of fluorine, chlorine and oxygen.

	F ⁻	Cl ⁻	O ²⁻
Electronegativity X_i	4.0	3.0	3.5
F_a	4.0	3.0	1.75

From the Raman spectra of binary 80TeO₂-20X (X = Na₂O, NaCl and NaF) glass system in figure 7.41, the intensities of deconvoluted 5 peaks and intensity ratios of peaks at 720 and 780 cm⁻¹ against 660 cm⁻¹ are shown in figure 7.52 and 7.53, respectively. The intensities at peaks A, B and C remain unchanged, intensities at D and E are higher in oxide than that in chloride and fluoride. From the intensity ratio in figure 7.53, I_D/I_C and I_E/I_C are the highest when X is Na₂O, it is slightly higher in chloride than that in fluoride.

From the Raman spectra of ternary 80TeO₂-10Na₂O-10X (X = BaO, BaCl₂ and BaF₂) glass system in figure 7.43, the intensities of deconvoluted 5 peaks and intensity ratios of peaks at 720 and 780 against 660 cm⁻¹ are shown in figure 7.54 and 7.55, respectively. The change of intensities and the ratio of peaks are very similar with that in binary glass system. It also shows the highest TeO₃/TeO₄ ratio when X is oxide. This suggests that chloride and fluoride do not produce more TeO₃ units than oxide modifier. When tellurite glass is modified by oxide, the reaction is following equation 7.5 to generate [TeO₃], [TeO₃]⁻ and [TeO₄]⁻ units. When halide replaces oxygen in tellurite glass, the reaction is to follow the model 1, it can be expressed by equation 7.6: H⁻ represents halide anion, halide anions stay in oxygen position to form tbp. Therefore, this reaction will strongly break the network to produce more non-bridging oxygen than oxide modifier, but the glass has less TeO₃ tp units than oxide modifier. Another possibility is that F⁻ and Cl⁻ share LPE in TeO₃ tp because of their strong electronegativity and transfer TeO₃ tp to TeHO₃ structure unit which is similar to TeO₄ tbp.



From the depolarisation ratio ρ , it is the same when X is BaO and BaCl₂, ρ is much higher when glass contains BaF₂, the reason is that Te-F is much stronger than Te-O and Te-Cl bond. The strength of Te-O and Te-Cl bond is very close. In the tbp

structure unit when F is in the O site, the distortion of tbp is much more than that when the site is oxygen and chlorine, it increases the asymmetry of the structure unit, this results in the increase of depolarisation ratio.

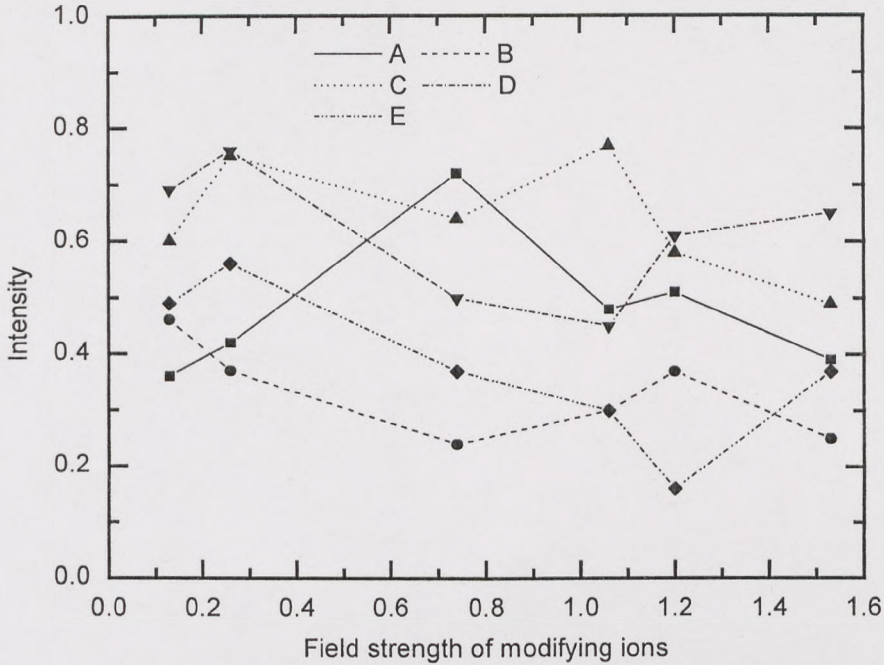


Fig. 7.50 Intensities of 5 deconvoluted peaks in $80\text{TeO}_2\text{-}10\text{Na}_2\text{O-}10\text{X}$ ($\text{X} = \text{K}_2\text{O}, \text{BaO}, \text{Ga}_2\text{O}_3, \text{GeO}_2, \text{Nb}_2\text{O}_5$ and WO_3) glass

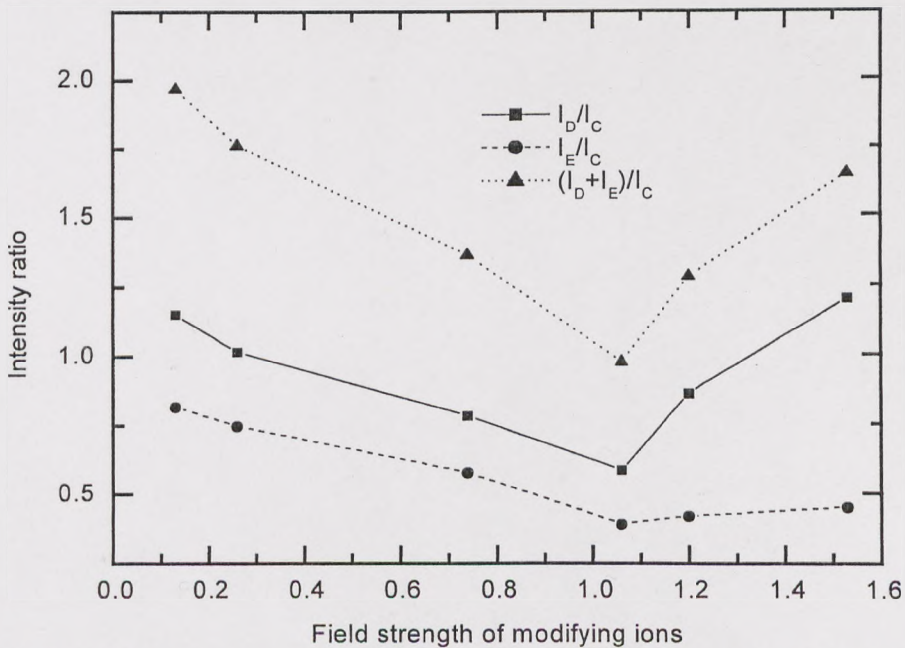


Fig. 7.51 Raman spectra peak intensity ratio in $80\text{TeO}_2\text{-}10\text{Na}_2\text{O-}10\text{X}$ ($\text{X} = \text{K}_2\text{O}, \text{BaO}, \text{Ga}_2\text{O}_3, \text{GeO}_2, \text{Nb}_2\text{O}_5$ and WO_3) glass

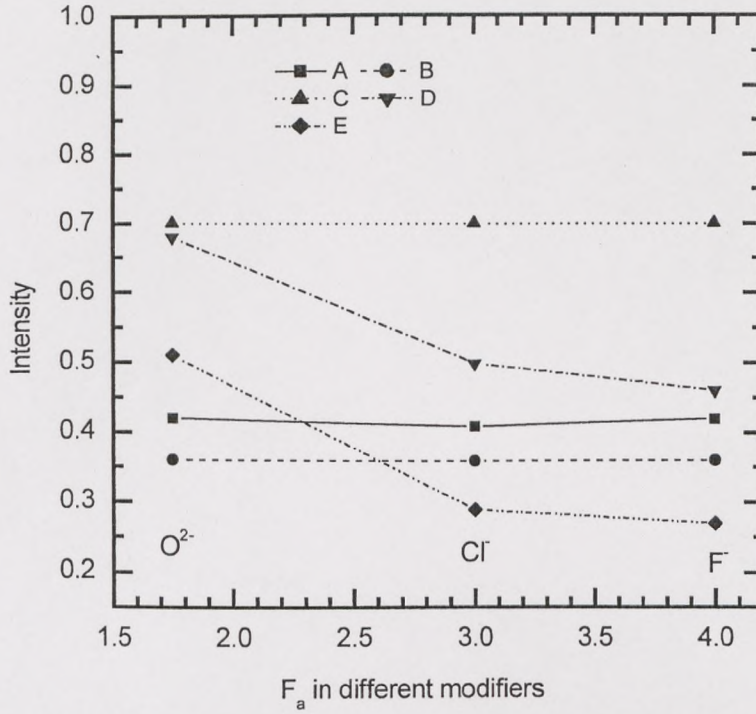


Fig. 7.52 Intensities of 5 deconvoluted peaks in 80TeO₂-20X (X = NaF, NaCl and Na₂O) glass

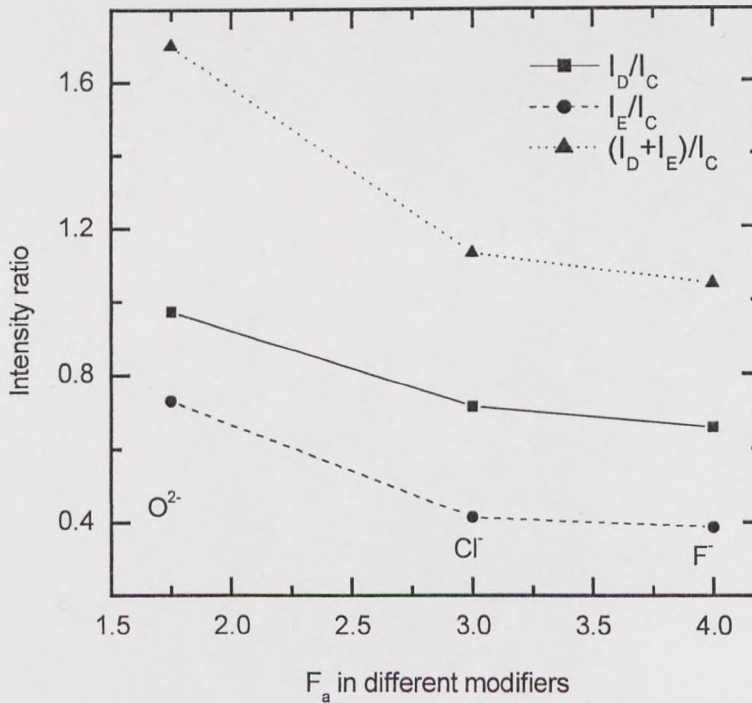


Fig. 7.53 Peak intensity ratio of Raman spectra in 80TeO₂-20X (X = NaF, NaCl and Na₂O) glass

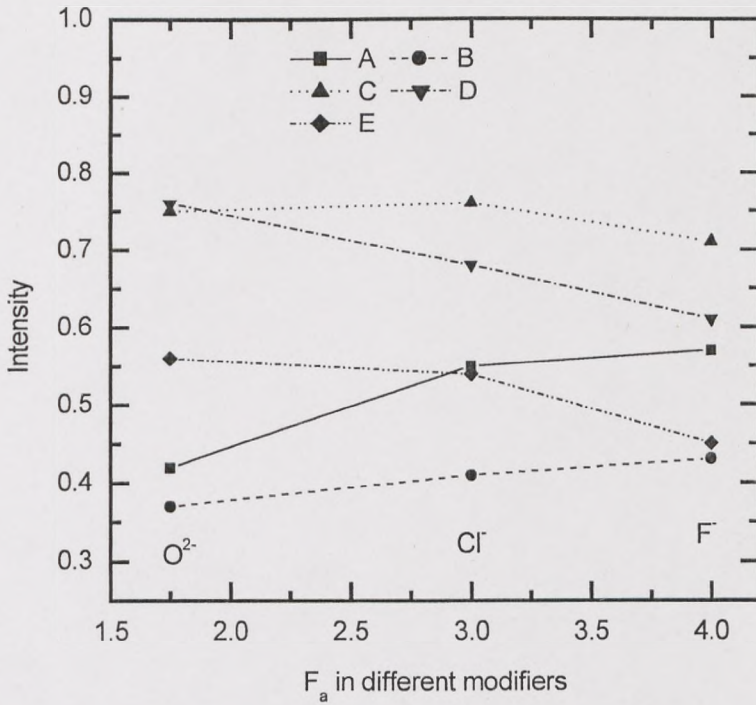


Fig. 7.54 Intensities of 5 deconvoluted peaks in $80TeO_2-10Na_2O-10X$ ($X = BaF_2, BaCl_2$ and BaO) glass

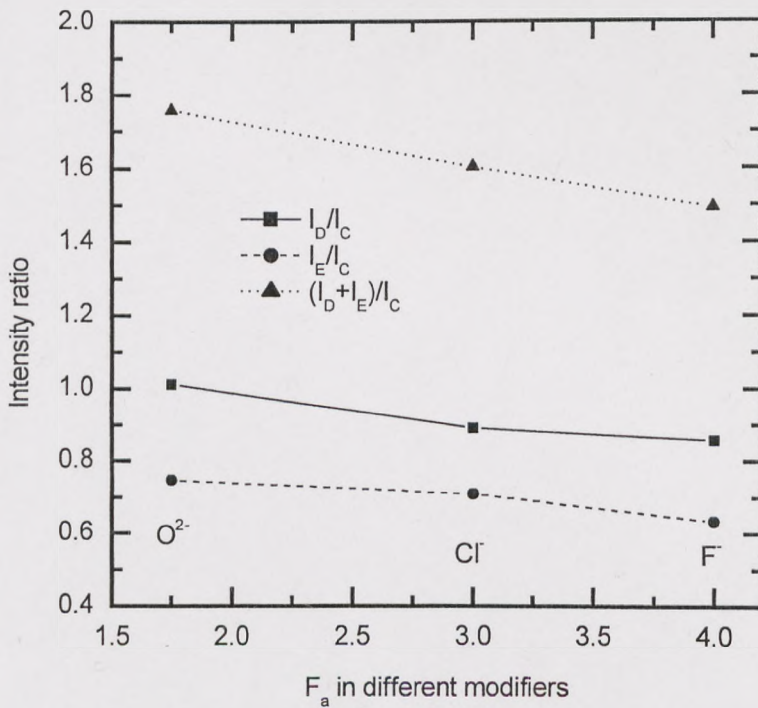


Fig. 7.55 Peak intensity ratio in $80TeO_2-10Na_2O-10X$ ($X = BaF_2, BaCl_2$ and BaO) glass

7.4.3.2 Low frequency range ($< 200 \text{ cm}^{-1}$)

The low-frequency broad band in the Raman spectrum, called the “Boson peak” (BP), is another universal characteristic of glasses. It is also present in numerous liquids. Though the origin of the Boson peak is still a subject of debate, it is generally accepted that it is characteristic of glassy state. In an amorphous solid, Shuker and Gammon [18] showed that the first order Raman scattered Stokes intensity could be written as equation 7.7.

$$I(\omega, T) = C(\omega) g(\omega) [n(\omega, T) + 1] / \omega \quad 7.7$$

where $n(\omega, T)$ is the Bose-Einstein population factor, $g(\omega)$ is the density of vibrational states (which in the Debye approximation is assumed to be equal to ω^2), and $C(\omega)$ is a constant representing the average coupling of the incident light to the vibrational modes of frequency ω . The reduced Raman intensity can then be written as equation 7.8 [19]:

$$I^R(\omega, T) = I(\omega, T) / \omega [n(\omega, T) + 1] = C(\omega) g(\omega) / \omega^2 \quad 7.8$$

Thus the Boson peak can be related to a maximum either in the coupling coefficient or in the density of vibrational states.

Several models have been proposed to describe the shape of BP [18-27]. Most of them [18, 21-26] associate the BP with a structure correlation length, R , by the relation: $R \sim V_t / \omega_{\max}$, where ω_{\max} is the frequency of the maximum of the BP expressed in wavenumber and V_t is the velocity of transverse sound waves. R assumes to be an average radius of ordered micro-regions within the glass [19], whether they are called blobs, clusters or chains of the size $\sim 2R$ [28]. In Martin-Berenig model, R can be obtained from the following relation as equation 7.9 [21].

$$R = V_t / 2\pi c \omega_{\max} \quad 7.9$$

where c is the velocity of light.

In tellurite glass, the band observed in the region around 40 cm^{-1} is assigned to the Boson peak. The BP is associated with light scattering due to acoustic-like vibrations

of a disordered structure. We assume the sound velocity in tellurite glass is constant, $V_t = 2.084 \times 10^5$ cm/s [29]. Using sound velocity and BP frequency, the calculation of $2R$ is shown in table 7.8 to 7.11 for different glasses.

Table 7.8 Values of structural correlation length in ternary $(90-x) \text{TeO}_2 - x\text{Na}_2\text{O} - 10\text{ZnO}$ ($x = 0, 10, 20$ and 30) glass system

	X=0	X=10	X=20	X=30
$\omega \pm 1 \text{ cm}^{-1}$	38	40	41	42
$2R \pm 0.01 \text{ nm}$	0.58	0.55	0.54	0.53

Table 7.9 Values of structural correlation length in ternary $70\text{TeO}_2 - 20\text{X} - 10\text{ZnO}$ ($\text{X} = \text{Li}_2\text{O}, \text{Na}_2\text{O}, \text{K}_2\text{O}$ and ZnO) glass system

	ZnO	Li_2O	Na_2O	K_2O
$\omega \pm 1 \text{ cm}^{-1}$	48	44	40	35
$2R \pm 0.01 \text{ nm}$	0.46	0.50	0.55	0.63

Table 7.10 Values of structural correlation length in binary $80\text{TeO}_2 - 20\text{X}$ ($\text{X} = \text{Na}_2\text{O}, \text{NaCl}$ and NaF) glass system

	X = Na_2O	X = NaCl	X = NaF
$\omega \pm 1 \text{ cm}^{-1}$	36	38	40
$2R \pm 0.01 \text{ nm}$	0.61	0.58	0.55

Table 7.11 Values of structural correlation length in ternary $80\text{TeO}_2 - 10\text{Na}_2\text{O} - 10\text{X}$ ($\text{X} = \text{BaO}, \text{BaCl}_2$ and BaF_2) glass system

	X = BaO	X = BaCl_2	X = BaF_2
$\omega \pm 1 \text{ cm}^{-1}$	38	42	44
$2R \pm 0.01 \text{ nm}$	0.58	0.53	0.50

The results in table 7.8 indicate that the diameter ($2R$) of the micro-region decreases with increasing Na_2O content, it also demonstrates the glass network was broken. This is in good agreement with correspond to the results discussed before.

The results in table 7.9 indicate that the 2R is the smallest when x is ZnO, glass has the smallest ordered micro-range. When x is alkali oxide, 2R increases following Li₂O, Na₂O, K₂O sequence. Because bivalent ion can break the network more than monovalent ion, among alkali ions, Li⁺ has the strongest field strength and smallest ion radius, Na⁺ has the second, K⁺ has the least field strength and largest radius, thus the tendency to break the network is stronger in Li₂O than in K₂O, this results in the ordered micro-range increases following Li₂O, Na₂O, K₂O sequence.

The results in table 7.10 and 7.11 indicate that fluorine is the strongest in breaking the chain TeO₄-TeO₃ network, chlorine is the second. By comparing table 7.9 and 7.11, bivalent Ba²⁺ is stronger than Na⁺ in breaking the chain TeO₄-TeO₃ network.

From these tables, 2R is in the range 0.46 to 0.63 nm, this is a distance corresponding to more than one and less than two polyhedra in the dimensions of structure unit, i.e. the cluster size only accommodate very few closely packed tbps and tps. Medium range order in the tellurite glass is limited to at the most two structural units of tbp and tp, these observations are consistent with the proposal that the modifying oxide in TeO₂ matrix disrupts the three dimensional glass network, and creates defects, thus reducing the length of TeO₄ chains and hence the radius of micro-region.

From the depolarisation ratio in table 7.3 and 7.4, ρ at Boson peak is much higher than that in the phonon vibration range, it is about 3 times. Because Boson peak is associated with light scattering from acoustic-like vibrations of disordered structure, it surely has higher depolarisation ratio than that of vibration modes from ordered structure units. Compared ρ with each other at Boson peak, it is higher when x is ZnO and BaF₂ than other modifiers. It shows the acoustic-like vibrations are also deformed more with higher valence cation and fluorine anion. This result is also similar to that in the phonon vibration range.

7.5 Conclusions

1. In $(90-x)\text{TeO}_2 - 9\text{ZnO} - x\text{R}_2\text{O} - 1\text{Er}_2\text{O}_3$ ternary glass system ($\text{R}_2\text{O} = \text{Li}_2\text{O}, \text{Na}_2\text{O}$ and K_2O , $x = 5, 10, 15, 20$), as x increases, the density and T_g of glass decrease, the molar volume decreases when R_2O is Li_2O and Na_2O , in K_2O containing glass, molar volume increases, UV and IR cut-off shift to shorter wavelength. From Raman spectra of these glasses, the glass network is broken more and has more tbps transferring to tps when x increases.
2. In $70\text{TeO}_2 - 9\text{ZnO} - 20\text{R}_2\text{O} - 1\text{Er}_2\text{O}_3$ ternary glass ($\text{R}_2\text{O} = \text{Li}_2\text{O}, \text{Na}_2\text{O}$ and K_2O), following $\text{Li}_2\text{O}, \text{Na}_2\text{O}$ and K_2O sequence, the density and T_g of glass decrease, the molar volume increases, and UV and IR cut-off shift to slightly shorter wavelength. From Raman spectra of these glasses, they are very similar to each other, the glass network connectivity slightly decreases and contains slightly more tps in K_2O containing glass than in Li_2O containing glass.
3. In $(89-x)\text{TeO}_2 - x\text{ZnO} - 10\text{R}_2\text{O}$ ternary glass ($\text{R}_2\text{O} = \text{Na}_2\text{O}$ and K_2O , $x = 4, 9, 14, 19$), as x increases, the density and molar volume of glass decrease, T_g slightly increases, UV and IR cut-off shift to shorter wavelength. From Raman spectra of glass, ZnO increases the glass network connectivity comparing alkali oxides.
4. When tellurite glass is modified by different valence cation oxides, from the results of Raman spectra, glass modifiers decrease network connectivity, glass former increases network connectivity, high valence cations create extra structure units.
5. When tellurite glass is modified by halides, F^- and Cl^- are supposed to replace O^{2-} or share LPE of tellurium to form tbp, tp in glass decreases, the connectivity of glass also decreases.
6. Crystallisation kinetics has been analysed in two tellurite glasses using isothermal and non-isothermal measurement methods. The devitrification process in both binary and ternary glasses was seen to conform to the Johnson-Mehl-Avrami theory of crystal growth.
7. Boson peak shifts to different wavelengths when tellurite glass is modified by different kinds of oxides and halides. The results from analysing Boson peak are consistent with those in middle and high frequency range. The depolarisation in Boson peak is much higher than in other peaks.

Reference:

1. Yakhkind, A. K., *J Am. Ceram. Soc.*, **49**, 671 (1966).
2. Scholze, H., *Glass: nature, structure and properties*, translated by M. J. Lakin, New York, London: Springer, c1991.
3. Vogel, W., *Glass Chemistry*, p38, The American Ceramic Society, 1985.
4. Wang, J. S., E. M. Vogel, and E. Snitzer, *Optical Materials*, **3**, 187 (Aug. 1994).
5. Worrel, C. A., and T. Henshall, *J. Non-Cryst. Solids* **29**, 283 (1978).
6. Pan, Z., D. O. Henderson and S. H. Morgan, *J. Chem. Phys.* **101**, 1767 (1994).
7. Verweij, H., and J. H. J. M. Buster, *J. Non-Cryst. Solids* **34**, 81 (1979).
8. Lipinska-Kalita, K. E., *J. Non-Cryst. Solids* **119**, 41 (1990).
9. Sekiya, T., N. Mochida, A. Ohtsuka and M. Tonokawa, *J. Non-Cryst. Solids* **144**, 128 (1992).
10. Burger, H., K. Kneipp, H. Hobert, and W. Vogel, *J. Non-Cryst. Solids* **151**, 134 (1990).
11. Sekiya, T., N. Mochida, A. Ohtsuka and M. Tonokawa, *J. Non-Cryst. Solids* **168**, 106 (1994).
12. Lindqvist, O., *Acta Chem. Scand.* **22**, 977 (1968).
13. Sekiya, T., N. Mochida, A. Ohtsuka and M. Tonokawa, *J. Ceram. Soc. Jpn* **97**, 1435 (1989).
14. Pine, A. S., and G. Dresselhaus, *Phys. Rev. B* **5**, 4087 (1972).
15. Himei, Y., A. Osaka, T. Nanba and Y. Miura, *J. Non-Cryst. Solids* **177**, 164 (1994).
16. Mysen, B. O., W. Larry, W. Finger, O. Virgo and F. A. Seifert, *Am. Miner.* **67**, 686 (1982).
17. Gan, F., *Optical and Spectroscopic Properties of Glass*, pp 40-44, Springer-Verlag Berlin Heidelberg and Shanghai Scientific and Technical Publishers, 1992.
18. Shuker, R., R. W. Gammon, *J Chem. Phys.* **55**, 1984 (1971).
19. Malinovsky, V. K., A. P. Sokolov, *Solid State Commun.* **57**, 757 (1986).
20. Duval, E., A. Boukenter, T. Achibat, *J. Phys.: Condens. Matter* **2**, 10227 (1990)
21. Martin, A., Brenig, *Phys Status Solidi (b)* **64**, 163 (1974).
22. Sokolov, A. P., A. Kislink, D. Quitman, E. Duval, *Phys. Rev. B* **48**, 7692 (1993).
23. Nemanich, R. J., *Phys. Rev. B* **16**, 1665 (1977).
24. Pang, T., *Phys. Rev. B* **45**, 2490 (1992).

25. Phillips, J. C., *J. Non-Cryst. Solids* **43**, 37 (1981).
26. Akermans, E., R. Maynard, *Phys. Rev. B* **32**, 7850 (1985).
27. Guervich, V. L., D. A. Parshin, J. Pelous, H. R. Shober, *Phys. Rev. B* **48**, 16318 (1993).
28. Benassi, P., A., Fontana, W. Frizzera, M. Montagna, V. Mazzacurati, G. Signorelli, *Philos. Mag. B* **71**, 761 (1995).
29. Duverger, C., M. Bouzaoui, S. Turrell, *J. Non-Cryst. Solids* **220**, 169 (1997).

Chapter 8

Properties of Er^{3+} doped tellurite glasses

In this chapter, the main studies are on the changes in glass physical property when the glass contains Er_2O_3 , Er^{3+} ion absorption and fluorescence properties in tellurite glasses, the analysis of Judd-Ofelt calculation its interpretations. The Judd-Ofelt theory is used to calculate the radiative lifetimes, oscillator strengths and nonradiative rates. These properties are compared with different kinds of glass hosts such as the silicate, germanate and fluoride glasses.

8.1 Physical properties change with various Er^{3+} concentration

8.1.1 UV cutoff

Figure 8.1 shows the UV edge absorption in $80\text{TeO}_2\text{-}10\text{ZnO-}10\text{Na}_2\text{O}$ tellurite glass doped with 0.3, 0.7, 1.1 and 2.5 wt% Er_2O_3 . The peak at 378 nm is due to the absorption of Er^{3+} ions. With the increase of Er_2O_3 content, the UV edge shifts to longer wavelength. It means the bandgap of tellurite glass becomes smaller. In the same ternary glass system of UV edge bandgap studied in figure 7.26, it indicated that the bandgap became larger as the Na_2O content increased in the glass. Therefore, the function of Er_2O_3 on bandgap is totally different from that of Na_2O in tellurite glass. In order to study the function of Er_2O_3 in tellurite glass, density, molar volume and glass transition properties with different Er_2O_3 concentration are measured and discussed in the following parts.

8.1.2 Density and molar volume

Figure 8.2 shows the density and molar volume changes with various Er_2O_3 content in $80\text{TeO}_2\text{-}10\text{ZnO-}10\text{Na}_2\text{O}$ tellurite glass. It indicates that with the increase of Er_2O_3 content, the densities of glass increase and molar volumes decrease. The scattered points are the measured results, the solid lines are linear fitted results. It shows that the density and molar volume change nearly linear. Therefore, with the increase of Er_2O_3 content, the glass structure becomes denser and more packed. There

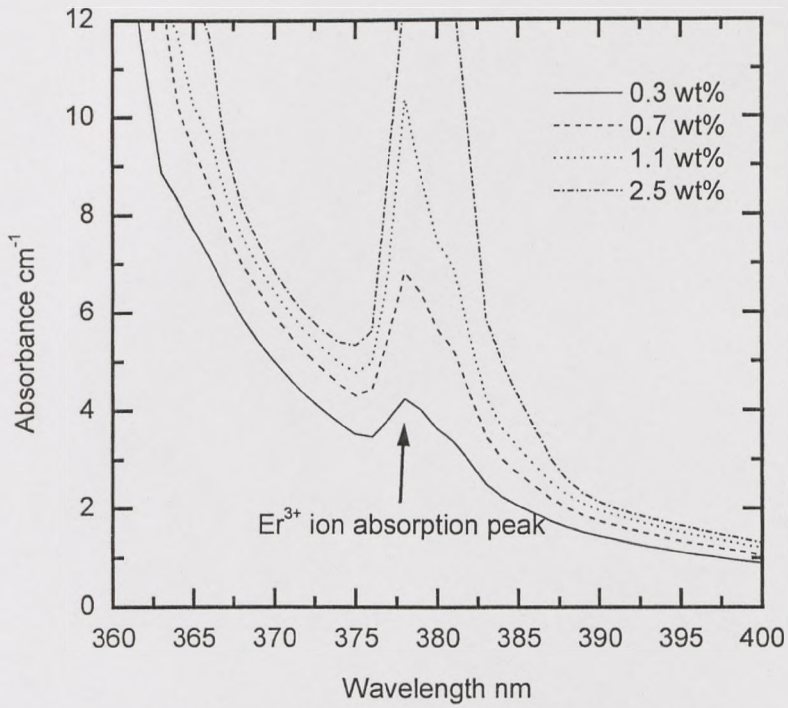


Fig. 8.1 UV edge absorption in tellurite glass with various Er_2O_3 concentration

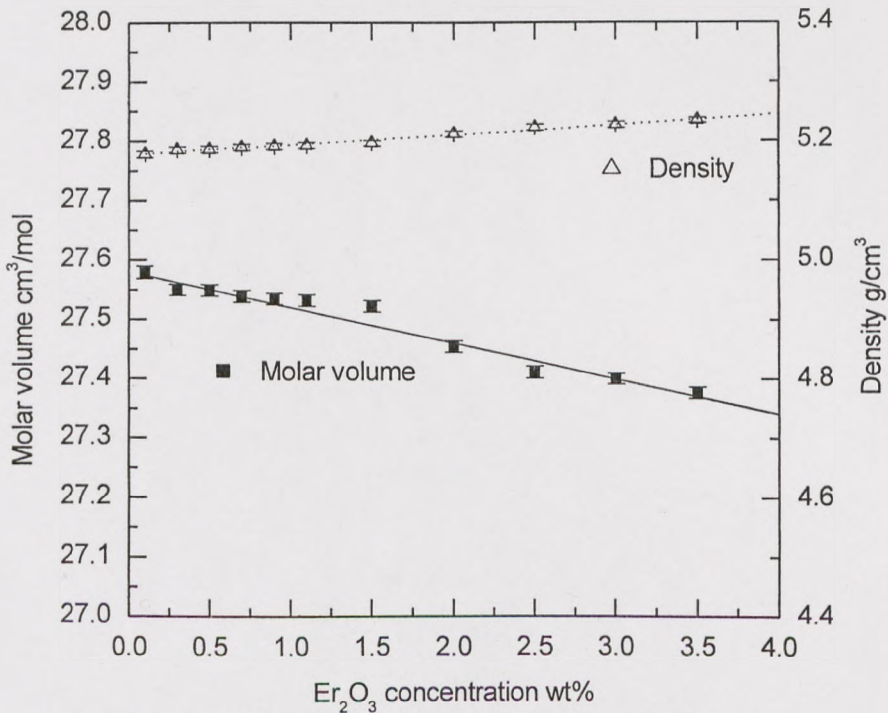


Fig. 8.2 Density and molar volume change with Er_2O_3 concentration in tellurite glass

are two ranges, when the content of Er_2O_3 less than 1.5 wt%, V_m and density change very gently, when it is above 1.5 wt%, the changing rate is much faster. It means the glass structure could be affected more with high content of Er_2O_3 dopants. From molar volume and density change with various Na_2O concentrations shown in figure 7.1, V_m increases and density decreases with increasing Na_2O concentration. Therefore, the behaviour of Er_2O_3 and Na_2O on V_m and density in tellurite glass is also opposite each other.

8.1.3 Glass transition property

Figure 8.3 shows the glass transition and crystallisation temperature changes with various Er_2O_3 content in $80\text{TeO}_2\text{-}10\text{ZnO-}10\text{Na}_2\text{O}$ tellurite glass. T_g is glass transition temperature, T_x is onset of crystallisation temperature, and T_p is peak crystallisation temperature. $T_x\text{-}T_g$ shows the glass thermal stability. With increasing Er_2O_3 concentration, all the characteristic temperatures T_g , T_x and T_p increase moderately and then level off. The glass stability $T_x\text{-}T_g$ also shows the same trend. The increase of these properties is an indication of strong bonding between Er^{3+} -ion and the host glass. From glass transition temperature change with various Na_2O concentrations in figure 7.7, T_g decreases with increasing Na_2O concentration. Compared with the thermal properties of Er_2O_3 and Na_2O in tellurite glass, the role of Er_2O_3 is also opposite to that of Na_2O .

8.1.4 Discussion the role of Er_2O_3

From the results of UV edge, glass density and molar volume, glass transition temperature and thermal stability, these properties change in an opposite direction with increasing Er_2O_3 content compared with increasing Na_2O content in $\text{TeO}_2\text{-ZnO-}\text{Na}_2\text{O}$ glass. The behaviour of Er_2O_3 in the network appears to be that it tries to connect the broken network. We can suggest that Er_2O_3 is an intermediate oxide in tellurite glass.

For rare-earth sesquioxide M_2O_3 , there are three types of structure A, B and C. In A and B type of M_2O_3 structures, the metal atoms are the 7-coordinated. Crystal structure of Er_2O_3 , it is C type in which the M atoms are 6-coordinated and O atoms are 4 coordinated [1]. From Raman spectrum analysis of $\text{TeO}_2\text{-ZnO-}\text{Na}_2\text{O}$ glass, the

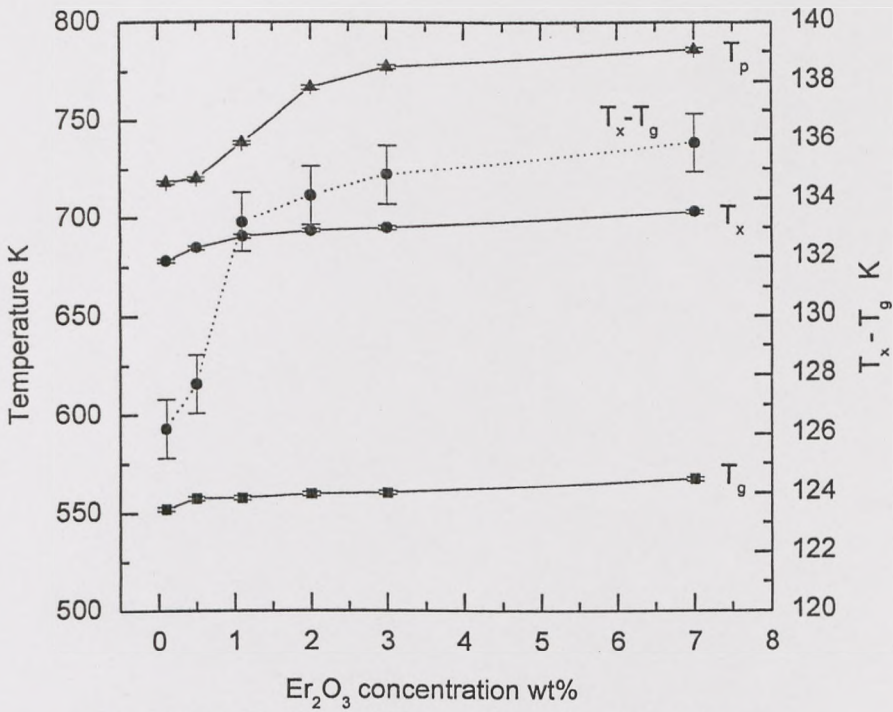


Fig. 8.3 T_g , T_x , T_p and $T_x - T_g$ of tellurite glass change with Er_2O_3 concentration

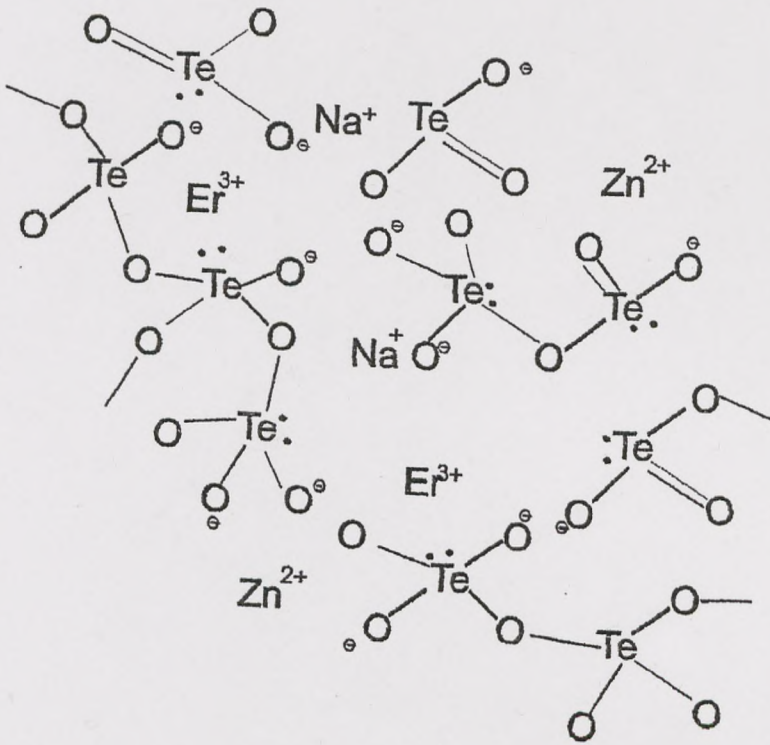


Fig. 8.4 Schematic representation of Er ions in TeO₂-ZnO-Na₂O glass

structure consists of TeO_4 tbp, TeO_{3+8} polyhedra and TeO_3 tp units, the glass network was broken by modifier Na_2O , it creates non-bridging oxygen site Te-O^- or Te=O . As Er_2O_3 is an intermediate oxide, it can gather those broken structure units by $[\text{ErO}_6]$ 6-coordination. Er^{3+} ions exist in the gap of these different structure units. Figure 8.4 shows the pattern of Er^{3+} ions in TZN tellurite glass. Due to the presence of LPE sites in tbp, tp and polyhedron structures, Er^{3+} ions in 6-fold co-ordination will pair with LPE sites, they may also be able to gather these non-bridging oxygen sites to improve the integrity of glass network. Therefore, with increasing Er_2O_3 content in glass, the packing density of the glass structure increases. This results in a higher glass density, lower molar volume, higher glass transition temperature and thermal stability.

8.2 Er^{3+} absorption spectrum in tellurite glass

For Er^{3+} doped glass, most of the interest pertains to the ${}^4\text{I}_{13/2} \rightarrow {}^4\text{I}_{15/2}$ transition at $1.5 \mu\text{m}$, since this is the most important and most extensively studied one. It is a three level lasing system. For a three-level lasing system, not only the stimulated emission but also the absorption cross-section plays important roles in determining the performance of a device. Figure 3.2 shows the whole absorption spectrum of Er^{3+} ions in tellurite glass. As it is aimed that Er^{3+} doped TeO_2 glass will be used as an optical amplifier, absorption bands at three pump wavelength 800, 980, 1480 nm and the operating wavelength $1.53 \mu\text{m}$ are more important than the rest of absorption peaks. These bands correspond to the energy transition originating from ${}^4\text{I}_{15/2}$ (ground level) $\rightarrow {}^4\text{I}_{9/2}$, ${}^4\text{I}_{11/2}$, ${}^4\text{I}_{13/2}$ respectively. In tellurite glass, we concentrate on the study of Er^{3+} absorption spectrum in $\text{TeO}_2\text{-ZnO-R}_2\text{O}$ ($\text{R}_2\text{O} = \text{Li}_2\text{O}, \text{Na}_2\text{O}$ and K_2O) ternary glass system, and also examine the effect of chloride and fluoride modified tellurite glasses on the absorption spectrum. We also compared these absorption bands with heavy metal germanate, modified silicate and ZBLAN fluoride glasses. From the absorption spectra, the absorption cross-sections and peak ratios were calculated to show the sensitivity of absorption with the change of compositions.

8.2.1 Er^{3+} absorption spectra in $\text{TeO}_2\text{-ZnO-R}_2\text{O}$ ($\text{R}_2\text{O} = \text{Li}_2\text{O}, \text{Na}_2\text{O}$ and K_2O) system glass

In $\text{TeO}_2\text{-ZnO-R}_2\text{O}$ ($\text{R}_2\text{O} = \text{Li}_2\text{O}, \text{Na}_2\text{O}$ and K_2O) ternary glass system, the compositions change always follow the method of modified oxides replacing TeO_2 while the glasses have the same concentration of Er_2O_3 .

When Na_2O replaces TeO_2 in $(90-x)\text{TeO}_2\text{-9ZnO-xNa}_2\text{O-1Er}_2\text{O}_3$ ($x=5, 10, 15, 20$) glass, the glasses are designated by N1, N2, N3 and N4 respectively. Figure 8.5 shows the Er^{3+} ion absorption spectrum changes with various Na_2O concentrations. From these absorption spectra, the absorption cross sections of these peaks have changed slightly, the shape of these absorption peaks keeps nearly the same. The cross sections of these peaks and the ratios of peaks at 800, 980 and 1495 nm against the peak at 1532 nm were calculated, figure 8.6 and 8.7 show these calculated results.

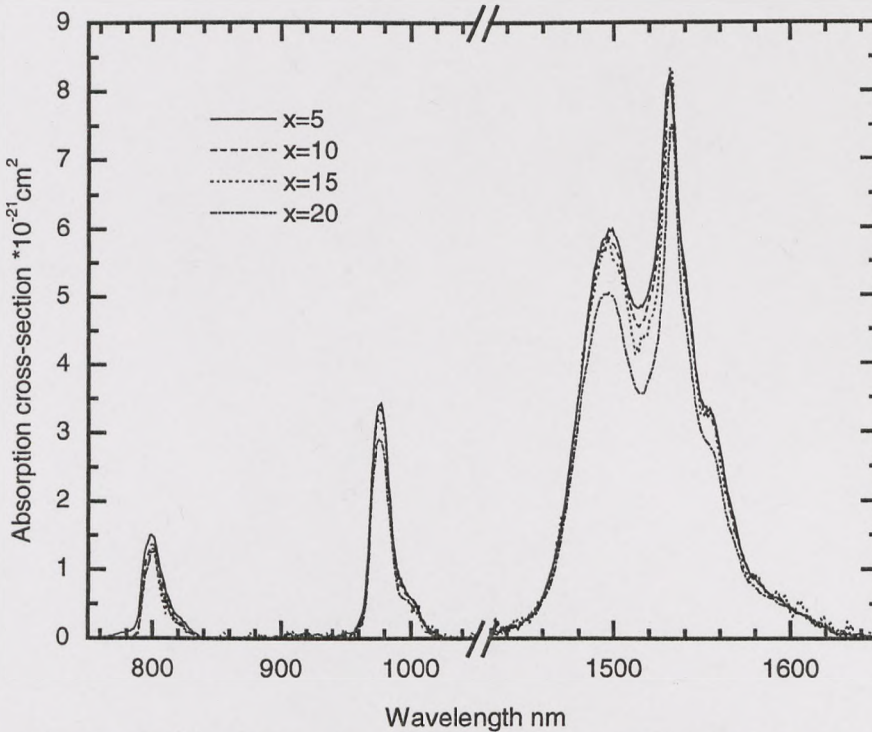


Fig. 8.5 Er^{3+} ion absorption spectra in $(90-x)\text{TeO}_2\text{-xNa}_2\text{O-9ZnO-1Er}_2\text{O}_3$ ($x=5, 10, 15$ and 20) glass

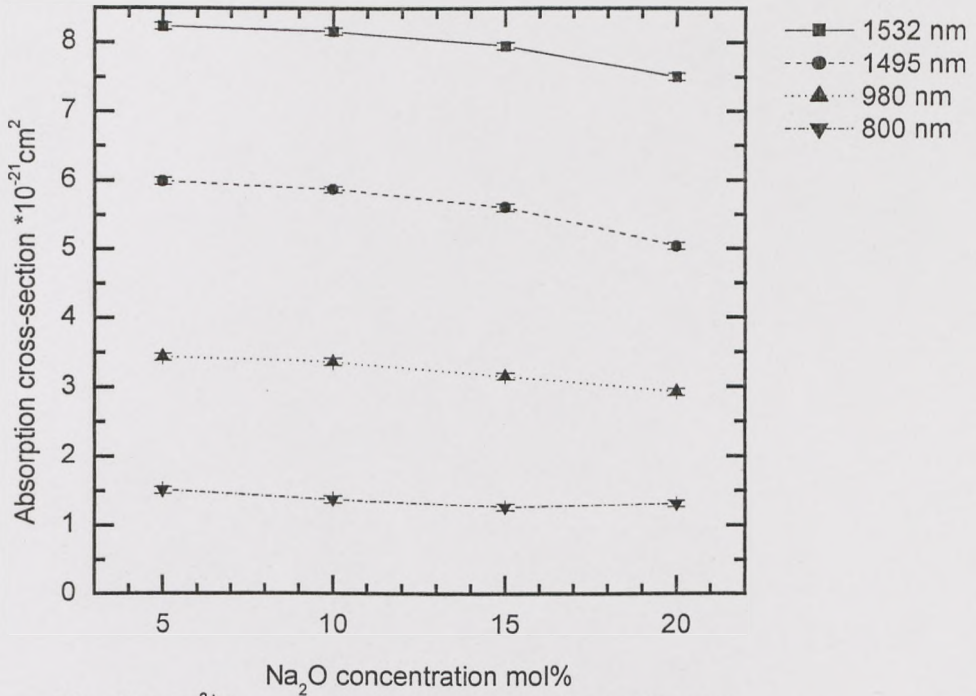


Fig. 8.6 Er³⁺ ion absorption cross-sections change with various Na₂O concentration in tellurite glass

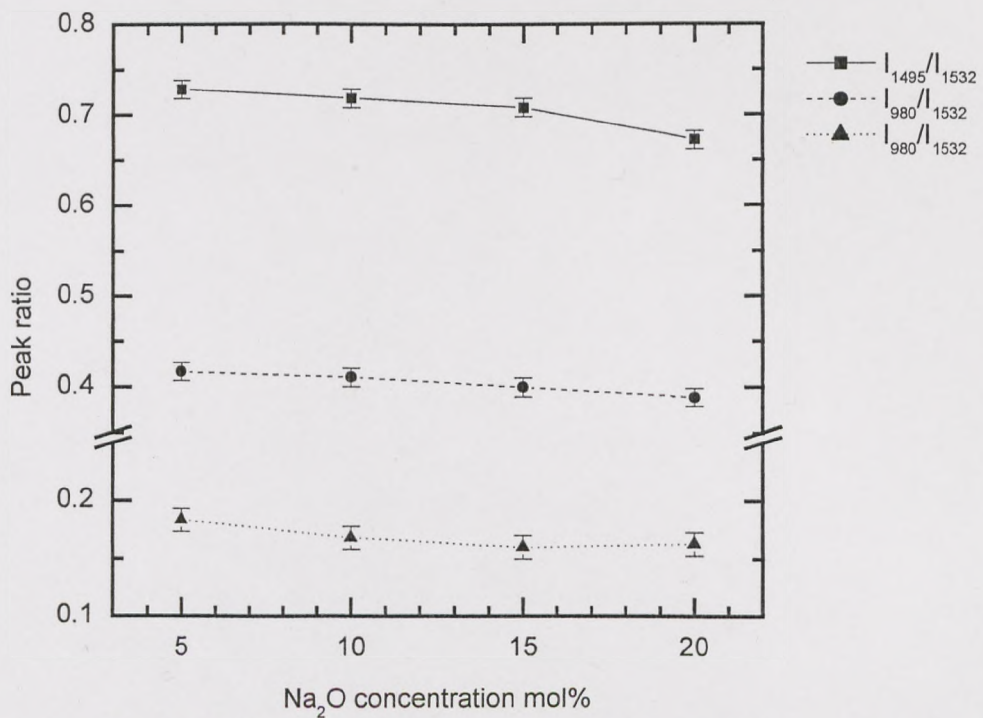


Fig. 8.7 Er³⁺ ion absorption peak ratio change with various Na₂O concentration in tellurite glass

When Li_2O replaces TeO_2 in $(90-x)\text{TeO}_2-9\text{ZnO}-x\text{Li}_2\text{O}-1\text{Er}_2\text{O}_3$ ($x = 5, 10, 15, 20$) glass, the glasses are designated by L1, L2, L3 and L4 respectively. Figure 8.8 and 8.9 show the absorption cross-sections of these four peaks and the peak ratios changes with various concentrations.

K_2O was also studied in $(90-x)\text{TeO}_2-9\text{ZnO}-x\text{K}_2\text{O}-1\text{Er}_2\text{O}_3$ ($x = 5, 10, 15, 20$) glass, the glasses are also designated by K0, K1, K2 and K3 respectively. Figure 8.10 and 8.11 show the absorption cross-sections of these four peaks and the peak ratios changes with various concentrations.

From figure 8.6, 8.8, 8.10, they all show the Er^{3+} absorption cross-sections of these four peaks decrease gently with increasing alkali ion concentrations. For these three pumping wavelengths, the absorption cross-section at 800 nm is less than half of that at 980 nm, and the 980 nm peak is nearly half of that at 1495 nm. From equation 3.11, the oscillator strength is very much dependent on the refractive index of glass. When Li_2O , Na_2O and K_2O replace TeO_2 , the refractive index of glass decrease, this will certainly result in the decrease of the cross-section. It is evident from Raman spectrum studies that when the alkali ions substitute TeO_2 , the structure becomes less closed packed with more non-bridging oxygen and $[\text{TeO}_3]$ tp units, therefore, the interaction between Er^{3+} ions and structure become weaker, this will also result in the decrease of absorption cross-section.

From figure 8.7, 8.9, 8.11, the ratios of these peaks change very gently with increasing alkali ion concentration, I_{800}/I_{1532} and I_{980}/I_{1532} remain virtually unchanged although the I_{1495}/I_{1532} ratio decreases slightly. These two peaks at 1495 and 1532 nm are from the same energy level transition but different sub-levels, the peak ratio between these two peaks reflect the distribution of these sub-levels, it decides the broadness and flatness of this most important transition. The decrease of the ratio is also due to the weaker interaction between Er^{3+} ions and glass structure units. The reason for the absorption cross-sections at 800 and 980 nm being less sensitive to the composition than 1495 and 1532 nm is that the energy levels ($^4I_{9/2}$ and $^4I_{11/2}$) have smaller J (total angular momentum), thus the Starks splitting levels are fewer than this $^4I_{13/2}$ level. Especially for the $^4I_{9/2}$ level (800 nm), the absorption cross-section and

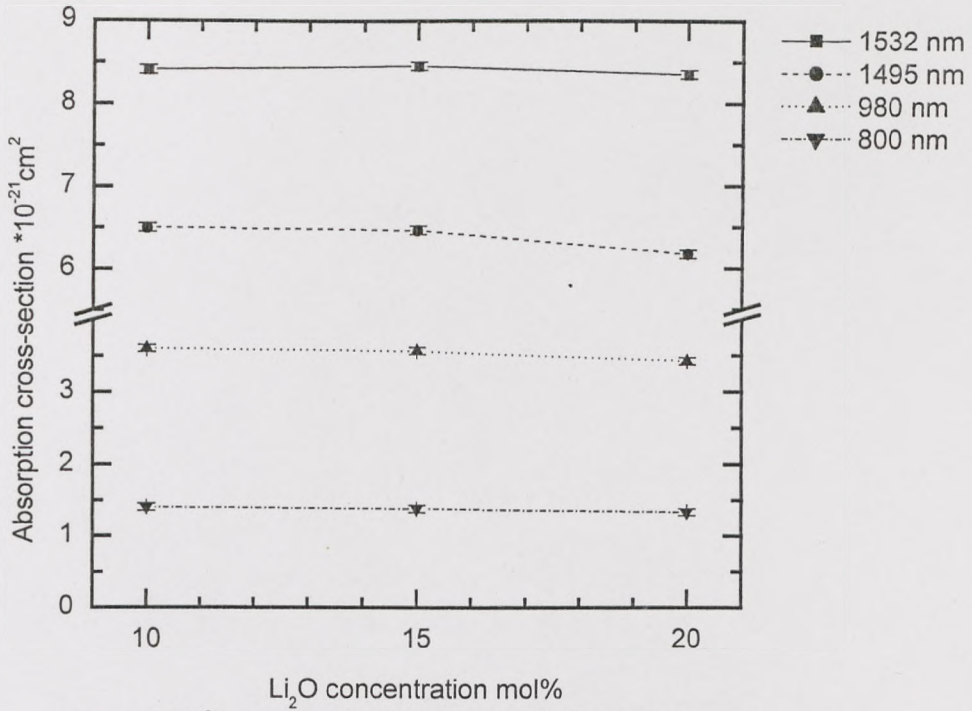


Fig. 8.8 Er³⁺ ion absorption cross-sections change with various Li₂O concentration in tellurite glass

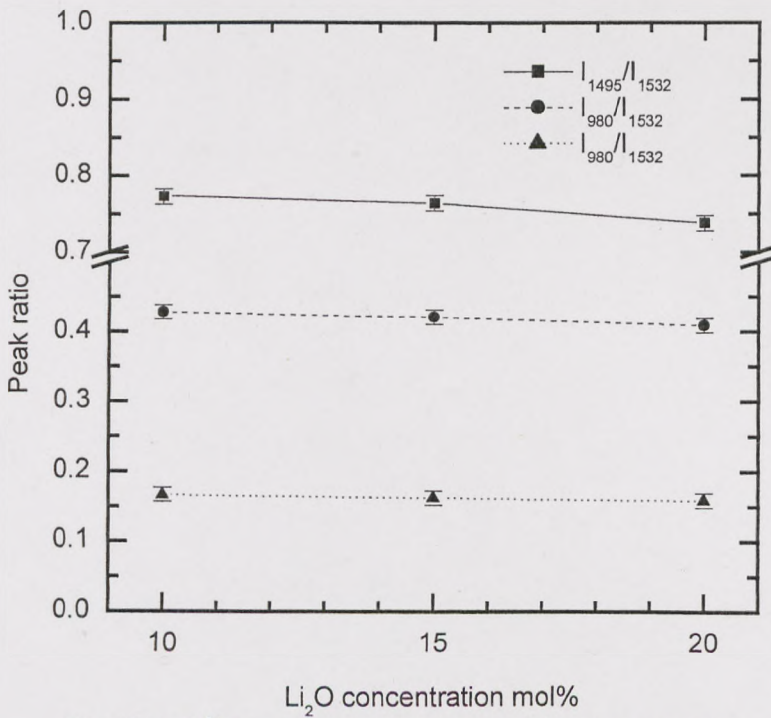


Fig. 8.9 Er³⁺ ion absorption peak ratio change with various Li₂O concentration in tellurite glass

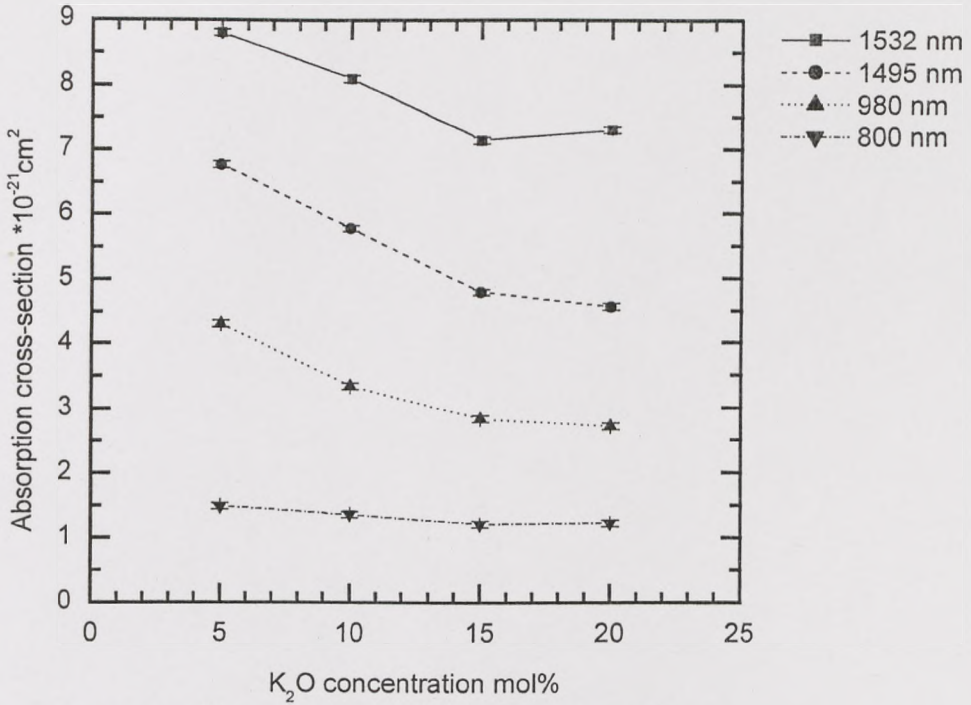


Fig. 8.10 Er³⁺ ion absorption cross-sections change with various K₂O concentration in tellurite glass

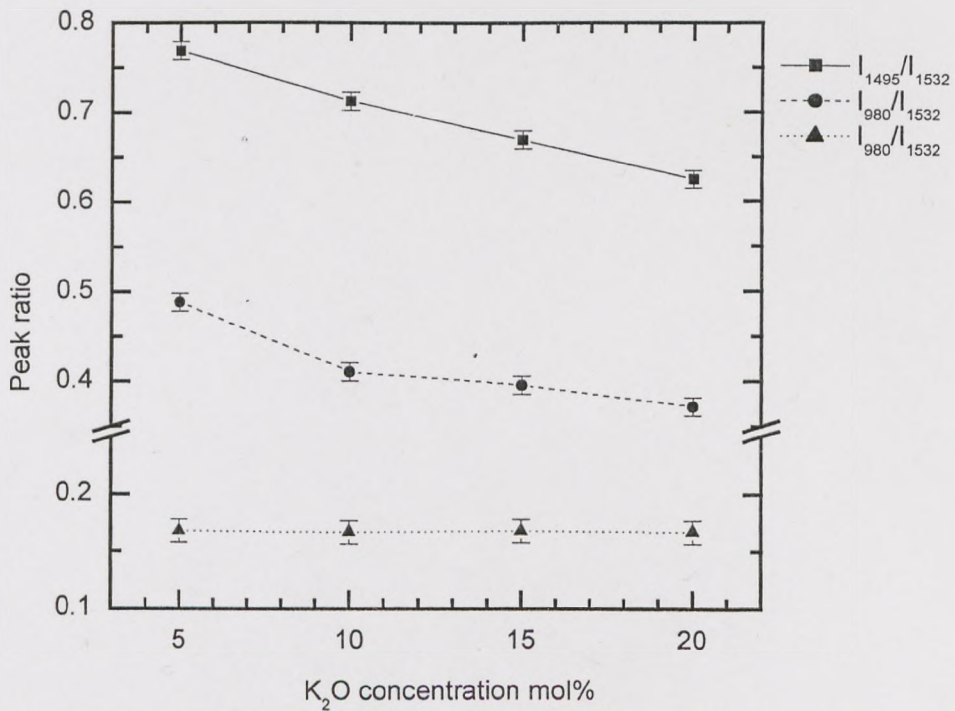


Fig.8.11 Er³⁺ ion absorption peak ratio change with various K₂O concentration in tellurite glass

peak ratio are nearly the same when the concentration of modifier changes or there are different kind of modifiers in tellurite glass.

The effect of alkali group of oxides on absorption spectra of ternary 70TeO_2 - 9ZnO - $20\text{R}_2\text{O}$ - $1\text{Er}_2\text{O}_3$ ($\text{R}_2\text{O} = \text{Li}_2\text{O}, \text{Na}_2\text{O}$ and K_2O) glass is compared in figure 8.12. It shows the Er^{3+} ion absorption spectra change with different kind of alkali ions. The absorption cross-sections of these four peaks and the peak ratio changes against the field strength of alkali ions are also shown in figure 8.13 and 8.14, respectively. From these figures, the absorption shapes are very similar in different alkali ion glasses, the cross-sections of these 4 peaks decrease gently following Li_2O , Na_2O and K_2O sequence (or increase as the field strength of alkali ions increases), the peak ratio of I_{1495}/I_{1532} also decreases while I_{980}/I_{1532} and I_{800}/I_{1532} change much less. The main reason is from the refractive index change of glass, with Li_2O , the glass has the highest density, smallest molar volume, therefore, it has the largest refractive index.

In the ternary glass system, Er^{3+} absorption properties are also measured with different ZnO concentration. When ZnO replaces TeO_2 in $(89-x)\text{TeO}_2$ - $x\text{ZnO}$ - $10\text{Na}_2\text{O}$ - $1\text{Er}_2\text{O}_3$ ($x = 4, 9, 14, 19$) glass, the glasses were numbered as Z1, Z2, Z3 and Z4 respectively. Figure 8.15 and 8.16 show the absorption cross-sections of these four peaks and the peak ratio changes with various ZnO concentration, respectively.

The cross-sections and peak ratios change very little, it shows Er^{3+} absorption spectrum does not have the same sensitivity with the change of alkali ions. Because ZnO is network intermediate, it breaks the network structure not so strongly as alkali oxides, the variation of glass structure changes less and the refractive index changes less. Therefore, the interaction between Er^{3+} ions with the glass has less change.

8.2.2 Er^{3+} absorption spectra in tellurite glass modified by heavy metal oxides

In chapter 5 and 6, we discussed Er^{3+} ion absorption and fluorescent properties in germanate and silicate glasses modified by heavy metal oxides (HMO) and fluorides. In tellurite glasses, HMO such as PbO , BaO , Bi_2O_3 and WO_3 are added in and the glass compositions are designed as:

TEWO: 70TeO₂-9Bi₂O₃-20 WO₃-1Er₂O₃

TEBAPB: 70TeO₂-14BaO-15PbO-1Er₂O₃

The Er³⁺ ion absorption properties in HMO tellurite glass are used to compare with that in sodium zinc tellurite glass,

N4: 70TeO₂-9ZnO-20Na₂O-1Er₂O₃

Table 8.1 illustrates the absorption cross-sections of these four peaks and the peak ratios changes in these three samples. Er³⁺ absorption cross –sections and peak ratios in TEBAPB and N4 are very close, in TEWO, the cross-sections at 1495 and 980 nm are slightly higher, at the other two peaks, the cross-sections are also very close with other samples. Especially for the increasing ratio of I₁₄₉₅/I₁₅₃₂, it means the interaction of Er³⁺ ions with glass structure becomes stronger with the addition of Bi₂O₃ and WO₃. From the Raman spectra in figure 7.39, WO₃ comes into the glass network, Bi₂O₃ has the same role with Ga₂O₃ in glass formation, these two HMO increased the integrity of glass, therefore, it increases the interaction between Er³⁺ ions with glass structure and provide more sites for Er³⁺ ions.

Table 8.1 Er³⁺ ion absorption cross-sections and peak ratio in tellurite glass modified by HMO

glass	Absorption cross-section $\pm 0.05 \cdot 10^{-21} \text{cm}^2$				Peak ratio ± 0.01		
	1532 nm	1495 nm	980 nm	800 nm	I ₁₄₉₅ /I ₁₅₃₂	I ₉₈₀ /I ₁₅₃₂	I ₈₀₀ /I ₁₅₃₂
TEWO	7.78	5.73	3.36	1.18	0.74	0.43	0.15
TEBAPB	7.70	5.20	2.96	1.26	0.68	0.38	0.16
N4	7.50	5.04	2.92	1.21	0.67	0.39	0.16

8.2.3 Er³⁺ absorption spectra in tellurite glass modified by chloride and fluoride

In Er³⁺ doped tellurite glass, Er³⁺ ion absorption properties were measured when glass was modified by chloride and fluoride. In 80.5TeO₂-10Na₂O-9X-0.5Er₂O₃ (X = BaO, BaCl₂ and BaF₂) glass, figure 8.17 shows the Er³⁺ ion absorption spectrum changes with modifiers BaO, BaCl₂ and BaF₂. The absorption cross-sections of these four peaks and the peak ratio changes against F_a, which is defined in chapter 7, are also shown in figure 8.18 and 8.19. They show that the absorption shapes are very similar, the cross-sections of these 4 peaks decrease gently following BaO, BaCl₂ and

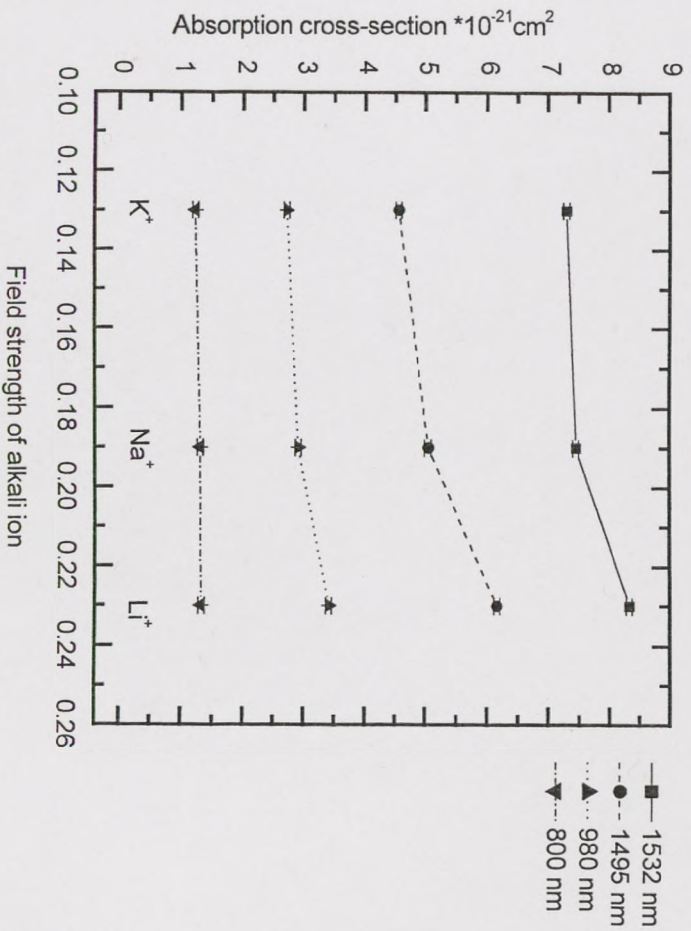


Fig. 8.13 Er^{3+} ion absorption cross-section change in $70\text{TeO}_2\text{-}9\text{ZnO-}20\text{R}_2\text{O-}1\text{Er}_2\text{O}_3$ ($\text{R}_2\text{O}=\text{Li}_2\text{O}, \text{Na}_2\text{O}$ and K_2O) glass

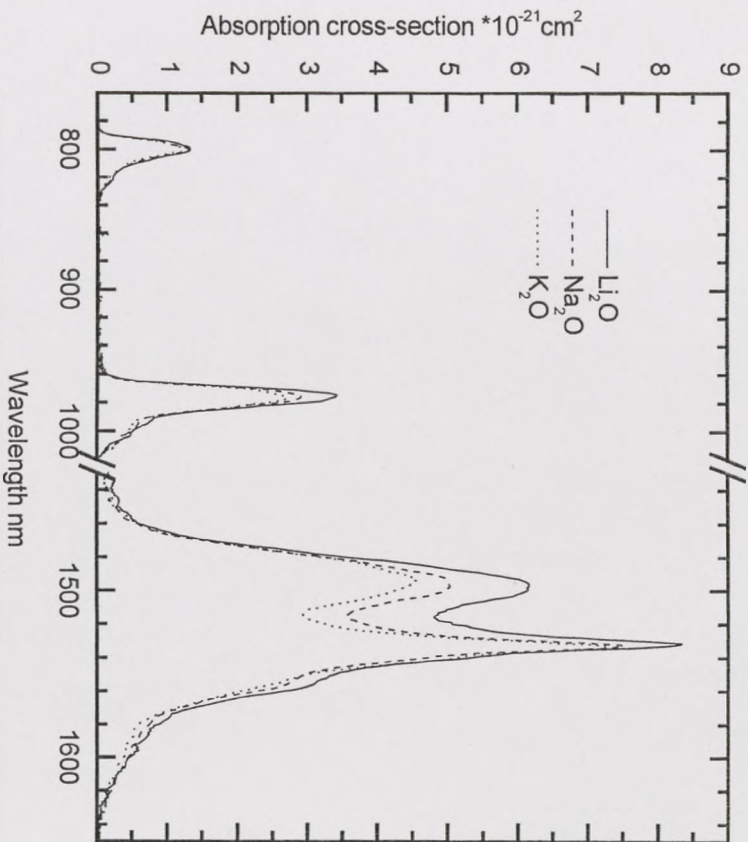


Fig. 8.12 Er^{3+} ion absorption spectra in 70TeO_2 - 9ZnO - $20\text{R}_2\text{O}$ - $1\text{Er}_2\text{O}_3$ ($\text{R}_2\text{O}=\text{Li}_2\text{O}$, Na_2O and K_2O) glass

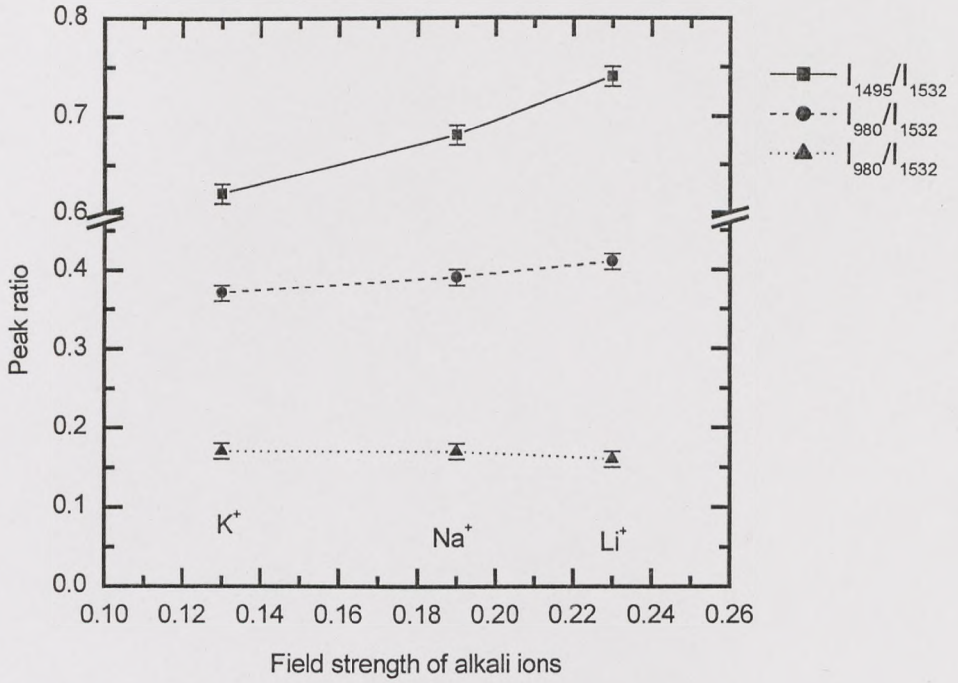


Fig. 8.14 Er³⁺ ion absorption peak ratio change in 70TeO₂-9ZnO-20R₂O-1Er₂O₃ (R₂O=Li₂O, Na₂O and K₂O) glass

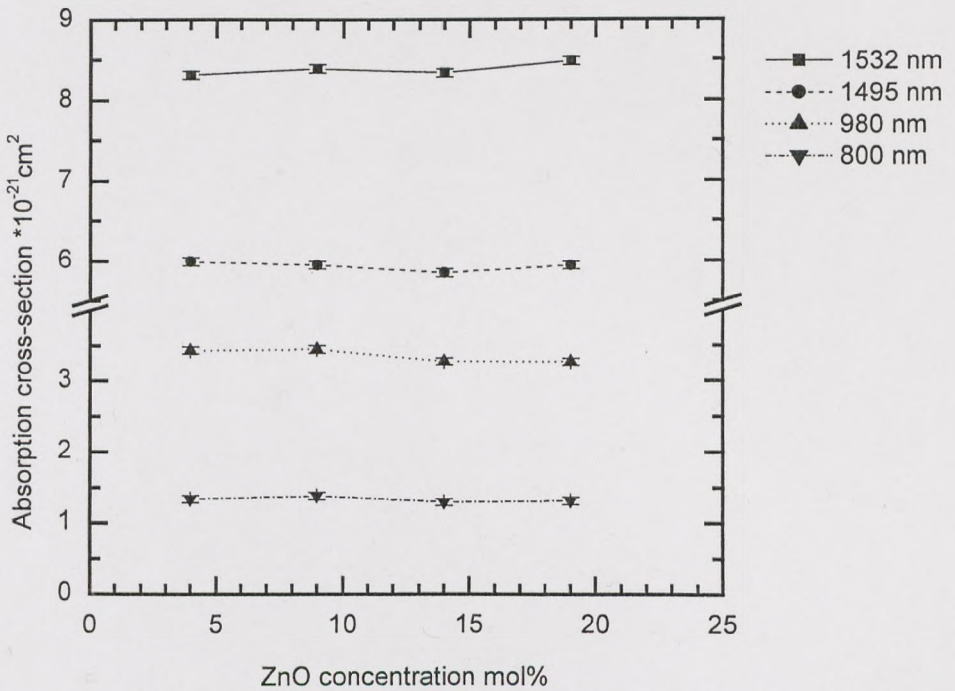


Fig. 8.15 Er³⁺ ion absorption cross-section change with various ZnO concentration in tellurite glass

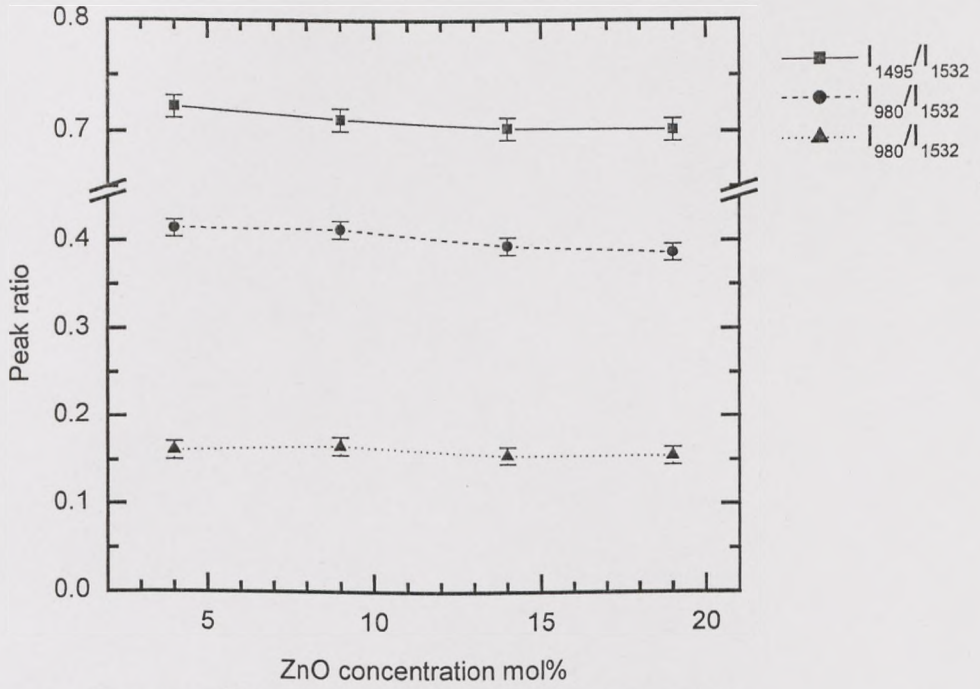


Fig. 8.16 Er³⁺ ion absorption peak ratio change with various ZnO concentration in tellurite glass

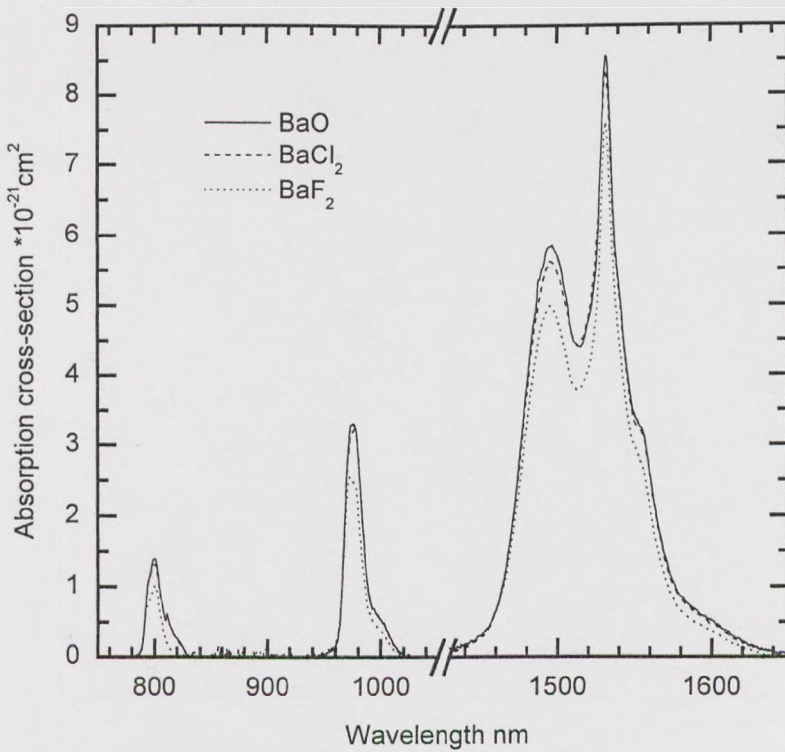


Fig. 8.17 Er³⁺ ion absorption spectra in 80.5TeO₂-10Na₂O-9X-0.5Er₂O₃ (X=BaO, BaCl₂ and BaF₂) glass

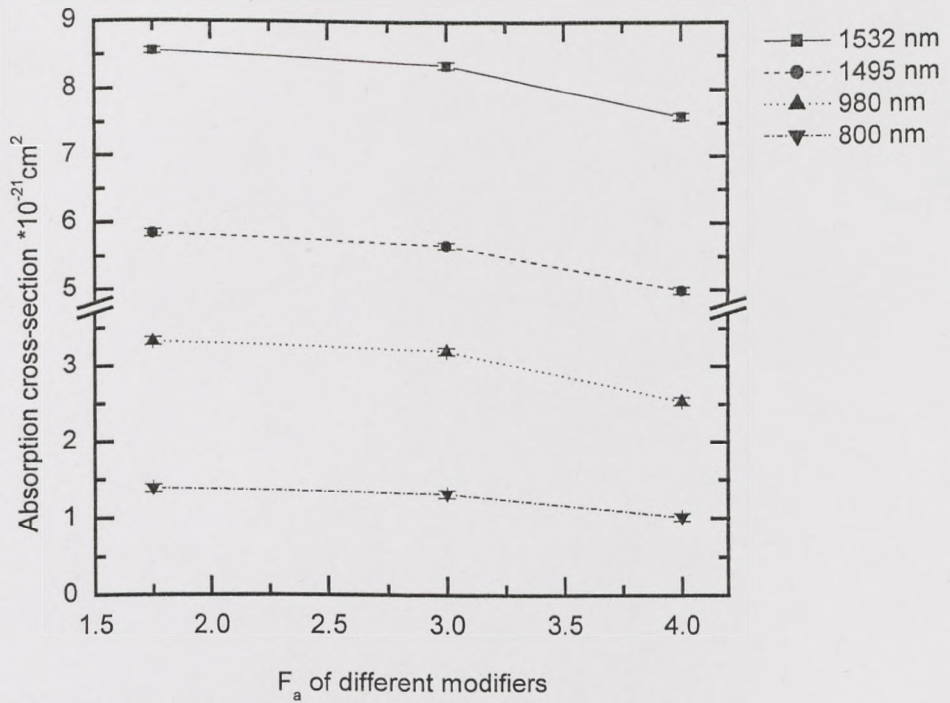


Fig. 8.18 Er^{3+} ion absorption cross-section in 80.5TeO_2 - $10\text{Na}_2\text{O}$ - 9X - $0.5\text{Er}_2\text{O}_3$ ($\text{X}=\text{BaO}$, BaCl_2 and BaF_2) glass

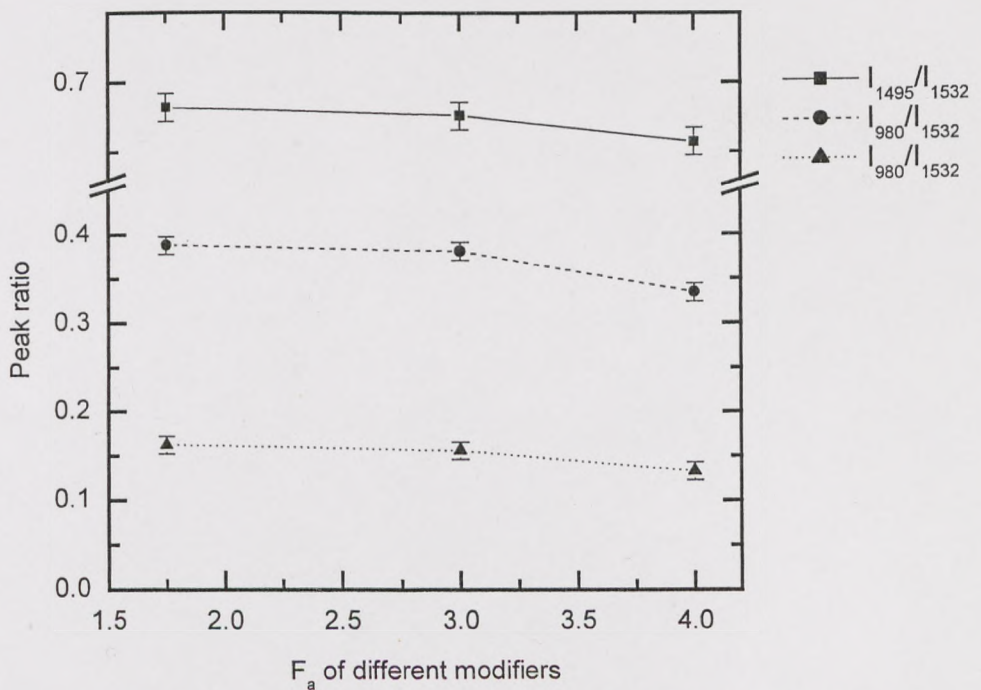


Fig. 8-19 Er^{3+} ion absorption peak ratio in 80.5TeO_2 - $10\text{Na}_2\text{O}$ - 9X - $0.5\text{Er}_2\text{O}_3$ ($\text{X}=\text{BaO}$, BaCl_2 and BaF_2) glass

BaF₂ sequence (as F_a increases), the peak ratios decrease more gently. These mean Er³⁺ ions mainly connect with oxygen by forming [ErO₆], chloride and fluoride ions connect with Te⁴⁺ to modify the strength of crystal field. Therefore the ionicity of the glass will increase. From the Raman spectra, fluorine ions can break the network more than oxygen and chlorine ions, this resulted in more non-bridging oxygen and looser structure to decrease the interaction between Er³⁺ ions with glass structure. The effect of chlorine ions is between fluorine and oxygen ions. Therefore, the absorption cross-sections gently decrease following BaO, BaCl₂ and BaF₂ sequence.

8.2.4 Er³⁺ absorption spectra in different kinds of glass

The absorption properties of Er³⁺ ion have been discussed in different kinds of tellurite glasses above. In chapter 5 and 6, these properties in HMO germanate and modified silicate glasses were also discussed respectively. ZBLAN is a very typical fluoride glass. In this part, Er³⁺ ion absorption properties in these four kinds of glasses will be compared and discussed. Figure 8.20 shows the absorption spectra in these four glasses. The absorption cross-sections of these four peaks and the peak ratio changes are also shown in table 8.2.

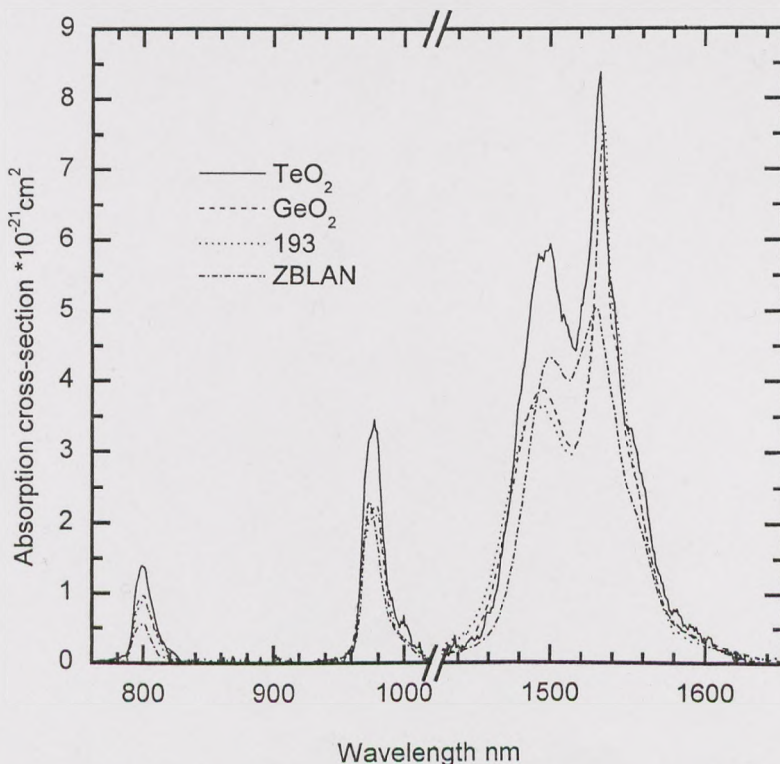


Fig. 8.20 Er³⁺ ion absorption spectra in different kind of glasses

Table 8.2 Er³⁺ ion absorption cross-sections and peak ratio in tellurite (N2), HMO germanate (GE3), modified silicate (193) and ZBLAN fluoride glasses.

glass	Absorption cross-section $\pm 0.05 \cdot 10^{-21} \text{cm}^2$				Peak ratio ± 0.01		
	1532 nm	1495 nm	980 nm	800 nm	I_{1495}/I_{1532}	I_{980}/I_{1532}	I_{800}/I_{1532}
TeO ₂ (N2)	8.39	5.96	3.46	1.39	0.71	0.41	0.17
HMO GeO ₂	7.40	3.88	2.26	0.97	0.52	0.31	0.13
Modified SiO ₂	7.60	3.70	2.13	0.89	0.49	0.28	0.12
ZBLAN	5.06	4.35	2.30	0.55	0.86	0.46	0.11

From figure 8.20, the main concern is about 1500 nm peak, there are shifts in the peak position, the spectra of Er³⁺ ions in modified silicate and HMO germanate glasses are very similar, including the shape and the height. They have the longest absorption peak wavelength, the heights are much higher than ZBLAN and lower than tellurite glass. Fluoride ZBLAN glass has the shortest absorption peak wavelength, and the absorption peak in tellurite follows the ZBLAN. From table 8.2, the cross-sections and peak ratios decrease in oxide glasses in the following order: TeO₂, GeO₂ and SiO₂. In ZBLAN fluoride glass, the cross sections at 1532 and 800 nm are the lowest, at the shoulder 1495 and 800 nm, they are higher than that in GeO₂ and SiO₂ and lower than that in TeO₂. The ratio of I_{1495}/I_{1532} is the highest in ZBLAN, it means the absorption spectrum shape is the flattest in ZBLAN. In order to discuss the property change in these four kinds of glasses, the bond properties of glass network former such as bond length, bond strength, bond ionicity and electronegativity of elements are listed in table 8.3. The bond ionicity is calculated from the difference of electronegativity [2].

Table 8-3 Bond properties of glass network former in the 4 kinds of glasses

Properties	Si-O	Ge-O	Te-O	Zr-F
Bond length Å	1.60	1.66	2.10	1.94
Bond strength $2Z/a^2$	2.6	2.4	1.5	1.7
electronegativity X_A	3.5	3.5	3.5	4.0
electronegativity X_B	1.8	1.8	2.1	1.4
$X_A - X_B$	1.7	1.7	1.4	2.6
Ionic character %	48	48	42	80
Phonon energy cm^{-1}	~1100	~900	650~750	~600

In ZBLAN fluoride glass, it is ionic bond glass, in oxide glasses, they are all covalent-ionic bonds, a slightly more covalent. In an ionic bond the electrons are highly localised because electrons are donated i.e. F is an electron acceptor. In a covalent bond, the electrons are not localised as they are shared. The tendency for delocalisation depends upon the nature of cation/anion interaction which is determined the by the ionicity and covalence of bond or the electronegativity of the elements. Because of the delocalised electrons, the rare earth ion electron 4f-shell experiences a greater dipole/dipole interaction which affects the strengths of absorption and emission spectra. From this point, the interaction between Er^{3+} ion and glass is weaker in the ZBLAN fluoride glass than in oxide glasses.

Figure 8.21 shows the electron-dipole interaction pattern between Er^{3+} ion and glasses. Because the Stark split is dependent on the interaction between the Er^{3+} ion and the glass former unit, the electron-dipole or multipole of Er^{3+} ion will determine this effect. In ZBLAN fluoride glass, the electron-dipole momentum P_1 of Er-F^- is smaller than that of Er-O^{2-} , this also results in a weaker interaction. The weaker interaction in fluoride glass will cause the narrower Stark split which was observed by Zemon [3]. The smaller absorption cross-sections of Er^{3+} ion in ZBLAN fluoride glass are also the results of the weaker interaction than in oxide glasses. The wavelength blue shifts in fluoride glass however more strongly dependent on the anionic field which in case of F^- is maximum.

Among oxide glasses such as modified silicate (193), HMO germanate (GE3) tellurite (N2) glasses, tellurite glass is less ionic due to the presence of LPE than the silicate and germanate glasses from table 8.3, consequently, the electron delocalisation will be greater than in silicate and germanate glasses, this results in stronger interaction between Er^{3+} ion and tellurite glass. From the quadrupole in figure 8.21, because of the bond strength change following $\text{Si-O} > \text{Ge-O} > \text{Te-O}$, the electron-dipole moment P2 in silicate glass is the highest and in tellurite glass is the lowest. The phonon energy derived from Raman spectra provides the evidence. When Er^{3+} ions form multipole in the non-bridge oxygen sites, the electron-dipole moment P1 will be the highest in tellurite glass. Thus the interaction of between Er^{3+} ions and glass former units will be the strongest in tellurite glass. In germanate glass is the second and the third is in silicate glass. Therefore, the Er^{3+} ion absorption cross-sections and peak ratio are the highest in tellurite glass, in germanate glass is a slightly higher than in silicate glass.

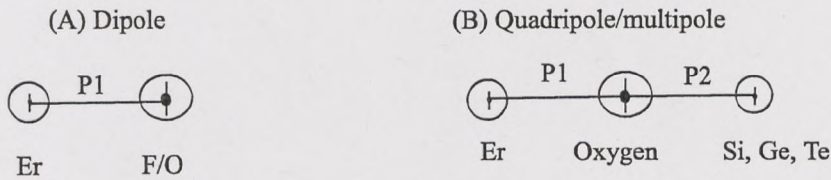


Figure 8.21 Er ion forms dipole and Quadruple in different glasses

8.3 Er³⁺ fluorescence properties in tellurite glass

The amplifier in the 3rd communication window is the ${}^4I_{13/2} \rightarrow {}^4I_{15/2}$ transition at 1.5 μm , consequently our study of Er³⁺ fluorescence properties in tellurite glass are concentrated on the metastable state ${}^4I_{13/2}$. The fluorescence properties include the lifetime of ${}^4I_{13/2}$, emission cross-section, oscillator strength and spectrum of the ${}^4I_{13/2} \rightarrow {}^4I_{15/2}$ transition. These properties will be measured in the same glass with various Er³⁺ concentrations and different glass compositions with the constant Er³⁺ concentration.

8.3.1 Er³⁺ fluorescence properties in a tellurite glass with different Er³⁺ ion concentration

8.3.1.1 Emission spectra

In the ternary 80TeO₂-10ZnO-10Na₂O tellurite glass, the concentration of Er₂O₃ was varied. Figure 8.22 shows the normalised emission spectra of Er³⁺ ions in different concentrations. With increasing Er₂O₃ concentration from 1,000 ppm to 50,000 ppm, the emission spectra become slightly broader. The spectrum shape is very similar, the peak position is the same. The shoulders around 1510 and 1560 nm are rising gently.

For a three-level system, McCumber theory has been successful in providing not only spectral information but also the absolute cross-sections. For the ${}^4I_{13/2} \rightarrow {}^4I_{15/2}$ transition in fluorophosphate glass, the measured stimulated emission cross-section with that calculated from the absorption cross-section using the McCumber theory are in excellent agreement [4]. In the 80TeO₂-10ZnO-10Na₂O tellurite glass doped with 3,000 Er₂O₃ ppm, figure 8.23 shows the measured absorption cross-section and emission spectrum. The emission cross-section is calculated from the McCumber theory. The shapes of the measured and calculated emission spectra are in good agreement although the shoulder around 1510 nm is a little lower from the McCumber theory. The maximum calculated emission cross-section is slightly higher than absorption cross-section.

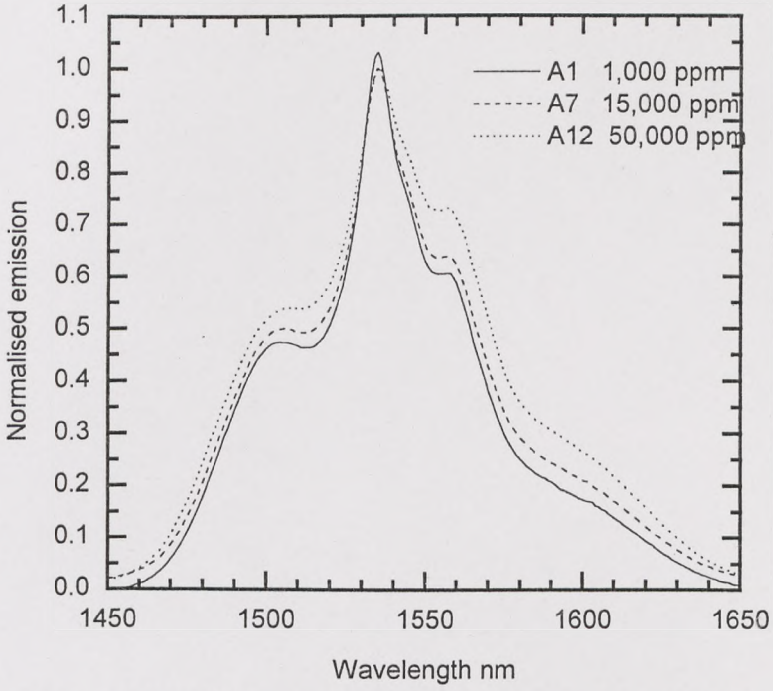


Fig. 8.22 Er^{3+} ion emission spectra with various Er_2O_3 concentrations in $80\text{Te}_2\text{O}-10\text{Na}_2\text{O}-10\text{ZnO}$ glass

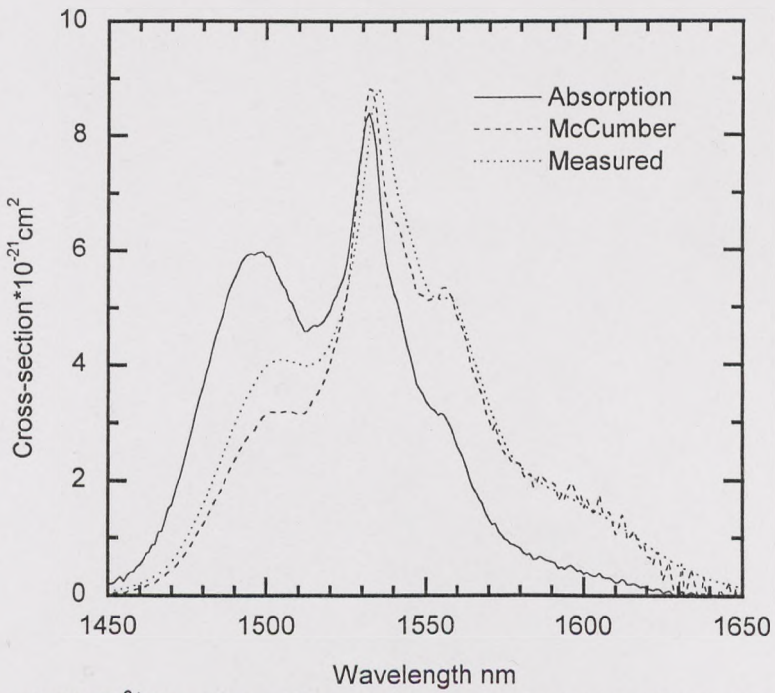


Fig. 8.23 Er^{3+} ion absorption and emission cross-sections measured and calculated from McCumber theory in tellurite glass

In Er^{3+} ion doped tellurite glass, we find there is very strong re-absorption and re-emission due to 3-level transitions and a large overlap between absorption and emission spectra. Figure 8.24 shows the normalised emission spectra of tellurite glass doped with 35,000 Er_2O_3 ppm when the pumping laser is launched at different places of the sample. When the pumping laser is launched very near the sample surface, the emission signals are collected near the surface, the spectrum is like the very low Er^{3+} ion concentration emission spectrum shape. When the pumping laser is launched at the middle of the sample, the emission signals are also collected near the surface, the emission spectrum is totally deformed. The spectrum shifts to longer wavelengths. This is caused by the re-absorption and re-emission of radiation by Er^{3+} ions. Because at 1.5 μm emission and absorption occur at the same energy levels with different sub-levels, when the stimulated fluorescent signals travel in the unpumped area, they are absorbed by the ions at the ground state $^4\text{I}_{15/2}$ to excite these ions to the metastable state $^4\text{I}_{13/2}$, these ions then re-emit 1.5 μm signals and come to the ground state. From the Er^{3+} ion absorption and emission spectra in figure 8.23, at short wavelength, the absorption cross-section is stronger than the emission; at long wavelength, emission cross-section is stronger than absorption. Therefore, the re-emission occurs in the long wavelength, thus the peak and the shape of emission spectrum shift to longer wavelengths, the shape becomes more flat and broader.

8.3.1.2 Oscillator strengths and radiative rate

From chapter 3, the oscillator strength was described in terms of the integrated absorption cross-section from the ground multiplet to some higher multiplet. The oscillator strengths of absorption transitions are calculated using Equation 3.2 from the absorption spectrum of Er^{3+} ion doped tellurite glass. All transitions are assumed to be electric dipole in nature, except for the $^4\text{I}_{15/2} \rightarrow ^4\text{I}_{13/2}$ transition, which has a substantial magnetic dipole component. Using Judd-Ofelt theory, parameters Ω_2 , Ω_4 and Ω_6 are determined by a best fit of calculated and observed oscillator strengths from Equation 3.11. These parameters may then be used to calculate the electric dipole contribution to the total spontaneous-emission probabilities. Figure 8.25 shows how these parameters change with different Er_2O_3 concentration. Although Ω_4 and Ω_6 remain virtually unchanged, the values of Ω_2 decrease very slightly with increasing

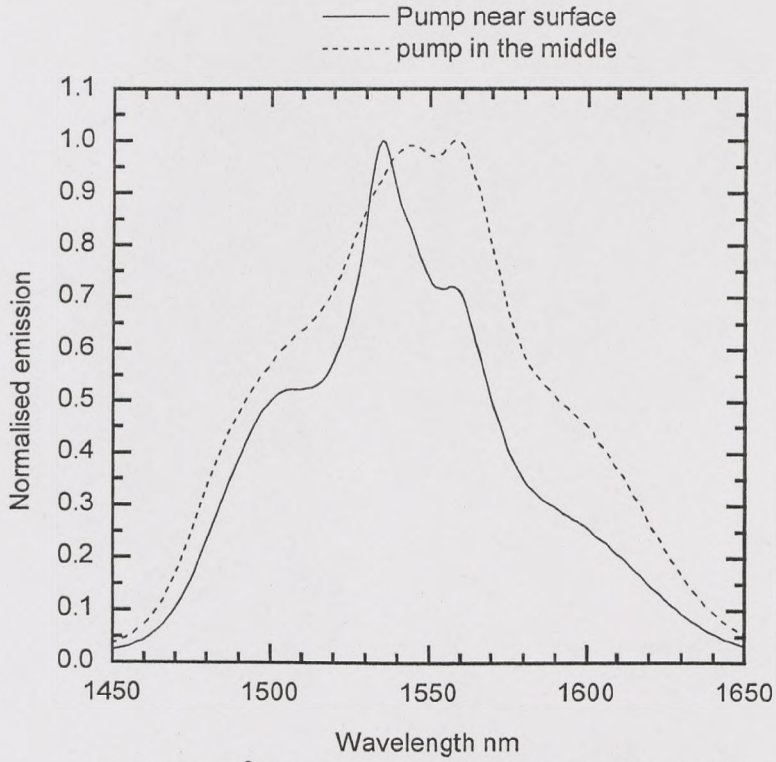


Fig. 8.24 Er^{3+} ion emission spectra with 3.5 wt% Er_2O_3 in tellurite glass with different pump position

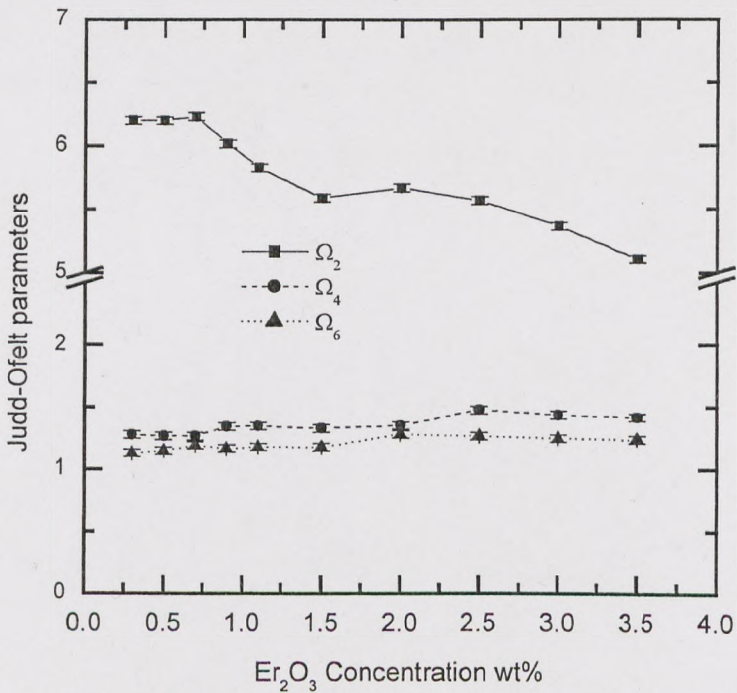


Fig. 8-25 Judd-Ofelt parameters in tellurite glass with various Er_2O_3 concentrations

Er_2O_3 concentration. These three intensity parameters Ω_t are host dependent and are determined for a given combination of dopant and host. There is no clear physical meaning to the intensity parameters other than that Ω_2 is related with the degree of covalency of materials: ionic materials like fluorides have very small values of Ω_2 , while covalent materials like silicates have large values. The slight decrease of Ω_2 give an evidence that Er^{3+} ions improve the integrity of glass network which is consistent with the change of molar volume and thermal property in tellurite glasses.

Table 8.4 illustrates the measured and calculated oscillator strengths for all absorption levels, the radiative rate for the ${}^4\text{I}_{13/2} \rightarrow {}^4\text{I}_{15/2}$ transition and Judd-Ofelt parameters for 4 selected different Er_2O_3 concentrations. With increasing Er_2O_3 concentration, the measured oscillator strength for ${}^4\text{I}_{15/2} \rightarrow {}^4\text{I}_{13/2}$ transition decreases slightly, the magnetic dipole oscillator strength decreases, the electric dipole oscillator strength increases, the magnetic dipole accounts for about 25% to 35% of total oscillator strength. For the other transitions, the measured and calculated electric dipole oscillator strengths are very close. The calculated radiative rate for ${}^4\text{I}_{13/2} \rightarrow {}^4\text{I}_{15/2}$ transition increases slightly but they are very close for different Er_2O_3 concentration.

8.3.1.3 Er^{3+} concentration quenching and OH^- impurity effect

Concentration quenching is the reduction in the quantum efficiency of an ion with increasing concentration of that ion. It usually manifests itself as a shortening of the excited state lifetime. Figure 8.26 shows the lifetime of Er^{3+} ion at ${}^4\text{I}_{13/2}$ level with different concentration in the same tellurite glass with different OH^- concentration. Er_2O_3 concentration varied from 500 ppm to 46,000 ppm. The OH^- ion concentration was changed by melting the glass in different atmospheres from air to dry air. Figure 8.27 shows the OH^- content in these two melting conditions. There is a very broad OH^- absorption peak near $3.3 \mu\text{m}$ in tellurite glass. This peak is much broader and at longer wavelength than that in silicate and fluoride glasses, in which the wavelength is 2.75 and $2.87 \mu\text{m}$, respectively [5, 6]. The lifetimes were measured by fitting the decay rate from ${}^4\text{I}_{13/2}$ lasing level. It was found to be a single exponential function in all samples, regardless of Er^{3+} ion concentration. One example of the goodness of a single exponential fit is shown in figure 8.28.

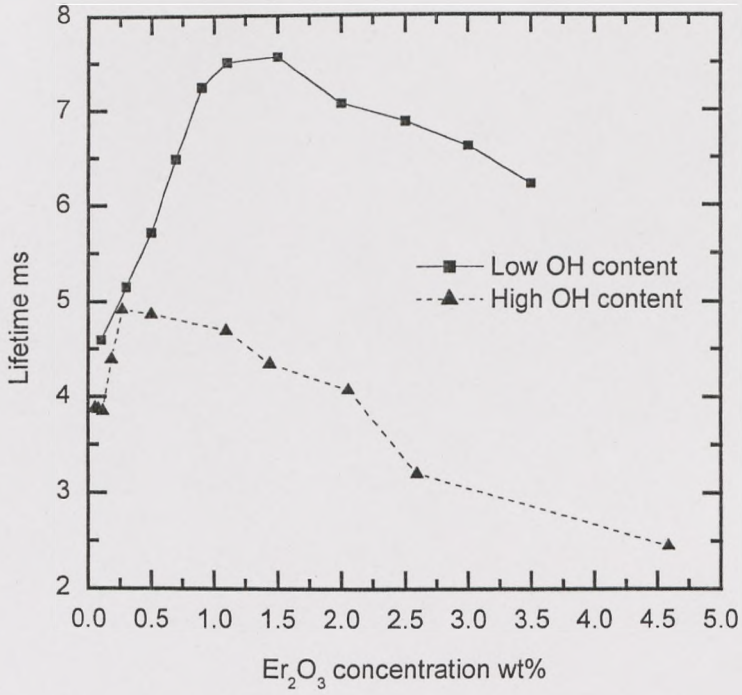


Fig. 8.26 Lifetimes for ${}^4I_{13/2} - {}^4I_{15/2}$ transition at $1.5 \mu\text{m}$ as a function of the Er_2O_3 concentration in tellurite glass

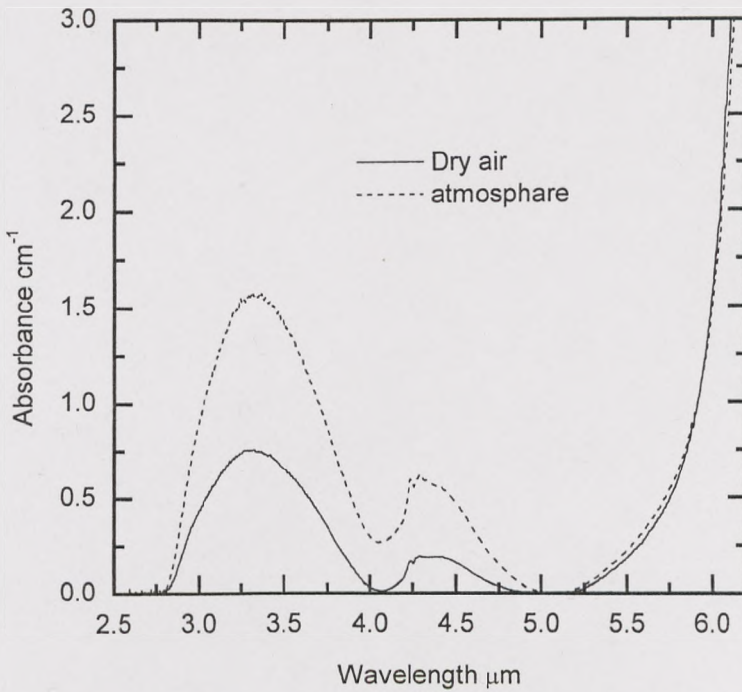


Fig. 8.27 OH⁻ absorption spectra in tellurite glass melted in different atmosphere

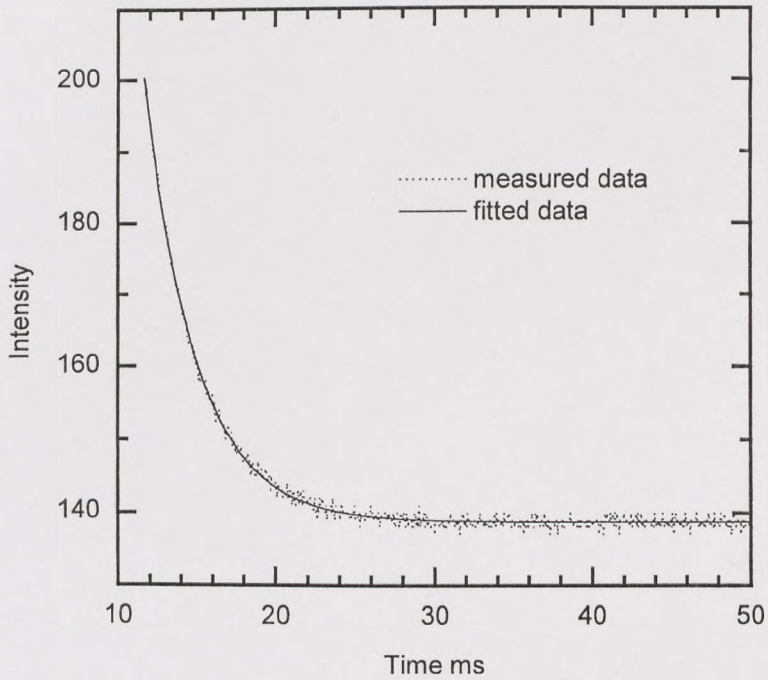


Fig. 8.28 Fluorescence decay of Er³⁺ ion in tellurite glass (N₂) at 1.5 μm

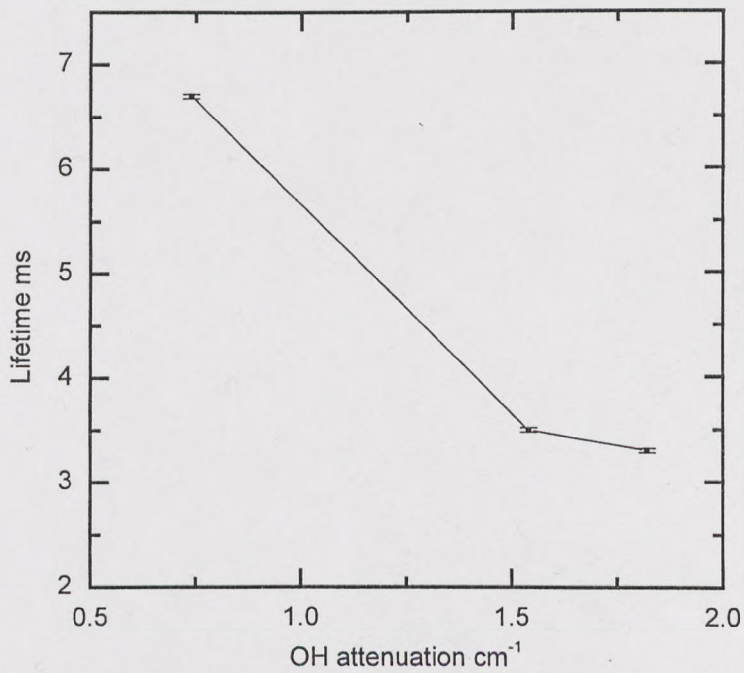


Fig. 8.29 Lifetimes for ⁴I_{13/2} - ⁴I_{15/2} transition at 1.5 μm as a function of the OH concentration in tellurite glass

Table 8.4 Measured and calculated oscillator strengths of Er^{3+} ion and calculated radiative rate ${}^4\text{I}_{13/2} \rightarrow {}^4\text{I}_{15/2}$ in the same host with different concentration. All transitions for oscillator strength are from the ${}^4\text{I}_{15/2}$ level to the levels indicated.

level	Total Oscillator strength ($\times 10^8$)							
	0.3 wt% Er_2O_3		0.7 wt% Er_2O_3		1.5 wt% Er_2O_3		3.5 wt% Er_2O_3	
	Meas ± 5	<i>Calc</i>	Meas ± 5	<i>Calc</i>	Meas ± 5	<i>Calc</i>	Meas ± 5	<i>Calc</i>
${}^4\text{I}_{13/2}$	264		259		249		247	
Magnetic dipole		85		77		68		59
Electric dipole		179		182		181		188
${}^4\text{I}_{11/2}$	89	89	91	93	85	90	84	91
${}^4\text{I}_{9/2}$	34	37	35	37	38	39	42	42
${}^4\text{F}_{9/2}$	337	266	323	271	313	277	307	294
${}^4\text{S}_{3/2}$	56	65	65	69	70	68	77	71
${}^2\text{H}_{11/2}$	1352	1376	1373	1382	1272	1264	1199	1183
${}^4\text{F}_{7/2}$	243	259	232	270	227	270	239	284
Radiative rate ± 5 ${}^4\text{I}_{13/2} \rightarrow {}^4\text{I}_{15/2} (\text{s}^{-1})$	237		248		247		256	
$\Omega_2 \pm 0.1 (10^{-20} \text{cm}^2)$	6.2		6.2		5.6		5.1	
$\Omega_4 \pm 0.1 (10^{-20} \text{cm}^2)$	1.3		1.3		1.3		1.4	
$\Omega_6 \pm 0.1 (10^{-20} \text{cm}^2)$	1.1		1.1		1.2		1.2	

From figure 8.26, the two lifetime quenching curves have two common characters, firstly the lifetimes increased at low Er_2O_3 concentration, secondly they have a maximum point which represents the longest lifetime. After the peak, the lifetime decreases with increasing Er_2O_3 concentration, the quenching rates are very slow. The difference between the two OH^- concentration data is that the peak has shifted from 11,000 ppm to 5,000 ppm of Er_2O_3 with higher OH^- concentration, and the lifetimes are much longer when glass contains lower concentration of OH^- . For lower OH^- concentration, the maximum lifetime of ~ 7.6 ms was observed at around 11,000 ppm Er_2O_3 . With the increase in OH^- ion concentration in host glass, the peak shifts to

lower concentration around 5,000 ppm having lifetime of ~ 4.9 ms. This is very different from Er^{3+} in silicate glass. In silicate glass, the lifetime drops continuously as the concentration of Er_2O_3 increases. Normally, the non-radiative rate should increase with the increase of Er^{3+} ion concentration, it is proportional to the square of dopant concentration which is shown in equation 8.1. If there is impurity of OH^- in glass, the impurity quenching rate is also proportional to the impurity and Er^{3+} ion concentrations which the relation is shown in equation 8.2. From these two equations, the measured decay rate can be expressed as equation 8.3.

$$\omega_{\text{quench}} \sim C_{\text{Er}}^2 \quad 8.1$$

$$\omega_{\text{quench}} \sim C_{\text{Er}} \times C_{\text{OH}} \quad 8.2$$

$$\omega_{\text{Meas}} = \omega_{\text{rad}} + A \times C_{\text{Er}}^2 + B \times C_{\text{Er}} \times C_{\text{OH}} \quad 8.3$$

where ω_{meas} is the measured decay rate, ω_{rad} is the calculated radiative rate, C_{Er} is Er^{3+} ion concentration, C_{OH} is OH^- ion concentration, A and B are constants.

For this Er^{3+} doped tellurite glass, Er^{3+} ion concentration quenching does not follow the above equations. The measured radiative rate is even lower than the rate calculated from Jud-Ofelt theory. This is probably related to the special structure of tellurite glass, and will be discussed later.

The data analysis confirms that there is an absence of Er^{3+} -ion clustering even at high doping level. For Er^{3+} -doped glass, concentration quenching at ${}^4\text{I}_{13/2}$ level is mainly from up-conversion process which was shown in figure 4.5. At concentration of Er^{3+} -ions less than 10,000 ppm, the sharp increase in the lifetime of ${}^4\text{I}_{13/2}$ level confirms that neither the OH^- activated quenching nor the ion-ion up-conversion is a dominating factor. Over 15,000 ppm, the lifetime drops more gently in low- OH^- glass than in a high- OH^- glass, indicating that the ion-ion up-conversion process dominates only after 15,000ppm. The lower values of the measured lifetimes in high- OH^- glass

are not unexpected, which is due to the increase in OH^- ion induced quenching. The following part will show the effect of OH^- ion concentration on the lifetime.

The lifetimes were measured in tellurite glasses with 1 mol% Er_2O_3 at various OH^- concentrations. Figure 8.29 shows the OH^- concentration quenching. Because we do not know OH^- extinction coefficient in tellurite glass, the OH^- attenuation was used to represent OH^- concentration. When OH^- concentration increases, the lifetime decreases fast at the beginning, then it levels off. Figure 8.30 show the measured decay rates change as a function of the OH^- concentration, it is linear relation with OH^- concentration following equation 8.2. If there is not OH^- impurity in glass, the lifetime could be about 20 ms in maximum in this tellurite glass without Er^{3+} ion concentration quenching.

The OH^- quenching mechanism is a deleterious process which involves energy transfer to the OH^- complex and acts as a trap. It is extremely effective at quenching excited Er^{3+} ions. At this OH^- concentration level, this process can occur through direct transfer from the excited ions to OH^- group. By the comparing the data in figures 8.26 and 8.29, OH^- concentration quenching rate is much faster than Er^{3+} ion quenching rate in the low concentration, which points out to the detrimental effect of the presence of OH^- ions in tellurite glass for designing an Er^{3+} doped optical fibre amplifier.

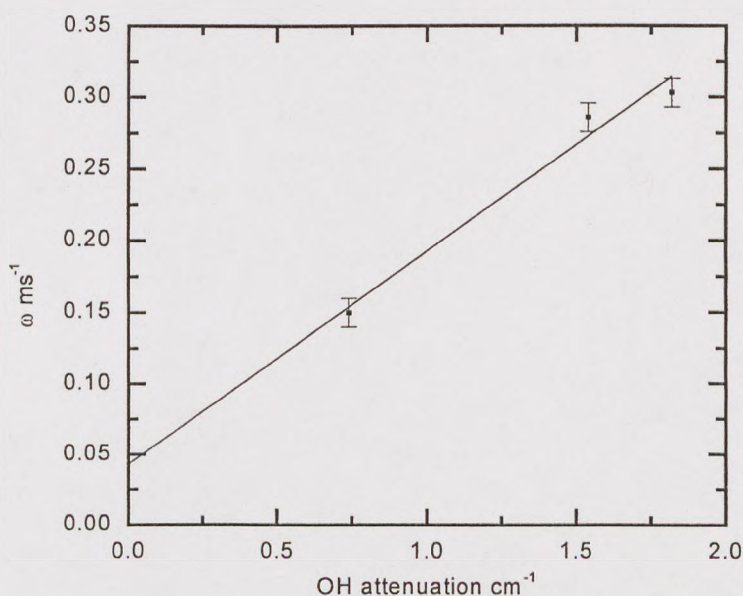


Fig. 8.30 Measured total rate for ${}^4I_{13/2} - {}^4I_{15/2}$ transition at $1.5 \mu\text{m}$ as a function of the OH^- concentration in tellurite glass

8.3.2 Er³⁺ fluorescence properties in tellurite glass with different composition and the same Er³⁺ ion concentration

8.3.2.1 Er³⁺ emission spectra and lifetimes in TeO₂-ZnO-R₂O (R₂O = Li₂O, Na₂O and K₂O) system glass

In this TeO₂-ZnO-R₂O (R₂O = Li₂O, Na₂O and K₂O) ternary glass system, the glass properties such as density, molar volume, IR, UV absorption edge and Er³⁺ ion absorption spectra with different content of Li₂O, Na₂O, K₂O and ZnO were studied before. Fluorescent properties of Er³⁺ ion such as emission spectrum and lifetime in these kinds of glass have also been measured. The following part is going to describe these properties.

As various alkali oxides substitute TeO₂, the Er³⁺ ion emission spectrum changes in (90-x)TeO₂-9ZnO-xR₂O-1Er₂O₃ (R₂O = Na₂O, K₂O and Li₂O; x = 5, 10, 15 and 20) glasses are shown in figure 8.31, 8.32 and 8.33 respectively.

When ZnO replaces TeO₂ in (85-x)TeO₂-xZnO-10Na₂O-1Er₂O₃ (x = 4, 9, 14, 19) glass, the glasses are designated as Z1, Z2, Z3 and Z4, respectively. Figure 8.34 shows the Er³⁺ ion emission spectrum changes with various ZnO concentrations.

In order to compare the effect of different alkali ions on the Er³⁺ ion emission spectrum, figure 8.35 shows the Er³⁺ ion emission spectrum changes with different kind of alkali ions in 70TeO₂-9ZnO-20R₂O-1Er₂O₃ (R₂O = Li₂O, Na₂O and K₂O) glass.

From figure 8.31 and 8.32, with increasing Na₂O and K₂O concentrations, the changes of Er³⁺ ion emission spectrum show the same trend: the spectrum shape is similar, the shoulders around 1510 and 1560 nm coming down and the spectrum becoming narrower.

From figure 8.33 and 8.34, with increasing Li₂O and ZnO concentrations in this glass system, the Er³⁺ ion emission spectra are nearly same, there is little change when Li₂O and ZnO replace TeO₂, which means the interaction between Er³⁺ ion with glass host has little change.

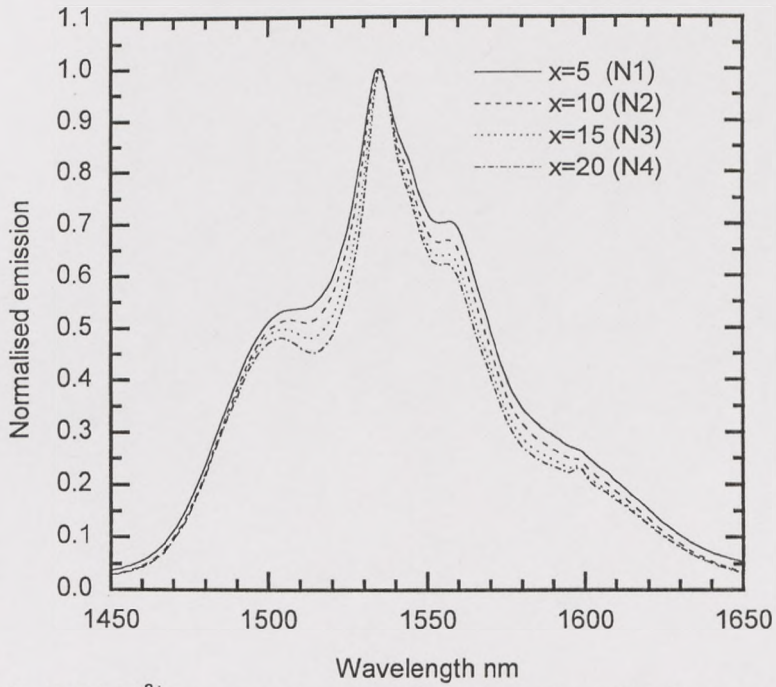


Fig 8.31 Er^{3+} ion emission spectra with various Na_2O concentration in $(90-x)\text{TeO}_2-9\text{ZnO}-x\text{Na}_2\text{O}-1\text{Er}_2\text{O}_3$ ($x=5, 10, 15$ and 20) glass

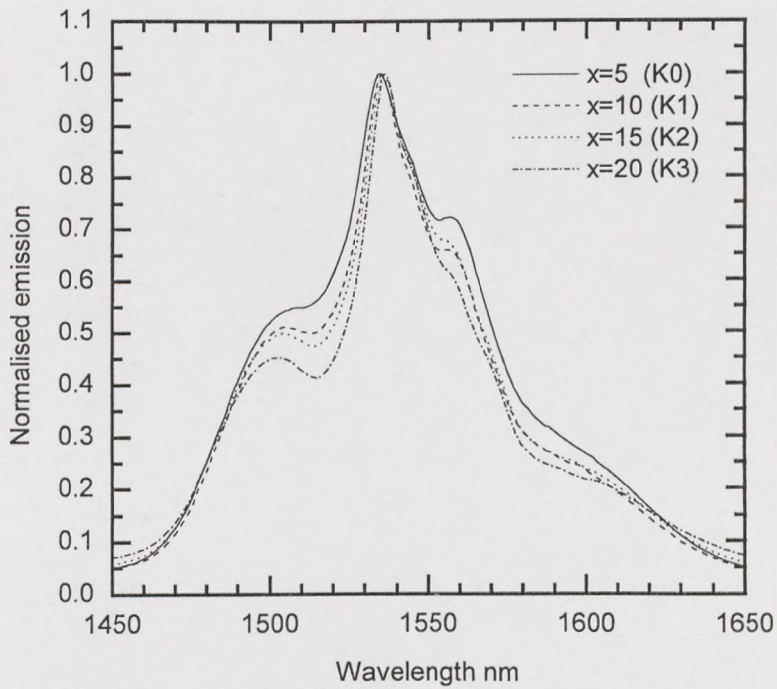


Fig. 8.32 Er^{3+} ion emission spectra with various K_2O concentration in $(90-x)\text{TeO}_2-9\text{ZnO}-x\text{K}_2\text{O}-1\text{Er}_2\text{O}_3$ ($x=5, 10, 15$ and 20) glass

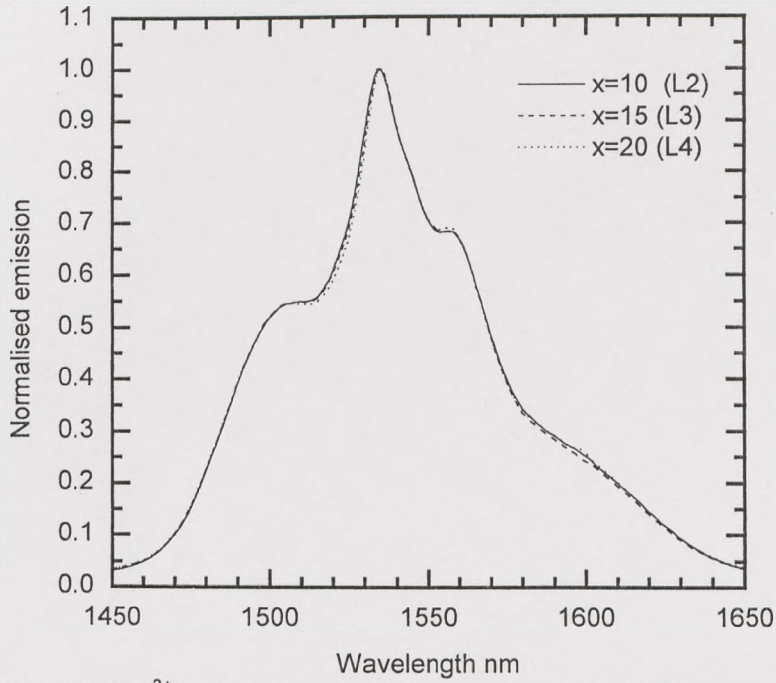


Fig. 8.33 Er^{3+} ion emission spectra with various Li_2O concentration in $(90-x)\text{TeO}_2-9\text{ZnO}-x\text{Li}_2\text{O}-1\text{Er}_2\text{O}_3$ ($x=10, 15$ and 20) glass

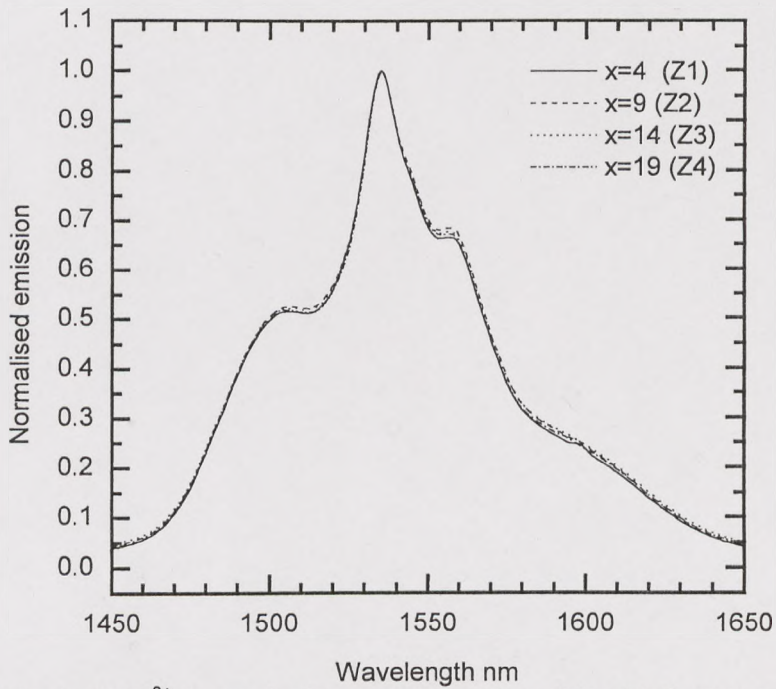


Fig. 8.34 Er^{3+} ion emission spectra with various ZnO concentration in $(90-x)\text{TeO}_2-x\text{ZnO}-10\text{Na}_2\text{O}-1\text{Er}_2\text{O}_3$ ($x=4, 9, 14$ and 19) glass

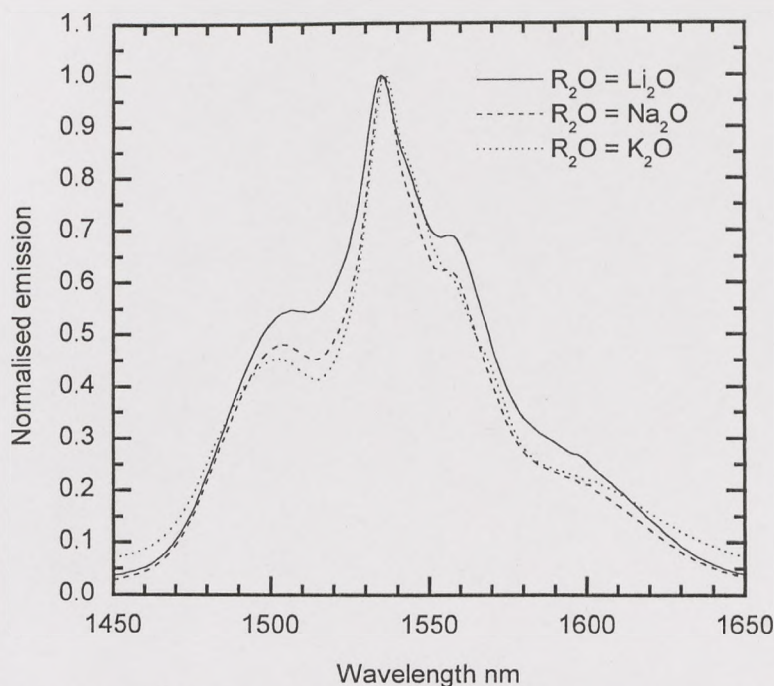


Fig. 8.35 Er^{3+} ion emission spectra with various alkali oxides in $70\text{TeO}_2\text{-}9\text{ZnO-}20\text{R}_2\text{O-}1\text{Er}_2\text{O}_3$ ($\text{R}_2\text{O}=\text{Li}_2\text{O}$, Na_2O and K_2O) glass

From figure 8.35, the Er^{3+} ion emission spectrum become narrower following Li_2O , Na_2O and K_2O in this sequence.

For all these samples, the Judd-Ofelt parameters and lifetimes can be calculated from Judd-Ofelt theory in equation 3.11 and 3.6, non-radiative rate at ${}^4\text{I}_{13/2}$ level can also be calculated from equation 3.19. Table 8.5 shows all these calculated data and measured lifetime. From this table, the Judd-Ofelt parameters Ω_2 , Ω_4 , Ω_6 are between 4.4~6.6, 1.3~2.0, $0.9\sim 1.5\times 10^{-20}$ cm^2 , respectively. For 1mol% Er_2O_3 doped tellurite glass, the calculated lifetimes are between 3.9~5.3 ms, the measured lifetimes are between 3.0~3.7 ms, non-radiative decay rates including Er^{3+} ion up-conversion and OH⁻ quenching rate are between 30~90 s^{-1} , these non-radiative rates are about 20 to 45% of total radiative rate. For different compositions instead of TeO_2 , the lifetime change is not as sensitive as that of absorption and emission spectra, they are similar to each other. There are two reasons, one is the lifetime of Er^{3+} ion at ${}^4\text{I}_{13/2}$ level is decided by Er^{3+} ion radiative rate which is dependent on the Er^{3+} ion, and by impurity OH⁻ concentrations. In these glasses, they are melted in the same condition and have the same Er_2O_3 concentration, therefore the impurity OH⁻ is also nearly the same in all of these glasses. The other reason is that Judd-Ofelt theory has about 10-15% error.

But there is still a trend that the calculated and measured lifetimes increase with increasing alkali oxides and ZnO concentration in tellurite glass because the absorption and emission cross-sections and refractive index decrease in glass.

Table 8-5 Judd-Ofelt parameters, calculated lifetime, measured lifetime and energy transfer rate for ${}^4I_{13/2} \rightarrow {}^4I_{15/2}$ level in Er^{3+} ion doped tellurite glass.

Sample	$\Omega_2 \pm 0.1$ 10^{-20} cm^2	$\Omega_4 \pm 0.1$ 10^{-20} cm^2	$\Omega_6 \pm 0.1$ 10^{-20} cm^2	τ_{calc} $\pm 0.3 \text{ ms}$	τ_{meas} $\pm 0.05 \text{ ms}$	$W_x \pm 10$ s^{-1}
N1	5.8	1.9	1.5	4.0	3.12	71
N2	5.8	1.7	1.2	3.9	3.25	53
N3	6.1	1.5	1.1	4.2	3.06	87
N4	5.6	1.4	1.1	4.6	3.37	81
K0	5.8	1.8	1.3	3.9	3.42	40
K1	6.0	1.5	1.1	4.1	3.08	82
K2	5.9	1.4	1.0	4.8	3.38	89
K3	6.5	1.3	0.9	5.2	3.63	85
L2	4.4	1.7	1.3	3.7	3.02	65
L3	5.7	1.5	1.4	3.5	3.13	41
L4	5.5	1.6	1.2	3.8	3.28	46
Z1	5.9	1.4	1.2	3.9	3.27	53
Z2	5.9	1.7	1.2	3.8	3.30	46
Z3	6.0	1.4	1.2	4.1	3.44	46
Z4	6.2	1.4	1.2	3.9	3.50	33

8.3.2.2 Er^{3+} emission spectra and lifetimes in tellurite glass modified by heavy metal oxides

For heavy metal oxides (HMO) modified Er^{3+} ion doped tellurite glass, the absorption spectra have been studied before. The fluorescent properties in these kinds of glass will be discussed in the following part. Figure 8.36 shows the emission spectra of Er^{3+} ion in HMO tellurite glass TEWO and TEBAPB, Zinc Sodium tellurite

ternary system glass N4, and another two binary glass system: Sodium tellurite and Zinc tellurite glasses.

TEWO: $70\text{TeO}_2 - 9\text{Bi}_2\text{O}_3 - 20\text{WO}_3 - 1\text{Er}_2\text{O}_3$

TEBAPB: $70\text{TeO}_2 - 14\text{BaO} - 15\text{PbO} - 1\text{Er}_2\text{O}_3$

N4: $70\text{TeO}_2 - 9\text{ZnO} - 20\text{Na}_2\text{O} - 1\text{Er}_2\text{O}_3$

TEZNO: $70\text{TeO}_2 - 29\text{ZnO} - 1\text{Er}_2\text{O}_3$

TENAO: $80\text{TeO}_2 - 19\text{Na}_2\text{O} - 1\text{Er}_2\text{O}_3$

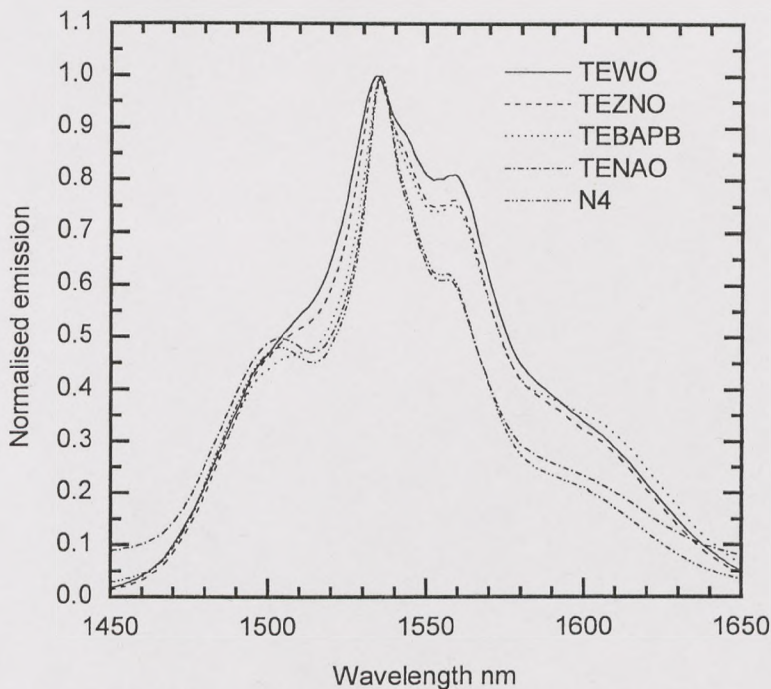


Fig. 8.36 Er^{3+} ion emission spectra in different tellurite glasses

From these spectra, N4 and TENAO are nearly the same, it is like 10 mol% ZnO instead of TeO_2 , we have already seen there is little change of the spectra from Z1 to Z4. In binary TEZNO glass which ZnO replaces all Na_2O , the left shoulder of spectrum becomes smooth, the right shoulder rises, the spectrum becomes much wider. When HMO replaces ZnO and Na_2O , the spectra from TEBAPB and TEWO glass are wider than N4, by rising both parts of the peak compared to the emission observed in N4. From the emission bandwidth, decreases in the following order: TEWO (FWHM = 72 nm), TEZNO (FWHM = 67 nm), TEBAPB (FWHM = 56 nm), TENAO (FWHM = 45 nm) and N4 (FWHM = 44 nm).

The reason for this kind of change is that WO_3 , Bi_2O_3 , ZnO and PbO are glass former or intermediate oxides, BaO and Na_2O are glass modifier oxides, these oxides affect the absorption spectra, which shows the ratio of I_{1495}/I_{1532} is higher when glass contains of Bi_2O_3 and WO_3 . With more intermediate oxides in glass, they will provide more sites for Er^{3+} ions, this will broaden the Er^{3+} emission spectrum. Especially when glass contains WO_3 , from the Raman spectrum in this glass, it has two extra peaks which show WO_3 connect with the glass network, it surely creates more sites than other HMO and modifying oxides such as BaO and Na_2O .

The lifetimes of Er^{3+} ion for ${}^4I_{13/2} \rightarrow {}^4I_{15/2}$ transition of these glasses are shown in table 8.6. The lifetime is slightly higher in HMO modified tellurite glass than that of N4 and TENAO glasses.

Table 8.6 Lifetime of Er^{3+} ion for ${}^4I_{13/2} \rightarrow {}^4I_{15/2}$ transition in different tellurite glass systems modified by HMO, Er_2O_3 concentration in all case is 1 mol%.

sample	Lifetime ± 0.02 ms	sample	Lifetime ± 0.02 ms
TEWO	3.85	N4	3.37
TEBAPB	3.77	TENAO	3.65
TEZNO	4.12		

8.3.2.3 Er^{3+} emission spectra and lifetimes in tellurite glass modified by chloride and fluoride

In Er^{3+} doped tellurite glass, Er^{3+} ion absorption properties were studied before when glass was modified by chloride and fluoride. In $80.5\text{TeO}_2\text{-}10\text{Na}_2\text{O}\text{-}9\text{X}\text{-}0.5\text{Er}_2\text{O}_3$ ($\text{X} = \text{BaO}$, BaCl_2 and BaF_2) glass, the fluorescent properties of Er^{3+} ion will be discussed in the following part. Figure 8.37 shows the Er^{3+} ion emission spectrum changes with modifiers BaO , BaCl_2 and BaF_2 . Their lifetimes of Er^{3+} ion for ${}^4I_{13/2} \rightarrow {}^4I_{15/2}$ transition are shown in table 8.7.

Table 8.7 Lifetime of Er^{3+} ion for ${}^4I_{13/2} \rightarrow {}^4I_{15/2}$ transition in tellurite glass modified by chloride and fluoride

sample	X = BaO	X = BaCl ₂	X = BaF ₂
Lifetime ± 0.02 ms	5.70	5.85	6.75

From figure 8.37, when BaO was replaced by BaCl₂ and BaF₂, the emission spectra become narrower, the right and left shoulders come lower. When glass contains BaCl₂ and BaF₂, the emission spectra of Er³⁺ ion are very similar and the shape is the same, we can suggest Er³⁺ ion mainly connect with oxygen rather than chlorine and fluorine. Chlorine and fluorine ions just modify the crystal field strength around the Er-O⁻ dipole. From the Raman spectra of these glasses, the connectivity of the glass containing BaO is higher than glass containing halides, this results in the stronger interaction between Er³⁺ ion and glass. From their absorption cross-sections and the peak ratio of I₁₄₉₅/I₁₅₃₂ in figure 8.19, glass containing BaO (lowest F_a) also has the highest absorption cross-sections and a slightly larger ratio of I₁₄₉₅/I₁₅₃₂. Therefore, it has a broader emission spectrum than glass modified by halides.

From their lifetimes in table 8.7, the lifetime increases following BaO, BaCl₂ and BaF₂ sequence. It is much longer when glass contains fluorine. This is caused by the lower refractive index of the host glass and weaker interaction between Er³⁺ ion and glass because of the addition of Cl⁻ and F⁻.

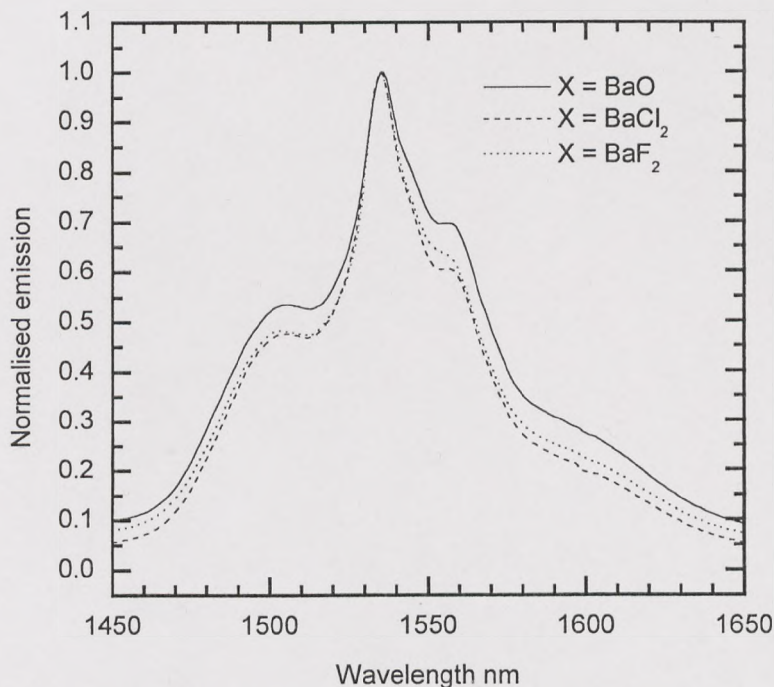


Fig. 8.37 Er³⁺ ion emission spectra with various anions in 80.5TeO₂-10Na₂O-9X-0.5Er₂O₃ (X = BaO, BaCl₂ and BaF₂) glass

8.3.2.4 Er^{3+} emission spectra and lifetimes in different kinds of glasses

The fluorescent properties of Er^{3+} ion in tellurite glass with different composition have been studied, these properties are also studied in modified silicate glass and HMO germanate glass, in this part, these properties will be compared among different kinds of oxide glasses and ZBLAN fluoride glass. Figure 8.38 shows the Er^{3+} ion emission spectra in these four glasses: tellurite glass (TEWO), modified silicate glass (193), HMO germanate glass (GE3) and ZBLAN fluoride glass. There is a common feature for these glasses: they all contain heavy metal cations.

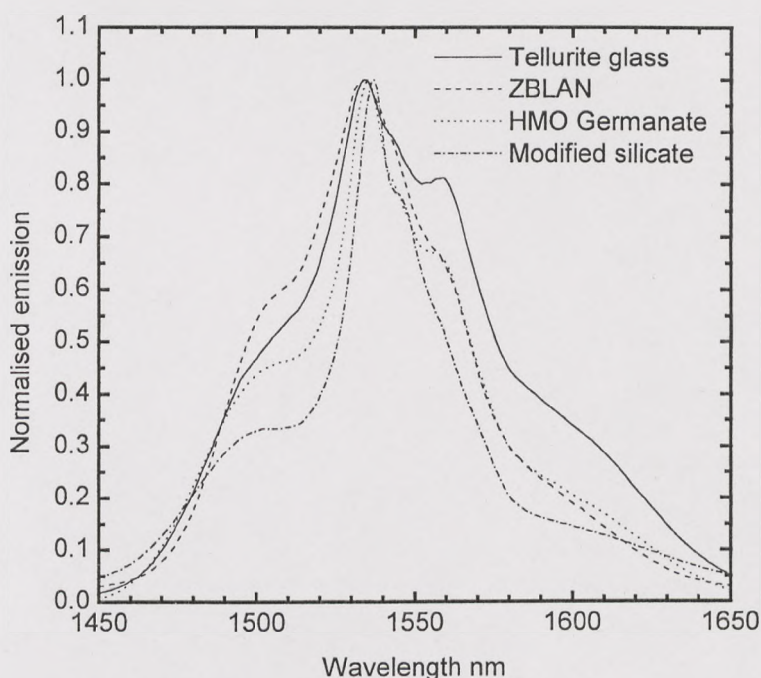


Fig. 8.38 Er^{3+} ion emission spectra in different kinds of glasses

From figure 8.38, modified silicate glass has the narrowest emission spectrum, the second is HMO germanate glass, the third is ZBLAN, TEWO tellurite glass has the widest emission spectrum. A ZBLAN glass modifies the short wavelength part of the emission curve more than any other composition by having the highest left shoulder of the spectrum, the second is tellurite glass, the third is germanate glass, silicate glass has the lowest shoulder, it declines with the increasing the bond strength of glass. In the right wing of these spectra, silicate glass has the lowest, the second is ZBLAN and germanate glass, they are nearly in the same position, tellurite glass has shifted the

emission to longer wavelength. From the previous discussion about the Er^{3+} ion absorption spectra of these four kinds of glasses, the emission spectrum in ZBLAN should be the narrowest because of the weakest interaction between Er^{3+} ion and glass, but the cross-sections are much lower than oxide glasses, the emission spectrum will be packed and denser, thus the normalised emission spectrum becomes flatter and broader. The emission spectrum peak also has a blue shift. Comparing the three kinds of oxide glasses, the strongest interaction to Er^{3+} ion in tellurite glass causes the broadest emission spectrum, the same reason for the narrowest emission in silicate glass.

For emission spectrum, FWHM (full-width at half maximum) is used as the indication of bandwidth. From the normalised emission spectra, the FWHM of these glasses have been calculated and been shown in table 8.8, the lifetimes of Er^{3+} ion at $^4\text{I}_{13/2}$ level and stimulated emission cross-sections for the $^4\text{I}_{13/2} \rightarrow ^4\text{I}_{15/2}$ transition which are calculated from McCumber are also shown in table 8.8. This table also includes the fluorescent properties of commercial Al/P silica glass for EDFA.

The gain bandwidth of an amplifier is determined largely by the width of the emission spectrum and the stimulated emission cross-section. We may therefore define a figure-of-merit (FOM) for bandwidth as the product $\sigma_{\text{emiss}} \times \text{FWHM}$. For amplifier, figure-of-merit (FOM) for gain is defined as the product $\tau \times \sigma_{\text{emiss}}$. FOM for these different glasses are shown in table 8.8.

Table 8.8 Er^{3+} lifetime, FWHM, emission cross section of $^4\text{I}_{13/2} \rightarrow ^4\text{I}_{15/2}$ transition and FOM at 1500nm in different kinds of glasses, pump wavelength is 980 nm.

Glass	τ $\pm 0.1\text{ms}$	FWHM $\pm 1\text{ nm}$	σ_{emiss} $\times 10^{-21}$ ± 0.02 cm^2	FOM gain $\tau \times \sigma_{\text{emiss}} \pm 0.1$ $10^{-24} \text{cm}^2 \text{s}$	FOM bandwidth $\sigma_{\text{emiss}} \times \text{FWHM} \pm 1$ $10^{-24} \text{cm}^2 \text{nm}$
Al/P silica [7]	10.8	43	5.50	59.4	237
193	10.2	35	7.78	79.4	272
Ge5	4.1	50	8.12	33.3	406
TEWO	3.9	71	8.40	32.8	596
ZBLAN	10.1	69	5.10	51.5	352

From table 8.8, the lifetime in tellurite glass is the shortest, in HMO germanate glass, it is slightly longer. Modified silicate, AL/P silica and ZBLAN glasses have nearly similar lifetime around 10 ms, they are much longer than that in tellurite and HMO germanate glasses. The emission cross-sections are different, tellurite glass has the largest cross-section, HMO germanate has the second, silicate glass has the third, ZBLAN has the lowest, it is about 40% lower than tellurite glass. As we discussed in absorption cross-section in figure 8.20, higher refractive index of glass, stronger interaction between Er^{3+} ion with glass host will result in shorter lifetime and larger absorption and emission cross-sections. The refractive index of ZBLAN is 1.50, 193 is 1.64, GE5 and TEWO are over 2.0, this is the main reason to cause the difference in lifetime and cross-sections.

From FOM gain, modified silicate glass is the best, the second is standard Al/P silica, ZBLAN is slightly lower than Al/P silica, tellurite and HMO germanate glasses have the smallest value.

For WDM systems, a broadband and flat gain amplifier is required, FOM bandwidth represents this requirement. Tellurite glass has the largest value, it is as twice as that in modified silicate glass, more than 50% higher than in ZBLAN fluoride glass. The standard Al/P silica has the smallest value. Therefore, tellurite glass is the best candidate for Er^{3+} doped glass host.

8.3.2.5 Emission spectra in Er^{3+} doped tellurite glass fibre

Based on the study of Er^{3+} ion doped tellurite glasses, proper compositions were selected and preform was made for fibre drawing. Figure 8.39 shows the fibre geometrical structure, the scale is 10 μm , the fibre diameter is in the range from 120 to 150 μm , the diameter of core changes from 4 to 50 μm , the loss in this fibre is around 10 dB/m. The 3 layer fibre is single mode, Er^{3+} ion emission spectra in this single mode fibre are shown in figure 8.40. It shows that the emission spectral shape is deformed and shifted to longer wavelength. This is due to the re-absorption and re-emission of Er^{3+} ion which were discussed in section 8.3.1.1 and the decline of pump power along the fibre.

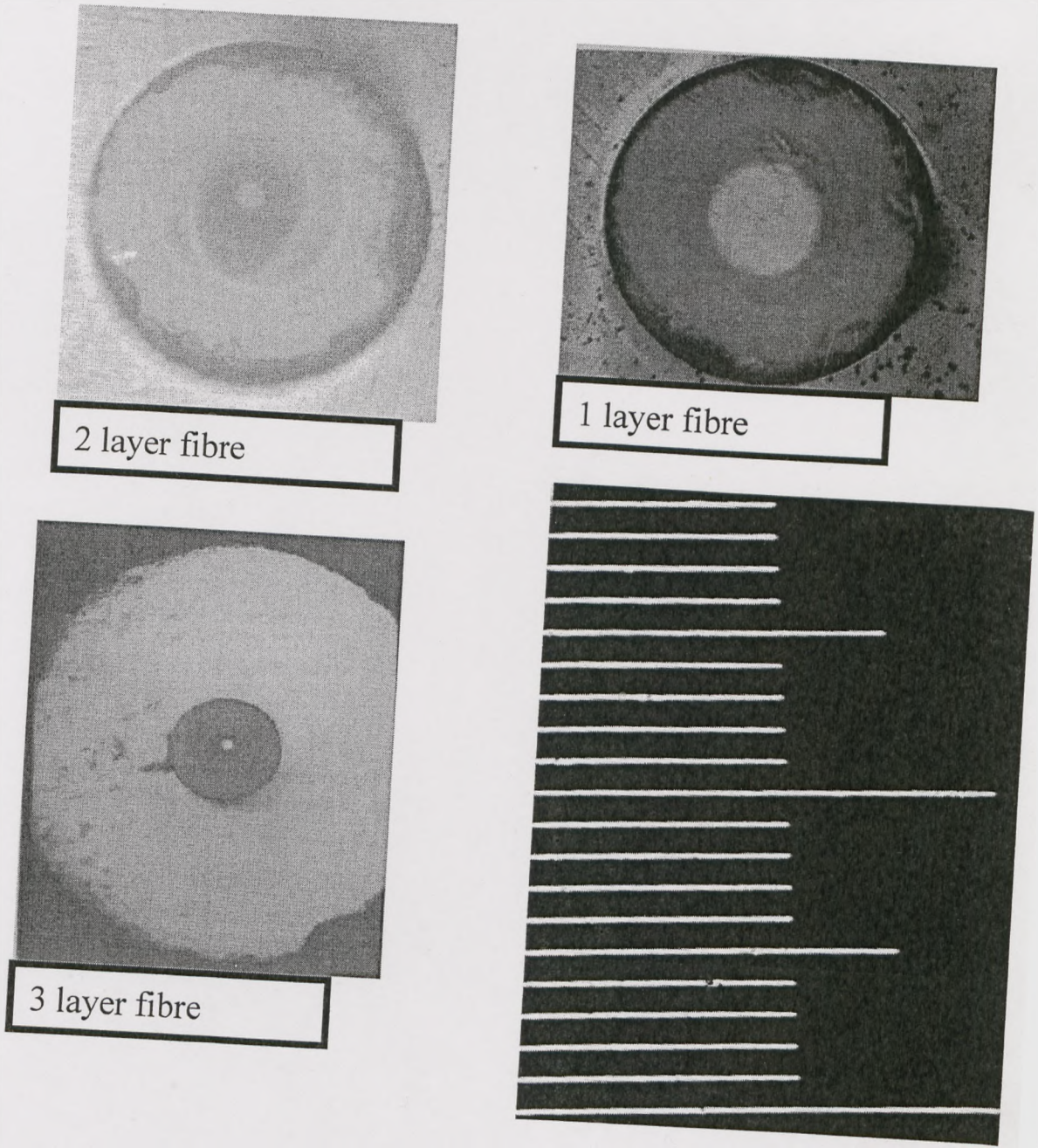


Figure 8.39 Photography of tellurite glass fibre

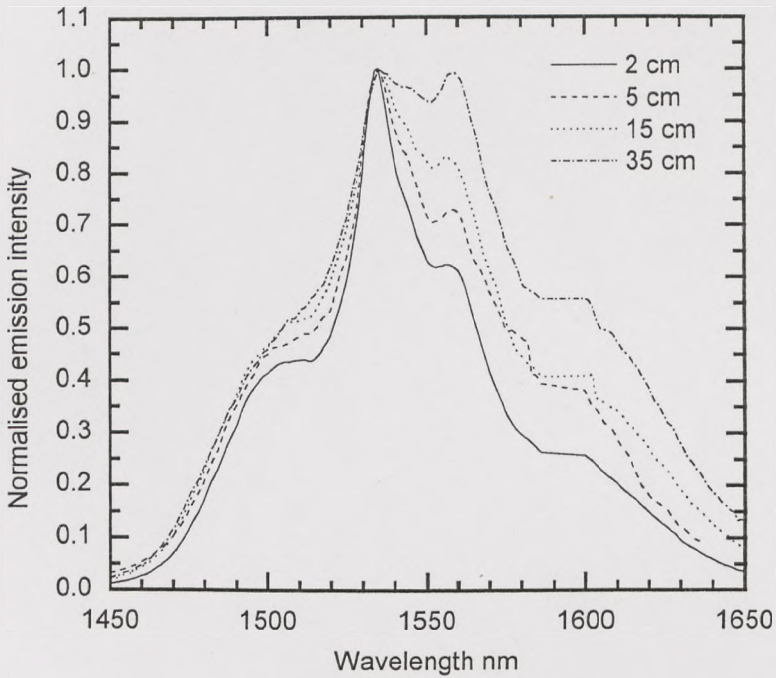


Fig. 8.40 Emission spectra of Er^{3+} ion in various tellurite glass fibre length

8.3.3 Discussion

8.3.3.1 Absorption and emission spectra in Er^{3+} ion doped glasses

From the analysis of absorption and emission spectra of Er^{3+} ion in all of those glasses, tellurite glass has the highest absorption and emission cross-sections and the widest emission spectrum among different kinds of glasses. Among tellurite glasses with different modifiers, glass with higher TeO_2 concentration or containing heavy metal intermediate oxides has slightly higher cross-sections and wider emission spectrum.

The following discussion will mainly explain the emission spectrum broadening.

In rare earth doped glass, the line strength and the shape of a transition between two states is dependent on the electronic-dipole which is governed by the ion-host ligand interaction shown in equation 3.1. The analysis of host glass structural units, which determines the dopant ion environment is essential in understanding the

emission line broadening. From figure 8.38 emission spectra in different kinds of glasses, the Er^{3+} emission spectrum in tellurite glass is significantly broader than in other glasses studied as EDFA hosts. The origin of spectral broadening of Er^{3+} -ion emission in tellurite glass can be explained on the basis of the various dopant sites in glass, the structural information deduced from Raman, and UV-visible spectroscopy.

Multicomponent fluoride glasses, such as ZBLAN, are known to have multiple dopant sites resulting in broad emission spectra [8]. Ligand fields in different dopant sites can variously affect the amount of Stark splitting and /or the strengths of transitions between Stark sub-levels, which are thermalised at room temperature. In the case of different Er^{3+} -doped glass hosts, the energies of Stark sub-levels involved in the 1.55 μm emission remain approximately constant and variations in spectra are caused primarily by changes in transition intensity [9]. Dopant populations in different sites will therefore have different emission spectra, and the aggregate spectrum will be inhomogeneously broadened. The width and shape of Er^{3+} emission spectrum in tellurite glass is broadly similar to that in a multi-site ZBLAN glass; moreover, the width varies considerably among different tellurite compositions. Therefore broad Er^{3+} emission in tellurite glass may be attributed to multiple dopant sites with large variations among them. The structure of tellurite glass also points to the existence of multiple sites [10].

From the Raman spectroscopy of TeO_2 glasses in chapter 7, the glass has three types of structural units: TeO_4 tbps, TeO_3 tps and a combined to TeO_4 and TeO_3 polyhedron structure. These structural units have a lone pair electron (LPE) from Te, which is equivalent to an O^{2-} anion. Because the LPE and the sites for oxygen interact with each other, the axial Te-O bonds (2.22 Å) are longer than equatorial Te-O bonds (1.88 Å) in tbp structure units. The difference in the Te-O bond lengths is the first contributory factor for the broadening of the emission spectrum in Er^{3+} -doped tellurite glass.

TeO_2 does not form glassy state, but requires network modifiers, such as divalent and monovalent oxides, to form stable glass. The modifying cations, as expected, also create non-bridging oxygen in the tellurite glass structures, as they do in the silicate, borate and germanate glasses. In silica glass, the solubility of rare earth ions is low

and extensive ion clustering takes place. The clustering of RE-ions is significantly reduced by the addition of Al^{3+} and P^{5+} ions, which modify the silica structure and disperse RE-ions in the environment of non-bridging oxygen ions. In tellurite glass, the network modifiers create a variety of dopant sites in the glass, associated with TeO_4 , TeO_3 and distorted TeO_{3+x} units. A range of dopant sites is clearly desirable for a broadband EDFA glass host. The combination of LPE and multi-structural units is the second contributory in producing a wide variety of field strength around Er^{3+} -ions.

In tellurite glass with different modifiers, the Er^{3+} ion absorption and emission spectra and cross-sections change slightly although these changes are less than those in different kinds of glasses. In $(90-x)\text{TeO}_2-9\text{ZnO}-x\text{R}_2\text{O}-1\text{Er}_2\text{O}_3$ ($x = 5, 10, 15, 20$) ternary system, when x increases, modifier oxides substitute for glass former TeO_2 , the UV edge shifts to shorter wavelength, it means the energy band gap increases. The shift of band edge energy is also an indication of the change in the cation field around the LPE. With higher energy band gap, the polarisability of ions in the glass is less, the field strength around Er^{3+} ions is weaker.

On the other hand, from Raman spectra, in pure TeO_2 , the glass structure units are mainly TeO_4 and with very little TeO_3 . With the increasing modifier oxides, the tellurite glass structure units are changing from TeO_4 to Te_3O_{11} , Te_2O_7 , TeO_3 , Te_3O_8 and Te_2O_5 , structure units are becoming smaller. This will also decrease the field strength around Er^{3+} ions, the interaction between Er^{3+} ion and glass host becomes weaker, the energy gap among Stark splitting sub-levels becomes lower, therefore, the emission spectra become narrower gradually.

When tellurite glass is modified by different alkali oxides, the emission spectra of Er^{3+} ion become wider following K_2O , Na_2O , and Li_2O . From the changes of molar volume and density of these glasses, glass containing Li_2O has the lowest molar volume and largest density. From their Raman spectra, glass containing Li_2O has the smallest ratio of $\text{TeO}_3/\text{TeO}_4$. From the absorption spectra peak ratio in figure 8.13, glass containing Li_2O has the highest ratio of I_{1495}/I_{1532} . All these changes from glass properties and glass structure illustrate that the glass has the stronger interaction

between Er^{3+} ion and glass when it contains Li_2O . These cause the change of emission spectra of Er^{3+} ion in tellurite glass modified by different alkali oxides.

ZnO is an important oxide in this ternary glass system. From the Raman spectrum research, the role of ZnO in tellurite glass is like an intermediate oxide, it can connect the glass network as $[\text{ZnO}_4]$. The changes of molar volume and transition temperature T_g with ZnO concentration give a clear evidence. From the emission spectra figure 8.34 and 8.36, when ZnO replaces TeO_2 , the emission spectra of Er^{3+} ion have little change because the integrity of the glass has changed very little, the interaction between Er^{3+} ion and glass thus has changed very little. The emission spectra vary little. When ZnO is replaced by 20 mol% Na_2O , the glass network is broken more, the integrity of the glass has decreased, thus the interaction between Er^{3+} ion and glass has also decreased, this is the reason that the emission spectra become much narrower (by comparing TEZNO and N4).

When tellurite glass modified by heavy metal oxides rather than alkali oxides, the emission spectra become slightly wider, one reason is there are more sites when glass contains WO_3 and Bi_2O_3 , another reason is the field strength around Er^{3+} ion has increased.

When tellurite glass modified by chloride and fluoride, the emission spectra of Er^{3+} ion become slightly narrower, absorption and emission cross-section become slightly smaller. Because chloride and fluoride can break the glass network stronger than oxide, it results in the looser structure. Therefore, the interaction between Er^{3+} ion and glass host becomes weaker as oxygen is replaced by chloride and fluoride. This affects the Stark splitting to cause narrower emission spectrum.

From figure 8.22, a significant broadening of emission with increased Er^{3+} ion concentration is clearly observed. The cause may be that as the concentration of Er^{3+} ions increases, more dopant sites become populated. Therefore the aggregate spectrum will be inhomogeneously broadened.

8.3.3.2 OH⁻ broadening

The multiplicity of LPE sites and non-bridging oxygen are responsible for the extensive broadening of OH⁻ peak in tellurite glass. Figure 8.41 shows the OH⁻ absorption peak in modified silicate glass (192), HMO germanate glass, and TZN tellurite glass (N2). Because we do not know the extinction coefficient and concentration of OH⁻ in germanate and tellurite glass, figure 8.41 only shows the normalised absorption peak. The absorption peak is much broader in HMO germanate and tellurite glass than silicate glass. It is also about 15% broader in tellurite than in HMO germanate glass. The peak shifts to longer wavelength from 2.9 μm in silicate glass to 3.3 μm in tellurite glass. The broad absorption peak is caused by a wide range of structural sites which are not available in silicate glass. As a result OH⁻ ions disperse and form hydroxyl bonds over range of sites. Arnaudov and co-workers [11] proposed the sites in barium-tellurite glasses are due to TeO-O...HOTeO units. The authors suggested that “the oxygen atom-electrodonors are strongly polarised and become non-bridging sites”.

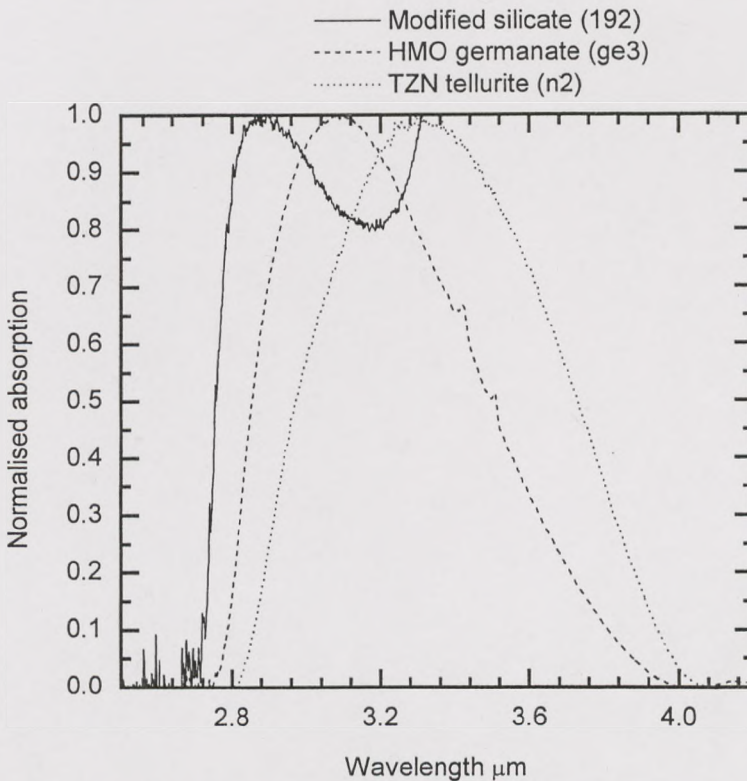


Fig 8.41 OH⁻ absorption spectra in modified silicate, HMO germanate and TZN tellurite glasses

In the present investigation, from the spectroscopic observations of Er^{3+} and OH^- ions, the behaviour of hydroxyl ions appears more complex and is described below. The oxide anion in OH^- acts an oxygen donor to TeO_4 structures at the LPE sites at low concentrations of OH^- (see effect of OH^- on lifetime in figure 8.29). This means that when a LPE site transforms into a non-bridging donated oxygen site (NDOS), by accepting the oxide anion from OH^- and then forms a bond with the neighbouring Er^{3+} ion, there would be a net negative charge deficiency in the environment of Er^{3+} ion. The oxygen ion donation will necessitate that the protons (H^+ ion) must move away at least into a second coordination cell of Er^{3+} -ion. This would also mean that the new O...H bond due to the release of a proton, will not be available in the immediate vicinity of Er^{3+} to induce the quenching of luminescence. The modifying ions in the same way donate oxygen to LPE sites to form NDOS and cause a major shift in the position of Urbach tail to short wavelengths. It is expected that in the presence of Er^{3+} ions coupled with NDOS, the excess protons will contribute to more non-bridging oxygen sites away from the original LPE sites. These are evident from the increase in the intensity of peaks C and D in $80\text{TeO}_2\text{-}10\text{Na}_2\text{O}\text{-}10\text{ZnO}$ glass Raman spectrum. Once all the LPE sites have transformed into NDOSs, the ion-ion energy transfer of Er^{3+} ions becomes dominant. There is an additional complementary information on the effect of OH^- ions on quenching of Er^{3+} luminescence. The initial slope of lifetime versus Er_2O_3 concentration has a steeper slope in glasses with higher concentrations of OH^- than glass with lower OH^- . This difference in the initial slopes between high and low OH^- glasses suggests that there are much fewer LPE sites, which have not transformed to NDSOs in a high- OH^- glass than in a low- OH^- glass.

8.3.3.3 Lifetime change in glass

Long radiative lifetimes are generally desired for transitions to be utilised for amplification. This will minimise the required pump power to maintain a reservoir of electrons in the desired excited state for the stimulated emission process. Lifetimes not only depend on the radiative transition probabilities between these states but also on the availability of alternative decay mechanisms. It is determined by the multiphonon decay, concentration quenching and impurity ions in glass.

Different kinds of glasses:

Under the same melting condition and Er^{3+} ion concentration, the fluorescent lifetime of Er^{3+} ion at this ${}^4\text{I}_{13/2}$ level are different in different kinds of glasses. The observed values are much longer in modified silicate and ZBLAN fluoride glasses than that in HMO germanate and tellurite glasses. Because the energy gap is about 6500 cm^{-1} , it is about 5 times as the highest phonon energy of those glass hosts, the non-radiative decay from multiphonon relaxation is relatively slow. The main reason for the lifetime difference is the refractive index. With higher refractive index in HMO germanate and tellurite glasses, the interaction between Er^{3+} ion and host is stronger, this results in shorter lifetime from equation 4.5 and 4.10. In the previous section, the absorption spectra of these 4 kinds of glasses have been discussed, the interaction of between Er^{3+} ions and glass former units in tellurite glass is the strongest. In germanate glass has less strong interaction, the third is in silicate glass, and ZBLAN fluoride glass is the weakest. Stronger interaction between Er^{3+} ion and glass host will cause shorter lifetime, this is the reason that the lifetimes vary in those 4 kinds of glasses.

R₂O replace TeO₂:

In tellurite glass with different oxide modifiers, like other properties, the fluorescent lifetime of Er^{3+} ion at this ${}^4\text{I}_{13/2}$ level are different. In $\text{TeO}_2\text{-ZnO-R}_2\text{O-1Er}_2\text{O}_3$ ternary system, when modifier oxides (Li_2O , Na_2O , K_2O and ZnO) substitute for glass former TeO_2 , there is a trend that the calculated and measured lifetimes increase with increasing R_2O and ZnO concentration. This arises due to the decrease of refractive index of glasses after this substitution. It has modified the local ligand field around Er^{3+} ion. As we discussed in the change of emission spectra, the interaction between Er^{3+} ion and glass host becomes weaker, the field strength around Er^{3+} ions will decrease. Therefore the lifetime will become longer.

Halide modified:

When tellurite glass modified by chloride and fluoride, the lifetime becomes longer. As Sidebottom [12] pointed out in zinc tellurite glass, there is a significant increase in the emission lifetime of Nd^{3+} from 150 to 250 μs with increasing fluorine substitution. In tellurite glass with 10% fluorine substitution, the Er^{3+} lifetime increases from 5.7 to 6.75 ms. As we discussed that the change of absorption and

emission spectra, it is clear that the halide substitution does significantly modify the local electrostatic field of the rare earth ion, the interaction between Er^{3+} ion and glass host becomes weaker as the replacement of oxygen by halides, and thus result in a substantial increase of the intrinsic radiative lifetime.

Various Er_2O_3 concentrations:

The emission lifetimes for Er^{3+} in TZN glass as a function of Er_2O_3 concentration is shown in figure 8.26. With increasing Er_2O_3 concentration, the lifetime of Er^{3+} ion at $^4\text{I}_{13/2}$ level increases firstly then comes down. This kind of similar quenching process has been reported in Er^{3+} doped tellurite glass by Wang et al [13]. It behaves in a different way in the $\text{Na}_2\text{O-SiO}_2$ glasses, the lifetime decreases straightway from 19 to 6 ms when Er_2O_3 concentration increases from 0.05 mol% to 3.0mol% [14]. When sodium silicate glass is melted in different temperature and atmosphere to modify the OH^- concentration in glass, the lifetime was observed to drop from 20 to 10 ms [15].

By melting the tellurite glass in different atmosphere, it appears that the Er^{3+} sites, which are quenched in the presence of high OH^- , are re-activated at lower concentrations. This would suggest that the environment of Er^{3+} -ions in this glass host is not identical. The sites, which are more active in the presence low OH^- , do not seem to contribute to ion-ion upconversion. At low OH^- , the maximum point shifts to 11,000 ppm Er_2O_3 with lifetime 7.8 ms. Comparing Er^{3+} ion quenching process in tellurite and silicate glasses, the much reduced effect of ion-ion upconversion in tellurite glass suggests that the average separation distance between Er^{3+} ions up to 11,000 ppm Er_2O_3 in TeO_2 oxide glasses is much greater than that of the same concentration in the silicate hosts.

There are two main reasons for a prolonged lifetime of 7.8 ms in 11,000 ppm Er_2O_3 doped tellurite glass structure. The first one is associated with an increased ion-ion separation distance, which may be at least of the order 0.390 nm (2 times the shortest Te-O bond), if not more. The second one is due to increased $\text{Er}^{3+}/\text{OH}^-$ ion distance. As proposed above that the LPE/NDSO transformation in the tellurite glass structure (and hence $\text{Er}^{3+}/\text{NDSO}$ interaction) causes the H^+ protons to move away in the second or higher co-ordination shells. As a result, on average the $\text{Er}^{3+}\text{-OH}^-$

separation distance is at least going to increase by a factor of 4. With the increasing distance, the probability of impurity induced quenching is greatly reduced.

8.4 Conclusions

1. In $(90-x)\text{TeO}_2-9\text{ZnO}-x\text{R}_2\text{O}-1\text{Er}_2\text{O}_3$ ternary glass system ($\text{R}_2\text{O} = \text{Li}_2\text{O}, \text{Na}_2\text{O}$ and K_2O , $x = 5, 10, 15, 20$), as x increases, the absorption cross sections of Er^{3+} ions slightly decrease, the emission spectra become slightly narrower, the calculated and measured decay lifetimes become slightly longer. As x is the same, the absorption cross sections and emission spectra respectively become lower and narrower following $\text{Li}_2\text{O}, \text{Na}_2\text{O}$ and K_2O .
2. In $(89-x)\text{TeO}_2-x\text{ZnO}-10\text{Na}_2\text{O}-1\text{Er}_2\text{O}_3$ ternary glass system ($x = 4, 9, 14, 19$), as x increases, the absorption cross sections ions and emission spectra of Er^{3+} have very little change. As ZnO is replaced by Na_2O in this glass system, the absorption cross sections and emission spectra respectively become lower and narrower.
3. When tellurite glass is modified by heavy metal oxides ($\text{WO}_3, \text{PbO}, \text{Bi}_2\text{O}_3$), cross-sections and peak ratios are slightly higher, the mission spectra become broader.
4. When tellurite glass is modified by halides (BaCl_2 and BaF_2), the cross sections and emission spectra Er^{3+} ions respectively become lower and narrower, the lifetimes become longer.
5. In TZN tellurite glass doped with different concentration of Er_2O_3 , the lifetime increases at low Er_2O_3 concentration, after a maximum value, it decreases slightly. This unique change is related to the tellurite glass structure units and OH^- concentration.
6. OH^- ion has the broadest absorption peak the longest absorption peak wavelength among oxide glasses.
7. Comparing Er^{3+} ion doped tellurite glass with silicat, germanate and ZBLAN fluoride glasses, tellurite glass has the largest cross-sections and widest emission spectra, the lifetime is the shortest.

References

1. Brown. P. J., J. B. Forsyth, *The Crystal Structure of Solids*, London: Edward Arnold, 1973.
2. Pauling, L., *The nature of the chemical bond*, New York, Cornell University Press, 1945.
3. Zemon, S., G. Lambert, W. J. Miniscalco, and L. J. Andrew, *Fibre Laser Sources and Amplifiers*, **1171**: SPIE, 219 (1989).
4. Miniscalco, W. J., and R. S. Quimby, *Opt. Lett.* **16**, 258 (1991).
5. Kaiser, P., *Appl. Phys. Lett.* **23**, 45 (1973).
6. France, P. W., PhD Thesis, Sheffield University, 1987.
7. Miniscalco, W. J, *IEEE/OSA J. Lightwave Technol.*, *LT-9*, 234 (1991).
8. Lucas, J., *J. Less-Common Metals* **112**, 27 (1985).
9. Miniscalco, W. J., "Optical and Electronic Properties of Rare Earth Ions in Glasses," in *Rare Earth Doped Fiber Lasers and Amplifiers*, M. J. F. Digonnet (Ed.), New York: Marcel Dekker, 1993.
10. A Jha, S Shen, M Naftaly, *Physical Review B* **62**, 10 (2000).
11. Arnaudov, M., Y. Dimitriev, V. Dimitrov, and M. dimitrova-Pankova, *Phys. Chem. Glass.* **27**, 48 (1986).
12. Sidebottom, D. L., M. A. Hruschka, B. G. Potter, and R. K. Brow, *J. of Non-Cryst. Solid* **222**, 282 (1997).
13. Wang, J. S., E. Snitzer, and G. H. Sigel, *Mat. Res. Soc. Sym. Proc.* **244**, 209 (1992).
14. Wang, J. S., E. M. Vogel, and E. Snitzer, *Optical Materials* **3**, Aug., 187 (1994).
15. Bruce, A. J., W.A. Reed, A. E. Neeves, L. R. Copeland, W. H. Grodkiewicz, and A. Lidgard, *Optical Waveguide Materials*, MRS, **244**, 157 (1992).

Chapter 9

Tm³⁺-doped tellurite glass for a broadband amplifier at 1.46 μm

Much of the interest for Tm³⁺-doped glass stems from its emission that occurs in the wavelength regime of 1400-1500 nm between the bands of Nd³⁺ and Er³⁺ doped glasses. Tm³⁺-doped tellurite glass is investigated as a host for a broadband amplifier at 1.46 μm. Tm³⁺ fluorescence spectrum, lifetime and cross-sections in tellurite glass are compared with those in ZBLAN fluoride glasses. The advantages of a Tm³⁺-doped tellurite amplifier are discussed, especially when employed in combination with an Er³⁺ doped tellurite amplifier at 1.55 μm and Nd³⁺ doped tellurite amplifier at 1.34 μm.

In recent years Tm³⁺-doped fluoride fibre amplifiers (TDFA) at 1.46 μm have attracted considerable attention as a means of extending the transmission bandwidth of optical fibres beyond the range available from Er³⁺-doped fibre amplifiers (EDFA). Several types of TDFA have been developed utilising different pumping schemes and methods of relieving the population in the lower laser level. Figure 9.1 (A) shows the energy level diagram of Tm³⁺. The 1.46 μm amplifying transition is $^3H_4 \rightarrow ^3F_4$. The 3H_4 level can be excited directly by a 790-800 nm pump. However, the 1.46 μm band lasing is limited by the fact that the lifetime of the upper level, 3H_4 , is shorter than that of the lower level, 3F_4 , which is a so-called “self-terminating” system. Therefore, since it is difficult to achieve population inversion between 3H_4 and 3F_4 , the lower level should be depopulated in order to achieve gain. The amplifier design must include means of quenching the 3F_4 level. Several successful schemes have been demonstrated in fluoride ZBLAN glass. Upconversion pumping at 1064 nm can be used both to excite the 3H_4 level and to depopulate the 3F_4 level [1-3]. This scheme is shown in figure 9.1 (B). The 1064 nm pump promotes Tm³⁺ ions to the intermediate 3H_5 level, whence they relax non-radiatively to 3F_4 level. The ions in the 3F_4 level, both those excited by the pump and those arriving via radiative decay from the 3H_4 level, then absorb another pump photon which excites them to the $^3F_3+^3F_2$ level, from where they relax nonradiatively to the lasing 3H_4 level.

In another scheme which is shown in figure 9.1 (C), the fibre was codoped with $\text{Tm}^{3+} + \text{Ho}^{3+}$ and pumped at $0.79 \mu\text{m}$ into the ${}^3\text{H}_4$ level of Tm^{3+} [4]. The ${}^3\text{F}_4$ level was quenched by energy transfer to the matching ${}^5\text{I}_7$ level of Ho^{3+} . Another method of depopulating the is to employ a “cascade” process [5], which also uses a $0.79 \mu\text{m}$ pump. The ${}^3\text{F}_4$ level is efficiently depopulated by stimulated emission at $1.86 \mu\text{m}$.

Despite considerable successes of these devices, TDFAs have not been accepted by the telecom industry, partly due to the difficulties associated with fabricating fluoride fibres and splicing them to the standard silica fibre. The oxide tellurite glass is highly stable and relatively easy to fabricate. In the following part, we propose that a Tm^{3+} -doped tellurite amplifier would provide a much broader gain bandwidth than a fluoride TDFA, as well as offering the advantages of oxide glass fabrication.

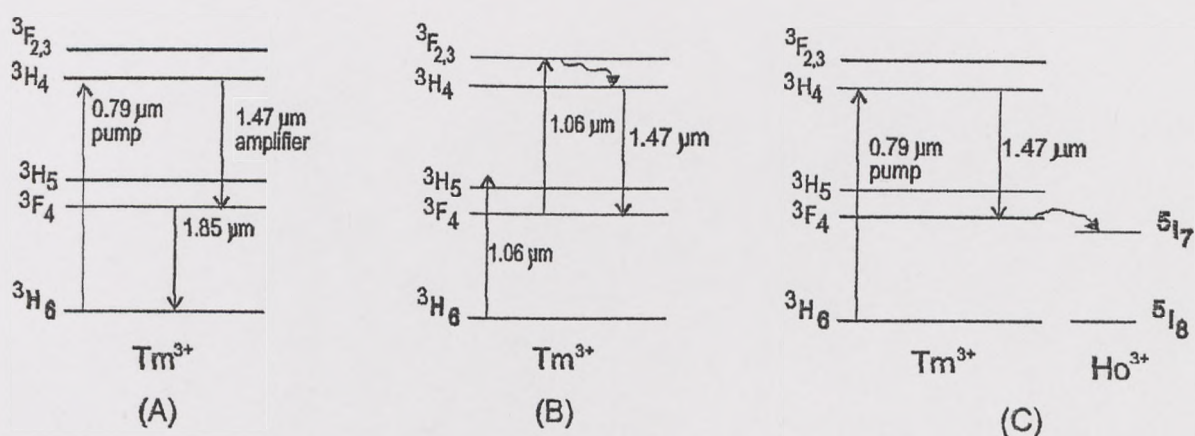


Fig. 9.1 Energy diagram of Tm^{3+} ions and amplification in the $1.4 \mu\text{m}$ region (A) Energy diagram, (B) upconversion pumping, (c) the codoping of acceptor ion

9.1 Absorption spectrum of Tm^{3+}

Figure 9.2 shows the Tm^{3+} ion absorption cross-sections in tellurite and ZBLAN glasses. The absorption cross-sections in tellurite glass are much higher than in ZBLAN. For most of the absorption peaks, the absorption cross-sections are about 60% larger in tellurite glass than in ZBLAN due to higher refractive index. The pump absorption cross-section at $0.79 \mu\text{m}$ is disproportionately large in the tellurite glass,

at nearly 3 times its value in ZBLAN. This is due to the hypersensitive nature of the ${}^3\text{H}_6 \rightarrow {}^3\text{H}_4$ transition, which results in the line strength being strongly dependent on the dopant site configuration. The enhanced pump absorption in tellurite glass will benefit amplifier operation.

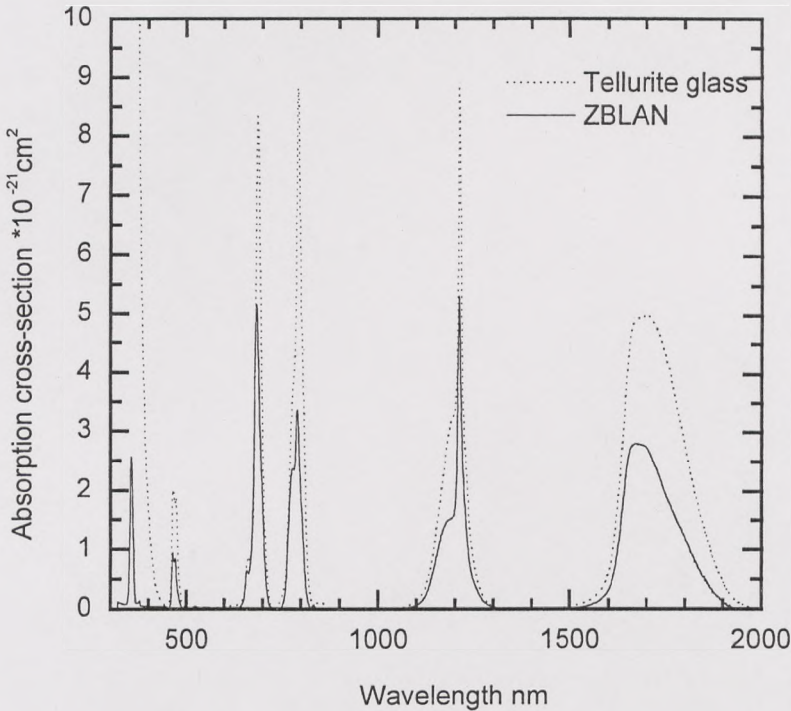


Fig. 9.2 Tm^{3+} absorption cross-section in tellurite and ZBLAN glasses

9.2 Fluorescent properties of Tm^{3+}

TZN ($\text{TeO}_2\text{-ZnO-Na}_2\text{O}$) tellurite glass was also investigated as host for the Tm^{3+} -doped amplifier. Figure 9.3 shows the normalised emission spectra of Tm^{3+} ion at $1.46 \mu\text{m}$ in tellurite and in ZBLAN. Tm^{3+} ion fluorescence is seen to be significantly broader in tellurite glass, with FWHM of 114 nm , than in ZBLAN where FWHM is 76 nm . As in the case of Er^{3+} , the broadening is due to multiple dopant sites in tellurite glass. The Tm^{3+} peak in tellurite glass is also red-shifted by approximately 6 nm to 1458 nm , compared with 1452 nm in ZBLAN, the nephelauxetic shift observed in tellurite glass is related to its high refractive index ($2\text{-}2.1$ in tellurite, 1.5 in ZBLAN).

Table 9.1 lists spectroscopic parameters of Tm^{3+} in tellurite and ZBLAN glasses. Stimulated emission cross-section for the ${}^3\text{H}_4 \rightarrow {}^3\text{F}_4$ transition and lifetimes for these two levels were calculated using the Judd-Ofelt analysis, and are similar to those reported by other workers [6-8]. Figure 9.4 shows this stimulated emission cross-section in tellurite and ZBLAN glasses. The high refractive index of tellurite glass causes the emission cross-section to be larger and the lifetime shorter than in ZBLAN.

The decay of the ${}^3\text{H}_4$ level is dominated by nonradiative relaxation for silica because of the high phonon energy (1150 cm^{-1}) and small energy gap (4150 cm^{-1}) between it and the ${}^3\text{H}_5$. The measured lifetime is about 0.02 ms [9]. The $1.46\mu\text{m}$ lifetime of Tm^{3+} measured in tellurite glass is 0.28 ms, it similar to that reported by Wang et al [6]. Figure 9.5 shows the $1.46\mu\text{m}$ fluorescence decay of Tm^{3+} in tellurite glass, the solid line is a single-exponential fit to the data. By contrast, the lifetime observed in our ZBLAN glass is much shorter (50-60%) than that reported by other investigators [1, 2, 4-6]. This is due to the high concentration of OH^- impurity, arising from glass processing conditions. In tellurite glass the OH^- impurity is much more easily reduced to lower levels, allowing longer lifetime to be observed.

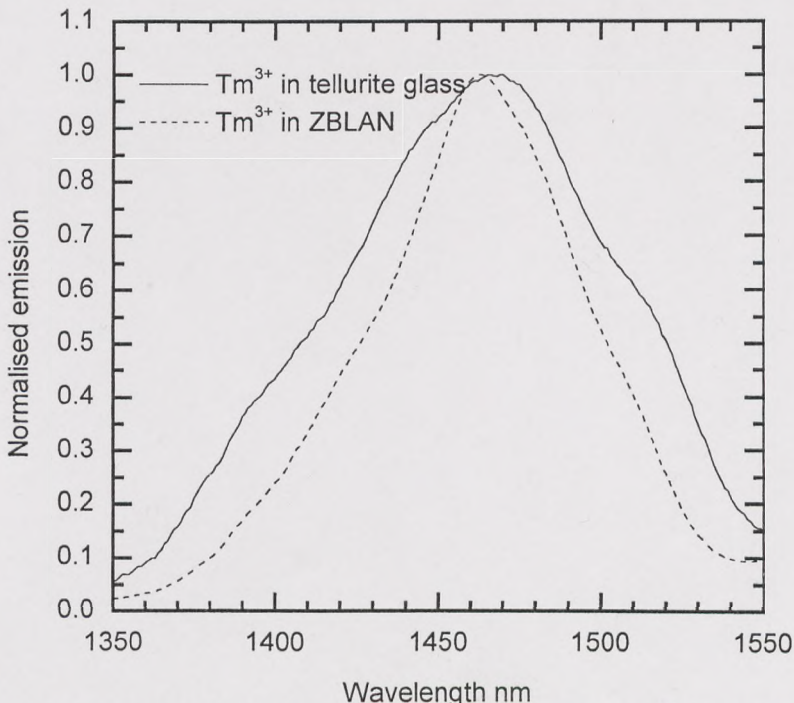


Fig. 9.3 Normalised emission spectra of Tm^{3+} ion in tellurite and ZBLAN glasses

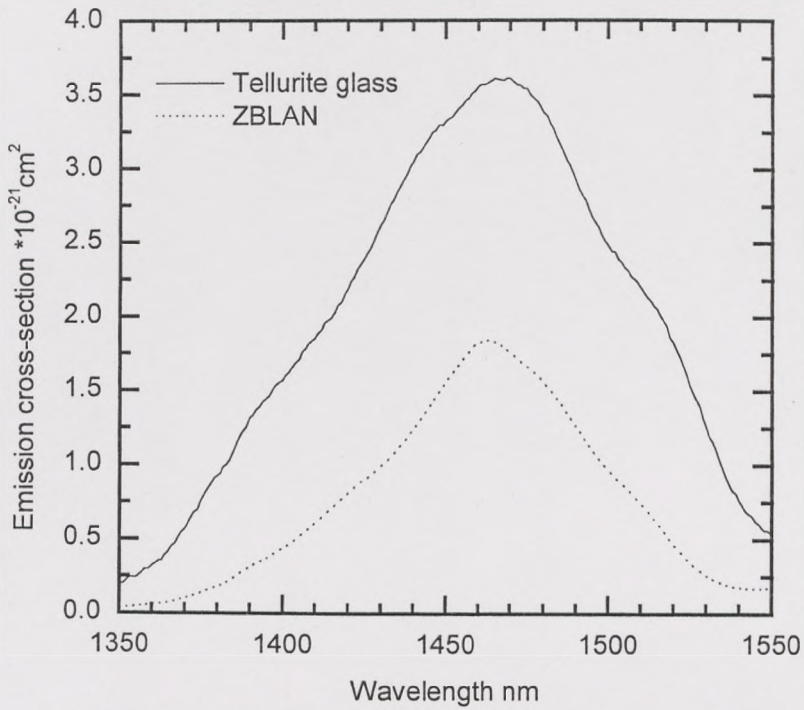


Fig. 9.4 Emission cross-section of Tm^{3+} ion in tellurite and ZBLAN glasses

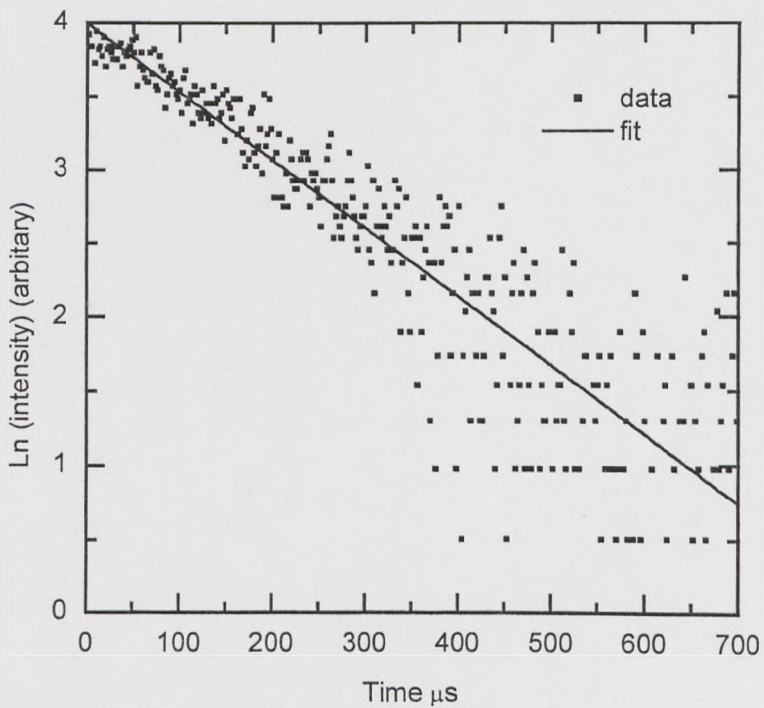


Fig. 9.5 Tm^{3+} at 1470 nm fluorescence decay in tellurite glass

The multiphonon relaxation lifetimes were calculated from [10]:

$$\tau^{-1} = W_{mp} = W_0 \exp(-\alpha\Delta E) \quad 9.1$$

where W_0 and α are respectively $6.3 \times 10^{10} \text{ s}^{-1}$ and $4.7 \times 10^{-3} \text{ cm}$ for tellurite, and $1.8 \times 10^{10} \text{ s}^{-1}$ and $5.8 \times 10^{-3} \text{ cm}$ for ZBLAN, and ΔE is the energy gap, equal to 4400 cm^{-1} . Although the phonon energy in tellurite glass (660 cm^{-1}) is higher than that in ZBLAN (580 cm^{-1}), leading to faster multiphonon decay, in both of these glasses, the multiphonon relaxation lifetime is much longer (by a factor of 50, see table 9.1) than the radiative lifetime. Therefore quantum efficiencies of nearly 100% should also be achievable in tellurite glass.

The nonradiative lifetimes τ_{nr} were calculated from the relation $\tau_{meas}^{-1} = \tau_{rad}^{-1} + \tau_{nr}^{-1}$, and were much shorter than the multiphonon decay lifetimes. An additional large contribution to nonradiative decay is impurity quenching, mainly by OH^- in the glass as discussed above. It is also possible that the high doping level (0.5 mol%) Tm^{3+} gives rise to concentration quenching effects, as observed by Wang et al [11] in a different type of tellurite glasses.

The branching ratio β from the ${}^3\text{H}_4$ state to ${}^3\text{H}_6$, ${}^3\text{F}_4$ and ${}^3\text{H}_5$ is the same between tellurite and ZBLAN.

The figure-of-merit (FOM) for gain has been defined in the last chapter as the product of stimulated emission cross-section and lifetime ($\sigma_{se} \times \tau_{meas}$). Here we have used FOM for gain, in order to discount the quenching effects of impurities. Generally, this product tends to decrease in high refractive index hosts because of the short lifetime. As a result, the FOM for gain is 50% lower in tellurite than in ZBLAN. However, the figure-of-merit gain bandwidth of an amplifier is determined largely by the width of the emission spectrum and cross-section which was defined as the product $\sigma_{se} \times \text{FWHM}$. The FOM for bandwidth is then nearly 3 times larger in tellurite than in ZBLAN. This definition may be justified by noting, for example, that when the emission cross-section is 0.16 pm (0.5 dB level in ZBLAN, 3.5 dB level in tellurite) the width of the spectrum is 40 nm in ZBLAN and 125 nm in tellurite glass. Yamada et al [12] describe a Tm^{3+} doped fluoride (ZBLAN) amplifier operating at

wavelength 1443-1484 nm with a bandwidth of 37 nm. Assuming that the FOM for bandwidth, as described above, is an indication of the achievable gain band, the results presented here suggest that a Tm^{3+} tellurite amplifier may have an extended bandwidth of over 100 nm.

Table 9.1. Spectroscopic parameters of Tm^{3+} -doped tellurite and ZBLAN glasses

	Tm^{3+} -tellurite glass	Tm^{3+} -ZBLAN glass
Host glass composition	75TeO ₂ :10ZnO:15Na ₂ O	52ZrF ₄ :20BaF ₂ :3LaF ₃ : 4AlF ₃ :20NaF
Refractive index at 633 nm	2.05	1.50
Peak emission wavelength $^3\text{H}_4 \rightarrow ^3\text{F}_4$, nm	1458 ± 1	1452 ± 1
FWHM of $^3\text{H}_4 \rightarrow ^3\text{F}_4$ emission, nm	114 ± 2	76 ± 2
τ_{meas} measured lifetime of $^3\text{H}_4$ level, ms	0.31 ± 0.01	0.74 ± 0.02 1.25-1.40 [1, 2, 4-6]
τ_{rad} calculated lifetime of $^3\text{H}_4$ level, ms	0.35 ± 0.03	1.31 ± 0.1
τ_{lower} calculated lifetime of $^3\text{F}_4$ level, ms	1.8 ± 0.2	7.2 ± 0.7
Non-radiative lifetime $\tau_{\text{nr}} = (\tau_{\text{meas}}^{-1} - \tau_{\text{rad}}^{-1})^{-1}$, ms	2.7 ± 1.3	1.7 ± 0.4
Multiphonon relaxation lifetime $^3\text{H}_4 \rightarrow ^3\text{F}_4$ τ_{mp} , ms	15 ± 3	6 000 ± 1000
Branch ratio β at $^3\text{H}_4$ level		
→ $^3\text{H}_6$, 0.8 μm	90 %	90 %
→ $^3\text{F}_4$, 1.46 μm	8 %	8 %
→ $^3\text{H}_5$, 2.3 μm	2 %	2 %
Quantum efficiency:		
$\tau_{\text{meas}} / \tau_{\text{rad}}$	80 ± 10%	55 ± 5%
predicted: $\tau_{\text{meas}} / \tau_{\text{rad}}$	98 ± 10%	~ 100% [1, 2, 4-6]
Stimulated emission cross-	0.36 ± 0.06	0.18 ± 0.03

section σ_{se} , pm^2		
Absorption cross-section for pump σ_{abs} , pm^2	0.89 ± 0.03	0.33 ± 0.01
Judd-Ofelt parameters		
Ω_2 , pm^2	3.8 ± 0.3	2.2 ± 0.2
Ω_4 , pm^2	1.8 ± 0.2	1.6 ± 0.2
Ω_6 , pm^2	1.3 ± 0.1	1.3 ± 0.1
FOM gain $\sigma_{se} \times \tau_{rad}$	0.13 ± 0.03	0.24 ± 0.05
FOM bandwidth $\sigma_{se} \times \text{FWHM}$	40 ± 5	15 ± 3

9.3 Broadband amplifiers

9.3.1 Tm^{3+} - Er^{3+} amplifier

Currently, there is a strong commercial imperative among designers of components for optical system to provide more sources of optical amplification that will cover all of the available bandwidth, and thereby allow further channels to be multiplexed over the same fibre. Therefore, broadband amplifiers are necessary for communication systems. A recent development in this direction has been the demonstration of tellurite glass EDFA having broadband flat gain bandwidth of 70 nm [13-18]. This device takes advantage of the broad emission and large cross-section of Er^{3+} in tellurite glass host. The gain bandwidth of tellurite EDFA can be extended further by combining it with a Tm^{3+} doped amplifier which offers gain on the short wavelength of the EDFA band [1, 3-4]. A combined device comprising a Tm^{3+} -doped fluoride amplifier and a tellurite EDFA has already been demonstrated [12]. However, the device exhibited two separated gain bands, at 1443-1484 nm (Tm^{3+} -fluoride band) and 1532-1608 nm (Er^{3+} -tellurite band). Clearly, a continuous gain band would be preferable. From the comparison of tellurite and fluoride glasses above, the gain bandwidth of Tm^{3+} doped tellurite glass has much more advantages than Tm^{3+} doped fluoride glass. In order to clarify the issues related to combining

two devices, figure 9.6 illustrates the Tm^{3+} and Er^{3+} emission spectra in the two glasses.

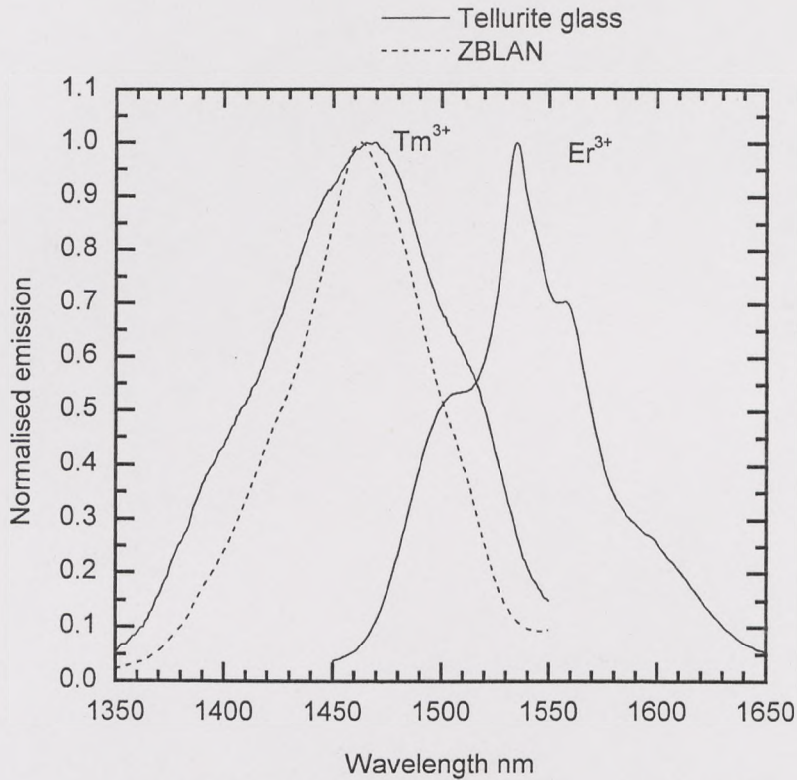


Fig 9.6 Tm^{3+} and Er^{3+} emission spectra in tellurite and ZBLAN glasses

The Tm^{3+} -tellurite and Er^{3+} -tellurite emission spectra intersect at a higher level and longer wavelength than do the Tm^{3+} -ZBLAN and Er^{3+} -tellurite spectra. The data therefore indicate that a Tm^{3+} -doped tellurite fibre amplifier will be more suitable for providing continuous gain when combined with a tellurite EDFA. This may be achieved, in particular, by pumping the tellurite EDFA at 980 nm, thus allowing gain at shorter wavelengths. Since Tm^{3+} tellurite amplifier may have an extended bandwidth over wavelengths of 1400-1520 nm, this combined amplifier device comprising Tm^{3+} - and Er^{3+} -doped tellurite fibres may produce a continuous gain band extending from around 1400 nm to around 1600 nm.

9.3.2 Nd^{3+} - Tm^{3+} - Er^{3+} amplifier

The amplifier bandwidth can be further extended to shorter wavelengths by adding a Nd^{3+} -doped tellurite glass module operating around 1340 nm. Over the

years, a variety of Nd^{3+} -doped glasses have been investigated as hosts for a 1.3 μm fibre amplifier [19-21]. Although the Nd^{3+} amplifier is highly efficient, the difficulty was to obtain gain below 1320 nm. Recently, the gain at 1310-1360 nm was demonstrated in fluoroaluminate glass [20, 21]. Nd^{3+} experiences a strong nephelauxetic shift [19], as a result, in tellurite glass the Nd^{3+} emission peak is red-shifted to 1340 nm. In a fibre geometry the 1.3 μm amplifying transition of Nd^{3+} suffers from the competition with amplified spontaneous emission (ASE) at 1.1 μm . Several methods of ASE filtering have been developed [21], and are applicable to tellurite fibres. Nd^{3+} doped tellurite glass fibre can therefore fill the gap between the Tm^{3+} -doped tellurite amplifier at 1.46 μm and the Nd^{3+} -doped fluoroaluminate amplifier at 1.32 μm . TZN tellurite glass was investigated as host for a Nd^{3+} -doped amplifier. Figure 9.7 shows the normalised emission spectra in TZN tellurite glass of Nd^{3+} , Tm^{3+} and Er^{3+} ions. The result on Nd^{3+} spectroscopy in TZN tellurite glass shows that a Nd^{3+} amplifier would complement Tm^{3+} and Er^{3+} devices in increasing further the available bandwidth.

Figure 9.8 shows the emission spectra of Nd^{3+} in tellurite and silicate glasses. There is a red shift in tellurite glass, the shoulder of the long wavelength emission spectra becomes lower and broader in silicate glass. Table 9.2 compares spectroscopic parameters of Nd^{3+} in tellurite and silicate glasses [19]. Silicate glass was chosen for comparison because it has the longest emission wavelength of all investigated (non-tellurite) glasses, and the preferred host for commercial devices. As was the case when Tm^{3+} emission was compared in tellurite and ZBLAN (above), the high refractive index of tellurite glass causes the emission cross-section of Nd^{3+} to be larger and the lifetime shorter than in silicate. As a result, the FOM for gain is 35% lower in tellurite than in silicate. In contrast with Tm^{3+} and Er^{3+} , the width of Nd^{3+} emission does not increase in tellurite glass and is similar to that in silicate. The FOM for bandwidth nevertheless benefits from the increased cross-section, and is 50% larger in tellurite than in silicate. However, the advantages of Nd^{3+} -doped tellurite glass as compared to silicate are not as great as in the case of Tm^{3+} and Er^{3+} , primarily because its emission profile does not change significantly and its width does not increase.

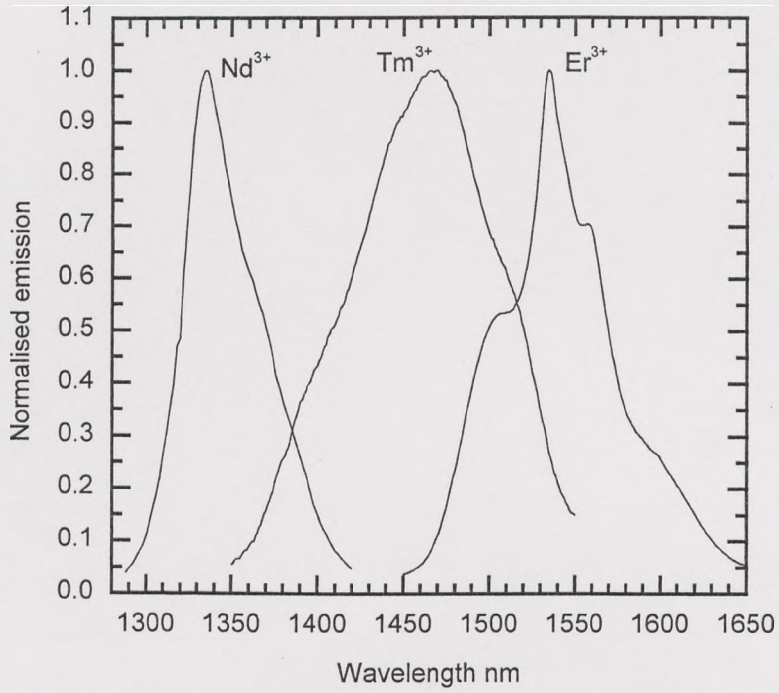


Fig. 9.7 Nd³⁺, Tm³⁺ and Er³⁺ emission spectra in tellurite glass

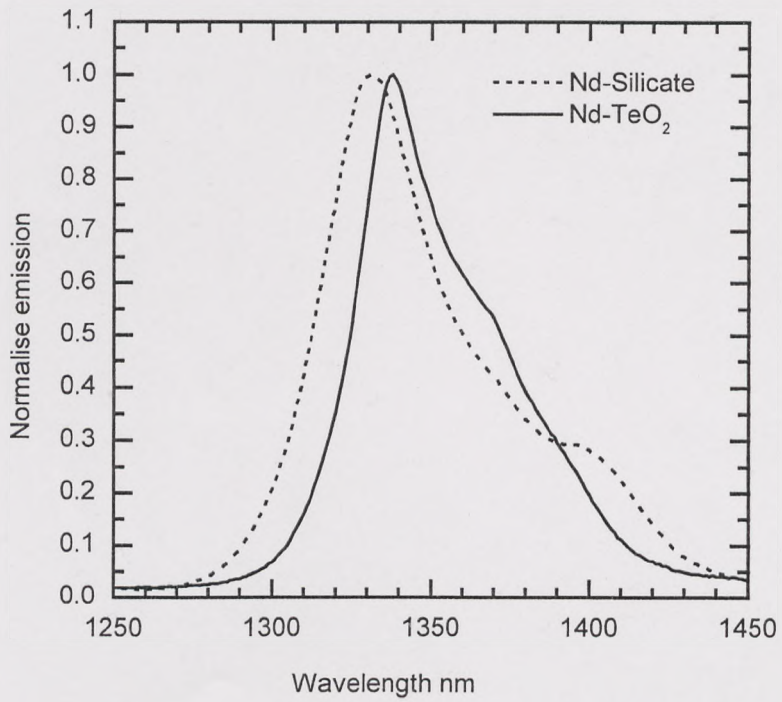


Fig. 9.8 Nd³⁺ emission spectra in silicate and tellurite glasses

Table 9.2 Emission parameters of Nd-doped TZN and silicate glasses

parameter	TZN	Silicate [19]
Peak emission wavelength, nm	1337 ± 1	1334 ± 1
FWHM of emission, nm	51 ± 1	54 ± 1
Fluorescence lifetime, μs	200 ± 5	436 ± 5
Stimulated emission cross-section σ_{se} , pm^2	0.98 ± 0.05	0.62 ± 0.05
FOM gain, $\sigma_{\text{se}} \times \tau$	196 ± 10	270 ± 10
FOM bandwidth, $\sigma_{\text{se}} \times \text{FWHM}$	50 ± 5	33 ± 3

From the emission spectrum and comparison with silicate glass, a Nd^{3+} doped amplifier operating around $1.34 \mu\text{m}$ is clearly desirable in TZN tellurite glass. Since it would bridge the wavelength gap between the 2nd and 3rd telecom windows, a continuous gain band extending from 1310 to 1600 nm may become possible by using Nd^{3+} , Tm^{3+} and Er^{3+} amplifiers. However, more work is required to determine whether TZN tellurite glass is the most advantageous host for such a device, or the glass composition can be redesigned to improve its performance.

9.4 Conclusions

1. In tellurite glass was shown to have several important advantages over ZBLAN as a host for a 1.47 μm Tm^{3+} -doped amplifier. The 1.47 μm fluorescence peak is 50% broader in tellurite, and the stimulated emission cross-section is twice as large. Although the radiative lifetime is much shorter, the quantum efficiency can approach 100%, as it does in ZBLAN. The pump absorption cross-section at 0.79 μm is three times larger, due to the hypersensitivity of this transition. Tm^{3+} -doped tellurite glass appears to be a highly promising host for a 1.47 μm amplifier capable of providing extended short-wavelength gain and a continuous band with the tellurite EDFA.
2. A Nd^{3+} -doped amplifier operating around 1.34 μm is clearly desirable in TZN tellurite glass. Since it would bridge the wavelength gap between the 2nd and 3rd telecom windows, a continuous gain band extending from 1310 to 1600 nm may become possible by using Nd^{3+} , Tm^{3+} and Er^{3+} amplifiers.

References

1. Percival, R. M., and J. R. Williams, *Electron Lett*, **30**, 1684 (1994).
2. Komukai, T., T. Yamamoto, T. Sugawa, and Y. Miyajima, *IEEE J. Quantum Elect.* **31**, 1880 (1995).
3. Kani, J., T. Sakamoto, M. Jinno, T. Kanamori, M. Yamada, and K. Oguchi, *Electron Lett*, **34**, 1118 (1998).
4. Sakamoto, T., M. Shimizu, T. Kanamori, Y. Terunuma, Y. Ohoshi, M. Yamada and S. Sudo, *IEEE Photon Tech Lett* **7**, 983 (1995).
5. Allen, R., L. Esterowitz and I. Aggarwal, *IEEE J. Quantum Elect.* **29**, 303 (1993).
6. Wang, J. S., E. M. Vogel, and E. Snitzer, *Optical Materials*, **3**, 187 (1994).
7. Spector, N., R. Reisfeld, and L. Boehm, *Chem Phys Lett*, **49**, 49 (1977).
8. Sanz, J., R. Cases, and R. Alcala, *J. Non-Cryst. Solids*, **93**, 377 (1987).
9. Smart, R. G., J. N. Carter, A. C. Tropper, and D. C. Hanna, *Opt. Commun.* **82**, 563 (1991).
10. Reisfeld, R. and C. K. Jorgensen, "Excited state phenomena in vitreous materials", ch 58 in "Handbook of physics and chemistry of rare-earths", ed K. A. Gschneider, jr and L-R Eyring, Elsevier, Amsterdam, pp1-90, 1987.
11. Wang, J. S., E. Snitzer, E. M. Vogel, and G. H. Sigel, Jr, *J Luminescence*, **60&61**, 145 (1994).
12. Yamada, M., A. Mori, k. k obayashi, H. Ono, T. Kanamori, K. Oikawa, Y. Nishida, and Y. Ohishi, , *IEEE Photon Tech Lett.* **10**, 1244 (1998).
13. Mori, A., Y. Ohishi, and S. Sudo, *Electronics Letters*, **33**, 863 (1997).
14. Mori, A., Y. Ohishi, M. Yamada, H. Ono, Y. Nishida, K. Oikawa, and S. Sudo, *OFC'97*, Washington, 1997, PD1.
15. Mori, A., K. Kobayashi, M. Yamada, T. Kanamori, K. Oikawa, Y. Nishida, and Y. Ohishi, *Electronics Letters*, **34**, 887 (1998).
16. Yamada, M., A. Mori, H. Ono, K. Kobayashi, T. Kanamori, and Y. Ohishi, *Electronics Letters*, **34**, 370 (1998).
17. Yamada, M., A. Mori, K. Kobayashi, H. Ono, T. Kanamori, K. Oikawa, Y. Nishida, and Y. Ohishi, *OAA'1998*, pp. 86-89
18. Nakai, T., Y. Noda, T. Tani, Y. Mimura, T. Sudo, and S. Ohno, *OAA'1998*, pp. 82-85.

19. Zemon, S., W. J. Miniscalco, G. Lambert, B. A. Thomson, M. A. Newhouse, P. A. Tick, L. J. Button, and D. W. Hall, "Comparison of Nd³⁺-doped glasses for amplification in the 1300-nm region", *Proc. SPIE*, Vol.1789, 1993.
20. Naftaly, M., A. Jha, E. R. Taylor, "Spectroscopic properties of Nd³⁺ in fluoroaluminate glasses for an efficient 1.3μm optical amplifier", accepted for publication in *J. Non-Cryst. Solids*.
21. Jha, A., M. Naftaly, E. R. Taylor, B. N. Samson, D. Marchese, D. N. Payne, *IR Glass Optical Fibres & Application*, **3416**, ch29, 115 (1998).

Chapter 10

Recommendations for further work

In Er^{3+} doped fluorosilicate and HMO germanate glasses, the emission broadness related to F/O ratio and heavy metal oxide could be studied further by Raman spectroscopy of these glasses. Making fibre and measuring Er^{3+} ion fluorescence in the fibre from these glasses are also very necessary for EDFA in fluorosilicate and HMO germanate glasses.

Site selection spectra for all Er^{3+} doped oxide glasses (fluorosilicate, HMO germanate and tellurite glasses) could be checked. The technique of fluorescence line narrowing (FLN) can be employed to detect the different sites.

Improve the quality of tellurite glass fibre: purifying the chemicals and improving the glass melting process including melting temperature, time and atmosphere, stirring and refining to achieve the loss in fibre less than 1 dB/m.

For Tm^{3+} doped tellurite glass, there is a lot composition search which must be completed to find an emission band which overlaps with the C-band of EDFA. After all, good quality fibre of this kind of tellurite glass is needed to make practical TDFA.

Appendix

A large portion of this work has been presented at national and international conferences. Papers have also been published in related journals. Two patents have been issued.

Publication List:

1. M Naftaly, S Shen, A Jha: "Tm³⁺-doped tellurite glass for a broadband amplifier at 1.46 μm", *Applied Optics*, Vol 39/27(2000), pp4979-4984.
2. A Jha, S Shen, M Naftaly: "The structural origin of spectral broadening of 1.5 μm emission in Er³⁺-doped tellurite glasses", *Physical Review B*, vol 62, No10, pp6215, Sept 2000.
3. S Shen, M Naftaly, A Jha: "Broadband 1.5 μm emission spectroscopy of Er³⁺-doped tellurite glasses", 11th International Symposium on Non-Oxide & New Optical Glasses, Sep 1998, Sheffield, Extended Abstract, pp177.
4. S Shen, M Naftaly, A Jha: "Emission Spectra and lifetimes in Er³⁺-doped tellurite glasses", PREP'99, Jan 1999, Manchester, Institute of Physics, pp57-64.
5. S Shen, M Naftaly, A Jha: "Tm³⁺- and Er³⁺-doped tellurite glass fibres for a broadband amplifier at 1430-1600 nm", *Infrared Optical Fibers and their Applications*, 1999, Vol 3849, Ch 23, pp 103-110, M Saad, JA Harrington eds., SPIE Conference on Infrared Optical Fibers and their Applications, Boston, MA, USA 21-22 September 1999.
6. M Naftaly, S Shen, A Jha: "Spectroscopy of Nd³⁺, Tm³⁺ and Er³⁺ ions in tellurite glasses and fibres for broadband optical fibre amplifiers in the 1350-nm to 1600-nm range", *Design, Fabrication and Characterization of Photonic Devices*, 1999, Vol 3896, Ch 92, pp 298-305, M Osinski, SJ Chua, SF Chichibu eds., SPIE Conference on Design, Fabrication, and Characterization of Photonic Devices, Singapore, Singapore, 30 November - 3 December 1999.
7. S Shen, M Naftaly, A Jha: "Crystallization kinetics of tellurite glasses studied by DSC and DTA", *Int. Symp. On Crystallisation in Glasses and Liquids*, Glastechn. Ber. Glass Sci. Technol. 73 C1(2000), pp111-118.
8. S Shen, A Jha, X Liu, M Naftaly, K Bindra, H. J. Bookey, and A. K. Kar, "TeO₂ glasses for broadband amplifiers and integrated optics", *American Ceramic Society, The proceedings of Photonic materials, components, and Applications*, paper A4-020-00.
9. S Shen, M Naftaly, A Jha: "Broadband Infrared Photoluminescence in Germanate Glass", CLEO/Europe'00 Conference, September 2000, Nice, France.

10. S Shen, M Naftaly, A Jha: "Broadband Infrared Photoluminescence in Heavy-Metal-Oxide", Glass and Optical Materials Division Fall Meeting, The American Ceramic Society, in Corning, NY, 1-4 Oct 2000.
11. S Shen, M Naftaly, A Jha: "Germanate and Germanate-tellurite Glasses for High-Gain EDFA", Glass and Optical Materials Division Fall Meeting, The American Ceramic Society, in Corning, NY, 1-4 Oct 2000.

Patent

1. ERBIUM DOPED OPTICAL GLASS, International Patent Application No. PCT/GB99/00726
2. A WIDE BAND OPTICAL AMPLIFIER, UK Patent Application No. 9914549.2